

LEED CRYSTALLOGRAPHIC STUDIES FOR CHEMISORPTION
ON RHODIUM AND ZIRCONIUM SURFACES

by

PHILIP C.L. WONG

B.S. Soochow University, 1975

M.A. University of Texas at Arlington, 1982

A THESIS SUBMITTED IN PARTIAL FULFILMENT
OF THE REQUIREMENTS FOR THE DEGREE OF
DOCTOR OF PHILOSOPHY

in

THE FACULTY OF GRADUATE STUDIES

(Department of Chemistry)

We accept this thesis as conforming
to the required standard

THE UNIVERSITY OF BRITISH COLUMBIA

July 1987

© Philip C.L. Wong, 1987

In presenting this thesis in partial fulfilment of the requirements for an advanced degree at the University of British Columbia, I agree that the Library shall make it freely available for reference and study. I further agree that permission for extensive copying of this thesis for scholarly purposes may be granted by the head of my department or by his or her representatives. It is understood that copying or publication of this thesis for financial gain shall not be allowed without my written permission.

Department of CHEMISTRY

The University of British Columbia
1956 Main Mall
Vancouver, Canada
V6T 1Y3

Date Sept. 30 1987

Abstract

The work in this thesis includes crystallographic investigations with low-energy electron diffraction (LEED) for the surface structures designated Rh(111)-($\sqrt{3}\times\sqrt{3}$)30°-S, Rh(111)-(2x2)-O, Zr(0001)-(1x1)-O and Zr(0001)-(1x1)-N. In each case intensity-versus-energy (I(E)) curves for a set of diffracted beams were measured with a video LEED analyzer, and then compared with the results of multiple scattering calculations made for various structural models. Levels of correspondence between experimental and calculated I(E) curves were assessed with the reliability index proposed by Pendry, and surface geometries were determined by the conditions for the best correspondence.

The LEED intensity analyses for both the Rh(111)-($\sqrt{3}\times\sqrt{3}$)30°-S and Rh(111)-(2x2)-O surface structures indicate that S and O atoms adsorb respectively 1.53Å and 1.23Å above the "expected" hollow sites of three-fold coordination. These values correspond to nearest-neighbor Rh-S and Rh-O bond distances equal to 2.18 and 1.98Å respectively. For the Zr(0001)-(1x1)-O and Zr(0001)-(1x1)-N surface structures studied, the multiple-scattering analyses suggest that the first involves O atoms occupying octahedral holes between successive bulk Zr layers, and that the substrate Zr layers undergo a fcc type reconstruction. By contrast the N atoms in Zr(0001)-(1x1)-N appear to just occupy octahedral holes between the first and second layers of hcp zirconium, exactly as reported by Shih et al. for the analogous structure formed on titanium. The LEED-determined

Zr-O and Zr-N bond distances are 2.30 and 2.27Å respectively, in very close agreement with the values determined by X-ray crystallography for bulk ZrO (2.31Å) and bulk ZrN (2.29Å).

A preliminary study of oxygen chemisorption on the Zr(0001) surface has been made in the low-exposure regime with Auger electron spectroscopy (AES) and with measurements of the width of a half-order LEED beam. Some observations and conclusions are: (i) the diffusion of O atoms to the bulk effectively starts at around 236°C; (ii) oxygen adsorbs in a disordered state at room temperature but orders sufficiently to show a (2x2)-type LEED pattern on heating to 220°C; (iii) with increasing O exposure, 1/4, 1/2 and 3/4 of the available sites can be systematically filled, prior to the establishment of an ordered (1x1)-O surface; (iv) the process in (iii) can be reversed by starting with the (1x1)-O surface and heating above 236°C.

LEED and AES have also been used to compare the adsorption and coadsorption of O₂ and H₂S on the Zr(0001) surface for exposures in the one to five Langmuir regime. The new observations made are: (i) sulfur forms a stable (3x3) surface structure after heating to 600°C; (ii) the Zr(0001) surface with high O coverage can still adsorb H₂S, whereas the Zr(0001) surface with high S coverage does not adsorb oxygen in detectable amounts; (iii) for surfaces with adsorbed H₂S the 150 eV to 92 eV Auger peak ratio suddenly increases on heating to 530°C. Observation (iii) has been tentatively interpreted in terms of hydrogen desorption. Finally, a set of I(E) curves were measured for normal incidence on the Zr(0001)-(3x3)-S surface.

Table of Contents

	Page
Abstract	ii
Table of Contents	iv
List of Tables	ix
List of Figures	x
Acknowledgements.	xviii
Chapter 1: Introduction	1
1.1 Introduction	2
1.2 Classification of Surface Structure	5
1.3 Reciprocal Net	6
1.4 Low Energy Electron Diffraction (LEED)	9
1.4.1 Electron Scattering in Solids	9
1.4.2 Conditions for Elastic LEED	10
1.4.3 Two-dimensional LEED Analysis	15
1.4.4 LEED Crystallography	19
1.4.5 Instrumental Response, Domains and Disorder	23
1.5 Auger Electron Spectroscopy (AES)	27
1.6 Aim of Thesis	30

	Page
Chapter 2: Calculation of LEED Intensities	33
2.1 Introduction	34
2.2 Geometrical and Non-geometrical Parameters	35
2.3 The Muffin-tin Approximation	38
2.4 Ion Core Scattering	42
2.5 Intralayer Scattering	45
2.6 Interlayer Scattering	50
2.6.1 Layer Doubling Method	51
2.6.2 Renormalized Forward Scattering Method	54
2.7 Application of Symmetry in the "Combined Space" Method	58
2.8 Evaluation of Results	59
 Chapter 3: Experimental Methods	 62
3.1 UHV Chamber and Apparatus	63
3.2 Sample Preparation	67
3.3 Cleaning in UHV Chamber	69
3.4 Apparatus for Auger Electron Spectroscopy	71
3.5 Apparatus for LEED	73
3.5.1 LEED Optics and Electron Gun	73
3.5.2 Measurement of LEED Intensities	76
3.5.3 Measurement of Spot Profile	82

	Page
Chapter 4: LEED Analysis for the Rh(111)-($\sqrt{3}\times\sqrt{3}$)30°-S Surface	
Structure	84
4.1 Introduction	85
4.2 Experimental	86
4.3 Calculations and Results	93
4.4 Discussion	98
Chapter 5: LEED Investigation of the Rh(111)-(2x2)-0 Surface	
Structure	105
5.1 Introduction	106
5.2 Experimental	107
5.3 Calculations	108
5.4 Results	110
5.5 Discussion	114
Chapter 6: Adsorption of Oxygen on the (0001) Surface of	
Zirconium	122
6.1 Introduction	123
6.2 Experimental	126
6.2.1 Sample Preparation and Cleaning	126
6.2.2 LEED Pattern for Oxygen Adsorption on	
Zr(0001)	128

	Page
6.2.3 AES and LEED Spot Profile Measurements for Zr(0001)-(2x2)-0	129
6.2.4 Measurements of I(E) Curves from the Lowest-coverage Zr(0001)-(1x1)-0 Surface Structure	135
6.3 Multiple Scattering Calculations for Zr(0001)-(1x1)-0	137
6.4 LEED Crystallographic Results for the Initial Zr(0001)-(1x1)-0 Structure	139
6.5 Discussion	147
Chapter 7: A LEED Crystallographic Investigation of a Surface Structure Designated Zr(0001)-(1x1)-N	151
7.1 Introduction	152
7.2 Experimental	152
7.3 Calculations	156
7.4 Results	161
7.5 Discussion	161

	Page
Chapter 8: Comparison of Oxygen and Sulfur Adsorption on the (0001) Surface of Zirconium	174
8.1 Introduction	175
8.2 Experimental	175
8.3 Results	176
8.3.1 Oxygen Adsorption	177
8.3.2 Hydrogen Sulfide Adsorption	177
8.3.3 Oxygen and Hydrogen Sulfide Coadsorption	180
8.3.3.1 O ₂ on Zr(0001)-(3x3)-S with R _s > 3.1	180
8.3.3.2 O ₂ on Zr(0001)-(3x3)-S with R _s < 3.1	180
8.3.3.3 H ₂ S on Zr(0001)-(2x2)-O	184
8.3.3.4 H ₂ S on Zr(0001)-(1x1)-O	185
8.3.3.5 Coadsorption without Annealing	185
8.4 Discussion	185
8.5 Further work	188
Concluding remarks	189
References	191

List of Tables

	Page
Table 1.1	Some surface techniques and their characteristics. 4
Table 4.1	Comparison of measured and predicted S-Rh bond lengths for S atoms adsorbed on the (111), (100), (110) surfaces of rhodium 104
Table 6.1	Five representative studies of the oxidation of zirconium using different surface techniques and surface treatments 124
Table 6.2	Values of Zr-O interlayer spacings and V_{or} corresponding to minima in contour plots of R_p for structural models of Zr(0001)-(1x1)-O 141
Table 6.3	Values of Zr-O interlayer spacings and V_{or} corresponding to minima in contour plots of R_p for two structural models of Zr(0001)-(1x1)-O using phase shift for negatively charged O 148
Table 7.1	Values of Zr-N interlayer spacings corresponding to minima in contour plots of R_p for structural models of Zr(0001)-(1x1)-N 162

List of Figures

	Page	
Figure 1.1	The five types of two-dimensional surface meshes (a) in real space (b) in reciprocal space	7
Figure 1.2	A two-dimensional net in real space (filled circles) described by unit translation vectors \mathbf{a}_1 , \mathbf{a}_2 and the associated net in reciprocal space (open circles) described by unit translation vectors \mathbf{a}_1^* , \mathbf{a}_2^*	8
Figure 1.3	Schematic energy distribution $N(E)$ of back-scattered electrons for a primary beam of energy E_p	11
Figure 1.4	Schematic diagram of the mean free path for electrons in a metallic solid as a function of energy	11
Figure 1.5	Conventions to describe the incidence direction for an electron beam interacting with a surface; θ is the polar angle relative to the surface normal and ϕ is an azimuthal angle relative to a major crystallo- graphic axis in the surface plane	13
Figure 1.6	Schematic diagram illustrating how the conservation conditions determine direction of a diffracted beam. The (00) beam corresponds to the specular reflection	16
Figure 1.7	Some common translational symmetries (unit meshes) for adsorption on fcc(111) or hcp(0001) surfaces using both Wood's notation and the matrix notation.	18
Figure 1.8	(a) Unit mesh of the $(\sqrt{3} \times \sqrt{3})30^\circ$ overlayer structure and four possible adsorption sites for sulfur adsorbed on Rh(111). The 3h and 3f sites are three- fold sites which are distinguished respectively by whether there is a substrate atom or not located directly below the second layer. (b) Schematic LEED pattern corresponding to the overlayer structure of (a)	20
Figure 1.9	Comparison of an $I(E)$ curve measured for the $(1/3$ $1/3)$ diffracted beam from Rh(111)- $(\sqrt{3} \times \sqrt{3})30^\circ$ -S at normal incidence with those calculated for the 3f and 3h adsorption sites over a range of the topmost S-Rh interlayer spacings	21

	Page	
Figure 1.10	A (2x2) structure on a fcc(111) or hcp(0001) surface is shown bottom left, while the corresponding LEED pattern is drawn schematically at bottom right (the half-order beams are identified by crosses). The top shows three domains of a (1x2) type structure which are related by 120° rotations. The total LEED pattern from a surface with equal populations of these domain types will be a superposition of the three individual patterns. This superposition gives spots in identical positions to the (2x2) pattern.	25
Figure 1.11	(a) Side view and (b) top view of the two types of domains resulting from the truncation of the hcp bulk structure parallel to the (0001) plane. The two domains are related to each other by a 180° rotation. (c) Superposition of the two 3-fold symmetrical LEED patterns (expected for normal incidence) to form a LEED pattern with 6-fold symmetry	26
Figure 1.12	Schematic representation of an Auger process in terms of atomic and valence band energy levels. This example is specifically for the production of a KL_2L_3 Auger electron	28
Figure 2.1	Example of relaxation at a fcc(111) surface. The three-dimensional propagation vectors \vec{ASB} and \vec{ASA} apply to the relaxed region and bulk region respectively. The corresponding interlayer spacings D' and D are shown to the left	36
Figure 2.2	Variation of potential for the muffin-tin model: (a) contour plot through an atomic layer, and (b) variation through a single row of ion cores along the x-axis	39
Figure 2.3	Scattering of a set of plane waves by a layer of ion cores with diffraction matrix $M^{\pm\pm}$	46
Figure 2.4	Graphitic-type oxygen overlayer for Rh(111)-(2x2)-0; there are two oxygen atoms (shaded circles) per unit mesh, one on a 3f site the other on 3h site (as in Figure 1.8(a))	48
Figure 2.5	Schematic diagram of transmission and reflection matrices at the nth layer. The dashed lines are midway between consecutive layers	48

	Page	
Figure 2.6	Schematic indication of the layer doubling method as applied to stacking four individual layers (with A.B.A.B... registries) into an slab (after Tong [62])	52
Figure 2.7	Schematic indication of the renormalized forward scattering method. (a) Each triplet of arrows represents the complete set of plane waves that travel from layer to layer. (b) Illustration of the vectors which store the amplitudes of the inward- and outward-travelling waves (after Van Hove and Tong [44])	55
Figure 2.8	LEED pattern at normal incidence from Rh(111)-(2x2)-0 (a) Symmetry-related beams are indicated by the same symbols. (b) Beams belonging to the same beam set are indicated by the same number (independent of angle of incidence)	60
Figure 3.1	Schematic diagram of the FC12 UHV chamber with some important facilities used for the experiments made in this work (CMA = cylindrical mirror analyzer)	64
Figure 3.2	Representation of the pumping system and gas handling line (I.P. = ion pump; S.P. = sorption pump; T.S.P. = titanium sublimation pump; D.P. = diffusion pump; T.C. = thermocouple)	66
Figure 3.3	Laser method to check the angular misalignment (θ) between the optical face and desired crystal plane. .	68
Figure 3.4	Schematic diagram to illustrate the measurement of Auger electron spectra using a cylindrical mirror analyzer in combination with a glancing angle electron gun	72
Figure 3.5	Schematic diagram of the electron optics for the LEED display system	74
Figure 3.6	Schematic diagram for the TV analyzing system which detects and measures diffracted beam intensities from the LEED screen.	77
Figure 3.7	A frame on the monitor screen to illustrate: (a) the 256x256 pixels structure, (b) the scanning course. .	79

	Page	
Figure 3.8	I(E) curves measured for six essentially equivalent beams for normal incidence on the Zr(0001)-(1x1)-0 surface. The close correspondence confirms the incidence direction. The averaged and subsequently smoothed I(E) curves are displayed in the bottom two curves	81
Figure 3.9	Measurement of spot profiles: (a) the LEED spot to be measured is covered with a user-selected window (10x10 pixels), (b) the spot intensity profile along X_{win}	83
Figure 4.1	Auger spectra from Rh(111) surface: (a) as mounted, with considerable S (151 eV) and C (272 eV) contamination; (b) after Ar^+ bombardment, to show reduced S, but increased C; (c) after annealing, to show reduced C, but increased S; (d) after a full cleaning routine	87
Figure 4.2	Auger peak height ratio S (151 eV)/Rh (304 eV) plotted as a function of H_2S exposure to a Rh(111) surface	89
Figure 4.3	Schematic indications of LEED patterns from surfaces designated: (a) Rh(111)-(1x1); (b) Rh(111)-($\sqrt{3} \times \sqrt{3}$)30°-S; (c) Rh(111)-c(2x4)-S	91
Figure 4.4	Beam notations for a LEED pattern from the Rh(111)-($\sqrt{3} \times \sqrt{3}$)30°-S structure	92
Figure 4.5	I(E) curves for the (2/3 2/3) and (1/3 1/3) beams measured at normal incidence for two independent experiments on the Rh(111)-($\sqrt{3} \times \sqrt{3}$)30°-S structure	94
Figure 4.6	Comparison of nine I(E) curves measured for normal incidence on Rh(111)-($\sqrt{3} \times \sqrt{3}$)30°-S with those calculated for the 3f, 3h, 2f and 1f adsorption models with Rh-S interlayer spacings which give the best overall match between experiment and calculation for each model	96
Figure 4.7	Contour plots for Rh(111)-($\sqrt{3} \times \sqrt{3}$)30°-S of R_p versus V_{or} and the Rh-S interlayer spacing for four different structural models	99

	Page	
Figure 4.8	Comparison of experimental $I(E)$ curves for some integral-order and fractional-order beams from $\text{Rh}(111)-(\sqrt{3}\times\sqrt{3})30^\circ\text{-S}$ with those calculated for the 3f model with sulfur either 1.45 or 1.55 Å above the topmost rhodium layer	100
Figure 5.1	(a) Unit mesh of the (2x2) overlayer structure for oxygen adsorbed on $\text{Rh}(111)$. (b) Schematic LEED pattern and beam notations corresponding to the overlayer structure of (a)	109
Figure 5.2	Comparison of experimental $I(E)$ curves for (1/2 1), (1/2 1/2) and (0 3/2) diffracted beams from $\text{Rh}(111)-(2\times 2)\text{-O}$ at normal incidence with those calculated for the 3f, 3h and 3f+3h models over a range of the topmost O-Rh interlayer spacings	111
Figure 5.3	Contour plots for $\text{Rh}(111)-(2\times 2)\text{-O}$ of R_p versus V_{or} and the Rh-O interlayer spacing for (a) 3f, (b) 3h and (c) 3f+3h structural models	115
Figure 5.4	Comparison of experimental $I(E)$ curves for some integral-order and fractional-order beams from $\text{Rh}(111)-(2\times 2)\text{-O}$ at normal incidence with those calculated for the 3f model with oxygen either 1.164 or 1.264 Å above the topmost rhodium layer	118
Figure 6.1	Auger spectra of two $\text{Zr}(0001)$ surfaces: (a) as mounted (b) cleaned	127
Figure 6.2	Normalized Auger peak height ratio R_o^T/R_o^{int} as a function of heating temperature for oxygen on $\text{Zr}(0001)$; the initial coverage corresponds to $R_o = 0.16$	130
Figure 6.3	Measured variations for the (1, 1/2) beam at 66 eV with oxygen coverage on $\text{Zr}(0001)$: (a) normalized 1/FWHM, (b) normalized integrated intensity	132
Figure 6.4	Measured variation with heating temperature of normalized 1/FWHM for the (1, 1/2) beam at 66eV for initial oxygen coverages on $\text{Zr}(0001)$ with R_o equal to: (a) 0.12, (b) 0.16 and (c) 0.20	134

	Page	
Figure 6.5	Reciprocal net and beam notation for the Zr(0001)-(1x1)-O structure	136
Figure 6.6	Partial view of the Zr(0001)-(1x1)-O structure corresponding to the model designated (B)A(C)BAB... . Atoms in the topmost Zr layer are in A-type positions (open solid circles), while the second Zr layer has atoms in B-type positions. The oxygen overlayer (smaller shaded circles) has atoms in B-type positions, while the underlayer O atoms (darker circles) occupy the octahedral holes in C type positions	138
Figure 6.7	Contour plot for Zr(0001)-(1x1)-O of R_p versus V_{or} and the Zr-O interlayer spacing for the model A(C)B(A)C(B)A...	142
Figure 6.8	Comparison of experimental I(E) curves (dashed) from Zr(0001)-(1x1)-O with those calculated for the single-underlayer model A(C)BAB... with d_{Zr-O} equal to 1.33Å (upper continuous line designated a) and 1.37Å (lower continuous line designated b)	143
Figure 6.9	Comparison of experimental I(E) curves (dashed) from Zr(0001)-(1x1)-O with those calculated for the multi-underlayer model A(C)B(A)C(B)... with d_{Zr-O} equal to 1.33Å (upper continuous line designated a) and 1.37Å (lower continuous line designated b)	145
Figure 7.1	Auger peak height ratio N(383eV)/Zr(92eV) plotted as a function of nitrogen exposure	154
Figure 7.2	Normalized nitrogen Auger peak height ratio R_N^T/R_N^{int} as a function of heating temperature for nitrogen on Zr(0001); the initial coverage corresponds to $R_N =$ 0.25	155
Figure 7.3	Variations of the Zr Auger peak around 147 eV with nitrogen exposure on Zr(0001)	157

- Figure 7.4 Comparisons for (11) and (10) beams at normal incidence of experimental $I(E)$ curves (dashed) from $Zr(0001)-(1 \times 1)-N$ with those measured for clean $Zr(0001)$ and calculated for two models of $Zr(0001)-(1 \times 1)-N$, namely for the model $A(C)BAB\dots$ with d_{Zr-N} equal to 1.287 \AA (curves designated A) and for the model $A(C)B(C)AB\dots$ with d_{Zr-N} equal to 1.330 \AA (curves designated B) 158
- Figure 7.5 Contour plot for $Zr(0001)-(1 \times 1)-N$ of R_p versus V_{or} and the $Zr-N$ interlayer spacing for the model $A(C)BAB\dots$ 164
- Figure 7.6 Comparison of experimental $I(E)$ curves (dashed) from $Zr(0001)-(1 \times 1)-N$ with those calculated for the model $A(C)BAB\dots$ with d_{Zr-N} equal to 1.287 \AA (upper continuous line designated a) and 1.330 \AA (lower continuous line designated b) 165
- Figure 7.7 Comparison of experimental $I(E)$ curves (dashed) from $Zr(0001)-(1 \times 1)-N$ with those calculated for the model $A(B)CAB\dots$ with d_{Zr-N} equal to 1.287 \AA (upper continuous line designated a) and 1.330 \AA (lower continuous line designated b) 168
- Figure 7.8 Comparison of experimental $I(E)$ curve for the (10) beam from $Zr(0001)-(1 \times 1)-N$ for normal incidence with that calculated for the model $A(C)BAB\dots$ with the $Zr-N$ interlayer spacing equal to 1.287 \AA , as well as that calculated for the similar model which just differs from the first by neglect of N . The interlayer spacing between first two Zr layers in both models is identical 173
- Figure 8.1 Experimental $I(E)$ curves for the (11) beam from (a) clean $Zr(0001)$, (b) $Zr(0001)-(2 \times 2)-0$ with $R_o = 0.16$, (c) $Zr(0001)-(1 \times 1)-0$ with $R_o = 0.23$ 178
- Figure 8.2 Experimental $I(E)$ curves for the (11) beam from (a) clean $Zr(0001)$, (b) $Zr(0001)-(3 \times 3)-S$ with $R_s = 1.9$, (c) $Zr(0001)-(3 \times 3)-S$ with $R_s = 2.4$, (d) $Zr(0001)-(3 \times 3)-S$ with $R_s = 3.1$ 179

	Page
Figure 8.3 Schematic diagram for LEED pattern and beam notation for the $\text{Zr}(0001)-(3 \times 3)\text{-S}$ structure	181
Figure 8.4 I(E) curves measured for normal incidence from the $\text{Zr}(0001)-(3 \times 3)\text{-S}$ surface with $R_s = 3.1$ for the diffracted beams: $(1/3 \ 1)$, $(2/3 \ 2/3)$, (10) , $(2/3 \ 1/3)$, $(1/3 \ 1)$, $(2/3 \ 1)$, $(4/3 \ 1/3)$, $(4/3 \ 0)$ and $(0 \ 5/3)$	182
Figure 8.5 Some possible S overlayer structures (shaded circles) for the $\text{Zr}(0001)-(3 \times 3)\text{-S}$ surface. The sulfur coverages with respect to Zr (open circles) are: (A) $1/9 \text{ ML}$, (B) $2/9 \text{ ML}$, (C) $1/3 \text{ ML}$, (D) $4/9 \text{ ML}$. Lateral shifts of the S overlayers are possible	187

Acknowledgements

It has been a rewarding experience to work under my supervisor, Professor K.A.R. Mitchell, during the course of this work. I have appreciated his guidance and encouragement of my research, as well as his advice and comments on this thesis. I am also grateful to Professor D.C. Frost for jointly sponsoring the early part of this study.

My sincere thanks are owed to Dr. M.A. Van Hove (University of California, Berkeley) and Dr. S.Y. Tong (University of Wisconsin, Milwaukee) for providing us with copies of their computer programs for LEED calculations. I am also grateful to my Guidance Committee for meeting with me during the course of my graduate work, and especially to Professor J. Trotter for his reading, at short notice, of the final version of this thesis.

I would like to acknowledge the contributions of other members of our surface science group. I owe a special gratitude to Professor M.Y. Zhou (Xiamen University, China) and Dr. K.C. Hui, for their patience in guiding me as a new graduate student, and later to Dr. R.A. McFarlane, for reading the first draft of this thesis. I also appreciate my interactions with Dr. M.A. Karelowski, Mr. H.C. Zeng and Dr. R.N.S. Sodhi.

I am indebted to many members of the electrical and mechanical workshops who have contributed so much in maintaining our equipment in working order.

Finally, but foremost, a deep sense of gratitude and love is directed towards my parents and my wife, Ling Wong, who have spiritually supported me throughout the course of my study. To them, I dedicate this thesis.

CHAPTER 1

Introduction

1.1 Introduction

During the past two decades studies of solid surfaces, to give information on chemical, electronic and vibrational properties, have had great impact in materials science (e.g. in semiconductor analysis, heterogeneous catalysis, polymer coatings, corrosion phenomena). Indeed for all reactions between solid-solid, solid-liquid and solid-gas phase combinations, the boundary region (the interface or surface region) always plays an important role, particularly in the initial process. Traditional surface chemical studies have usually focused on macroscopic properties of "real" or "dirty" surfaces of polycrystalline material, but modern surface science emphasizes the use of "clean and well-defined" surfaces, especially of single crystals. The latter is leading to new and fundamental insights into the physics and chemistry of condensed matter, particularly when the surface structure is taken into account. Attempts to understand surface properties, without having adequate knowledge of structure at the atomic level, have in the main been unsuccessful.

Ideally the "clean surface approach" uses a single crystal surface which is well characterized with regard to chemical composition and defect structure; to control composition it must be held in an ultra high vacuum (UHV) environment (pressure $< 10^{-9}$ Torr). Low pressure is also essential for the operation of some surface analytical techniques such as low energy electron diffraction (LEED) and Auger electron spectroscopy (AES) which are involved in this work.

The arrangement of atoms and the distribution of electrons near the surface of a crystal can be different from those in the bulk of the crystal. Insofar as one can imagine a crystal as an array of balls connected by springs, then, as the springs are cut to form a surface, surface atoms would be expected to move away from the bulk positions. In turn other properties can be affected, including chemical reactivity. The structural changes that occur in the surface region may involve one or more atomic layers. The structural changes that occur on formation of a single-crystal surface are conventionally classified in relation to the structure of the corresponding plane in the bulk. If the diperiodicity does not change, the surface is said to have relaxed, whereas if the diperiodicity changes, the surface is said to have reconstructed. LEED distinguishes these possibilities. For example, the (111) surface of rhodium and the (0001) surface of zirconium, involved in this work, are slightly relaxed [1,2], while the (111) surface of silicon, annealed after cleaning by ion bombardment, undergoes a surface reconstruction and shows a (7x7) LEED pattern [3].

Recently there has been a rapid growth in available techniques for characterizing surfaces. The probe sources include electrons, photons, atoms and ions, and Table 1.1 summarizes some important surface analytical techniques for assessing composition as well as geometrical, electronic and vibrational structure. More details can be found in the references quoted under the first column in Table 1.1. In general, each technique may have particular advantages, but a "multi-technique strategy" can provide the most detailed overall view of a surface. In general, at least two

Table 1.1: Some surface techniques and their characteristics.

Technique	Acronym	Probe particle	Measured particle	Information
Auger electron spectroscopy [4,5]	AES	Electron	Electron	Composition
Secondary-ion mass spectroscopy [6]	SIMS	Ion	Ion	Composition
X-ray photoelectron spectroscopy [5]	XPS	Photon	Electron	Composition, valence states
Low-energy electron diffraction [7,8]	LEED	Electron	Electron	Geometrical structure
Reflection high-energy electron diffraction [9]	RHEED	Electron	Electron	Geometrical structure
X-ray diffraction [10]	XD	Photon	Photon	Geometrical structure
Photoelectron diffraction [11,12]	PD	Photon	Electron	Geometrical structure
Near-edge X-ray absorption fine structure [13]	NEXAFS	Photon	Photon, electron	Intramolecular bonding
Surface Extended X-ray absorption fine structure [13,14]	SEXAFS	Photon	Photon, electron	Geometrical structure
Rutherford back scattering [15]	RBS	Ion	Ion	Composition, geometrical structure
High-resolution electron energy loss spectroscopy [16]	HREELS	Electron	Electron	Vibrational structure
Ultra-violet photoelectron spectroscopy [17]	UPS	Photon	Electron	Valence state

complementary techniques are needed to answer the most fundamental questions of a surface region:

- (i) What atoms are present?
- (ii) How are these atoms arranged?

Of the techniques listed in Table 1.1 the most commonly and conveniently used methods to answer these questions are the combination of LEED and AES, although X-ray photoelectron spectroscopy is particularly valuable for assessing the state of atoms at a surface. LEED remains the most developed method for providing structural information, although other important techniques include photoelectron diffraction, SEXAFS, and ion scattering.

1.2 Classification of Surface Structure

A surface of a single crystal is conveniently classified with reference to the parallel plane within the bulk crystal. In addition, for a surface region, all equivalent points in a plane parallel to the surface are related by two-dimensional (diperiodic) translational vectors

$$\underline{t} = m\underline{a}_1 + n\underline{a}_2. \quad (m, n = \text{integers}) \quad (1.1)$$

The unit vectors \underline{a}_1 and \underline{a}_2 define a unit mesh in analogy with the unit cell of triperiodic crystallography, while the complete set of values of m and n generate a net in analogy with the use of the term lattice in triperiodic crystallography. Five types of unit mesh are possible. They are shown in

Figure 1.1(a) and they are analogous to the 14 Bravais unit cells of triperiodic crystallography. A surface studied in LEED is three-dimensional, but only diperiodic since, for the top few layers, no periodicity can be rigorously established in the direction normal to the surface. Details of various conventions in surface crystallography can be found in an article by Wood [18] and in the International Tables for X-ray crystallography [19].

1.3 Reciprocal Net

As in the bulk, it is very convenient to utilize a reciprocal space construction for representing diperiodic diffraction. Given unit vectors \underline{a}_1 and \underline{a}_2 in real space, the corresponding unit vectors \underline{a}_1^* and \underline{a}_2^* in reciprocal space are generated from

$$\underline{a}_i \cdot \underline{a}_j^* = 2\pi\delta_{ij}, \quad (i, j = 1, 2) \quad (1.2)$$

where $\delta_{ij} = 0$ if $i \neq j$ and $\delta_{ij} = 1$ if $i = j$ (i.e. $\underline{a}_1 \perp \underline{a}_2^*$, and $\underline{a}_2 \perp \underline{a}_1^*$ as is shown in Figure 1.2). These unit vectors define a reciprocal net from

$$\underline{g} = h\underline{a}_1^* + k\underline{a}_2^* \quad (h, k = \text{integers}) \quad (1.3)$$

The five possible types of reciprocal net are shown in Figure 1.1(b).

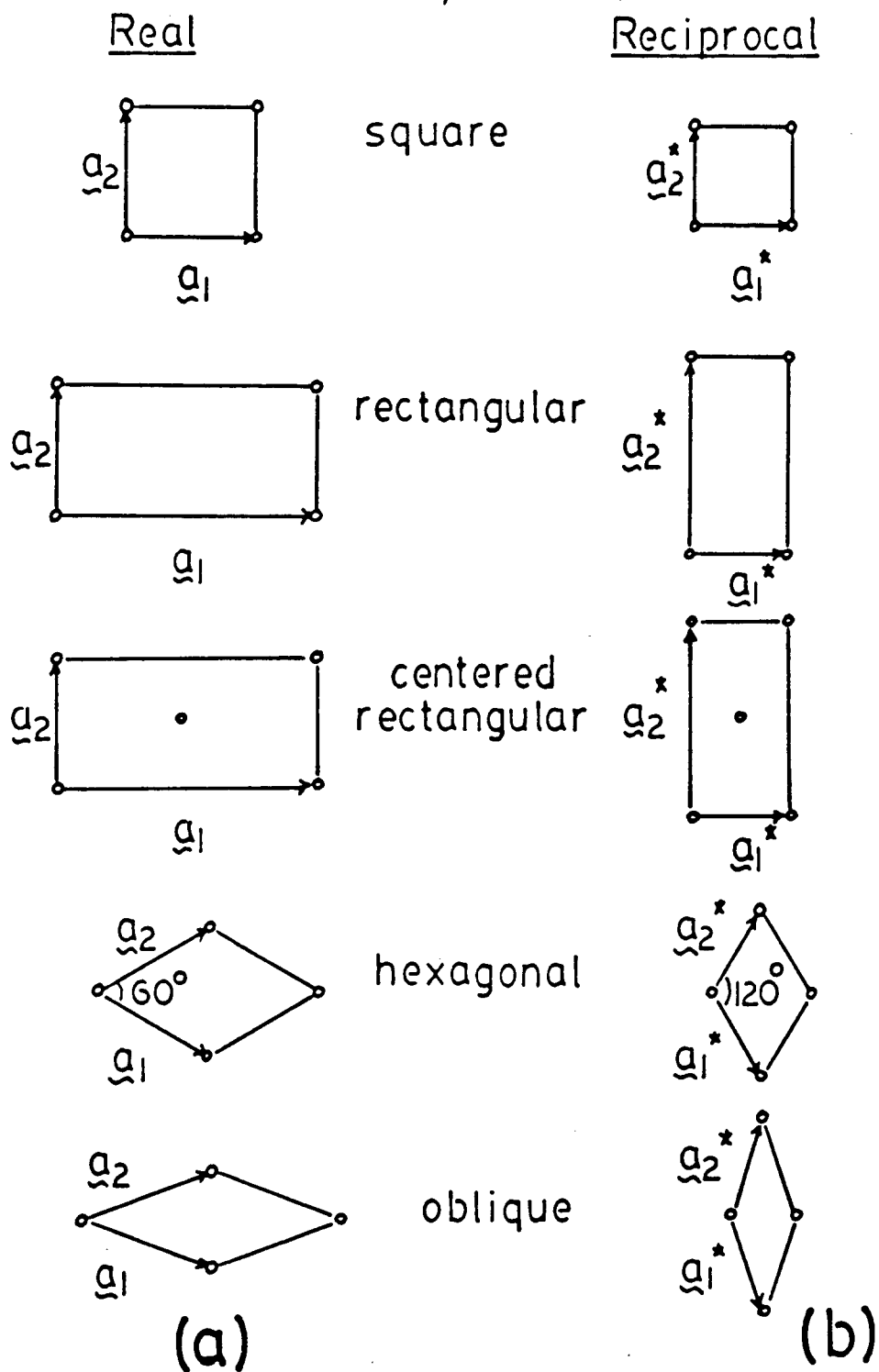


Figure 1.1: The five types of two-dimensional surface meshes (a) in real space (b) in reciprocal space.

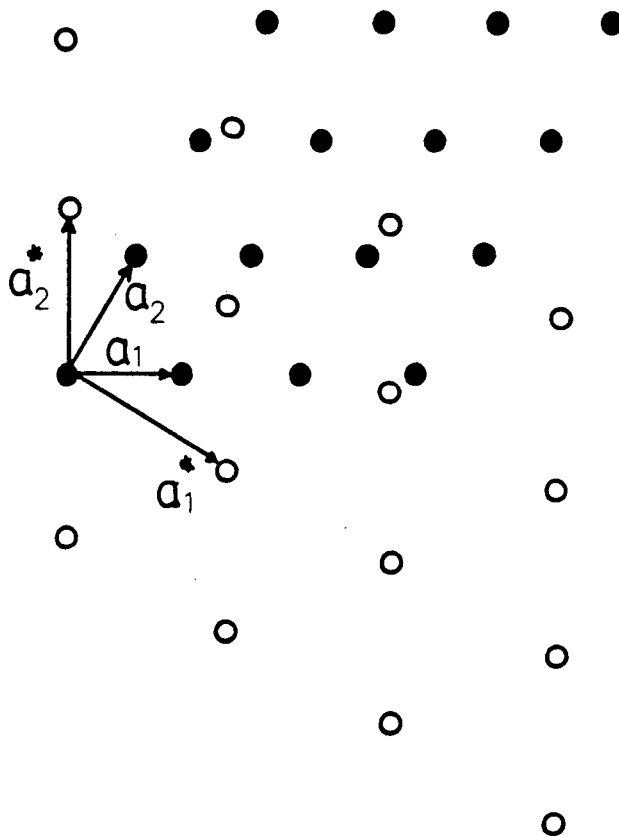


Figure 1.2: A two-dimensional net in real space (filled circles) described by unit translation vectors a_1 , a_2 and the associated net in reciprocal space (open circles) described by unit translation vectors a_1^* , a_2^* .

1.4 Low Energy Electron Diffraction (LEED)

1.4.1 Electron Scattering in Solids

A beam of electrons with a definite energy, E_p , impinging on a surface, will give backscattered and secondary emitted electrons whose energy distribution is shown schematically in Figure 1.3. For the purpose of LEED, this distribution may be divided into three regions. Region I contains elastically scattered electrons as well as the "quasi-elastic" electrons which have suffered small energy losses (≤ 0.1 eV) due to interactions with surface phonons. The latter are not detected with conventional LEED optics, but with an analyzer of high resolution the surface vibration modes can be studied (as in HREELS). Typically in LEED only a few percent of the incident electrons are elastically backscattered. In region II, small peaks observed on the slowly-varying background correspond to inelastically scattered electrons associated with interband and plasmon excitations [20]; in addition peaks resulting from the emission of Auger electrons are present. The Auger peak energies are independent of E_p , and therefore they can be distinguished from the loss peaks by varying E_p . The so-called "true secondary electrons" located in region III at low energies are associated with a series of inelastic scatterings occurring in a cascade-type process [5].

Applications of LEED to surface crystallography depend on two factors:

- (1) the wave nature of electrons ensures that the energy (E in eV) is related to wavelength (λ in Å) according to de Broglie's relation

$$\lambda = \sqrt{150.4/E} . \quad (1.4)$$

This immediately implies that electrons whose energies are around 100 eV have wavelengths of the order of atomic spacings. Such electron waves scattered from a periodic crystal surface can then be expected to interfere, and to give probability distributions which, as for X-ray diffraction, contain geometrical information.

- (2) The observation of elastic scattering by low-energy electrons (typical energy range from 20 eV to 500 eV) implies a process of high surface sensitivity. This is inevitable because electrons of energy to 1 keV have a high probability to be scattered inelastically.

A useful parameter for discussing inelastic scattering is L , defined as the mean distance travelled by an electron before it is scattered inelastically. This satisfies

$$I = I_0 \exp(-\lambda/L), \quad (1.5)$$

where the incident intensity, I_0 , at a particular energy is attenuated to I on passage through a distance λ . The characteristic dependence of L on the electron energy for metals is shown in Figure 1.4; typically in the low-energy range L then corresponds to just a few Å. That emphasizes that these electrons are ideally suited for surface studies. More details on electron mean free paths can be found in ref. 21.

1.4.2 Conditions for Elastic LEED

In LEED, an incident electron beam with known energy (E) and

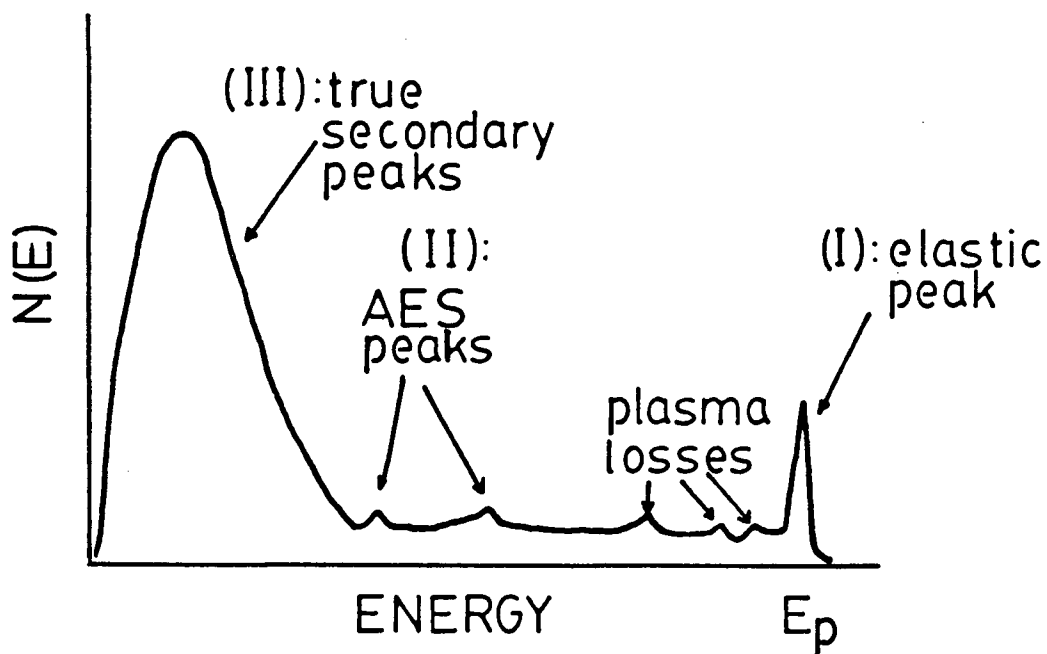


Figure 1.3: Schematic energy distribution $N(E)$ of back-scattered electrons for a primary beam of energy E_p .

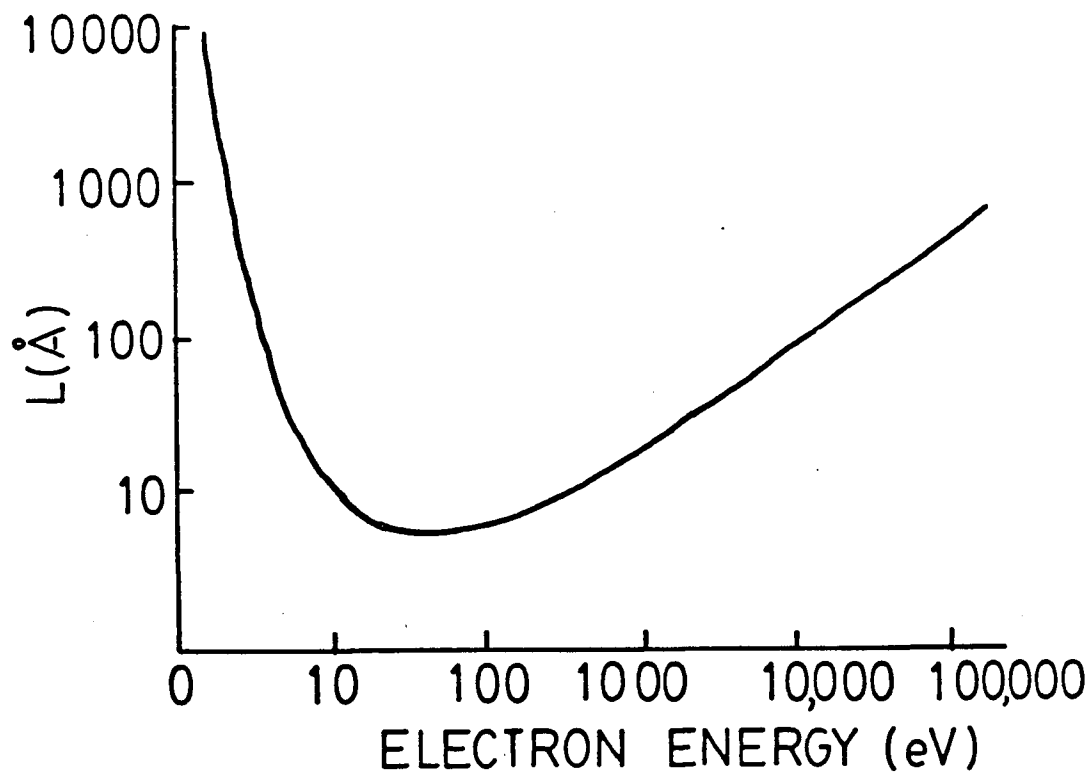


Figure 1.4: Schematic diagram of the mean free path for electrons in a metallic solid as a function of energy.

direction (θ, ϕ) impinges on a face of a single-crystal, as is shown in Figure 1.5, and a small portion of the incident electron flux is elastically back-scattered in discrete directions. The incident and diffracted beams are conveniently represented by plane waves

$$\psi_{\underline{k}}(\underline{r}) = \exp(i\underline{k} \cdot \underline{r}), \quad (1.6)$$

where \underline{k} is a wave vector which specifies the beam direction. The magnitude of \underline{k} (i.e. $2\pi/\lambda$) relates to energy by

$$E = \hbar^2 |\underline{k}|^2 / 2m, \quad (1.7)$$

where m is the electron's mass and \hbar is Planck's constant divided by 2π . For incident and diffracted beams of wave vectors \underline{k}_0 and \underline{k}' respectively, the differential scattering cross-section can be expressed quite generally as

$$\frac{d\sigma}{d\Omega} = (m/2\pi\hbar^2)^2 |\langle \psi_{\underline{k}'} | T | \psi_{\underline{k}_0} \rangle|^2, \quad (1.8)$$

where T is the appropriate transition operator [22,23,24]. For a symmetry operation S , the matrix elements in equation (1.8) satisfy

$$\langle \psi_{\underline{k}'} | T | \psi_{\underline{k}_0} \rangle = \langle \psi_{\underline{k}'} | S^{-1} T S | \psi_{\underline{k}_0} \rangle = \langle S \psi_{\underline{k}'} | T | S \psi_{\underline{k}_0} \rangle \quad (1.9)$$

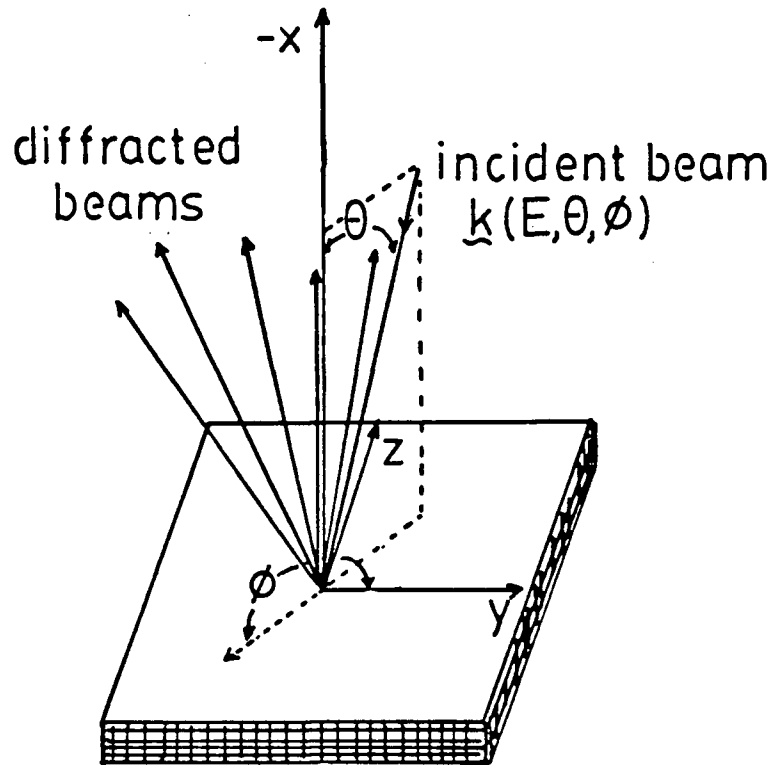


Figure 1.5: Conventions to describe the incidence direction for an electron beam interacting with a surface; θ is the polar angle relative to the surface normal and ϕ is an azimuthal angle relative to a major crystallographic axis in the surface plane.

When S represents translation by a net vector \underline{t} , then

$$S\phi_{\underline{k}}(\underline{r}) = \phi_{\underline{k}}(\underline{r}+\underline{t}) = \exp(i\underline{k}\cdot(\underline{r}+\underline{t})), \quad (1.10)$$

and equation (1.9) requires

$$\langle \phi_{\underline{k}}, |T| \phi_{\underline{k}_0} \rangle = \exp[i(\underline{k}_0 - \underline{k}) \cdot \underline{t}] \langle \phi_{\underline{k}}, |T| \phi_{\underline{k}_0} \rangle. \quad (1.11)$$

This can hold only if either $\langle \phi_{\underline{k}}, |T| \phi_{\underline{k}_0} \rangle = 0$ or $\exp[i(\underline{k}_0 - \underline{k}) \cdot \underline{t}] = 1$. The first corresponds to zero scattered intensity, but the second necessarily holds when $(\underline{k}_0 - \underline{k}) \cdot \underline{t} = 2n\pi$ for n integral. This is in turn automatic if the parallel components of the wave vectors satisfy

$$\underline{k}'_{||}^- = \underline{k}_0_{||}^+ + \underline{g}(h,k), \quad (h,k = \text{integers}) \quad (1.12)$$

where the superscripts +/- specify the wavevector directions into/out of the crystal. The $\underline{g}(h,k)$ are vectors of the reciprocal net as in equation (1.3). The equation (1.12) is a statement of momentum conservation parallel to the surface. That equation along with the conservation of energy for elastic scattering, namely

$$|\underline{k}'_{||}^-|^2 = |\underline{k}_0_{||}^+|^2, \quad (1.13)$$

forms the diffraction conditions for LEED. The indices (h,k) conveniently label the diffracted beams (e.g. the (00), (10), (11) beams). In a conventional LEED experiment, the diffracted electrons are collected on a hemispherical fluorescent screen, the crystal being positioned at the center of curvature of the grid and screen system. The intersections of the diffracted beams with the screen give a distribution of spots (i.e. the LEED pattern), which are directly determined by the reciprocal net associated with the particular crystal surface. An example is detailed in Figure 1.6. From equation (1.12), the (00) (or specular) beam is formed by electrons which have interacted with the surface without transfer of momentum parallel to the surface, and therefore the position of its spot on the screen remains invariant as the incident energy is changed (provided that the electrons are moving in a field-free space and the direction of incidence is fixed). As E is increased, the perpendicular component of each diffracted beam (i.e. k_{\perp}') is necessarily increased, and this results therefore in the non-specular beams moving toward the (00) beam. For off-normal incidence, the position of the (00) spot on the screen enables the angles of incidence to be fixed [7].

1.4.3 Two-dimensional LEED Analysis

The geometry of a two-dimensional LEED pattern (i.e. the reciprocal net) gives information on the size and shape of the unit mesh for the real surface, and those for adsorption systems are generally compared with the corresponding clean surface. Two helpful nomenclatures are available for the two-dimensional LEED analyses, namely Wood's notation [18] and matrix

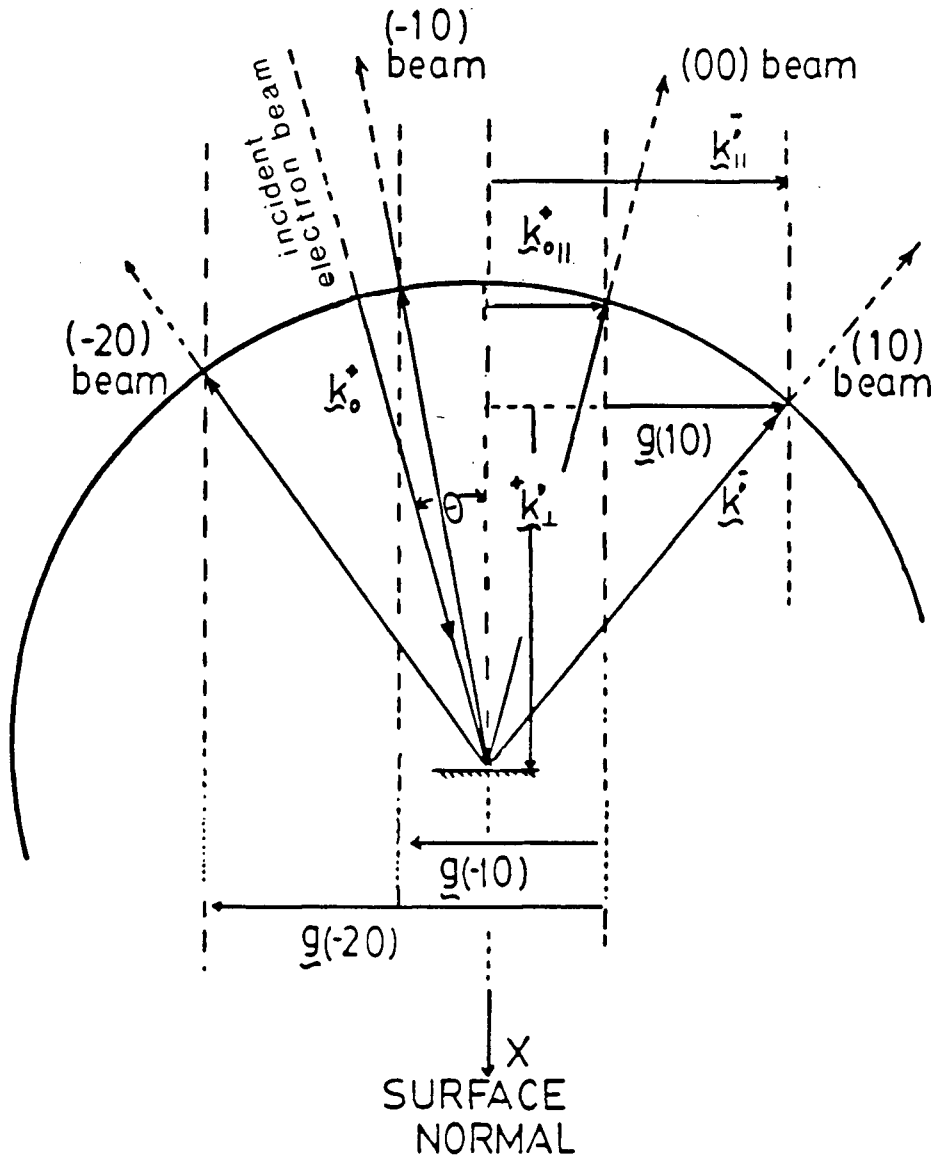


Figure 1.6: Schematic diagram illustrating how the conservation conditions determine direction of a diffracted beam. The (00) beam corresponds to the specular reflection.

notation [25,26], and they both relate the unit vectors \underline{b}_1 and \underline{b}_2 for the adsorption structure to those of the substrate, \underline{a}_1 and \underline{a}_2 . If there is a common rotation angle, θ , between them, then Wood's notation specifies the adsorption structure as $(m \times n) - \theta$, where $|\underline{b}_1|/|\underline{a}_1| = m$, $|\underline{b}_2|/|\underline{a}_2| = n$. Reference to the angle is conventionally dropped if it is zero. The most general relation of \underline{b}_1 and \underline{b}_2 to \underline{a}_1 and \underline{a}_2 is

$$\begin{bmatrix} \underline{b}_1 \\ \underline{b}_2 \end{bmatrix} = \begin{bmatrix} a_{11} & a_{12} \\ a_{21} & a_{22} \end{bmatrix} \begin{bmatrix} \underline{a}_1 \\ \underline{a}_2 \end{bmatrix} \quad (1.14)$$

or $\underline{b} = A \underline{a}$, the matrix A provides a general designation of a surface with respect to the substrate. Figure 1.7 shows some examples of these notations for adsorption on fcc(111) or hcp(0001) surfaces.

The variation of LEED patterns with various parameters (e.g. coverage of adsorbed species, temperature) is often assessed to describe some surface features (e.g. reconstruction, reaction, segregation) in a qualitative sense; indeed a two-dimensional LEED analysis may be utilized to construct surface phase diagrams [27]. In addition, the sharpness of LEED spots is associated with surface order. When changes occur that result in broader and weaker diffraction spots, and with increased diffuse scattering between them, it can be concluded that the surface is becoming less ordered.

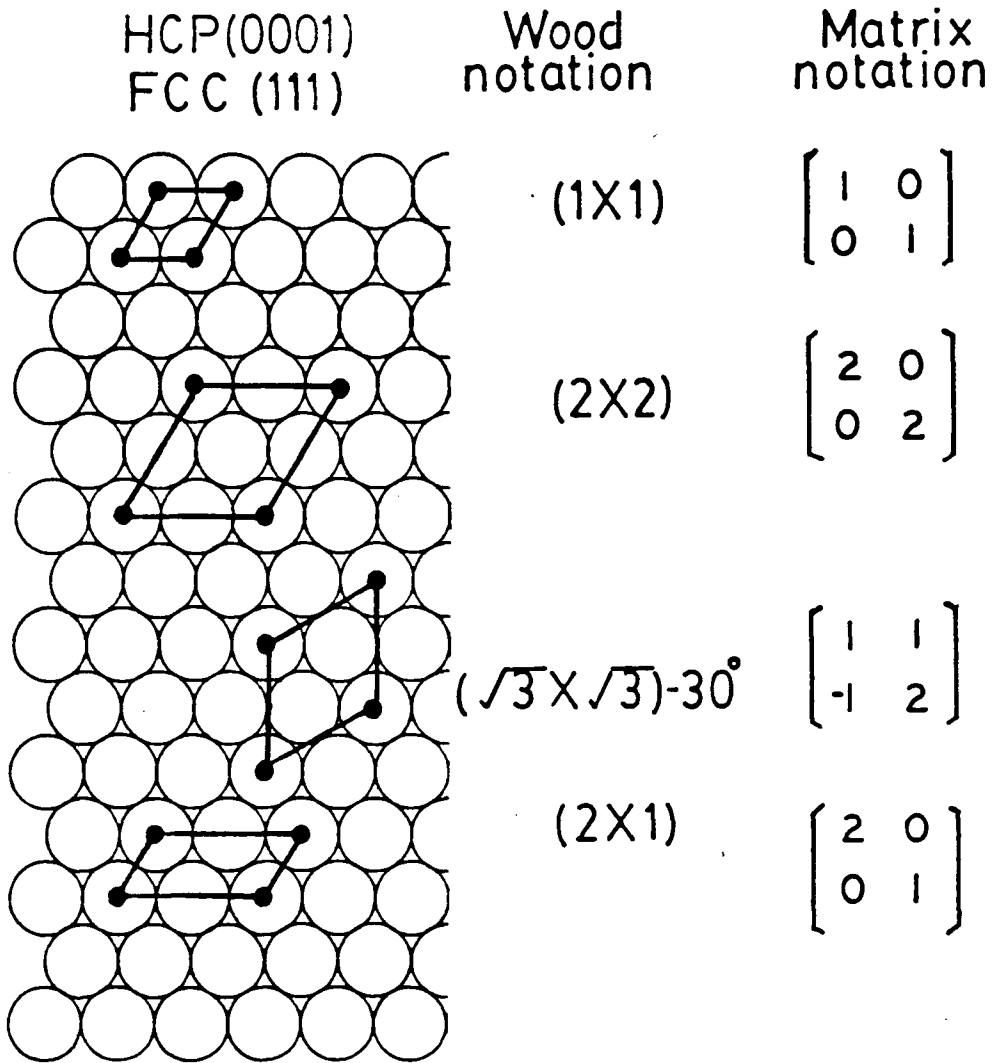
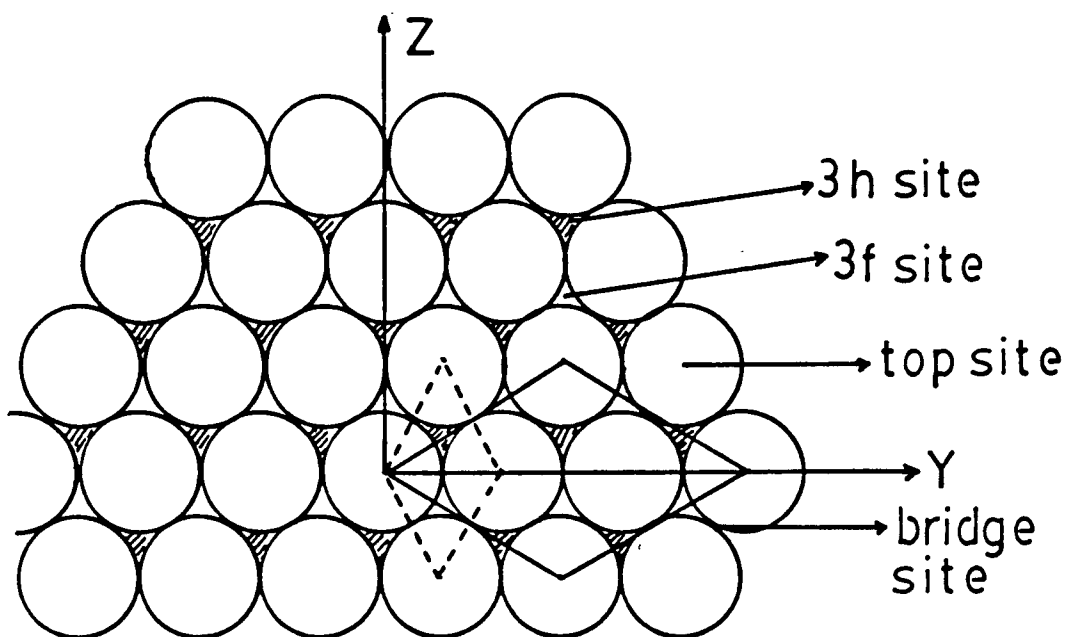


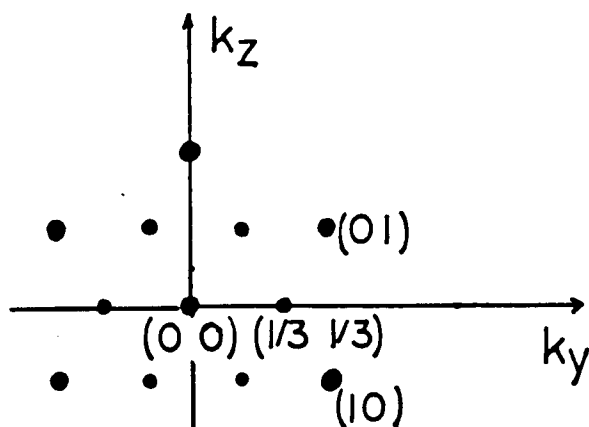
Figure 1.7: Some common translational symmetries (unit meshes) for adsorption on fcc(111) or hcp(0001) surfaces using both Wood's notation and the matrix notation.

1.4.4 LEED Crystallography

The determination of the relative positions of surface atoms (i.e. structural information) can not be made by a two-dimensional LEED analysis. For example, Figure 1.8(a) illustrates four possible adsites on the (111) surface of rhodium which are available for the adsorption of sulfur atoms; these can all exhibit a $(\sqrt{3} \times \sqrt{3})30^\circ$ LEED pattern as is shown in Figure 1.8(b). In LEED crystallography, the two-dimensional LEED analysis is supplemented by analyzing the intensities of the diffraction spots, and this is most readily done by measuring the variation of spot intensities as a function of electron energy [8]. The production of intensity-versus-energy curves, namely $I(E)$ curves, or just occasionally $I(\theta)$ or $I(\phi)$ curves (for variation of the polar or azimuthal incident angles, respectively), serve as the basis for the experimental contribution to LEED crystallography. The theoretical $I(E)$ curves for a particular surface structure are then calculated by multiple-scattering methods (Chapter 2). By comparing the experimental $I(E)$ curves with the calculated $I(E)$ curves for various trial structures, it is possible to extract the correct structural arrangement. Consequently, the detailed surface structural information such as the determination of adsite for adsorbates, the distances between atoms within each unit mesh and the distances between surface layers are also obtained. Figure 1.9 shows the comparisons of one experimental $I(E)$ curve with calculated $I(E)$ curves for various topmost interlayer spacings corresponding to two given different adsites.



a



b

Figure 1.8: (a) Unit mesh of the $(\sqrt{3} \times \sqrt{3}) 30^\circ$ overlayer structure and four possible adsorption sites for sulfur adsorbed on Rh(111). The 3h and 3f sites are threefold sites which are distinguished respectively by whether there is a substrate atom or not located directly below the second layer. (b) Schematic LEED pattern corresponding to the overlayer structure of (a).

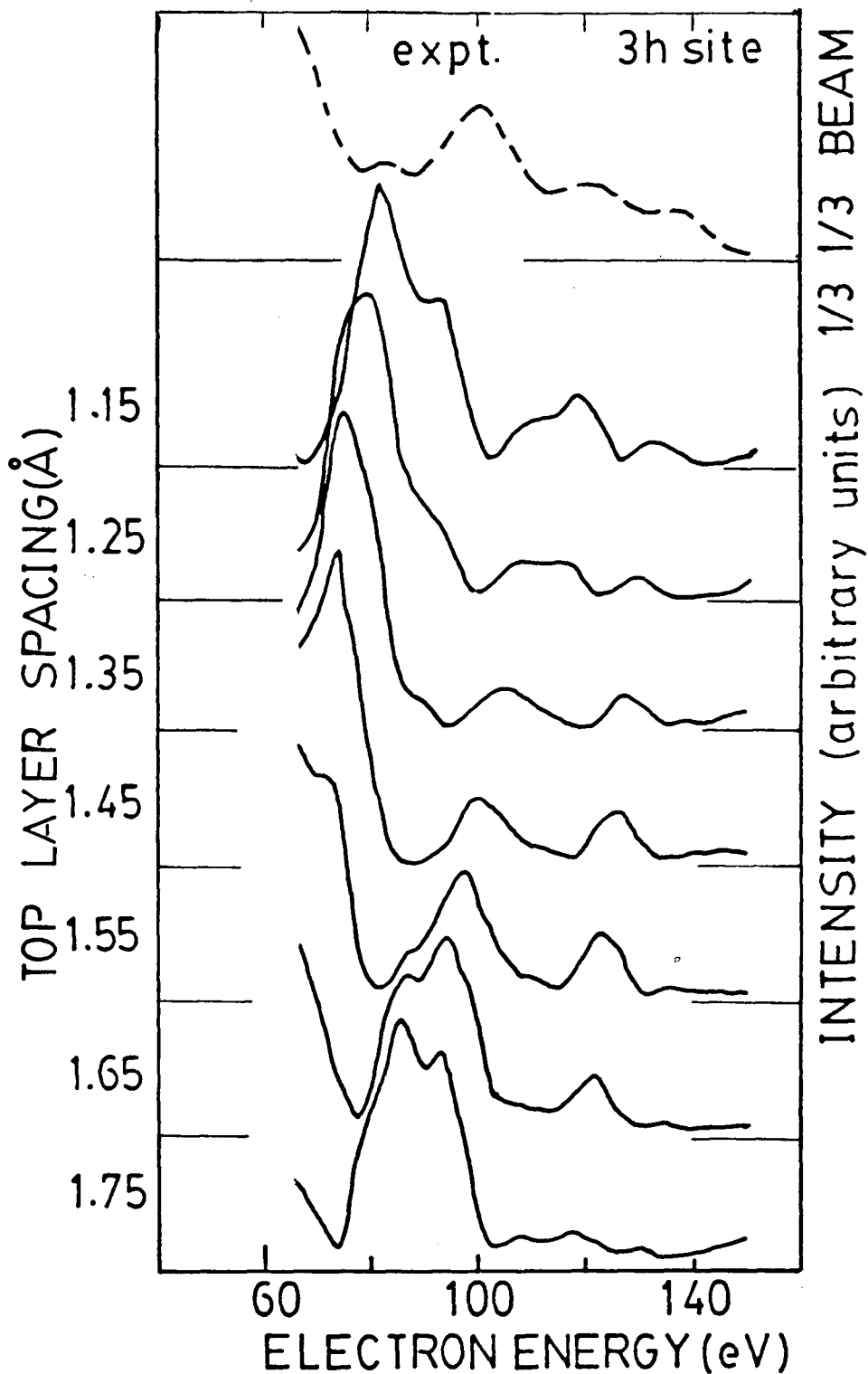


Figure 1.9: Comparison of an $I(E)$ curve measured for the $(1/3\ 1/3)$ diffracted beam from $\text{Rh}(111)-(\sqrt{3}\times\sqrt{3})30^\circ\text{-S}$ at normal incidence with those calculated for the 3f and 3h adsorption sites over a range of the topmost S-Rh interlayer spacings.

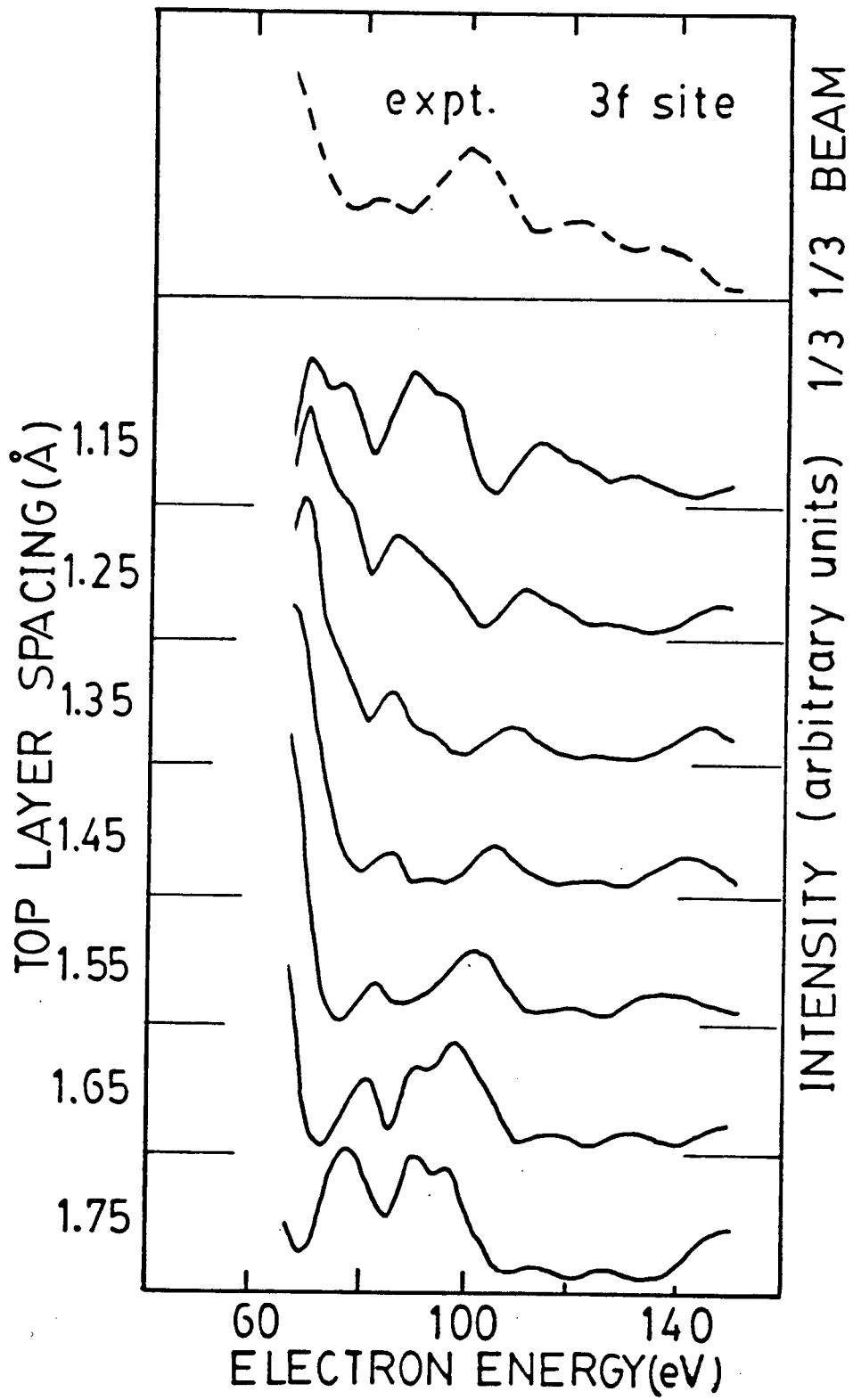


Figure 1.9: (continued)

1.4.5 Instrumental Response, Domains and Disorder

In the discussion of electron diffraction so far two implicit assumptions have been made. The first is that a crystal surface studied by LEED can be perfectly ordered over an infinite extent. Secondly, it has been assumed that the incident beam and diffracted beams are simple plane waves whose properties are uniform across the wavefronts. In fact, these two assumptions can never be satisfied exactly. In a LEED experiment the electron gun usually produces a beam about 1 mm in diameter, which is made up of electrons with angular and energy deviations associated with the finite size and high temperature of the source; there is also a finite size for the detector. These experimental flaws limit the information that can be obtained from a diffraction measurement. In this context, Park et al. [28] defined an instrumental response function which yields a characteristic dimension, the transfer width L , over which the instrument is sensitive as a probe of the surface periodicity [29]. In conventional LEED a typical transfer width is approximately 10^2\AA , and this dimension sets a limit on the spatial information obtainable by the diffraction experiment (although strictly the experimental precision also affects the distance over which order can be detected [142]). In our work, the incident beam inevitably has a cross section whose dimension is large compared with L ; as a result the LEED patterns are actually made up of a sum of contributing patterns from restricted areas (of the order of L^2). In any event, a real surface which is formed by cutting inevitably has an appreciable defect

concentration resulting especially from the presence of steps. At the microscopic level, then, such a surface is inevitably heterogeneous, being composed of many separate islands or domains. Aspects of disorder may affect LEED patterns in several different ways. Indeed if a surface is well ordered within domains of dimension at least L , "good" LEED patterns can be observed even if there are substantial imperfections between the ordered regions [29]. Secondly, beam splitting and broadening can occur with antiphase scattering [26] from areas whose dimension is small compared with L . Also domains may lead to some ambiguity in interpretation of a LEED pattern, for example one exhibiting a complete set of half-order diffracted beams from the (111) face of a fcc crystal (and equally from a (0001) face of a hcp crystal). Such a pattern can be attributed either to a simple (2x2) surface structure or to three rotationally-related domains of the types shown in Figure 1.10. The positions of spots in the LEED patterns would be identical in either case.

Another interesting contrast of a similar type is shown by considering the LEED patterns resulting from the clean Rh(111) and Zr(0001) surfaces. Both these surfaces have one 3-fold rotational symmetry axis and appropriate mirror symmetries perpendicular to the surface. Nevertheless at normal incidence the latter exhibits a LEED pattern with 6-fold symmetry whereas the former exhibits a 3-fold pattern. This anomalous situation for Zr(0001) is a result of the coexistence of two types of domain which are related by a 2-fold rotation as is shown in Figure 1.11. These domains correspond to the two possible terminations (i.e. A.B.A.B... and B.A.B.A...) when the zirconium crystal is truncated parallel to the (0001)

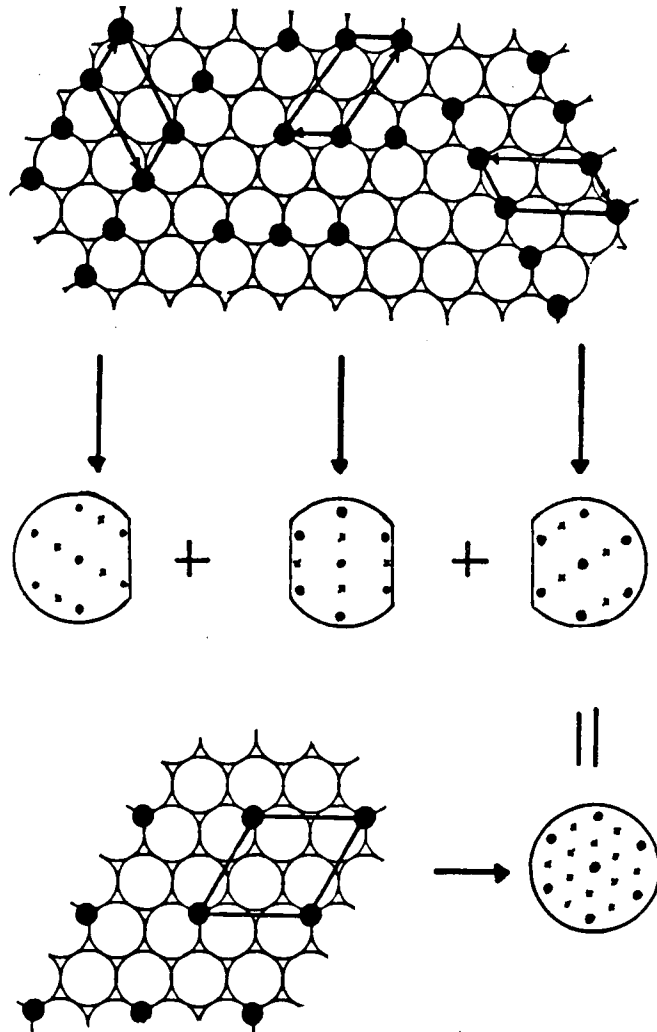


Figure 1.10: A (2x2) structure on a fcc(111) or hcp(0001) surface is shown bottom left, while the corresponding LEED pattern is drawn schematically at bottom right (the half-order beams are identified by crosses). The top shows three domains of a (1x2) type structure which are related by 120° rotations. The total LEED pattern from a surface with equal populations of these domain types will be a superposition of the three individual patterns. This superposition gives spots in identical positions to the (2x2) pattern.

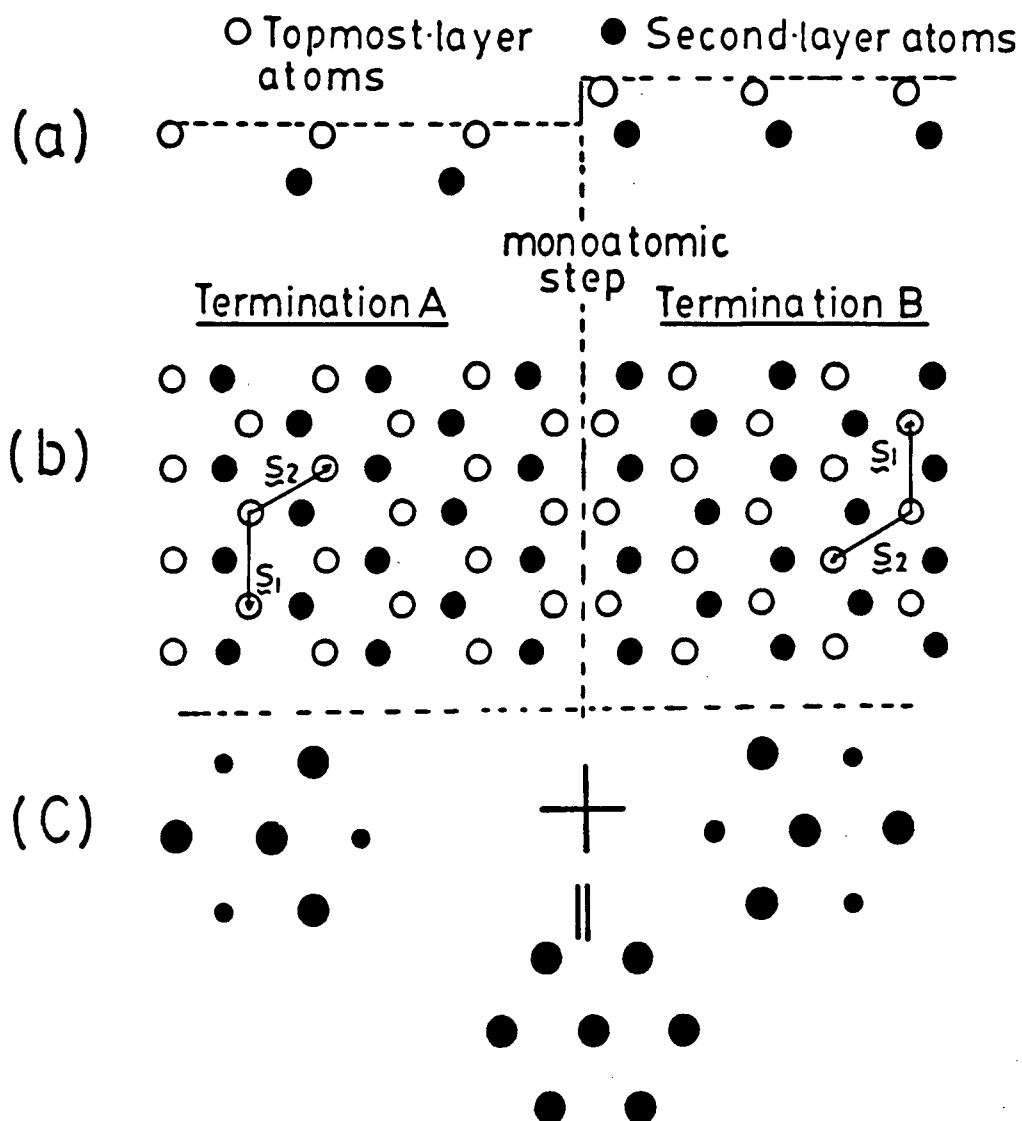


Figure 1.11: (a) Side view and (b) top view of the two types of domains resulting from the truncation of the hcp bulk structure parallel to the (0001) plane. The two domains are related to each other by a 180° rotation. (c) Superposition of the two 3-fold symmetrical LEED patterns (expected for normal incidence) to form a LEED pattern with 6-fold symmetry.

plane. When the probabilities of the two domains appearing on the surface region probed by the primary electron beam are approximately equal, a 'domain averaged' LEED pattern having 6-fold symmetry appears for normal incidence. A discussion of domain averaging in a more-complicated context has been given by Wang et al. [30].

1.5 Auger Electron Spectroscopy (AES)

The phenomenon now covered by the term Auger electron spectroscopy was first observed and interpreted by Pierre Auger in 1925 [31]. Auger electrons are ejected from a target atom by a mechanism like that illustrated in Figure 1.12. The first step involves ionization from an inner shell (i.e. the K-shell for the example shown), and the vacancy left can then be filled with an electron from a higher shell (i.e. L_2). The excess energy (i.e. $E_K - E_{L_2}$) is simultaneously transferred to eject another electron (i.e. an Auger electron from L_3) with a kinetic energy which approximately equals $E_K - E_{L_2} - E_{L_3}$. Hence Auger electrons have energies characteristic of the atoms from which they emerge, and this allows for their use in identifying all atoms of the periodic table except for hydrogen and helium.

For surface chemical analysis, the main interest is in Auger electrons with energies in the approximate range 50-900 eV which are characterized by short mean free path lengths in solids. Although the Auger transition process can also be initiated by X-radiation and ion bombardment, electron bombardment only is used in this work. In practice the Auger electrons that are collected from surface atoms are inevitably accompanied by large numbers of secondary electrons. Auger spectra are

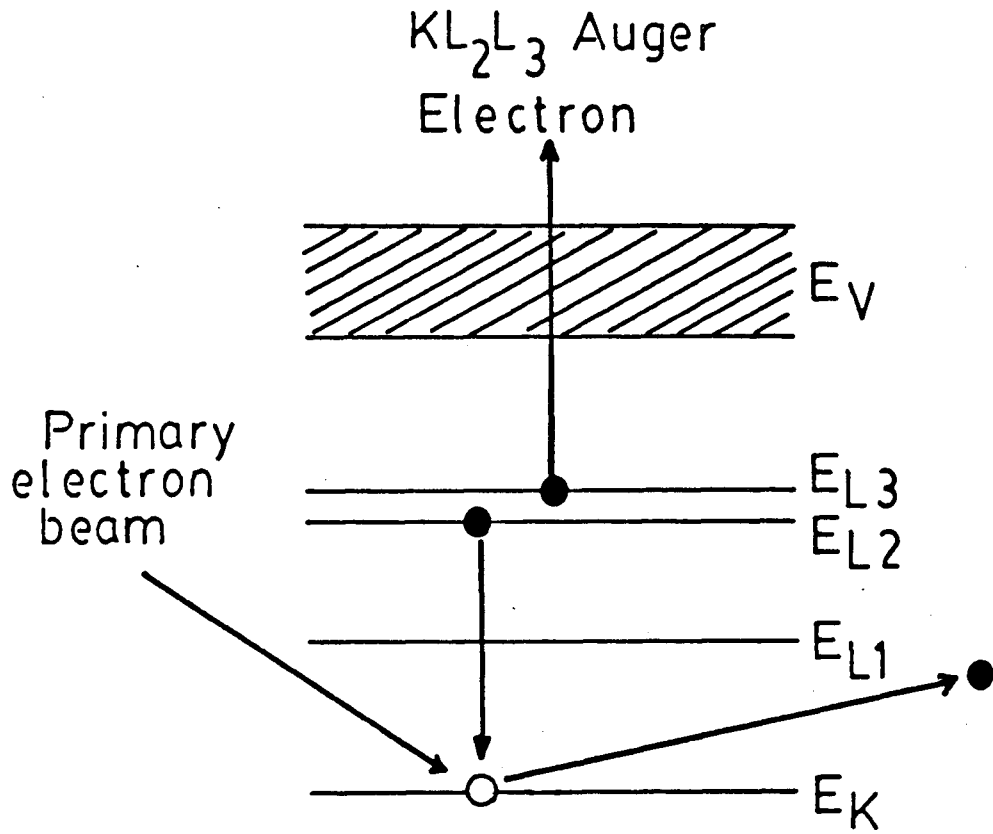


Figure 1.12: Schematic representation of an Auger process in terms of atomic and valence band energy levels. This example is specifically for the production of a KL_2L_3 Auger electron.

commonly presented in the first derivative form of the relative energy distribution in Figure 1.3; differentiation can minimize the effect of the high but slowly-varying background of scattered electrons. It is customary to catalog Auger energies by positions of the negative peaks in differential spectra. A representative AES spectrum for a sulfur and carbon contaminated Rh(111) surface is shown in Figure 4.1(a).

High Auger electron yields are advantageous for the application of AES to surface chemical analysis. A relaxation process which competes with Auger emission is X-ray fluorescence. This occurs when the excess energy associated with the electron relaxation into the initial vacancy is released as a photon (in lieu of being transferred to eject an Auger electron). In general, for atoms with atomic numbers below 30, the Auger transition process is more probable than that for X-ray fluorescence; for heavier atoms Auger emission still dominates provided the energy of the Auger transition is less than around 2 keV.

The use of AES for qualitative surface analysis is achieved by comparing measured spectra with standard representative spectra [32] or with tabulated energies [33]. Although changes in chemical environment can result in energy shifts of the order of a few eV [34], these are too small in general to seriously affect applications to qualitative analysis. When AES is studied under low resolution, some overlapping of Auger peaks occurs not infrequently (e.g. the S_{150} and Zr_{147} peaks in Figure 6.1(a)). The existence of several Auger energies for most elements (e.g. Auger energies at 92, 116, 124 and 174 eV for zirconium) usually eliminates any ambiguity in assignment. The technique is capable of being quantified, although this

is done most often by calibrating with other measurements rather than using the first-principles approach [35]. To avoid instrumental artefacts, adsorbate concentrations on a single crystal surface are frequently quantified by comparing values of a relative Auger peak height ratio of adsorbate to that of the substrate (e.g. the ratio A_{151}/A_{304} used in Chapter 4).

1.6 Aim of Thesis

The objectives of the studies presented in this thesis are to contribute to the subject of LEED crystallography, and to relate the new surface structural information to structural chemical principles. The particular surfaces studied were made by gas adsorption on the Rh(111) and Zr(0001) surfaces, to form new structures designated Rh(111)- $(\sqrt{3}\times\sqrt{3})30^{\circ}$ -S, Rh(111)-(2x2)-O, Zr(0001)-(2x2)-O, Zr(0001)-(1x1)-O, Zr(0001)-(1x1)-N and Zr(0001)-(3x3)-S. Both rhodium and zirconium have important technological applications. For example, the interaction of oxygen with rhodium plays an important role in several catalytic reactions including ketone reduction [36], methanation [37], nitrogen oxide reduction [38], and the oxidation of hydrogen [39]. In contrast to oxygen, sulfur is a known catalytic poison for rhodium. Nevertheless, the studies of sulfur on the Rh(111) surface in this work attempt to further our understanding at the atomic level for such features as adsorption site and surface bond length. The studies for sulfur on Rh(111) should give further insight into the nature of the Rh-S surface chemical bond, particularly by comparing with earlier studies for sulfur adsorption on the Rh(100) and Rh(110) surfaces [40,41].

The substantial potential interest in the surface chemistry of zirconium [42], as well as the very limited experimental data available so

far for adsorption on surfaces of hexagonal close-packed metals, provided an impetus for analyses of surface structures formed by chemisorption on the Zr(0001) surface. Such studies are not helped by the high reactivity of this metal. Other factors which have possibly retarded the studies of the surface chemistry of zirconium can be summarized as follows:

- (1) Single crystals of zirconium are not commercially available.
- (2) The bulk phase transition (hcp \leftrightarrow bcc) at 862°C restricts possibilities for surface preparation, in relation to cleaning and to annealing as required to achieve an ordered surface.
- (3) The common low-weight atoms have a strong tendency to diffuse into the bulk, thereby resulting in difficulties in cleaning and in defining proper exposure ranges for the formation of the intended surface structures.

For zirconium this work aims to develop a reliable method for surface cleaning and to clarify some uncertainties associated with the one earlier structural investigation for adsorption at the Zr(0001) surface, as reported by Hui et al. [43] for the Zr(0001)-(2x2)-0 structure. The new work made here analyzes the lowest-coverage Zr(0001)-(1x1)-0 structure, with the view to gaining more information about the initial stages of the oxidation of Zr(0001). Additionally, this work aims to elucidate the structure of two previously unstudied surfaces, namely Zr(0001)-(1x1)-N and Zr(0001)-(3x3)-S. The coadsorption of oxygen and H₂S on Zr(0001) was also studied in an attempt to gain insight into the interactions between adsorbed sulfur and oxygen at this surface.

The layout of this thesis is described as follows. Chapter 2 briefly discusses the 'combined space' approach in LEED multiple scattering calculations, and the important non-geometrical parameters required in the calculations. The reliability index routine used for making comparisons of experimental and calculated $I(E)$ curves is also described. Chapter 3 reviews the experimental aspects of these LEED/AES studies. Chapter 4 reports observations for the adsorption of H_2S on $Rh(111)$. An analysis of diffracted beam intensities is performed for the $Rh(111)-(\sqrt{3} \times \sqrt{3})30^\circ-S$ structure. Chapter 5 reports investigations of the $Rh(111)-(2 \times 2)-0$ surface structure, including LEED intensity measurements in the presence of some electron beam disordering of the adsorbed oxygen overlayers. Chapter 6 includes an examination of the oxygen coverage in surface structures which give $Zr(0001)-(2 \times 2)-0$ type LEED patterns. The emphasis involves measuring a half-order diffracted beam profile as a function of exposure and heating temperature. Chapter 7 reports LEED crystallographic and AES investigations of a surface designated $Zr(0001)-(1 \times 1)-N$. Finally, Chapter 8 reports observations for the $Zr(001)-(3 \times 3)-S$ structure, and includes comparisons between oxygen and sulfur adsorption on this surface. LEED intensity curves were measured from the $Zr(0001)-(3 \times 3)-S$ structure, although a multiple-scattering analysis has not yet been undertaken.

CHAPTER 2

Calculation of LEED Intensities

2.1 Introduction

The analysis of LEED intensities requires a theory of the diffraction process. A simple single-scattering theory (such as is used in X-ray crystallography) is not suitable for describing the scattering of low-energy electrons from a solid surface. This is mainly due to the fact that the low-energy electrons interact very strongly with solids (the high surface sensitivity results especially from strong inelastic scattering), but even for elastic scattering electrons in the low-energy range have much larger scattering cross-sections than for X-ray scattering (by a factor of around 10^6). Compared with X-rays a much larger fraction of electrons is backscattered; also there is a much larger probability that the back-scattered electrons will scatter several times before emerging from the surface. The latter gives rise to the multiple scattering peaks which are readily observable in measured $I(E)$ curves, and which cannot be accounted for by single scattering theory with reasonable geometries. Inevitably, then, multiple scattering or dynamical calculations are required for LEED intensity analyses. Detailed descriptions of the theoretical methods are discussed in books by Van Hove and Tong [44] and by Pendry [45]. All the main computing programs used in the research of this thesis are from either Van Hove and Tong's book [44] or the magnetic tape provided by Van Hove [46]. The objectives of this chapter are to provide an overview of the physical processes involved and to outline the computer subroutines utilized in this study.

2.2 Geometrical and Non-geometrical Parameters

All ordered surface regions, whether they involve adsorbed layers, or relaxed or reconstructed clean surfaces, can be envisaged as built from diperiodic layers which are stacked parallel to the surface plane. Usually the overall diperiodicity of the surface region can be recognized directly from the form of the LEED pattern; however the way the (surface) layers are related to one another can only be determined by analyzing the diffracted beam intensities. LEED analyses particularly aim to determine those geometrical parameters which establish the relationship between all surface layers and the underlying substrate, whose structure is generally known. For the underlying substrate, the relative atomic positions can be described by the known geometrical parameters such as two-dimensional translational vectors (\underline{t}) and three-dimensional propagation vectors ($A\underline{S}A$) for the intraplanar atoms and interplanar atoms, respectively, as is illustrated in Figure 2.1. The LEED crystallographic studies in this thesis particularly aim to determine adsorption sites, interlayer spacings and layer registries which are identified from a trial-and-error type of analysis [8].

Apart from geometrical parameters, various non-geometrical parameters describing the strong interaction of a LEED electron with a solid are also required for the computation of $I(E)$ curves. The potentials responsible for the scattering within and between these vibrating scattering centers (i.e. the "non-local ion cores") play important roles in a multiple scattering calculation. The potential of a solid is usually approximated by the "muffin-tin" model, in which the potential is assumed

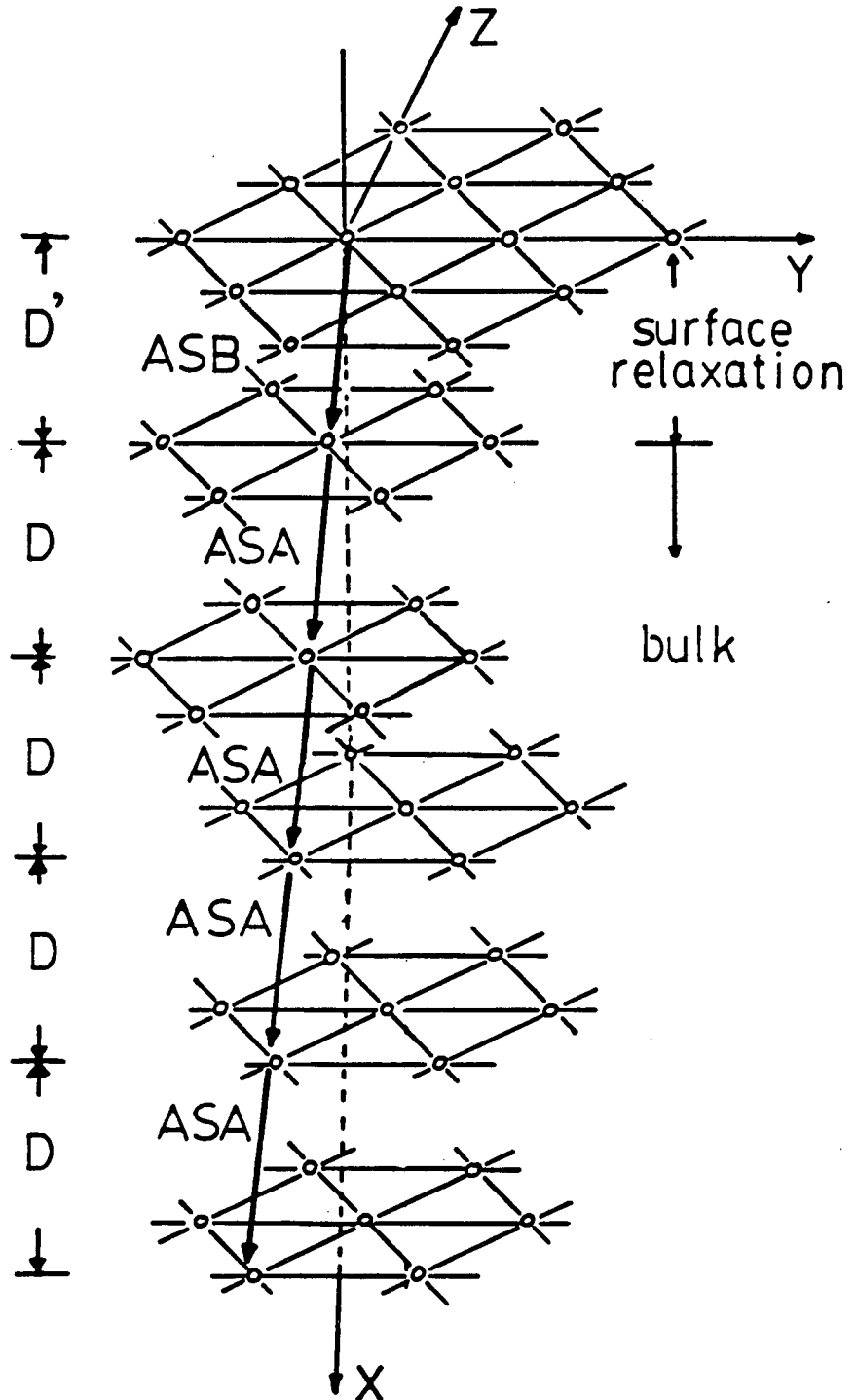


Figure 2.1: Example of relaxation at a fcc(111) surface. The three-dimensional propagation vectors ASB and ASA apply to the relaxed region and bulk region respectively. The corresponding interlayer spacings D' and D are shown to the left.

spherically symmetrical within each atomic region, while in the region between ion cores the potential is treated as a constant. Section 2.3 will use this model for a solid; it is natural to express the wave function of a LEED electron as either a spherical wave (in angular-momentum or L-space) or a plane wave (in linear-momentum or K-space). In general, plane waves can be described in terms of a series expansion of spherical waves [23], and vice versa. The spherical waves are convenient for describing scattering by the spherically symmetrical ion cores, as well as the multiple scattering between atoms in individual layers parallel to the surface. On the other hand, the plane waves are convenient for describing the interlayer multiple scattering (the diffraction by each layer produces a discrete set of "beams", each of which can be represented by a plane wave).

The usual procedures for calculating LEED intensities split the whole scattering problem into a series of simpler steps as indicated in the following sequence:

- (1) Compute the single atom scattering amplitude in L-space.
- (2) Calculate in L-space all scatterings among atoms within a single layer.
- (3) All individual layers are stacked and the interlayer scattering is calculated in K-space.

In the final step, the wavefield outside the crystal

$$\psi^{\text{out}}(\underline{r}) = \exp(i\tilde{k}_0^+ \cdot \underline{r}) + \sum_{\substack{\tilde{g} \\ \sim}} C_{\tilde{g}} \exp(i\tilde{k}_{\tilde{g}}^- \cdot \underline{r}) \quad (2.1)$$

is matched to the wavefield inside the crystal at the solid-vacuum interface [47]. In equation (2.1) \tilde{k}_0^+ and \tilde{k}_g^- depict the incident beam and diffracted beams respectively, and the \tilde{C}_g are coefficients in the expansion of the total wavefield outside the crystal. The calculated intensity of the beam \tilde{g} is

$$I_{\tilde{g}} = (\tilde{k}_{g\perp}^- / \tilde{k}_{o\perp}^+) |\tilde{C}_{\tilde{g}}|^2, \quad (2.2)$$

where $\tilde{k}_{o\perp}^+$ and $\tilde{k}_{g\perp}^-$ represent the perpendicular components of the incident and diffracted beams, and the superscripts '+/-' denote wave propagation in the +x/-x directions (Figure 2.1).

2.3 The Muffin-tin Approximation

The muffin-tin model is illustrated schematically in Figure 2.2. Surrounding each atom is a spherically symmetrical potential, V_g , which extends to an appropriate radius; the region between the atoms has a constant potential, V_o (i.e. the muffin-tin constant). Roughly speaking, V_o is responsible for the interaction of a LEED electron with the relatively delocalized valence electrons, whereas V_g relates to the interaction with the ion cores. The actual potential varies smoothly through the surface from vacuum to the solid's interior, so the scattering resulting from any discontinuity in a model potential must be ignored for

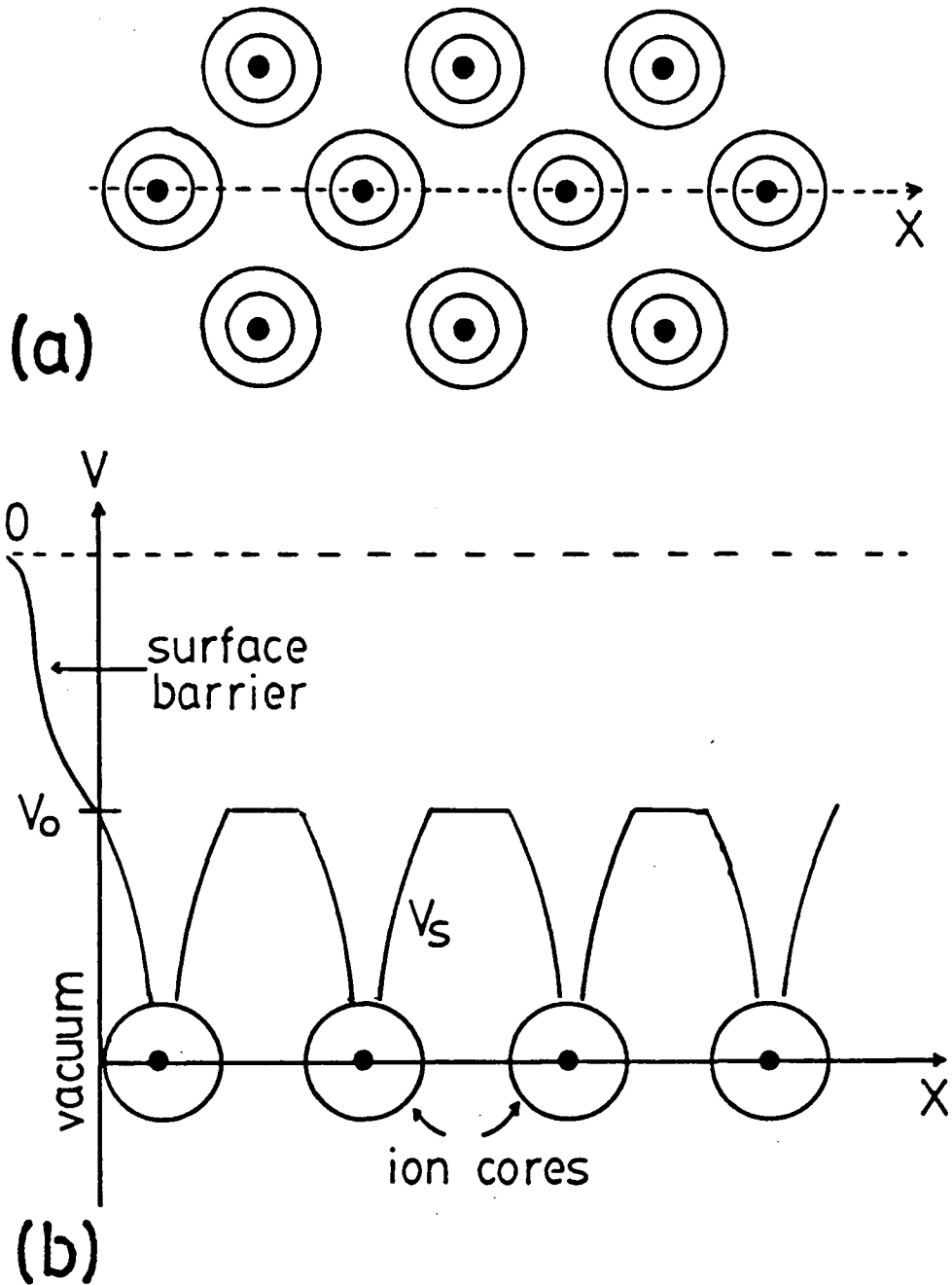


Figure 2.2: Variation of potential for the muffin-tin model: (a) contour plot through an atomic layer, and (b) variation through a single row of ion cores along the x -axis.

comparing with experimental intensities. In LEED multiple scattering calculations, the muffin-tin constant V_o is generally represented as the sum of a real component (V_{or}) and an imaginary component (V_{oi}).

$$V_o = V_{or} + i V_{oi} \quad (2.3)$$

The real part V_{or} typically has a value between -5 and -15 eV, and it accounts for an electron inside a crystal experiencing a lower potential than in vacuum. This effect speeds up an electron inside a solid, so giving the electron a lower wavelength compared with the electron in vacuum. In practice appropriate values for V_{or} vary with the specific atomic potential used in the multiple scattering calculations. Therefore this parameter is generally set empirically from the comparisons between calculated and experimental $I(E)$ curves. Strictly, exchange and correlation effects give V_{or} an energy dependence [48], although it is most often treated as energy-independent for LEED crystallographic studies. In this thesis, V_{or} is often referred, following a common usage, to the 'inner potential' [49-51], a term that has traditionally noted the constant shift in experimental intensity-voltage curves required to align with the corresponding calculated curves [44].

The imaginary component V_{oi} is a negative quantity which accounts for the electron damping effect due to inelastic scattering. The lifetime, τ , defined as the average time an incident electron spends in the solid prior to being inelastically scattered relates to V_{oi} according to

$$\tau = \hbar/2|V_{oi}| \quad (2.4)$$

An increase in inelastic scattering gives a decrease in lifetime which corresponds in turn to an increase in $|V_{oi}|$. Appropriate values of V_{oi} can be determined from peak widths, ΔE_w , in experimental $I(E)$ curves. By using the time-energy uncertainty principle, Pendry [45] relates the peak width ΔE_w to V_{oi} according to

$$\Delta E_w > 2|V_{oi}| \quad (2.5)$$

In general, V_{oi} is treated as either constant or weakly energy-dependent in LEED intensities calculations. For the latter, Demuth et al. [52] used expressions of the type

$$V_{oi} = -BE^{1/3}, \quad (2.6)$$

where B is a material-dependent parameter. This equation was used in the studies here for rhodium surfaces, where B was set equal to $0.819 \text{ (eV)}^{2/3}$. However, for the studies on zirconium, V_{oi} was kept constant at -5 eV . This was found to eliminate some non-convergence problems which occurred at low energies when equation (2.6) was used.

The ion-core potential, V_s , depends on the specific atom considered. For metals it is generally derived from band-structure potentials [53], whereas for light atoms appropriate potentials have been developed from superposition models [54] designed to simulate atoms in overlayer

situations [55]. A variety of atomic potentials for these atoms has been supplied by Van Hove [46].

2.4 Ion Core Scattering

By solving the Schrödinger equation

$$\left[-\left(\frac{\hbar^2}{2m}\right)\nabla^2 + V_s\right]\psi = E\psi, \quad (2.7)$$

where E is energy set by the vacuum level, the scattering of a plane wave with wavevector \underline{k} by a spherically symmetric ion core potential, V_s , gives the asymptotic form [23]

$$\psi_{\underline{k}}(r, \theta_s) = \exp(ikr \cos \theta_s) + T(k, \theta_s) \exp(ikr)/r. \quad (2.8)$$

In equation (2.8) r is the distance from the atomic nucleus, θ_s is the scattering angle, and $T(k, \theta_s)$ is the ion core scattering amplitude which can be expanded as

$$T(k, \theta_s) = 4\pi \sum_{\ell=0} (2\ell+1) t_{\ell}(k) P_{\ell}(\cos \theta_s), \quad (2.9)$$

where P_{ℓ} is the Legendre polynomial associated with the angular momentum quantum number ℓ , and $t_{\ell}(k)$ is the t -matrix element

$$t_{\ell} = (1/4ik)[\exp(2i\delta_{\ell})-1] \quad (2.10)$$

In equation (2.10), the δ_ℓ are phase shifts which can be evaluated by solving equation (2.7) for the appropriate ion core potential and matching to solutions in vacuum at the muffin-tin radius. Although equation (2.9) suggests an infinite number of ℓ values are needed, in practice the expansions converge quite rapidly; the numbers required increase with both the atom's scattering strength and the energy. Additionally, the atomic phase shifts relate to the total elastic scattering cross-section according to

$$\delta_{el} = (4\pi/k^2) \sum_{\ell=0} (2\ell+1) \sin^2 \delta_\ell. \quad (2.11)$$

The atomic phase shifts are important input parameters for a LEED calculation.

It has been known since the earliest LEED studies by Davisson and Germer [56] that beam intensities decrease with increasing temperature; indeed a Debye-Waller analysis can be applied in close analogy with that used in X-ray crystallography. Assuming the harmonic approximation for the lattice vibrations [57], the effects of thermal vibrations are usually included in LEED calculations by multiplying each ion core's scattering amplitude $T(k, \theta_s)$ by an isotropic Debye-Waller factor [50]

$$T(k, \theta_s)_T = T(k, \theta_s) \exp(-M) \quad (2.12)$$

With the temperature-dependent ion core scattering amplitudes, a set of temperature-dependent phase shifts $\delta_{\ell T}$ can be obtained from

$$t_{\lambda}^T(k) = \left(\frac{1}{4ik}\right) [\exp(2i\delta_{\lambda T}) - 1]. \quad (2.13)$$

The value of M in the exponential term of equation (2.12) is [44]

$$M = \frac{1}{6} |\Delta k|^2 \langle (\Delta \mathcal{L})^2 \rangle_T. \quad (2.14)$$

In equation (2.14) Δk is the momentum transfer resulting from the atomic scattering and $\langle (\Delta \mathcal{L})^2 \rangle_T$ is the mean square vibration amplitude given as a function of the temperature. For the latter, Van Hove and Tong [44] propose using the low-temperature and high-temperature limits as in the average

$$\langle (\Delta \mathcal{L})^2 \rangle_T = \sqrt{[\langle (\Delta \mathcal{L})^2 \rangle_{T \rightarrow 0}]^2 + [\langle (\Delta \mathcal{L})^2 \rangle_{T \rightarrow \infty}]^2} \quad (2.15)$$

where: $\langle (\Delta \mathcal{L})^2 \rangle_{T \rightarrow 0} = 9/mk_B \theta_D (1/4 + 1.642T^2/\theta_D^2), \quad (2.16)$

$$\langle (\Delta \mathcal{L})^2 \rangle_{T \rightarrow \infty} = 9T/mk_B \theta_D^2. \quad (2.17)$$

The k_B and m are the Boltzmann constant and the atomic mass in atomic units, respectively. In most LEED structural determinations the atomic vibrations are taken as isotropic in the calculations, although an anisotropic M can also be used in equation (2.12). With a vibrating lattice more phase shifts are required for convergence than is the case for the stationary lattice model;

in practice for LEED crystallographic studies to about 220 eV, eight phase shifts are generally sufficient for each atom type [44,54]. Further details of the implementation of these points are discussed by Van Hove and Tong [44].

2.5 Intralayer Scattering

The diffraction of plane waves by an ordered atomic layer, having one atom per unit mesh (i.e. a subplane), will be outlined briefly here. An incident plane wave of unit amplitude and wavevector \tilde{k}_g , which is scattered on either side of the subplane, will give scattered plane waves of wavevector \tilde{k}'_g as shown in Figure 2.3. The intralayer scattering diffraction amplitudes are particular elements $M_{\tilde{g}'\tilde{g}}^{\pm\pm}$ of the single-layer diffraction matrix $M_{\tilde{g}\tilde{g}}^{\pm\pm}$ which describes the scattering of plane waves incident on either side of a layer parallel to the surface. The $M_{\tilde{g}'\tilde{g}}^{\pm\pm}$ are given by Pendry [45] as

$$M_{\tilde{g}'\tilde{g}}^{\pm\pm} = \frac{16\pi^2 i}{Ak_{\perp}^{\pm}} \sum_{LL'} Y_L(\tilde{k}_g^{\pm}) Y_{L'}^*(\tilde{k}'_g^{\pm}) \tau_{LL'}(k_0) \quad (2.18)$$

where the superscript signs '+/-' specify propagation directions of the plane waves with respect to the x axis, L and L' represent, respectively, pairs of angular momentum quantum numbers (ℓ, m) and (ℓ', m'), A is the unit

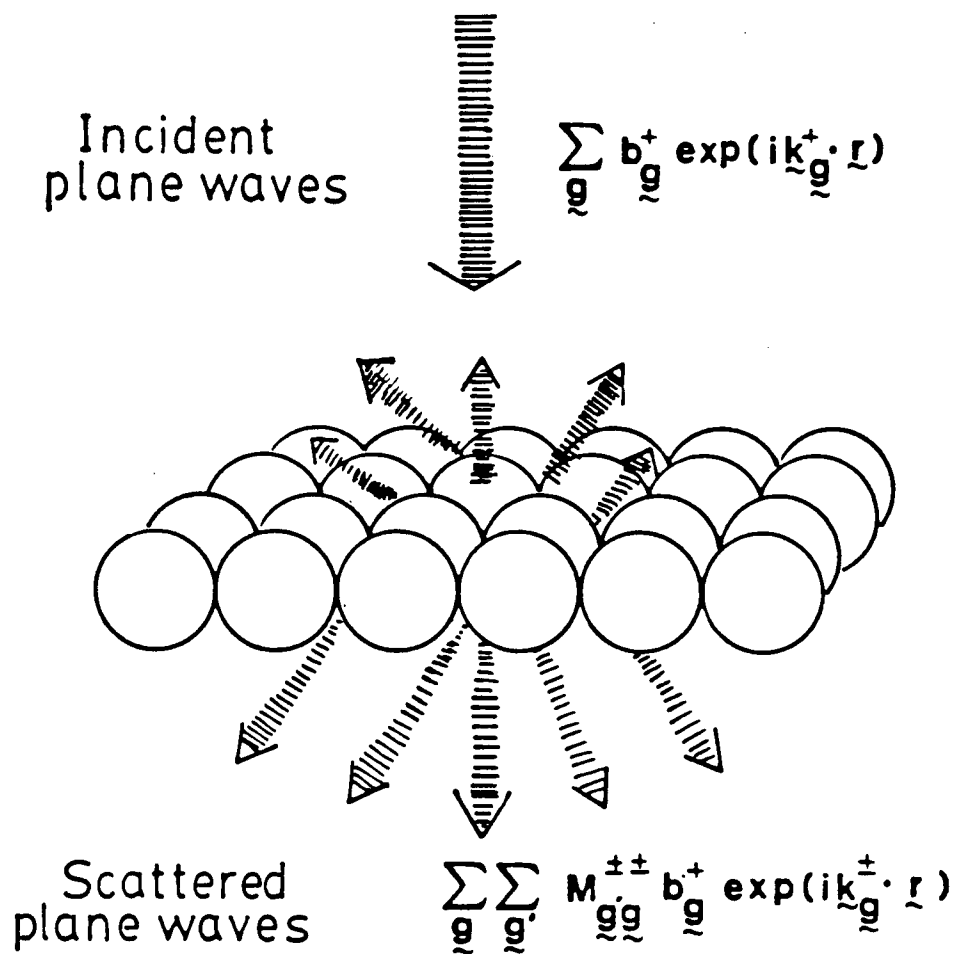


Figure 2.3: Scattering of a set of plane waves by a layer of ion cores with diffraction matrix $M_{\vec{g}\vec{g}'}^{++}$.

mesh area, and the $Y_L(k_g)$ are spherical harmonics for the angle between k_g and the surface normal; '*' represents a complex conjugate. Also in equation (2.18), $\tau_{LL'}(k_o)$ is the LL' element of the planar scattering matrix, $\tau(k_o)$ which is defined as

$$\tau(k_o) = t_s(k_o) [I_s - X_s]^{-1}, \quad (2.19)$$

where $t_s(k_o)$ is the diagonal ion core t-matrix whose non-zero elements are given by equation (2.10). The unit matrix, I_s , represents unscattered plane waves and the intraplanar scattering matrix, X_s , is defined as

$$X_s = G_s(k_o^+) t_s(k_o). \quad (2.20)$$

The structural factor $G_s(k_o^+)$ describes the intraplanar propagator in L-space.

The evaluation of M_s^{++} is complicated in general, although discussions are available in the literature [44,45,58]. Additionally, when more than one atom per unit mesh is considered, the layer should be treated as a composite layer in which the entire layer of atoms (heterogeneous or homogeneous) is split into separate subplanes. Figure 2.4 shows a graphitic (2x2) oxygen overlayer on Rh(111) where the composite layer has two oxygen atoms per unit mesh (i.e. two oxygen subplanes). In such cases the individual planar scattering matrix τ_s^i is calculated for each isolated

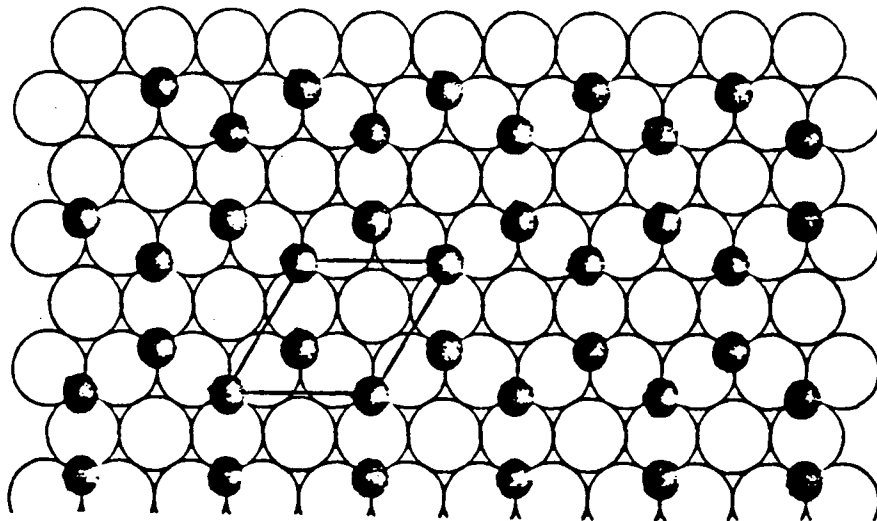


Figure 2.4: Graphitic-type oxygen overlayer for Rh(111)-(2x2)-0; there are two oxygen atoms (shaded circles) per unit mesh, one on a 3f site the other on 3h site (as in Figure 1.8(a)).

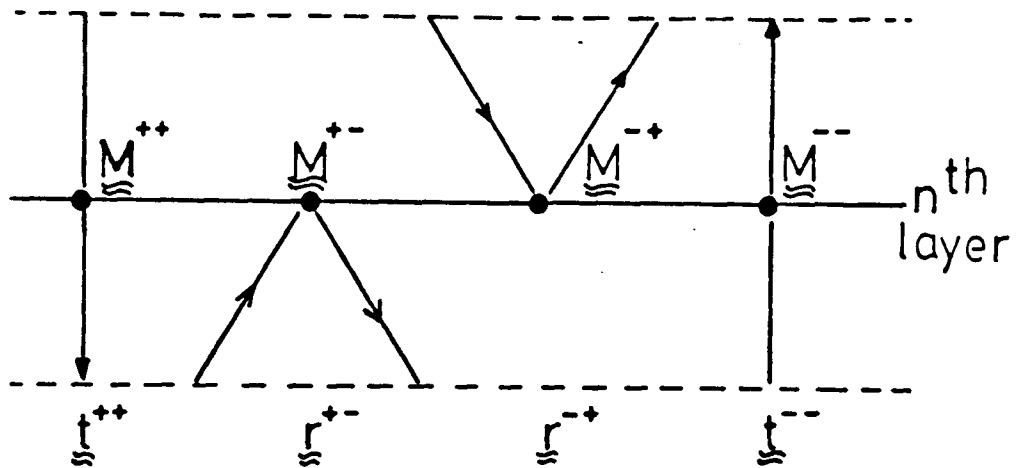


Figure 2.5: Schematic diagram of transmission and reflection matrices at the n th layer. The dashed lines are midway between consecutive layers.

subplane i , and subsequently the total scattering matrix T_s^i is obtained for that particular subplane resulting from multiple scattering with other subplanes within the composite layer. Following Beeby [59], the matrix T_s^i can be calculated for a composite layer having N subplanes by solving a set of linear equations such that

$$\begin{bmatrix} T_s^1 \\ T_s^2 \\ \vdots \\ T_s^N \end{bmatrix} = [A_s]^{-1} \begin{bmatrix} 1 \\ 2 \\ \vdots \\ N \end{bmatrix} \quad (2.21)$$

The matrix A_s consists of N^2 smaller matrices, called A_s^{ij} which are defined as:

$$A_s^{ii} = I_s, \text{ and } A_s^{ij} = -T_s^i G_s^{ij}, \quad (2.22)$$

where, the structural factor G_s^{ij} describes the interplanar propagator from subplane j to subplane i . The general expression for the diffraction matrix element $M_{g, g}^{\pm, \pm}$ of a composite layer having N subplanes is given by

[44,60]

$$M_{\tilde{g}'\tilde{g}}^{\pm\pm} = \frac{16\pi^2}{Ak_{\tilde{g}'\perp}^+} \sum_{LL'} Y_L(\tilde{k}_{\tilde{g}}^{\pm}) Y_{L'}^*(\tilde{k}_{\tilde{g}'}^{\pm}) \sum_{i=1}^N R_{\tilde{g}}^{i\pm} (R_{\tilde{g}'}^{i\pm})^{-1} T_{LL'}^i, \quad (2.23)$$

where $R_{\tilde{g}}^{i\pm} = \exp(\pm k_{\tilde{g}}^{\pm} \cdot \tilde{r}_{\perp 1})$ describes the position vector $\tilde{r}_{\perp 1}$ relating to an arbitrary origin of the composite layer. The expressions $M_{\tilde{g}'\tilde{g}}^{\pm\pm}$ in equations (2.18) and (2.23) are valid only if the origin of the coordinates within a layer is at an ion core center. The subroutine that computes $M_{\tilde{g}}^{\pm\pm}$ is called MSMF on the magnetic tape provided by Van Hove [46].

2.6 Interlayer Scattering

Computations for the single layer diffraction matrix $M_{\tilde{g}}^{\pm\pm}$, whether for subplanes or a composite layer, can be done by exact methods which calculate all scatterings to infinite order in L-space, although the exact methods are very demanding on both computing time and storage [60]. However big simplifications are possible with perturbational approaches to the problem of calculating the total diffraction by a slab of such layers. The inelastic scattering experienced by electrons propagating among isolated layers ensures that a finite stack of layers will be sufficient to represent the whole surface diffraction. Often the final stacking procedures can be done just with plane waves (in K-space) rather than with spherical waves (in L-space), although for close interlayer spacings L-space calculations are needed [44]. An efficient perturbational approach

called the combined space method [60] has been developed for LEED calculations. In the combined space method, the interlayer scattering can be treated either by the layer doubling method [45] or the renormalized forward scattering method [61]; these methods are now outlined.

2.6.1. Layer Doubling Method

As indicated in Figure 2.5 a single layer is associated with a pair of layer reflection matrices (r_s) and a pair of layer transmission matrices (t_s); they relate to the diffraction matrix M_s^{++} according to

$$r_s^{+-} = M_s^{+-}; \quad r_s^{-+} = M_s^{-+}; \quad t_s^{++} = M_s^{++} + I_s; \quad t_s^{--} = M_s^{--} + I_s. \quad (2.24)$$

In practice, with mirror plane symmetry, these matrices satisfy $r_s^{+-} = r_s^{-+}$ and $t_s^{++} = t_s^{--}$. Further the subscripts '+/-' specify the propagation of waves into and out of the layer respectively; these subscripts are read from right to left.

A schematic diagram illustrating the layer doubling method is shown in Figure 2.6, where the stacking is started with a pair of layers A and B, whose reflection and transmission matrices are known. The combined slab C has new diffraction matrices given by [44]:

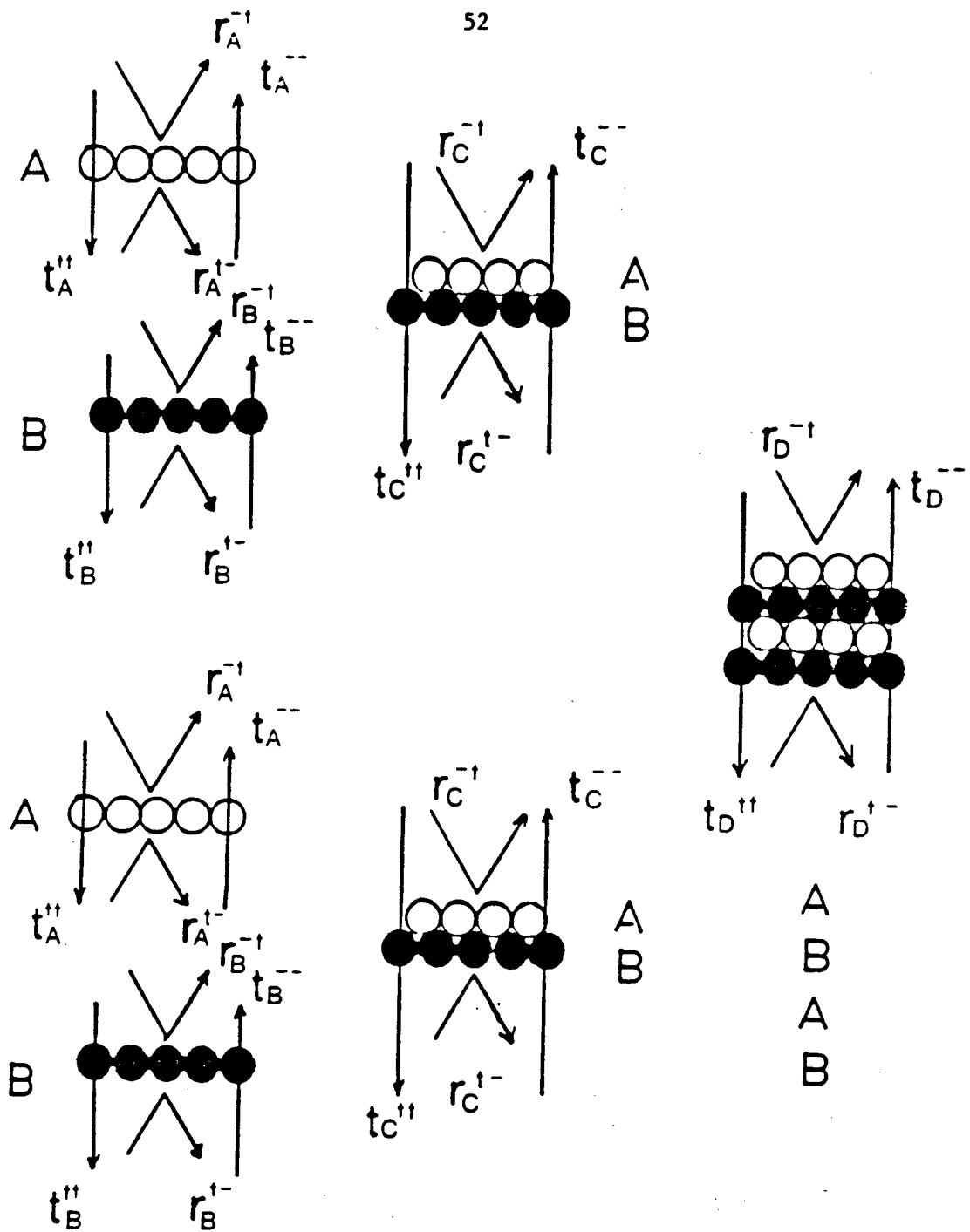


Figure 2.6: Schematic indication of the layer doubling method as applied to stacking four individual layers (with A.B.A.B... registries) into a slab (after Tong [62]).

$$\begin{aligned}
r_C^{-+} &= r_A^{-+} + t_A^{-+} P_A^{-+} r_B^{-+} P_B^{-+} [I - r_A^{-+} P_A^{-+} r_B^{-+} P_B^{-+}]^{-1} t_A^{-+}, \\
t_C^{++} &= t_B^{++} P_B^{++} [I - r_A^{-+} P_A^{-+} r_B^{-+} P_B^{-+}]^{-1} t_A^{-+}, \\
r_C^{+-} &= r_B^{+-} + t_B^{++} P_B^{++} r_A^{-+} P_A^{-+} [I - r_B^{-+} P_B^{-+} r_A^{-+} P_A^{-+}]^{-1} t_B^{-+}, \\
t_C^{--} &= t_A^{-+} P_A^{-+} [I - r_B^{-+} P_B^{-+} r_A^{-+} P_A^{-+}]^{-1} t_B^{-+}, \tag{2.25}
\end{aligned}$$

where P^- and P^+ are diagonal matrices describing the propagations of plane waves from a reference point in layer A to a reference point in layer B and vice versa.

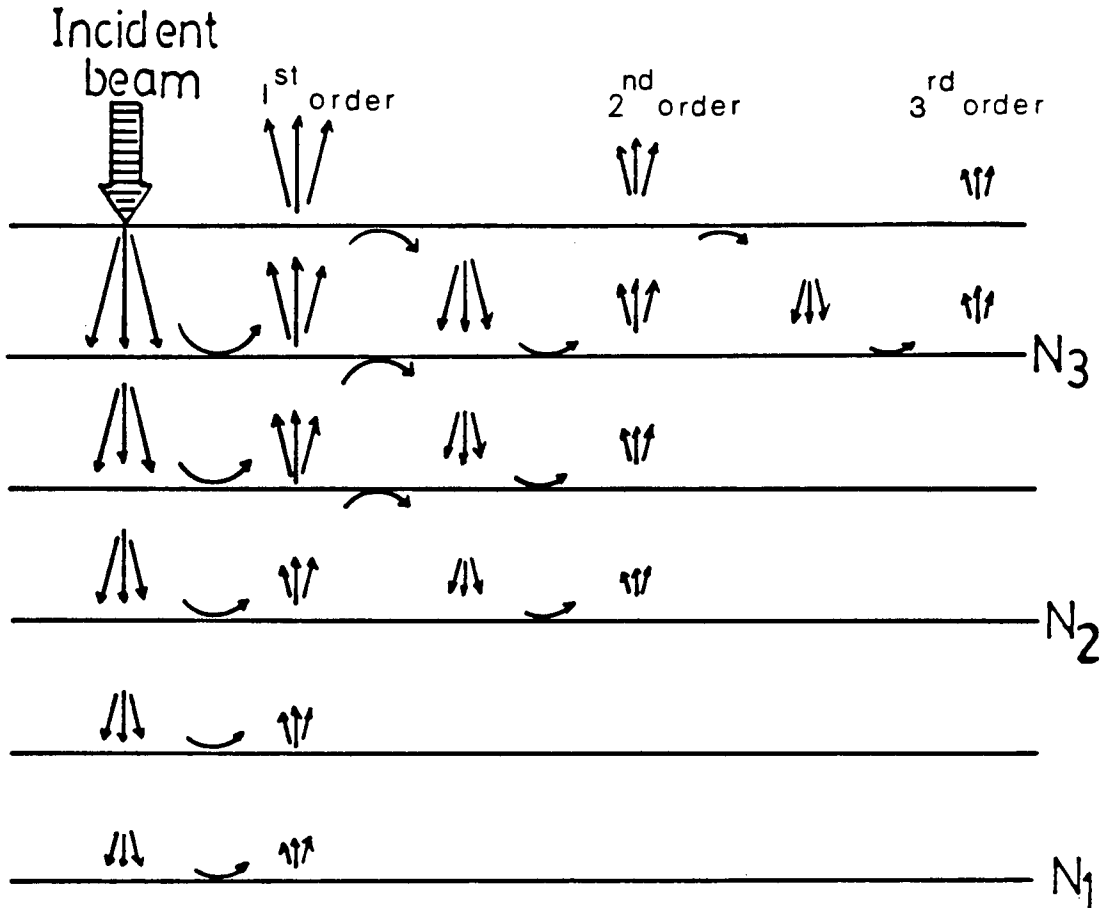
For the stacking of four layers, the results from the left-hand sides of equation (2.25) are substituted into the right-hand sides to produce a new left-hand side; this can be further iterated for 8,16,... layers until the matrix r^{-+} corresponding to a finite thick slab has converged. For most metals three or four iterations are sufficient. In Van Hove and Tong's program the subroutine DBG is used to add an overlayer to the 'combined slab'. Beam intensities calculated by the layer doubling method are obtained from the final reflected amplitudes $|r_{g_0}^{-+}|$ such that

$$I_{\tilde{g}} = (k_{\tilde{g}_l}^- / k_{o_l}^+) |r_{\tilde{g}_o}^-|^2. \quad (2.26)$$

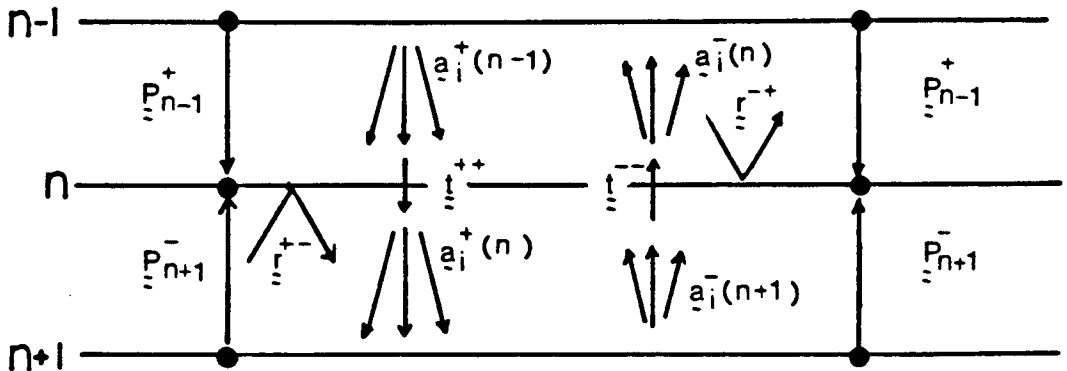
The layer doubling method requires all interlayer spacings to be greater than around 0.5\AA . The method is most convenient for bulk structures having a A.B.A.B... type of stacking sequence. The composite layer method has to be used when there are interlayer spacings of less than 0.5\AA .

2.6.2 Renormalized Forward Scattering Method

In the renormalized forward scattering (RFS) method, forward scattering processes are treated exactly, while the weaker backward scatterings are treated perturbationally. This results in considerable saving of computational effort. Figure 2.7(a) illustrates the iterative interlayer scattering treated in the RFS method. The first-order calculation includes all scattering paths with a single beam reflection process; correspondingly the second and third order calculations have three and five back reflection processes respectively. The computation is continued until the sum of the amplitudes of forward scattered beams at the deepest level considered is less than some predetermined fraction of the incident beam amplitude on the first layer (e.g. 0.3%). This limits the numbers of penetrated layers and iterations that are significant. Typically, the RFS method uses 12-15 layers and 3-4 iterations for convergence.



(a) N_1 , N_2 and N_3 denote the deepest layer reached in the 1st, 2nd, 3rd penetration, respectively.



(b) Amplitude of the inward-travelling waves (a_i^+) and outward-travelling waves (a_i^-).

Figure 2.7: Schematic indication of the renormalized forward scattering method. (a) Each triplet of arrows represents the complete set of plane waves that travel from layer to layer. (b) Illustration of the vectors which store the amplitudes of the inward- and outward-travelling waves (after Van Hove and Tong [44]).

The mathematical treatment of the RFS method is now briefly described in relation to Figure 2.7(b). For scattering at the n th layer, the amplitude $\underline{a}_1^+(n)$ can be expressed as [44]

$$\underline{a}_1^+(n) = \underline{t}_s^{++} \underline{P}_s^+(n-1) \underline{a}_1^+(n-1) + \underline{r}_s^{+-} \underline{P}_s^-(n+1) \underline{a}_1^-(n), \quad (2.27)$$

where n runs from 1 to N_i (the deepest layer included for the i th iteration). The corresponding amplitude for beams moving in the outward direction is given by:

$$\underline{a}_1^-(n) = \underline{t}_s^{--} \underline{P}_s^-(n+1) \underline{a}_1^-(n+1) + \underline{r}_s^{-+} \underline{P}_s^+(n-1) \underline{a}_1^+(n), \quad (2.28)$$

where n runs from (N_i-1) to 0. The calculated amplitudes $\underline{a}_1^+(n)$ and $\underline{a}_1^-(n)$ are conveniently stored as column vectors and, on this basis, a unit amplitude of the incident beam in vacuo can be written as

$$\underline{a}_1^+(0) = \begin{bmatrix} 1 \\ 0 \\ 0 \\ \vdots \\ \vdots \\ \vdots \end{bmatrix}, \quad (2.29)$$

while all other $\underline{a}_i^+(0)$ for $i > 1$ are necessarily null vectors. Somewhat similarly all $\underline{a}_i^-(n)$ are null vectors. The iteration starts with the input

of $a_1^+(0)$ (i.e. $n = 1$) into the right-hand side of equation (2.27) to obtain the $a_1^+(1)$, which will in turn be input to equation (2.27) for calculating $a_1^+(2)$. This is repeated through to $a_1^+(N_1)$, which is substituted into the right-hand side of equation (2.28) to obtain $a_1^-(N_1)$. Equation (2.28) is then used successively to generate $a_1^-(0)$, the reflected amplitude for the first iteration. Similar procedures are repeated to obtain the next orders $a_2^-(0)$, $a_3^-(0)$ The sum of the total reflected amplitudes is

$$A^- = a_1^-(0) + a_2^-(0) + a_3^-(0) + \dots \quad (2.30)$$

and at convergence the beam intensities are given by

$$I_{g_{\perp}} = \left(\frac{k_{g_{\perp}}^-}{k_{o_{\perp}}^+} \right) |A_{g_{\perp}}^-|^2. \quad (2.31)$$

In practice, the RFS method fails to converge well when the multiple scattering between any pair of successive layers is very strong or the interlayer spacing is small ($\leq 1.0\text{\AA}$). In such cases either the layer doubling method or the composite layer method have to be used, even though they are slower. In Van Hove and Tong's program, the subroutines RFS02 and RFS03 are responsible respectively for stacking the A.B.A.B... and A.B.C.A.B.C... type of diffraction layers. The more-recently available subroutine RFSG has been generalized by Van Hove [46] to handle a variety of stacking sequences, and it has been used extensively in this work for

the calculations on zirconium. In the RFSG program, the surface is divided into regions which are periodic and non-periodic in the direction normal to the surface. Each region may contain any stacking sequence of layers. Within these regions, the layers can be classified as corresponding to a primitive (1x1) type structure (as for the substrate) or to a superlattice structure (as for adatom layers of different translational symmetry). For example, in the (B).A.(C).B.A.B... model for the Zr(0001)-(1x1)-0 surface structure (where the letter in parenthesis depicts an oxygen layer), the three top layers (B).A.(C) represent a non-periodic region involving three primitive structures, whereas the underlying substrate layers constitute a periodic region with the B.A.B.A... stacking sequence. Details of the application of the subroutine RFSG are discussed in Chapters 6 and 7.

2.7 Application of Symmetry in the 'Combined Space' Method

The number of plane waves involved in K-space calculations, such as with the layer doubling or RFS methods, determines the dimension of the layer scattering diffraction matrix $M_{\mathbf{g}}^{\pm\pm}$, and therefore this directly controls the time required to calculate LEED intensities. By utilizing symmetry elements within the surface region, individual beams can often be grouped into symmetrized wavefunctions. This procedure reduces the number of plane waves (i.e. beams) required for the calculation. For example, in the calculation of Rh(111)-(2x2)-0, the adsorbed oxygen layer with a unit mesh area four times that of the substrate produces four times as many diffracted beams as the clean Rh(111) surface at a given energy. This is

shown in Figure 2.8(a), where the beams in the (2x2) pattern divide into the subsets labelled 1-4 in Figure 2.8(b). In the case of normal incidence (i.e. the incident beam coincides with the 3-fold rotational axis and the (xz) mirror plane), the beam sets labelled 2-4 can be grouped as a single symmetrized set. Hence, only this set plus the remaining beam set are needed for this calculation. At off-normal incidence the situation is less favorable in general, although if the incident beam coincides with the mirror plane the beam sets 2 and 3 can still be grouped together.

2.8 Evaluation of Results

The determination of surface structure with LEED involves a trial-and-error analysis designed to find that geometrical model which gives calculated $I(E)$ curves which have the best correspondence with the experimental $I(E)$ curves. This comparison may be done visually by comparing the positions and shapes of peaks, troughs and other structure in the two sets of curves. However such an approach inevitably has a subjective content; also it quickly becomes unwieldy in practice. Therefore, considerable effort has been expended in LEED to find suitable reliability indices (or R-factors to use the terminology of X-ray crystallography). The objective here is to find mathematical measures of correspondence so that the closer the match-up between the sets of experimental and calculated $I(E)$ curves, the smaller is the index. Various R-factors have been constructed for LEED [63], but those introduced by Zanazzi and Jona [64] and by Pendry [65] are perhaps the most commonly used. The latter emphasizes the positions of peaks and troughs, while the former is sensitive also to peak shapes and

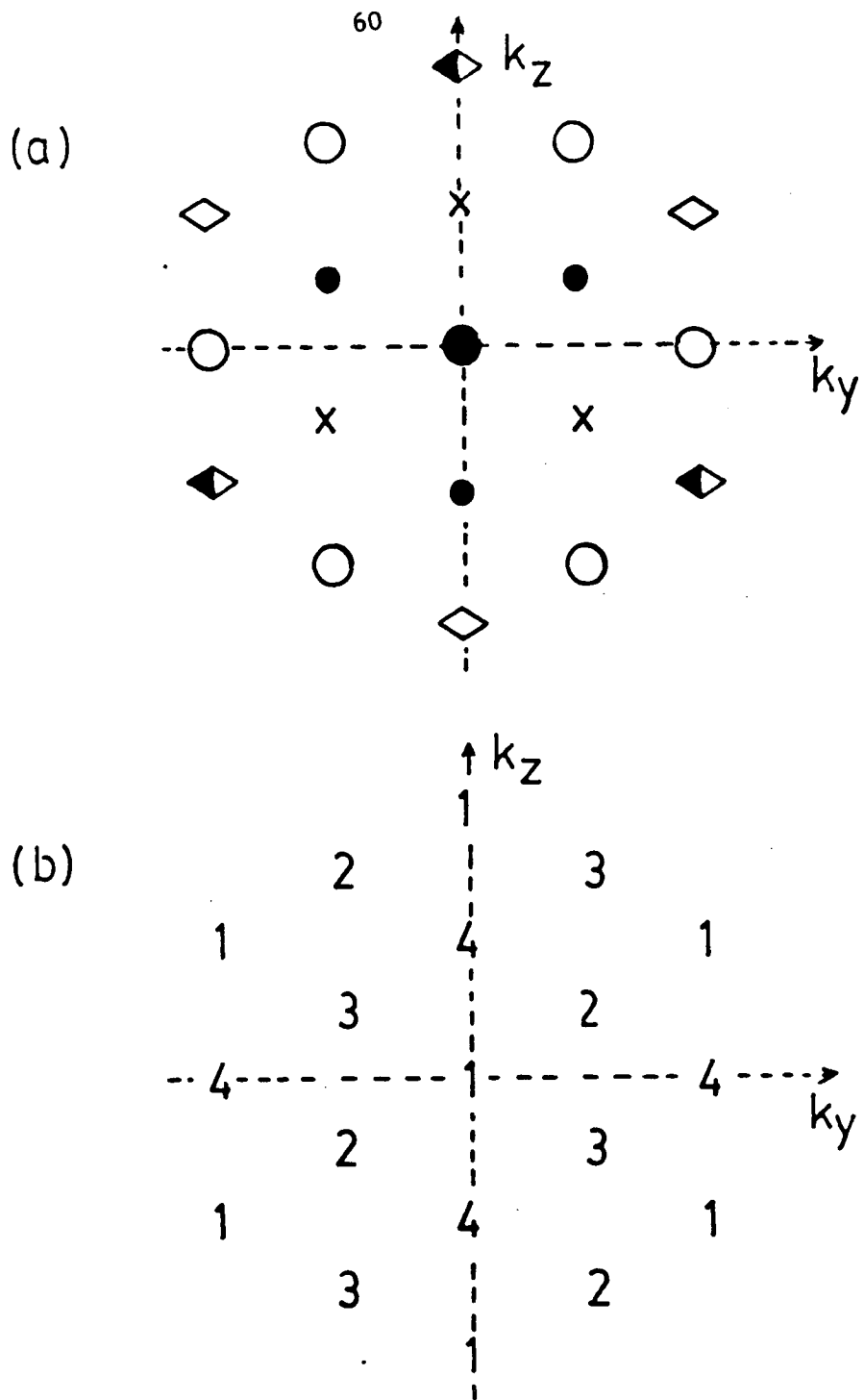


Figure 2.8: LEED pattern at normal incidence from Rh(111)-(2x2)-0.
 (a) Symmetry-related beams are indicated by the same symbols.
 (b) Beams belonging to the same beam set are indicated by the same number (independent of angle of incidence).

heights [66]. All the R-factor analyses in this work were done with the Pendry R-factor (R_p), which uses only first derivatives and is cheaper than the use of the Zanazzi-Jona R-factor. Pendry's multi-beam R-factor is expressed as

$$R_p = \frac{\sum_i \int (Y_{i \text{ calc}} - Y_{i \text{ expt}})^2 dE}{\sum_i \int (Y_{i \text{ calc}}^2 + Y_{i \text{ expt}}^2) dE}, \quad (2.32)$$

where the summation is over the individual beams, the Y_i are defined as

$$Y_i = L^{-1} / (L^{-2} + V_{oi}^2), \quad (2.33)$$

where $L = d \ln I(E) / dE,$ (2.34)

and V_{oi} is simply the imaginary component of the constant muffin-tin potential used in the calculation.

Normally in LEED crystallography, values of R-factors are plotted as functions of appropriate geometrical parameters and of V_{or} in order to find conditions for the best correspondence between experiment and calculation (i.e. the smallest value of R_p). The variation with V_{or} is important for refining the value used in the multiple-scattering calculations. Specific R-factor analyses for LEED crystallography are discussed in Chapters 4 and 6. Representative contour plots for Rh(111)-($\sqrt{3} \times \sqrt{3}$)30^o-S of R_p versus V_{or} and the Rh-S interlayer spacing for four different adsorption sites are shown in Figure 4.7.

CHAPTER 3

Experimental Methods

3.1 UHV Chamber and Apparatus

All the experiments in this work were carried out in a Varian FC12 vacuum chamber, made of non-magnetic stainless steel components joined together by flanges with copper gaskets. Figure 3.1 shows an overall schematic diagram of this particular chamber, which is equipped with LEED optics and screen (Varian 981-0127), a single-pass cylindrical mirror analyzer (Varian 981-2043) coupled with a glancing incidence electron gun as well as various other facilities. The instrumental details related to AES and LEED will be discussed in Sections 3.4 and 3.5 respectively, but the functions of other facilities inside the vacuum chamber are reviewed briefly in the following.

The manipulator (Varian 981-2530) is equipped with a flip assembly (Varian 981-2532) and includes a sample heater and liquid nitrogen cooling coil, on which the sample is mounted with a molybdenum sample cup. The manipulator flange has a pair of liquid nitrogen feed-throughs and several electrical feed-throughs mounted on it which can be used for cooling or heating the sample and measuring the temperature by means of a thermocouple welded to the sample cup. The manipulator allows the sample to be rotated in the plane of the CMA and LEED optics, as well as allowing horizontal and vertical displacements. This design also provides rotation around an axis perpendicular to the surface plane, which is necessary for intensity measurements at off-normal directions of incidence. Other basic facilities in the chamber are:

- (1) a window to monitor the sample position and diffraction pattern on the fluorescent screen;

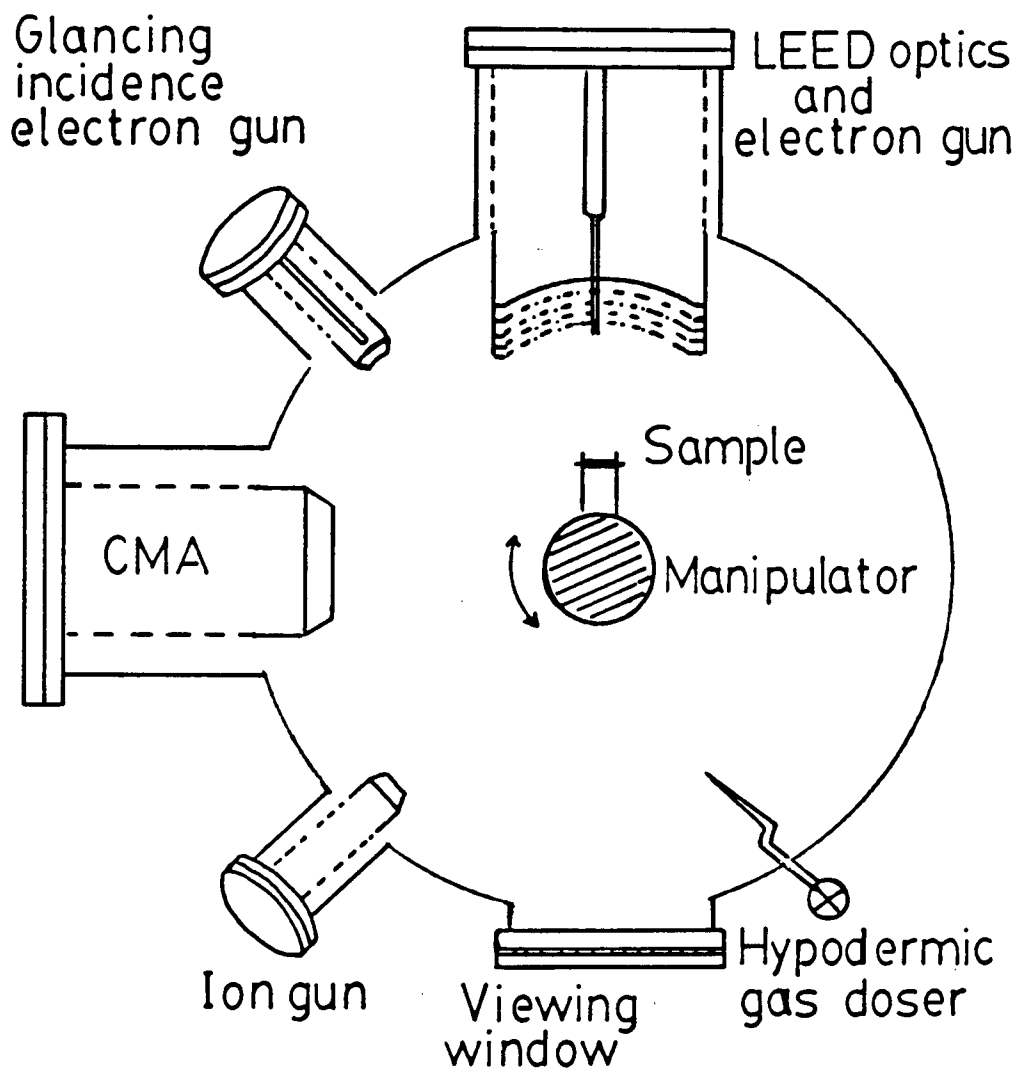


Figure 3.1: Schematic diagram of the FC12 UHV chamber with some important facilities used for the experiments made in this work (CMA = cylindrical mirror analyzer).

- (2) a nude ion gauge to monitor the system pressure;
- (3) a hypodermic gas doser connected to a variable leak valve for dosing gas on to the sample and for introducing argon for ion sputtering;
- (4) an ion-bombardment gun for cleaning the sample.

The chamber enclosing the above system is connected to a series of pumps. These include a pair of sorption pumps, an oil-diffusion pump, a titanium sublimation pump, a main ion getter pump (200 L s^{-1}) and a small ion pump (20 L s^{-1}) on the gas handling line. A schematic illustration of the pumping system and gas handling line is shown in Figure 3.2. The pumping sequence from atmospheric pressure to the 10^{-11} Torr range is as follows:

- (1) The system is roughed with the sorption pumps, which consist of zeolite cooled by liquid nitrogen. Once the pressure of the chamber is reduced to around 10^{-3} Torr, the valve between the rough line and the main chamber is closed.
- (2) The diffusion pump is used to pump the system to around 10^{-7} Torr, and then it is isolated from the main chamber.
- (3) The main ion pump is then turned on, and the system's pressure would normally reduce quickly to the $\sim 10^{-8}$ Torr range.
- (4) The whole chamber is baked, typically at 200°C for 10 hours. The titanium sublimation pump is turned on to pump away excess gaseous molecules (e.g. H_2O) which desorb from the walls of the chamber.
- (5) All filaments (e.g. ion gauge, electron gun) are degassed while the chamber is still hot ($\sim 80^\circ\text{C}$) to ensure that they do not produce unwanted degassing during normal operation.
- (6) The baking and subsequent procedures may be repeated until a pressure

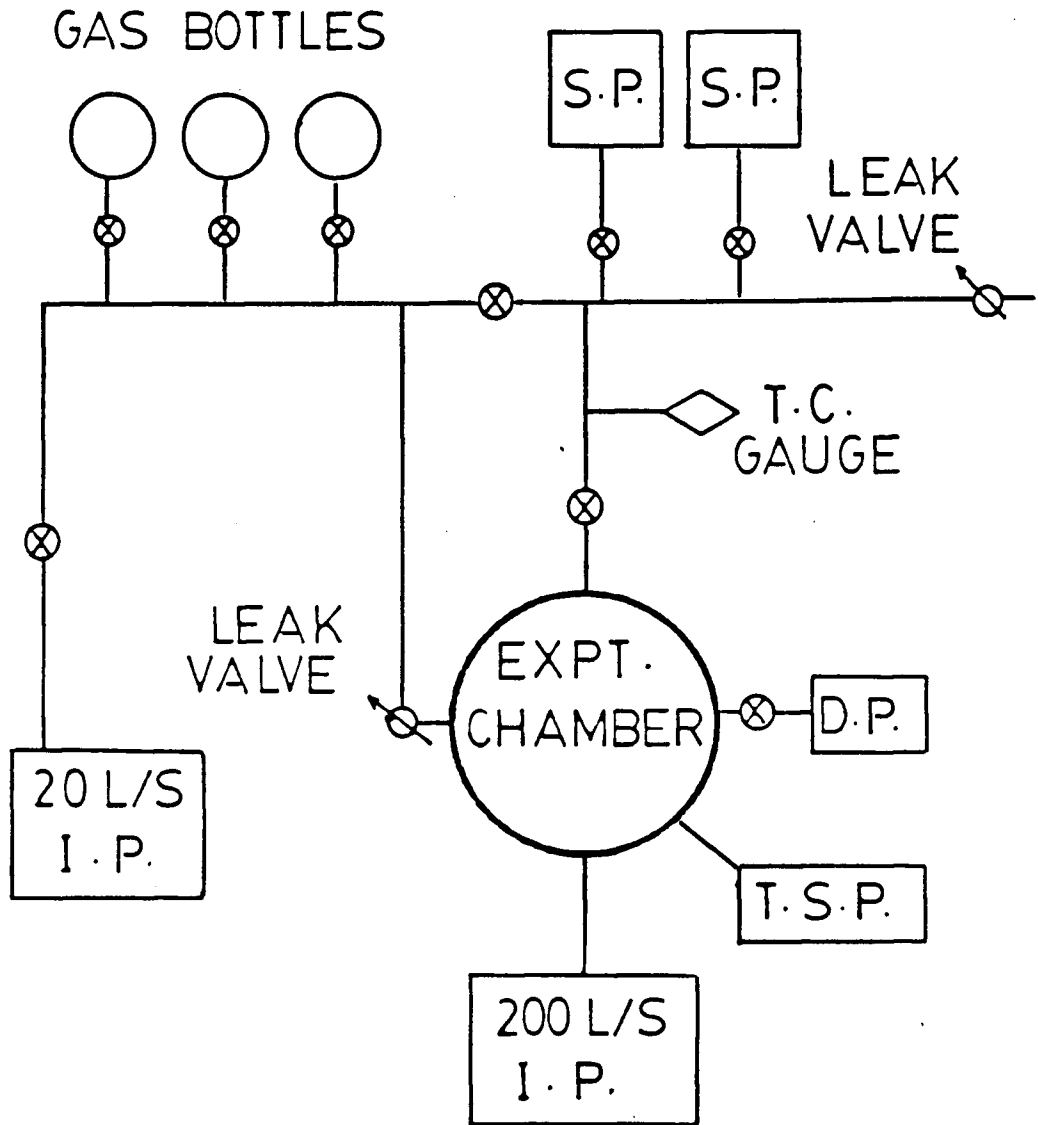


Figure 3.2: Representation of the pumping system and gas handling line (I.P. = ion pump; S.P. = sorption pump; T.S.P. = titanium sublimation pump; D.P. = diffusion pump; T.C. = thermo-couple).

of the order of 10^{-11} Torr is attained. The gas handling line is baked separately with heating tape wrapped around it; the pressure in the line is monitored by the gauge on the small ion pump or by the thermocouple gauge.

3.2 Sample Preparation

The samples used in this work were obtained from high purity single crystal rods. In each case, the crystal was mounted on a goniometer, and oriented using the Laue back reflection method [67] to ensure that the desired crystallographic plane was perpendicular to the X-ray beam. After orientation, cuts parallel to the desired plane are made using the spark erosion technique ('Agietion', Agie, Switzerland) to produce a sample disc form, which is then mounted in an acrylic resin ('Quickmount', Fulton Metallurgical Products Corp., U.S.A.) and glued to a polishing assembly equipped with alignment micrometers. That enables checks of sample orientation with Laue X-ray diffraction, and readjustment to minimize any errors resulting from the cutting or the later polishing steps. The mechanical polishing of the sample is done with progressively finer diamond paste (from 9 to 3 micron) while the jig is mounted on a planetary lapping system (DU 172, Canadian Thin Film Ltd.). Subsequently, a one-micron polish is accomplished by hand using an artificial deer skin (Microcloth, Buchler 40-7218). The whole jig with crystal assembly is then fixed to an optical bench with a He/Ne laser in order to check that the optical polished face is parallel to the desired crystallographic plane to within half a degree (this alignment test is indicated in Figure 3.3). Once the orientation is deemed satisfactory, the sample assembly is dismounted and immersed in

acetone to dissolve the resin. The sample is washed, degreased progressively with acetone, methanol and distilled water in an ultrasonic bath, dried, and mounted in the sample cup with a resistive heater (Varian 981-2058). A 0.005" alumel-chromel thermocouple is then spot-welded to the top of the sample cup in order to be able to monitor the temperature of the sample during procedures carried out in the UHV chamber.

3.3 Cleaning in UHV Chamber

After following the pumping procedures described in Section 3.1, it is important to sputter-etch the surface of the metal sample with a short and gentle argon ion bombardment before heating the sample for the first time. Such a treatment eliminates many impurities that may have been left over on the surface from washing and rinsing processes, and which may otherwise diffuse into the sample during the first heat treatment. The Ar^+ bombardment is done with the main ion pump off, and high-purity argon (99.9995% Matheson) is introduced into the chamber until the pressure is approximately 10^{-5} Torr. The initial gentle Ar^+ bombardment is done with the gun voltage set at about 600 V; the ion current on the surface should be around 3 to 4 μA . It is also advisable to operate the titanium sublimation pump during the Ar^+ bombardment to pump away impurities bombarded off from the surface and maintain the purity of argon gas. After the initial Ar^+ bombardment, Auger electron spectroscopy is employed to monitor the behaviour of impurities on the surface, including as a function of temperature. Also the sample and the sample-holder need to be outgassed at this point. The appropriate temperature depends on the characteristics of the

metal, but in general this outgassing should be done at a somewhat higher temperature than what will be required for annealing in the later stages of surface preparation. Ultimately, the pressure in the chamber should remain in the 10^{-10} Torr range while the sample is kept hot for periods of the order of one hour.

After the first heating treatment, the main surface cleaning operations can start. In most cases, the cyclic Ar^+ bombardments followed by annealing treatments are sufficient to achieve a well-ordered and clean surface without any appreciable impurities detected by Auger electron spectroscopy. The chemical cleaning method works successfully in some cases, in which impurities (e.g. C) on a surface are reacted with an dosing gas (e.g. O_2) to form a product which is easily desorbed and pumped away. However, the key to obtaining a clean and well-ordered surface is to understand the behaviors of all the impurities on the surface as a function of temperature. This is determined with Auger electron spectroscopy; then recipes for Ar^+ bombardment (e.g. ion energy, bombardment time) and heating temperature and time can be derived for an efficient cleaning procedure. Vigorous Ar^+ bombardment will result in much surface damage; a careful balance is required since higher annealing temperatures may also cause problems with impurity segregation or diffusion. In addition to following chemical composition with AES, it is also important to regularly examine the LEED pattern (e.g. after each Ar^+ bombardment and annealing treatment) to ensure that the whole preparation procedures are ordering, as well as cleaning, the surface. In general, the combination of a low background and sharp LEED pattern, without any additional fractional order beams,

indicates that a well-ordered and clean surface has been obtained, although the presence of any impurities on the surface has to be primarily detected by AES.

After a sharp (1x1) pattern of the clean surface has been obtained, then gas molecules can be adsorbed; the surface after a proper annealing procedure may then show a well-defined LEED pattern of an adsorption system. The adsorbate coverage plays an important role in a LEED analysis, although this cannot in general be determined directly from the LEED pattern. For example, an observation of a $(\sqrt{3}\times\sqrt{3})30^\circ$ LEED pattern often indicates a surface coverage of 1/3 monolayer, although Shih et al. [68] recognized a pattern formed by N on the Ti(0001) surface which occurs after the one monolayer coverage. It is often helpful to monitor the coverage of adsorbates on surfaces by measuring adsorption uptake curves using AES, or by monitoring the intensities and or profiles of fractional order beams [69]. In general, the more quantitative information on coverage available from the experiments, the easier it is to eliminate unreasonable structural models prior to undertaking the analysis with the multiple scattering calculations.

3.4 Apparatus for Auger Electron Spectroscopy

AES is an invaluable analytical tool, by which the elemental composition of a surface can be qualitatively, and even semi-quantitatively, monitored. The experimental arrangement for obtaining Auger spectra is illustrated in the Figure 3.4. The glancing incidence electron gun provides a primary electron beam having an energy around 2-3 keV, a current up to 200 μA , and a cross-sectional area of about 1 mm^2 . Auger electrons

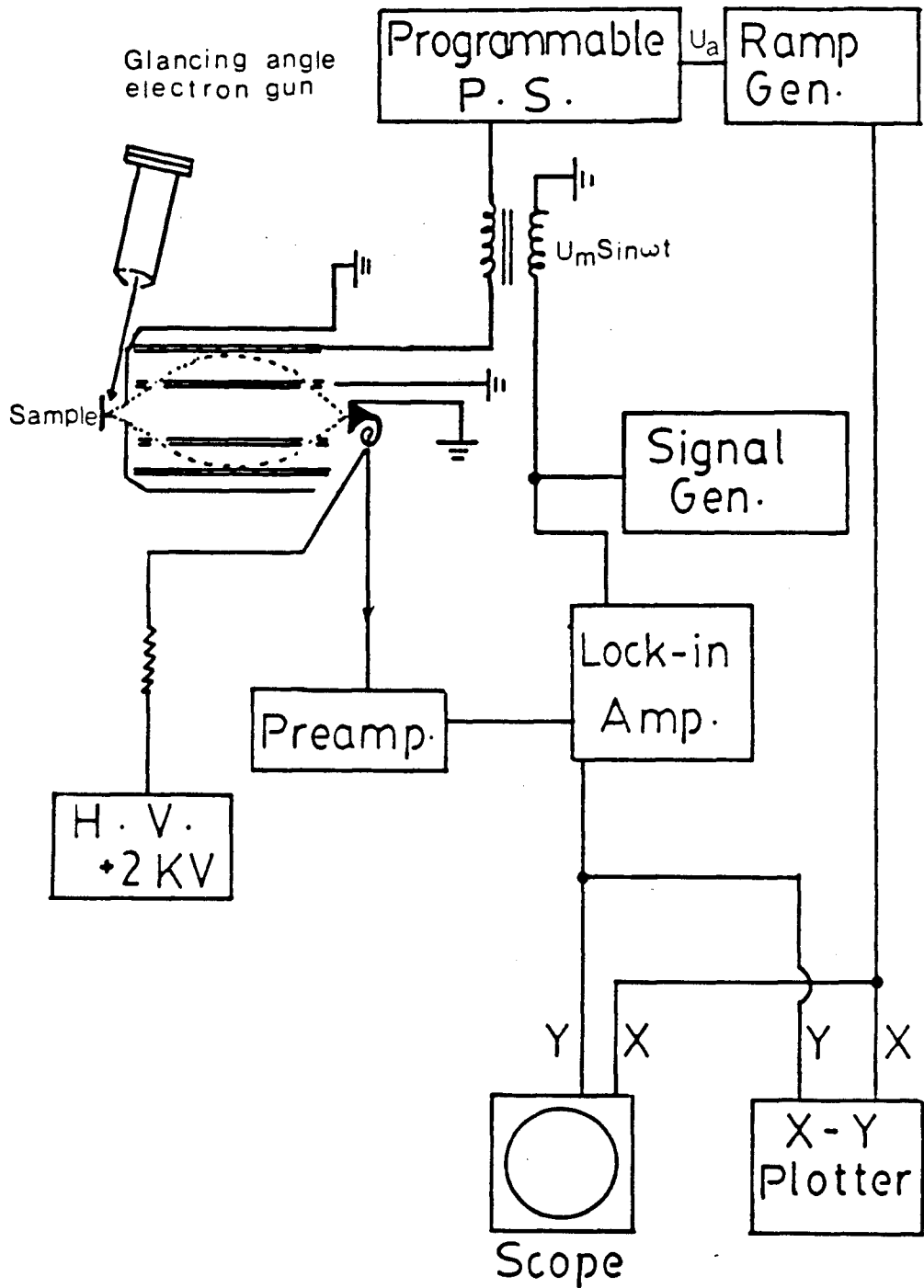


Figure 3.4: Schematic diagram to illustrate the measurement of Auger electron spectra using a cylindrical mirror analyzer in combination with a glancing angle electron gun.

emitted from the surface are detected with a single-pass cylindrical mirror analyzer (CMA). The CMA is a dispersive type analyzer which consists of a channel electron multiplier and two coaxial cylindrical electrodes. A field with cylindrical symmetry is created when a negative potential (U_a) is applied to the outer cylinder while the inner cylinder is grounded. For a particular value of the outer cylinder potential U_a , the electrons in a narrow energy range $E \pm \Delta E$ can pass through two grids in the inner cylinder and be focussed electrostatically for detection by the electron multiplier. By sweeping the retarding voltage on the outer cylinder and measuring the resulting current collected, an energy distribution curve of the electrons emanating from the sample surface (Figure 1.3) is generated [4]. In order to emphasize the Auger electron peaks, the energy distribution is differentiated. This is accomplished by modulating the retarding voltage U_a with an alternating voltage, $U_m \cdot \sin \omega t$, where U_m is approximately 3V and the frequency ω is around 5-10 KHz. The signal collected by the CMA with the modulated frequency is proportional to $\frac{dN(E)}{dE}$ [70].

3.5 Apparatus for LEED

3.5.1 LEED Optics and Electron Gun

The electron energy analyzer used is indicated in Figure 3.5. An incident beam is produced by heating the filament in the electron gun, and it is collimated by the lens system. The electron beam passes through the drift tube and strikes the sample surface; the drift tube being held at the

same potential as the sample. The energy of the electron beam is fixed by the potential difference (U) between the filament and the sample. Typical energies used in our work are between 10 and 300 eV, for which the diameter of the incident beam is about 1 mm at the sample surface due to the finite size of the cathode. The energy spread in the beam is typically 1 eV as a result of the thermal energy distribution from the heated filament [4].

The beam current is usually kept at around 1 μA for energies above 100 eV, but the current available declines almost linearly to about 0.2 μA as the energy is reduced below 100 eV. This variation has to be recorded for normalizing the measured beam intensities, otherwise the measured intensities would appear artificially reduced at low energies. For displaying the LEED pattern corresponding to the energy eU , the electrons which are elastically backscattered from the sample surface are passed through all four hemispherical concentric grids (i.e. G1 to G4 in Figure 3.5), and they are accelerated on to the fluorescent screen by a positive potential (~ 5 kV). For the normal mode of operation the first grid (G1) is grounded, as are the sample and drift tube to ensure that the scattered electrons travel in a field free region between sample and the first grid. The double retarding grids (G2 and G3) have a negative potential whose magnitude is slightly smaller than U , so that essentially all of the inelastically scattered electrons are filtered out. The fourth grid (G4) is grounded to screen the double grids from the high voltage on the collector screen.

Thus a series of LEED patterns corresponding to varying energies can be displayed on the screen by systematically modifying the primary beam energy and simultaneously the potential applied to the retarding grids.

3.5.2 Measurement of LEED Intensities

A commercial video LEED analyzer (Data-Quire Corp., Stony Brook, N.Y.) is used in conjunction with an intensified silicon intensified target type of TV camera (COHU 4410/ISIT) to measure $I(E)$ curves for diffraction spots exhibited on a LEED display screen. A schematic diagram of the system for measuring the real-time LEED spot intensity using a video LEED analyzer (VLA) is shown in Figure 3.6.

An ISIT camera basically contains a photocathode tube and a silicon target. As light from the LEED spots is focussed through the camera lens on to the photocathode tube, photoelectrons are emitted and accelerated to the silicon target. This results in the production of secondary electrons, and hence higher currents to improve the measurement of the LEED spots. This magnifying effect can allow a reduction in the incident beam current required for producing a measurable LEED pattern, and thereby reduce the possibilities for unwanted electron-beam effects during the measurements. The latter is also favored by the on-line TV camera method which can measure intensities of LEED spots much faster than the more-traditional methods of using a moveable Faraday cup collector or an external spot photometer [71,72]. A detailed review of recent approaches to quantitative measurements of LEED intensities has been given by Martin and Lagally [73].

Along with the TV camera, a central part of the system in Figure 3.6 is the 32K microprocessor (Motorola 6800), by which the video signals from the camera are digitized using an A/D converter and the LEED gun voltage is remotely controlled via a D/A converter. When the camera is directed at a LEED pattern, the image on the monitor screen defines a frame consisting

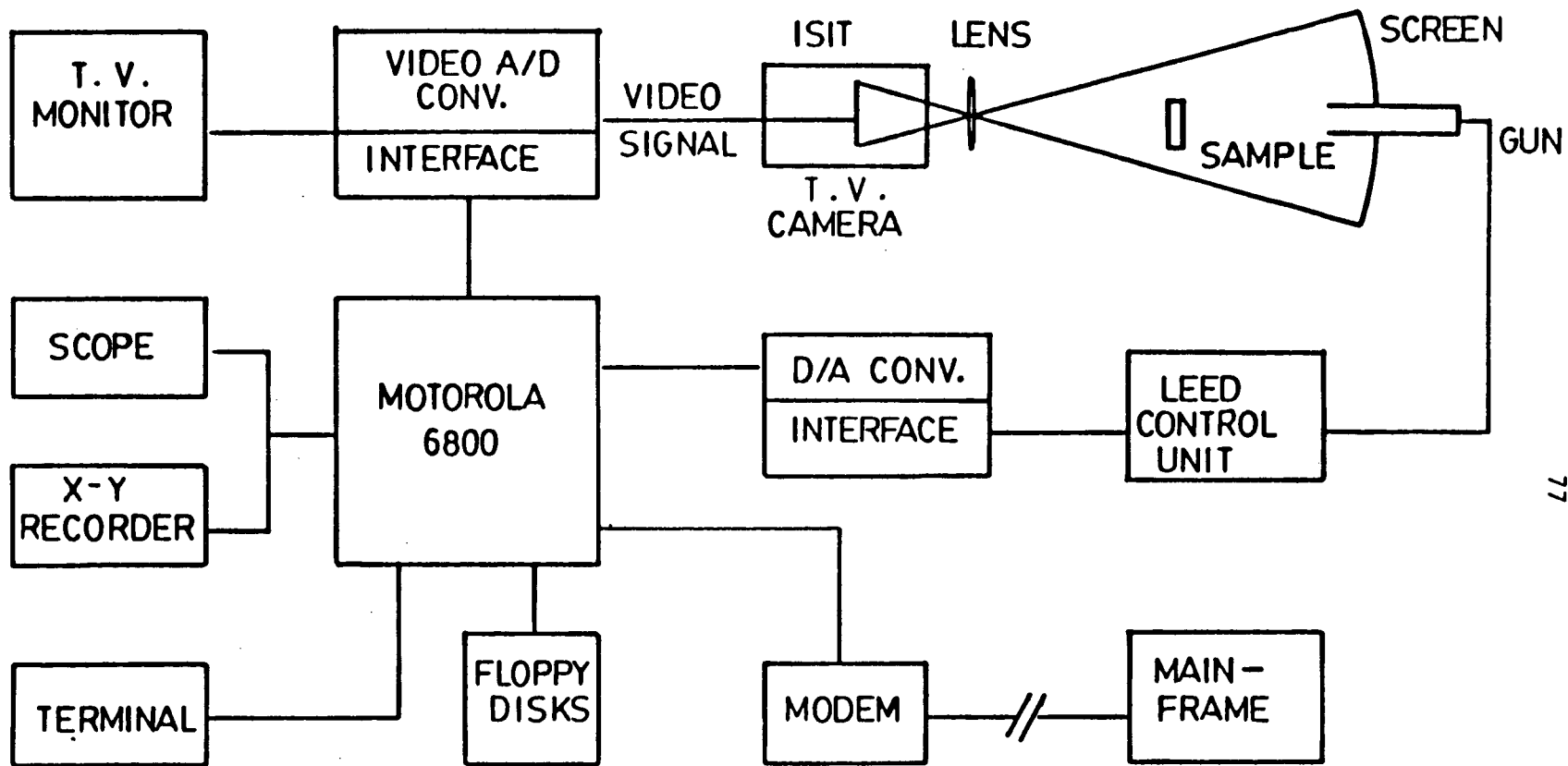


Figure 3.6: Schematic diagram for the TV analyzing system which detects and measures diffracted beam intensities from the LEED screen.

of 256 x 256 picture elements (or pixels). Such a frame corresponds to fixed parameters of the incident beam (energy, direction of incidence). The intensity of each pixel within a frame is digitized using an intensity scale (or gain level) between 0 and 255. The scanning of such a single frame is completed in 1/60 s. Each scanning starts from the upper left corner of the frame (Figure 3.7) and it proceeds horizontally one pixel at the time along the topmost row until the 256th pixel is reached. This scanning course is repeated on the next horizontal line, and so on until all 256 horizontal lines have been scanned from the left to right.

In contrast to the scanning course, the digitizing course is always perpendicular to the scanning course, and only the intensities of pixels within a single column can be simultaneously digitized and recorded during each scanning. On the other hand, if there are n pixels within a row parallel to the scanning course, it will take n scans (i.e. $n/60$ s) to complete the digitization processes. Therefore the complete digitization of the whole frame needs 256/60 s, although that is not needed in practice for LEED, where only the diffraction spots are digitized. The VLA provides user-selected 10 x 10 pixel windows as shown in Figure 3.9(a), which define the region to be digitized, and which are superimposable on particular LEED spots observed on the video screen. Just 10 scans (i.e. 1/6 s) are needed for digitizing an isolated window, and the intensity of each individual LEED spot is obtained by summing the intensities of all 100 pixels within the window. The VLA system in this laboratory provides up to 49 isolated windows for digitizing the LEED spots simultaneously for each

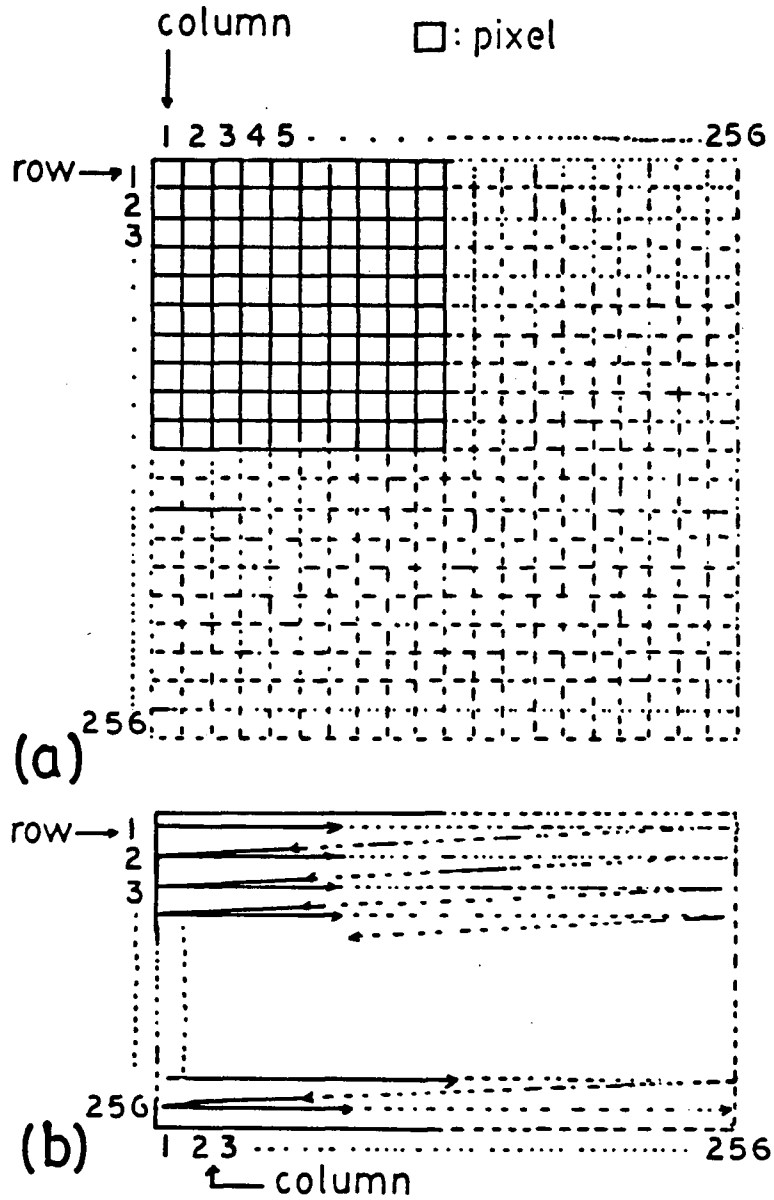


Figure 3.7: A frame on the monitor screen to illustrate: (a) the 256x256 pixels structure, (b) the scanning course.

frame (i.e. at a fixed energy). Once a frame is digitized, the next frame appears when the voltage of the incident beam is changed by an increment. Each 10 x 10 window is then automatically matched to the new spot position for the next digitization process. This matching is done by the computer using previously supplied information on unit mesh dimensions and direction of incidence. The present software does not allow us to vary the window size during measurements, so precluding separate measurements for background subtraction. The effect of the background in measurements is minimized by appropriately setting the gain level in the digitization process for individual beams. In practice it is better to measure fractional order beams separately from integral beams, with different gain level settings. There is no serious loss in this for the purpose of LEED crystallography since the final comparisons between measurements and calculations emphasize relative intensities only. Nevertheless, beam intensities measured with the VLA are normalized with respect to the incident beam according to

$$I = i/i_0, \quad (3.1)$$

where i and i_0 are diffracted and incident beam currents respectively.

In practice in our laboratory, the incident beam for LEED is chosen to coincide with a symmetry element of the surface structure. The diffraction pattern then exhibits symmetrically related beams, and correspondingly the fast VLA method can enable the user to check rapidly that the measured $I(E)$ curves do indeed show the expected symmetries. As an example, Figure 3.8 shows $I(E)$ curves measured for six beams from a Zr(0001)-(1x1)-0 surface;

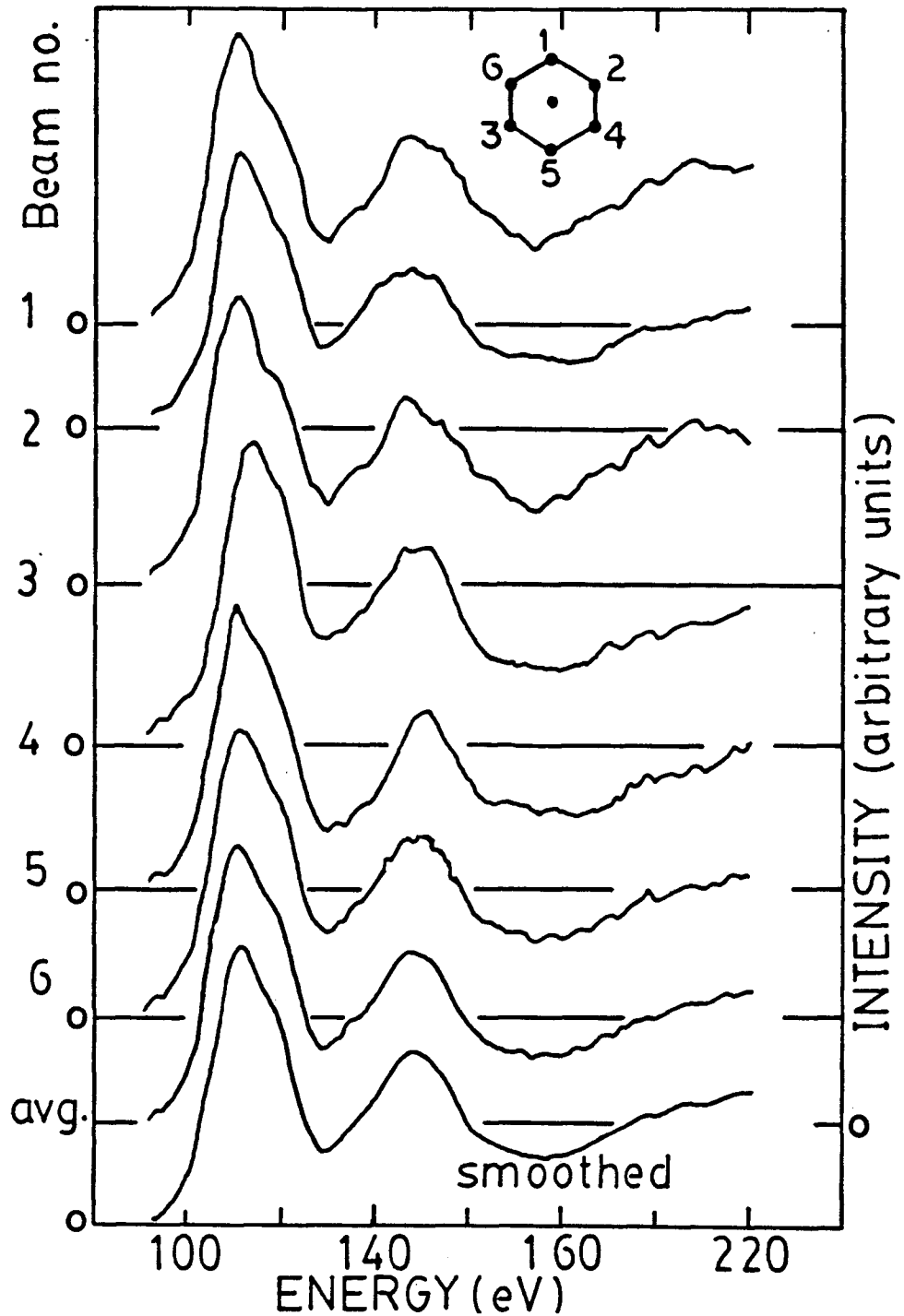


Figure 3.8: $I(E)$ curves measured for six essentially equivalent beams for normal incidence on the $Zr(0001)-(1 \times 1)-O$ surface. The close correspondence confirms the incidence direction. The averaged and subsequently smoothed $I(E)$ curves are displayed in the bottom two curves.

that they are essentially equivalent confirms the incidence direction is very close to normal. Such sets of $I(E)$ curves are averaged to minimize any further small experimental uncertainties [74]. Finally, our usual practice is to smooth the resulting averaged curve with two cubic spline operations to establish a final experimental $I(E)$ curve (bottom curve in Figure 3.8), which is then available for the comparison with calculated $I(E)$ curves.

3.5.3 Measurement of Spot Profile

The intensity of a LEED spot, corresponding to an individual frame (or energy) described in Section 3.5.2, is defined as the summation of the digitized intensities of the 100 pixels in the window covering the spot. An additional measurement is of the intensity distribution across the spot, which is generally referred to as the spot (or beam) profile. Such measurements at fixed energy, especially for fractional order beams, can provide useful information about surface ordering phenomena (see Chapter 6). The LEED spot profile measurement is outlined in Figure 3.9(a) where the user-selected window (10x10 pixels) covers completely the spot to be measured. Ten scans are needed to digitize this whole spot, and as shown in Figure 3.9(b) the intensity profile along the X_{win} direction can be obtained by joining the maximum positions of ten profiles. The full-width at half-maximum (FWHM) for such a profile provides a quantitative measurement of spot sharpness; generally the larger the value of $1/\text{FWHM}$ the greater is the surface order, although it must be recognized that there is always a beam broadening effect introduced by the instrument [29].

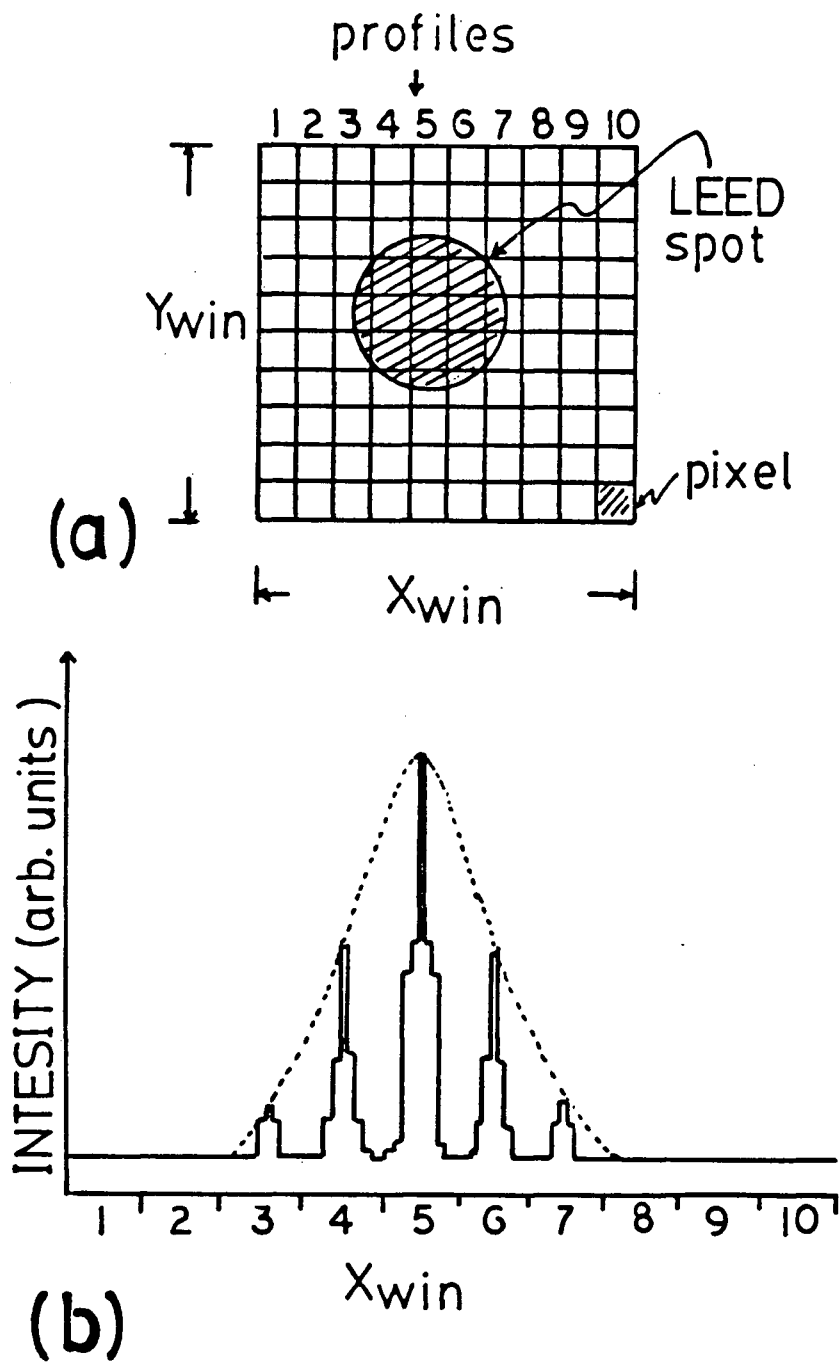


Figure 3.9: Measurement of spot profiles: (a) the LEED spot to be measured is covered with a user-selected window (10x10 pixels), (b) the spot intensity profile along X_{win} .

CHAPTER 4

LEED Analysis for the Rh(111)- $(\sqrt{3}\times\sqrt{3})30^\circ$ -S
Surface Structure

4.1 Introduction

So far only very limited structural data are available for the ordered adsorption of sulfur atoms on close-packed (111) surfaces of face-centered cubic (fcc) metals, and that provided a motivation for the present study [75]. At the time this work was undertaken, structural information for surfaces of this type were restricted to the (111) surfaces of iridium and nickel. In each of these cases, low coverages of ordered S atoms apparently adsorb on the so-called "expected" 3-coordination sites [76,77], and similar observations have since been reported for S chemisorption on the Pd(111) and Pt(111) surfaces [78,79]. (The "unexpected" and "expected" hollow sites of 3-coordination are distinguished by whether the 3-fold rotation axis which passes through each site respectively intersects an atom or not in the second metal layer; these sites can be identified as 3h or 3f, a notation that recognizes the hcp and fcc stacking sequence for the topmost three layers as is indicated in Figures 1.8(a).) A simple interpretative model developed on the basis of available structural data from surface crystallography [80] predicts a S-Ir bond length of 2.25Å for S adsorbed on Ir(111), and this compares quite closely with the value of 2.28Å reported from the LEED crystallographic analysis [77]. By contrast, the predicted S-Ni distance (2.15Å) for S adsorbed on Ni(111) seems rather long compared with the reported measured value of 2.02Å [76].

In order to have more information for assessing the adsorption bond lengths for S on fcc(111) surfaces, a LEED crystallographic analysis has been made for the surface structure designated Rh(111)-($\sqrt{3} \times \sqrt{3}$)30°-S. This system also allows further comparisons to be made with the structural data

already available for S adsorbed on the two other low-index surfaces of rhodium, namely the surface structures Rh(100)-(2x2)-S [40] and Rh(110)-c(2x2)-S [41]. Additional LEED crystallographic analyses have been reported for adsorption on Rh(111) surfaces, and they span a range of structural situations. For example, for the system Rh(111)-($\sqrt{3}\times\sqrt{3}$)30°-CO at a coverage of one-third monolayer (ML) [81], the CO molecules adsorb perpendicularly and on-top of Rh atoms (adsorption site referred to as 1f to emphasize the 1-fold coordination), while for Rh(111)-(2x2)-CO, at the coverage 0.75 ML, CO adsorbs both near 1f sites and on the bridge sites of two-fold (2f) coordination [82]. However, the ethylidyne group in Rh(111)-(2x2)-C₂H₃ at 0.25 ML [83] apparently adsorbs at the "unexpected" sites of 3-fold coordination (i.e. the 3h sites). These latter examples remind of the significance of organo-rhodium systems in catalytic reactions, and therefore of the potential importance for developing an understanding of structure and bonding for chemisorption on rhodium.

4.2 Experimental

The Rh(111) surface was cut and polished as described in Section 3.2. After mounting in the vacuum chamber, Auger electron spectroscopy revealed substantial structure at 151 and 272 eV (Figure 4.1(a)) and therefore appreciable amounts of sulfur and carbon contamination. It was found that Ar⁺ bombardment (800 V, $\sim 5 \mu\text{A cm}^{-2}$) for one hour was the most effective way to remove the sulfur from the surface, although the Auger peak for carbon showed a relative increase after the bombardment (see the Figure 4.1(b)). This latter effect appears to result from the low

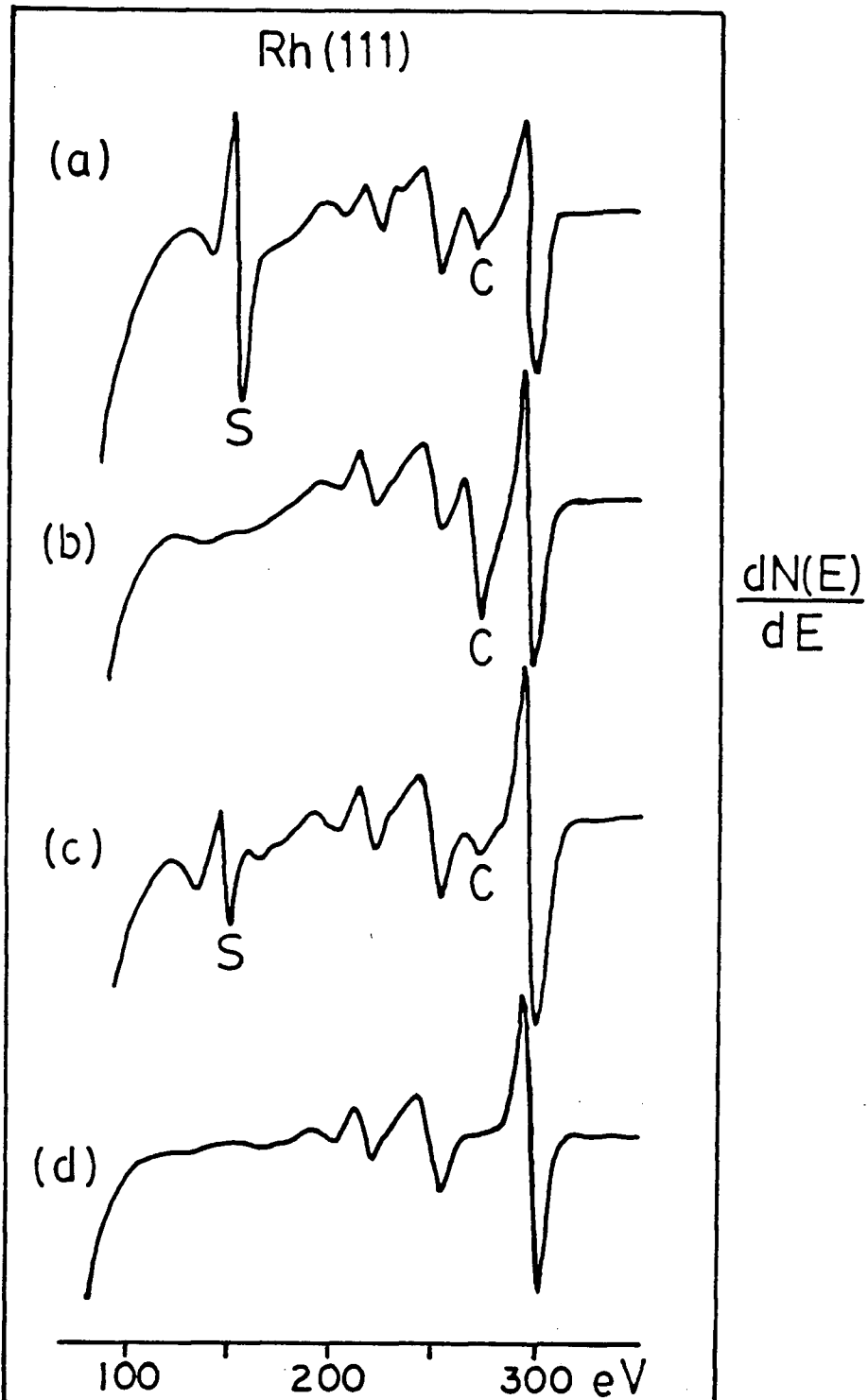


Figure 4.1: Auger spectra from Rh(111) surface:
 (a) as mounted, with considerable S (151 eV) and C (272 eV) contamination;
 (b) after Ar^+ bombardment, to show reduced S, but increased C;
 (c) after annealing, to show reduced C, but increased S;
 (d) after a full cleaning routine.

sputtering cross-section of carbon, nevertheless the carbon Auger signal could be simply removed by annealing the sample at 1000°C for 15 minutes. This annealing apparently causes the carbon to diffuse into the bulk crystal, although simultaneously sulfur segregates to the surface region (see Figure 4.1(c)). Cycles of Ar⁺ bombardment followed by annealing at around 1000°C were found to provide an effective method for reducing the levels of S and C contamination within the surface region probed by AES. Reactive treatment with oxygen appeared ineffective to remove the surface carbon from the surface. During these cleaning procedures, the LEED pattern was assessed from time to time. That for Rh(111) exhibits a three-fold rotational symmetry and appropriate symmetry planes at normal incidence. The above procedures led to the preparation of a well-ordered and clean Rh(111) surface which showed a sharp (1x1) LEED pattern (see Figure 4.3(a)) without any C and S contamination as detected by AES (Figure 4.1(d)). High purity H₂S (Matheson) was then dosed on to the clean Rh(111) surface at room temperature and a pressure of about 10⁻⁸ Torr. Figure 4.2 displays a typical sulfur up-take curve as measured by

$$R = A_{151}/A_{304}$$

(i.e. the ratio of the Auger peak height for S at 151 eV to that of Rh at 304 eV) as a function of exposure in Langmuirs (1 L = 10⁻⁶ Torr s). This curve, and others measured independently show definite breaks in slope (close to R = 0.65 and 0.85) which are suggestive of change in structure. LEED indicates that the first break corresponds to the formation of the

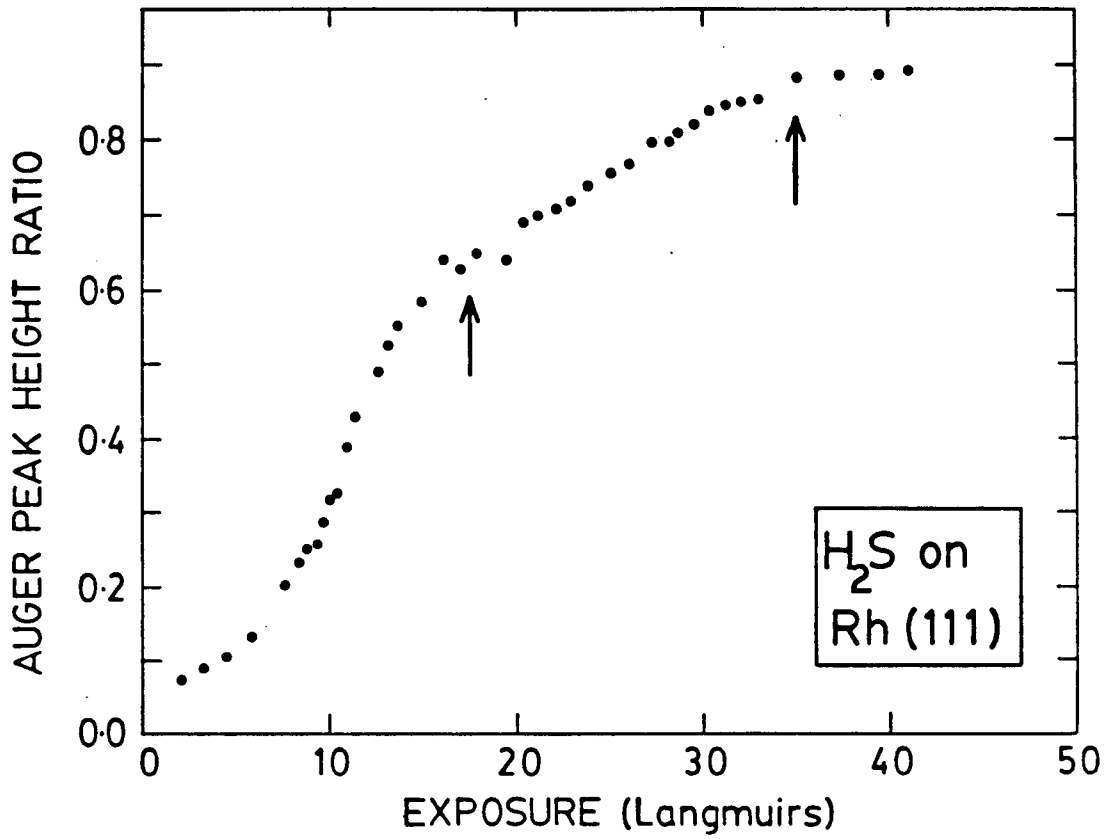


Figure 4.2: Auger peak height ratio S (151 eV)/Rh (304 eV) plotted as a function of H₂S exposure to a Rh(111) surface.

$(\sqrt{3} \times \sqrt{3})30^\circ$ surface structure (see Figure 4.3(b)), whereas the second break appears to be associated with the formation of a high coverage $c(4 \times 2)$ structure as is shown in Figure 4.3(c). Good quality $(\sqrt{3} \times \sqrt{3})30^\circ$ LEED patterns are observed with R around 0.75 after exposing the clean Rh(111) surface at room temperature and annealing for a few minutes at 200°C .

It is believed that H_2S dissociatively adsorbs on the Rh(111) surface. A $(\sqrt{3} \times \sqrt{3})30^\circ$ LEED pattern could also be obtained by heating the Rh(111) sample under conditions where some sulfur impurity migrates to the surface from the bulk as noted in the cleaning process. Corresponding observations have been reported by others, including Hengrasmee *et al.* [40] in their preparation of Rh(100)-(2x2)-S, and Castner *et al.* [84]. The $I(E)$ curves measured from the Rh(111)- $(\sqrt{3} \times \sqrt{3})30^\circ$ -S surface obtained by the migration of the bulk sulfur impurity agreed closely with those prepared by H_2S adsorption. Some evidence for H_2S dissociating on a metal surface has been provided by Keleman and Fischer's study on the Ru(0001) surface with the additional techniques of ultra violet photoemission and thermal desorption spectroscopy [85]. This work indicated that H_2S dissociated upon adsorption over the entire range of coverage. In Rh(111)- $(\sqrt{3} \times \sqrt{3})30^\circ$ -S, the adsorbed sulfur atoms are held strongly to the surface and could only be removed by extensive Ar^+ bombardment.

Intensity-versus-energy ($I(E)$) curves were measured for the Rh(111)- $(\sqrt{3} \times \sqrt{3})30^\circ$ -S surface structure at normal incidence for the diffracted beams designated (01), (10), (20), (11), (02), $(\frac{1}{3} \frac{1}{3})$, $(\frac{1}{3} \frac{4}{3})$, $(\frac{2}{3} \frac{2}{3})$, and $(\frac{4}{3} \frac{1}{3})$, using the beam notation shown in Figure 4.4. The unit mesh of the superstructure corresponding to the LEED pattern has been shown in

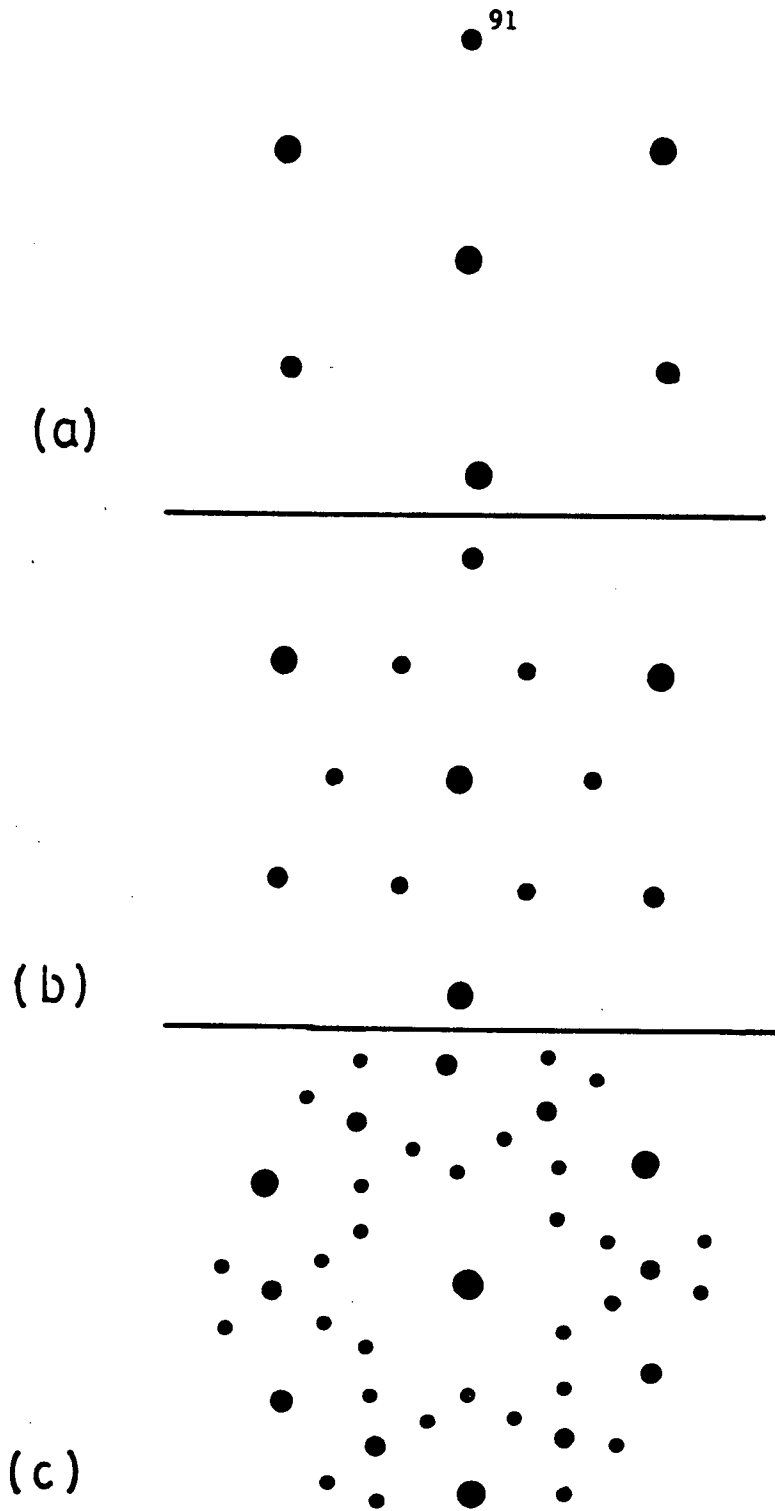


Figure 4.3: Schematic indications of LEED patterns from surfaces designated:
 (a) Rh(111)-(1x1);
 (b) Rh(111)-($\sqrt{3} \times \sqrt{3}$)30°-S;
 (c) Rh(111)-c(2x4)-S.

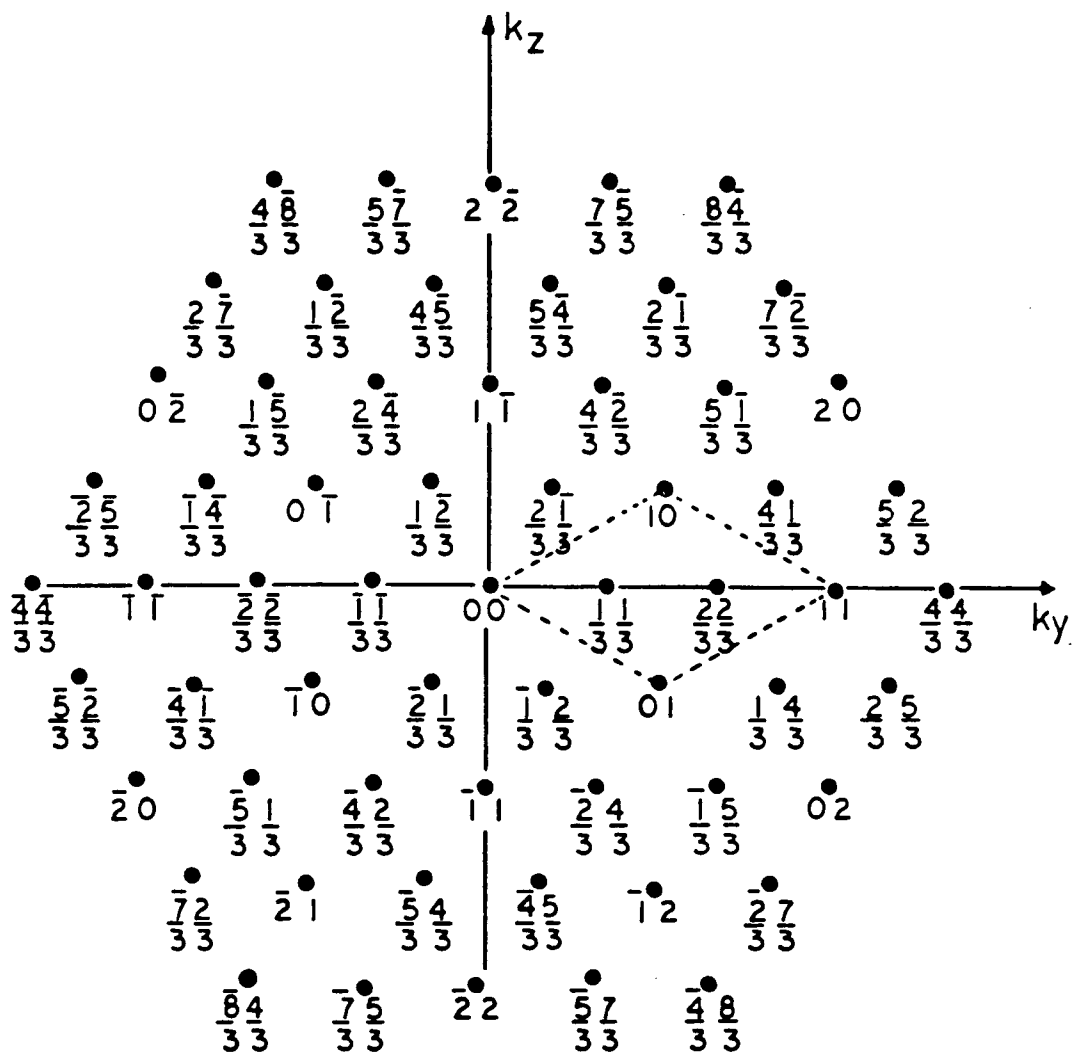


Figure 4.4: Beam notations for a LEED pattern from the Rh(111)- $(\sqrt{3} \times \sqrt{3})30^\circ$ -S structure.

Figure 1.8(a). These measurements were made using the VLA system as described in Section 3.5.2. At the outset, $I(E)$ curves for sets of beams which are expected to be equivalent at normal incidence were displayed on the oscilloscope. This enabled the normal-incidence setting to be fine-tuned on-line. With the normal-incidence direction set, integrated beam intensities were measured as the energy was varied from 50 to 250 eV with a constant increment of 2 eV. Each spot on each frame was scanned five times, and the multiply-summed integrated intensities were normalized to the incident beam current. The symmetrically equivalent beams were averaged with equal weightings to minimize some further minor experimental uncertainties associated with any misalignment of the sample [74], and the averaged intensity curves were finally smoothed with two cubic spline operations. Figure 4.5 shows two $I(E)$ curves collected from two independent sets of measurements.

4.3 Calculations and Results

The simplest models for the $(\sqrt{3} \times \sqrt{3})30^\circ$ structure have sulfur atoms adsorbed on the unreconstructed (111) surface of a fcc metal, and they are conveniently designated according to the site of adsorption as indicated in Section 4.1 and Figure 1.8(a). $I(E)$ curves for the various diffracted beams were calculated using the renormalized forward scattering method for models with adsorption on the expected 3-fold (3f) sites, the unexpected 3-fold (3h) sites, the on-top (1f) sites and the bridge (2f) sites. These calculations included symmetry, for example the 3-fold rotation and mirror plane symmetries were utilized for the models corresponding to the $p31m$

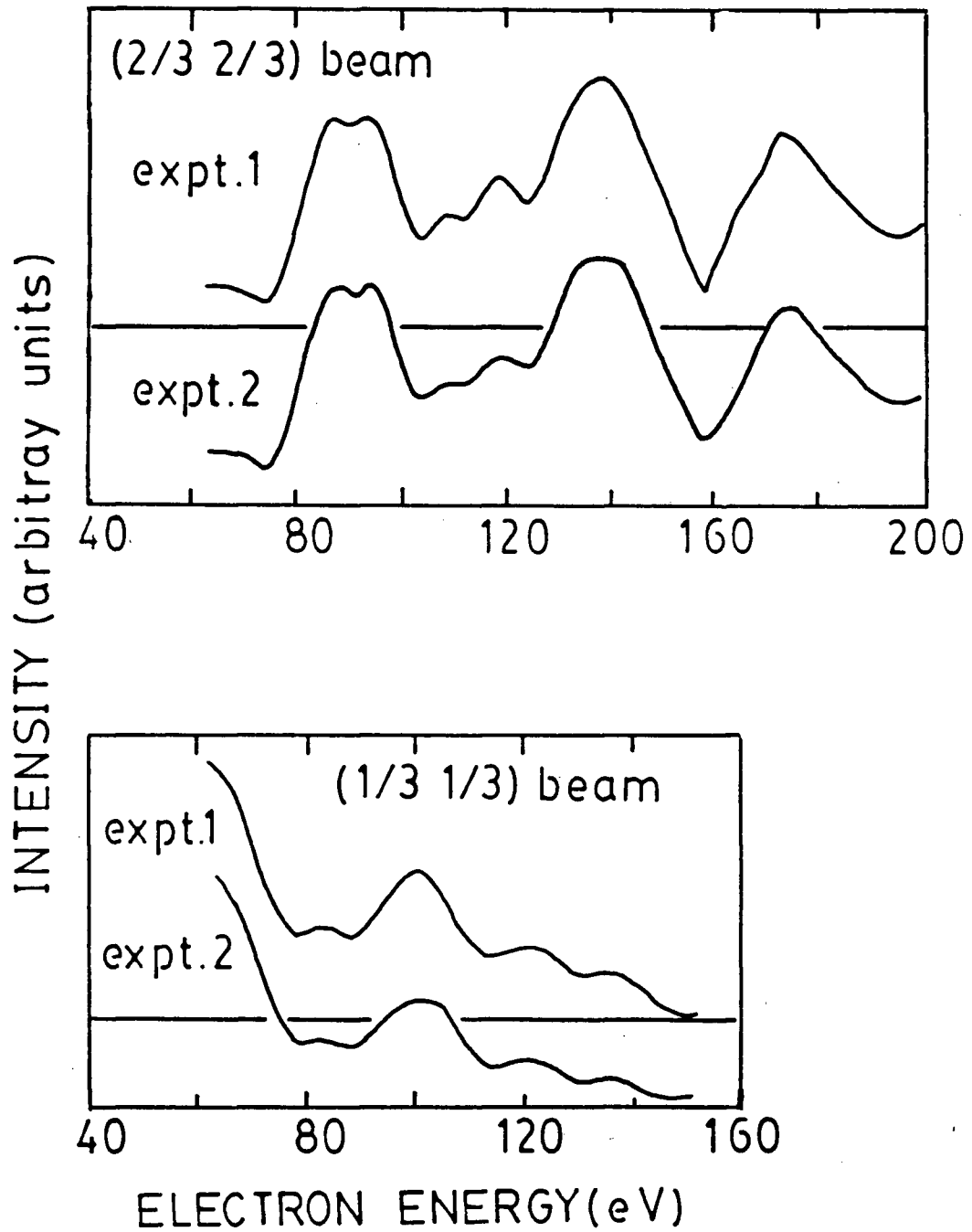


Figure 4.5: $I(E)$ curves for the $(2/3 \ 2/3)$ and $(1/3 \ 1/3)$ beams measured at normal incidence for two independent experiments on the $\text{Rh}(111)-(\sqrt{3}\times\sqrt{3})30^\circ\text{-S}$ structure.

diperiodic space group, and a maximum of 29 inequivalent beams were used (13 integral-order and 16 fractional-order beams). For adsorption on the 2f sites only a single mirror plane reflection symmetry is present. Then, the beam intensities require the appropriate averaging to account for the expected presence of rotationally-related domains. A maximum of 64 inequivalent beams were included to 200 eV for the 2f model.

The non-structural parameters used in these calculations are as follows. The atomic potential of rhodium was characterized by phase shifts (up to $l = 7$) derived from a band structure calculation [53], and the real part of the constant potential (V_{or}) between the atomic spheres (in the muffin-tin model) was set initially at -10.0 eV. For the sulfur overlayer region, the superposition potential obtained by Demuth *et al.* [86] was used. The Debye temperatures were taken equal to 480 K for rhodium and 335 K for sulfur [86], while the imaginary part (V_{oi}) of the constant potential between all spheres was equated to $0.819 E^{1/3}$ eV (where E is the electron energy in eV with respect to the vacuum level).

The structural parameters for Rh(111)-($\sqrt{3} \times \sqrt{3}$)30°-S were simplified by fixing all interlayer spacings for rhodium at the bulk value (2.195Å). This follows Shepherd's observations that the clean Rh(111) surface is not reconstructed and has a topmost interlayer spacing which is very close to the bulk value [1]. The Rh-S interlayer spacings were varied over the ranges: 1.15 - 1.75Å for the 3f and 3h models, 1.84 - 2.44Å for the 1f model and 1.68 - 2.28Å for the 2f model.

Figure 4.6 shows comparisons for nine diffracted beams between the experimental and the closely optimized calculated $I(E)$ curves from the four

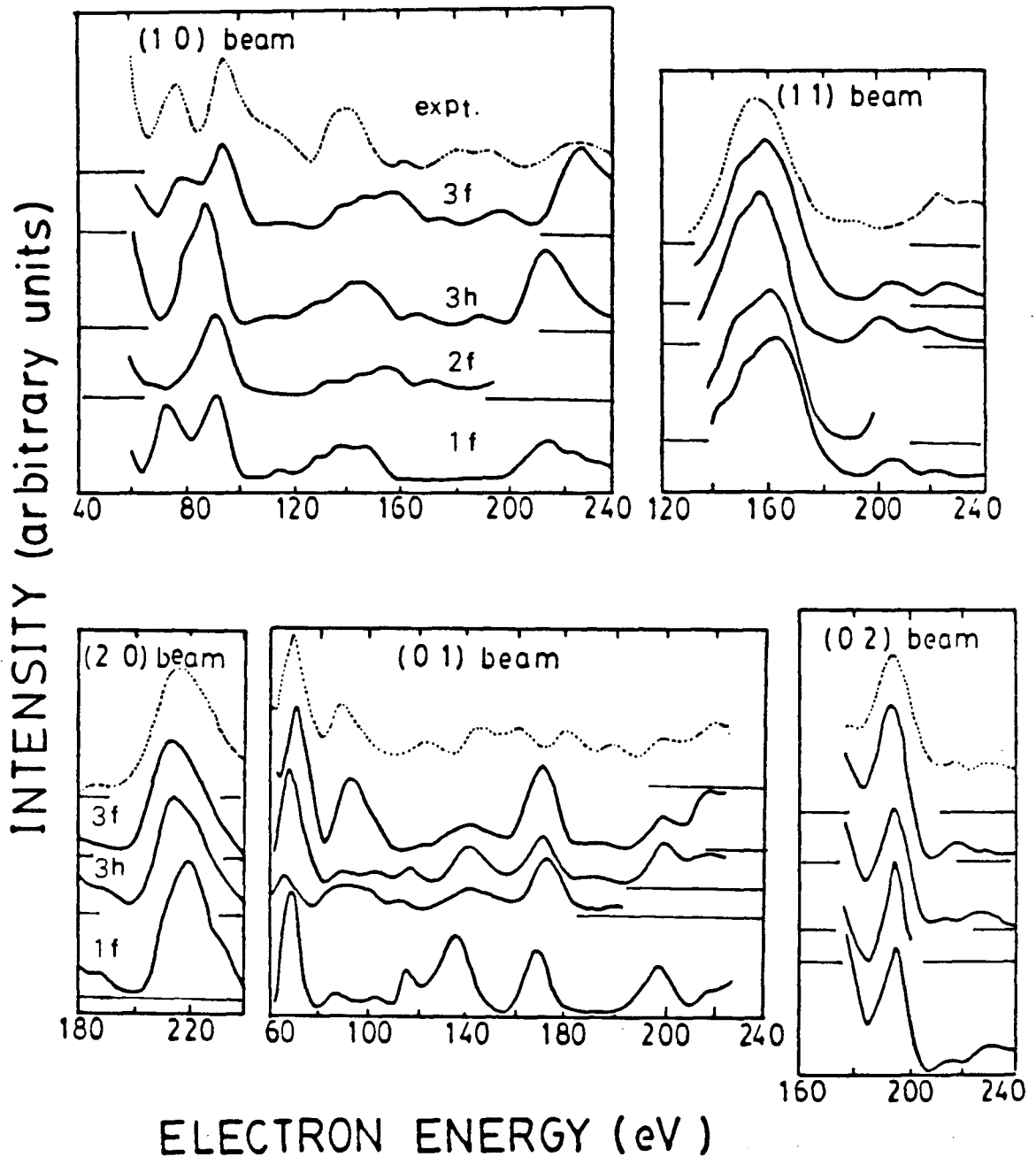


Figure 4.6: Comparison of nine $I(E)$ curves measured for normal incidence on $\text{Rh}(111)-(\sqrt{3}\times\sqrt{3})30^\circ\text{-S}$ with those calculated for the 3f, 3h, 2f and 1f adsorption models with Rh-S interlayer spacings which give the best overall match between experiment and calculation for each model.

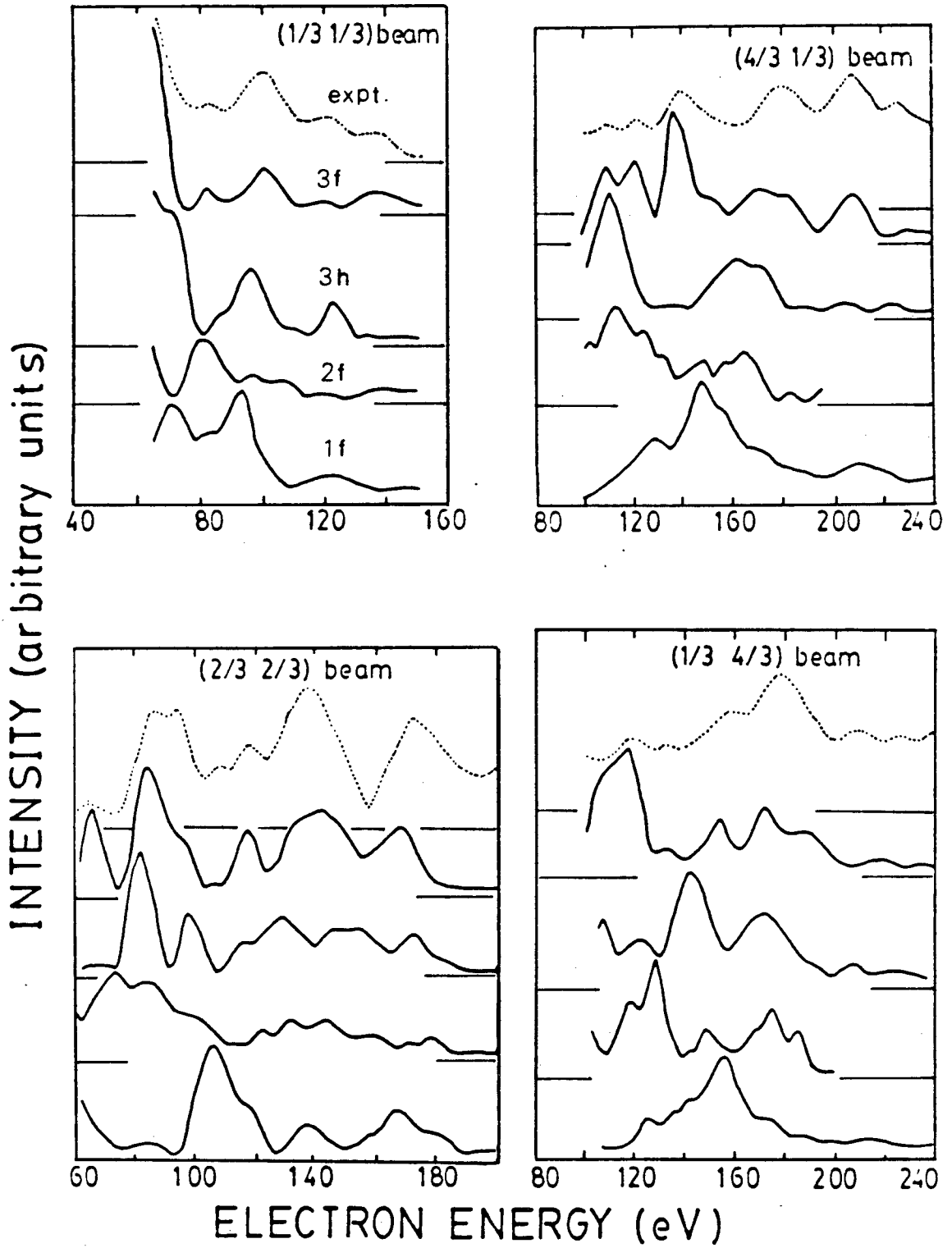


Figure 4.6: (continued)

models. These comparisons at the visual level apparently suggest that the 3f site is favored over the others. This is confirmed by Figure 4.7 which shows contours plots for the reliability index R_p as a function of overlayer spacing and V_{or} for the four different adsorption sites; the lowest values of R_p are clearly for the 3f adsorption site. Consequently, both a visual comparison of the calculated and experimental $I(E)$ curves, as well as an analysis with the reliability index R_p shows that the best correspondence is for the 3f site with the S-Rh interlayer spacing in the vicinity of 1.45 and 1.55 Å. Comparisons for the various diffracted beams are shown in Figure 4.8 for these structures. The minimum value of R_p (0.27), which indicates a moderate level of agreement between experiment and calculation, corresponds to a S-Rh interlayer spacing which equals to 1.53 Å; for these conditions V_{or} equals -9.8 eV.

4.4 Discussion

The evidence presented in the previous section suggests that the Rh(111)-($\sqrt{3} \times \sqrt{3}$)30°-S structure has S atoms adsorbed on the expected (3f) sites of the Rh(111) surface at about 1.53 Å above the topmost rhodium layer. If no surface relaxation is experienced by the metal atoms, each S atom is then bonded to three neighbouring Rh atoms at a distance of 2.18 Å. This value is significantly less than the average Rh-S distances in Rh₂S₃ (2.37 Å) [87] and Rh₁₇S₁₅ (2.33 Å) [88], although Rh-S distances in unhindered coordination complexes are known to range from 2.23 to 2.38 Å [89-91]. With a hard-sphere model for the Rh and S atoms, the bond length determined here corresponds to a S atomic radius equal to 0.83 Å, which is a

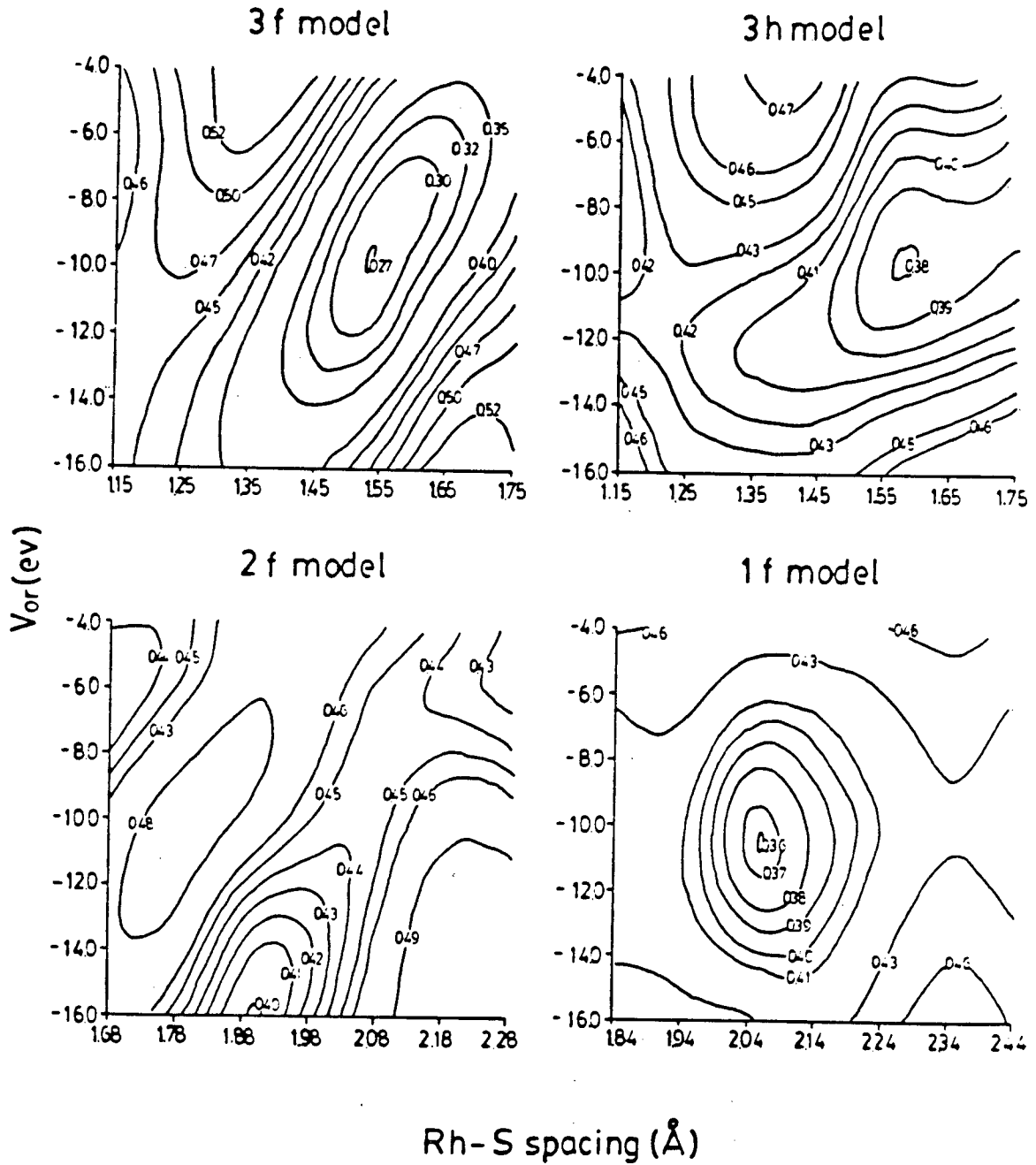


Figure 4.7: Contour plots for Rh(111)- $(\sqrt{3}\times\sqrt{3})30^\circ$ -S of R_p versus V_{or} and the Rh-S interlayer spacing for four different structural models.

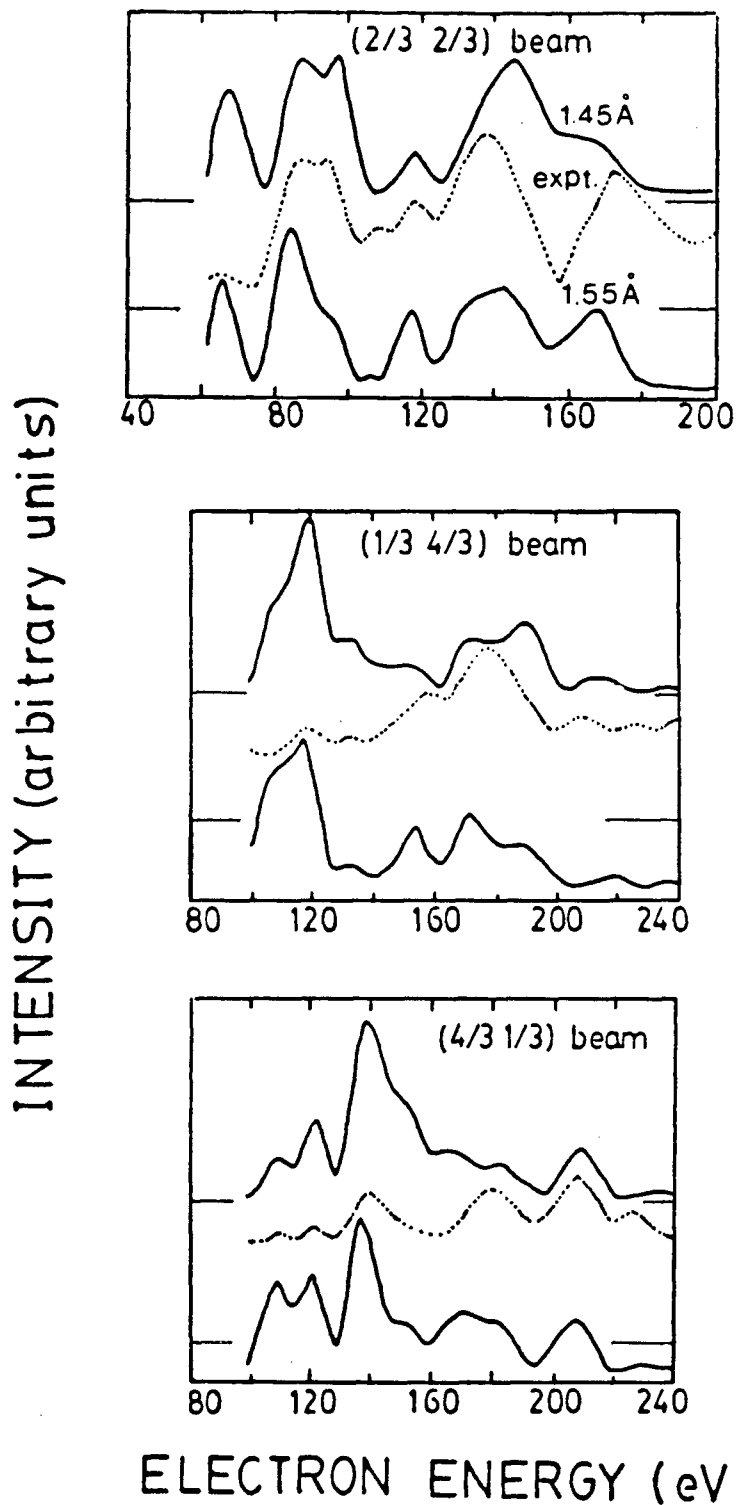


Figure 4.8: Comparison of experimental $I(E)$ curves for some integral-order and fractional-order beams from $\text{Rh}(111)-(\sqrt{3}\times\sqrt{3})30^\circ\text{-S}$ with those calculated for the 3f model with sulfur either 1.45 or 1.55 Å above the topmost rhodium layer.

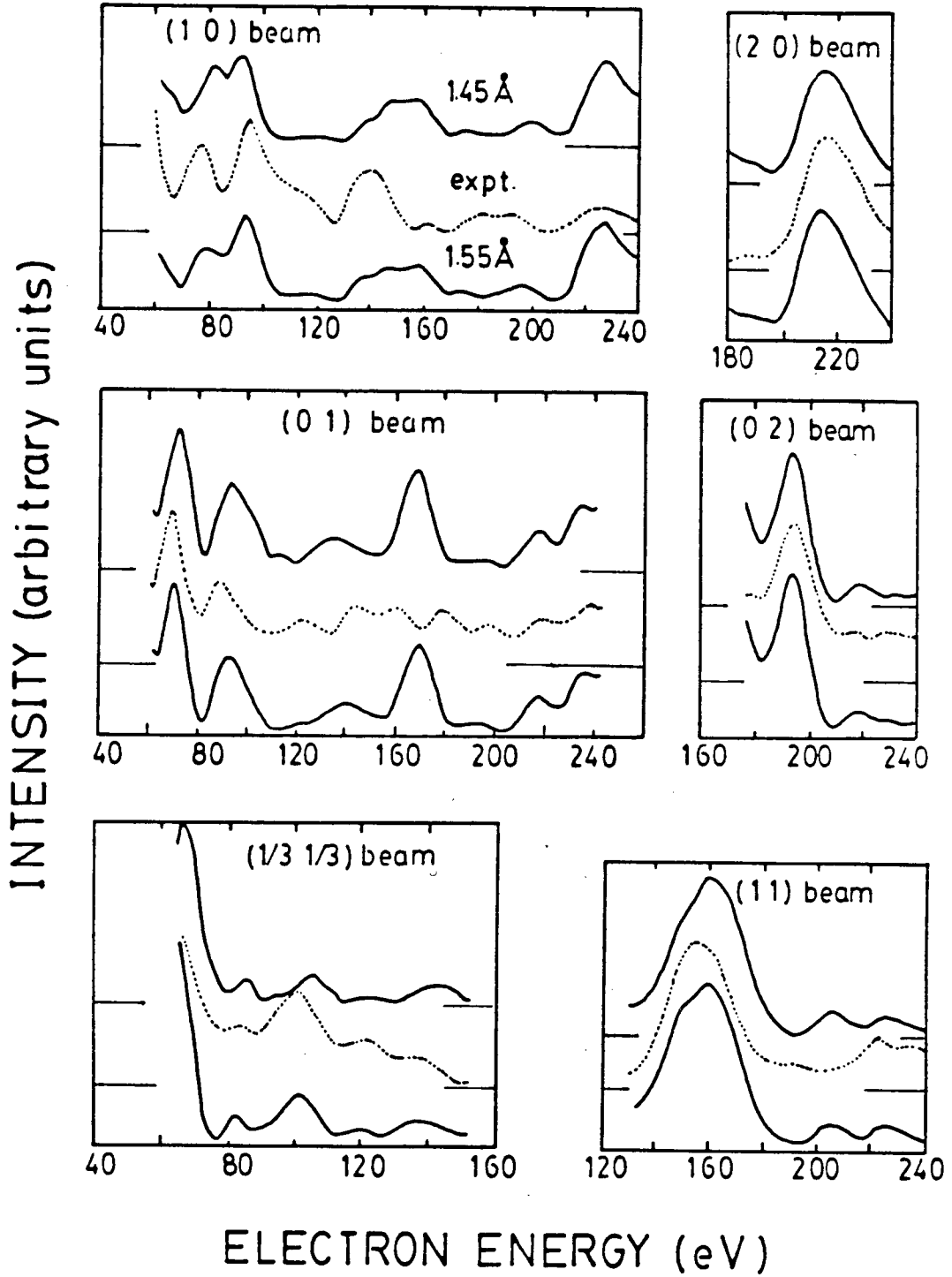


Figure 4.8: (continued)

relatively low value for S (values from 0.77\AA to 1.04\AA have been reported from surface crystallography [92]).

An objective of surface crystallographic research is to relate the determined structure to chemical bonding concepts. Initial studies have been made utilizing Pauling-type expressions to predict adsorption bond distances [80,93,94], for example with

$$r = r_0 - 0.85 \log s, \quad (4.1)$$

where r is the interatomic distance (e.g. from an adsorbed atom X to a neighboring metal atom M) for a bond valence s , and r_0 is the corresponding distance for the bond of unit valence. Given r_0 , X - M bond lengths can be calculated with equation (4.1) on the assumption that the sum of bond valencies at each X equals the atomic valence v , which in the following is taken as the normal group value (e.g. 1 for F , Cl ,...; 2 for O , S , ...). For the case that X adsorbs on a metallic surface with n equivalent neighboring M atoms, all the bond valencies equal v/n .

The crystallographic analysis for $Rh(111)-(\sqrt{3}\times\sqrt{3})30^\circ-S$ completes initial information for surface bond lengths for S adsorbed on the three low-index surfaces of rhodium, and Table 4.1 summarizes these experimental results. In all these examples the S atoms are believed to adsorb on the expected sites (i.e. those sites which would be occupied if another layer of metal were added). In addition to the S - Rh bond lengths from LEED crystallography in Table 4.1, the corresponding predicted values are given from a study by Mitchell et al. [93]. Two sets of predictions are given

utilizing equation (4.1); they differ by the method used to estimate r_0 . In set I r_0 is deduced from a modified algorithm of Brown and Altermatt [95], whereas in Set II r_0 is derived from the structural details of the bulk solid $\text{Rh}_{17}\text{S}_{15}$ [88]. It is clear that each set of experimental data in Table 4.1 broadly follows the trend anticipated for atoms adsorbed on the expected sites for (111), (100), (110) surfaces of fcc metals, for which values of n are 3, 4 and 5 respectively. For a fixed valency for the adsorbed atom, average bond orders should reduce along this series and correspondingly the bond lengths increase. Exact correspondence between the experimental and predicted values in Table 4.1 is not expected in general, and this is both because of the incomplete information currently available for surface bonding (which in turn is required as input to an empirically-based predictive model) and because of the uncertainties present in the currently-reported surface crystallographic determinations. Nevertheless, a general level of consistency is found.

Some clear discrepancies in structural features between the calculated and experimental $I(E)$ curves for $\text{Rh}(111)-(\sqrt{3}\times\sqrt{3})30^\circ\text{-S}$ are apparent in Figure 4.8, for example that in the (01) beam in the vicinity of 170 eV. Their existence suggests some refinement to current analysis may be necessary. It is hoped later to undertake calculations of LEED intensities for structural models which allow both vertical and lateral relaxations for atoms in the surface region. Such relaxations in the positions of the metal atoms have been reported by surface crystallography in one or two other contexts involving S adsorption (e.g. lateral relaxations on $\text{Fe}(110)$ [96], vertical relaxations on $\text{Ni}(110)$ [97]).

Table 4.1: Comparison of measured and predicted S-Rh bond lengths for S atoms adsorbed on the (111), (100), (110) surfaces of rhodium.

<u>System</u>	<u>n</u>	<u>S-Rh bond lengths (\AA)</u>		
		<u>Predicted</u>		<u>LEED crystallography</u>
		<u>Set I</u>	<u>Set II</u>	
Rh(111)-($\sqrt{3} \times \sqrt{3}$)30 ⁰ -S	3	2.28	2.16	2.18
Rh(100)-(2 x 2)-S	4	2.39	2.27	2.30
Rh(110)-c(2 x 2)-S	4	2.52	2.45	2.45
	1	2.31	2.11	2.12

CHAPTER 5

LEED Investigation of the
Rh(111)-(2x2)-0 Surface Structure

5.1 Introduction

The chemisorption of oxygen on surfaces of the Group VIII transition metals has stirred much interest due to the important roles played by oxygen and oxygen-containing molecules as surface species in heterogeneous catalysis. In general, the interactions between oxygen and these metals can be complex, and the experimental work reported to date still leaves many questions to be answered. An understanding is required for developing atomistic models, both for simple chemisorption and ultimately for surface reactivity [98]. Surface crystallographic analyses have been made, with either LEED or SEXAFS, for three examples of oxygen adsorption on the (111) surfaces of face-centered cubic metals, and, at low coverage, the O atoms adsorb above this type of surface in hollow sites of three-fold coordination for aluminum [99-101], iridium [102] and nickel [103]. Further, the measured oxygen-to-metal interatomic bond lengths can be accounted for quite well by assuming a bond order of $2/3$, which is reasonable for divalent O interacting with three neighbouring metal atoms. Such analyses to date have emphasized using a Pauling-type bond length-bond order relation [94].

After completing the LEED crystallographic analysis for the Rh(111)- $(\sqrt{3} \times \sqrt{3})30^\circ$ -S surface, it seemed natural to study the low-coverage structure formed by oxygen on the Rh(111) surface. In earlier work, Thiel *et al.* [104] studied this chemisorption system with thermal desorption spectroscopy, AES and LEED; these authors reported the formation of a (2x2) overlayer structure but no surface crystallographic analysis was made. A major focus of this chapter is provided by a LEED crystallographic analysis to determine the geometric details for the Rh(111)-(2x2)-O surface [105].

5.2 Experimental

A well-ordered and clean (111) surface of rhodium, showing a sharp (1x1) LEED pattern, was prepared by following the procedures described in Section 4.2. When the Rh(111) surface was exposed to approximately 6 L (1 L = 10^{-6} Torr s) of research grade oxygen (Matheson 99.99%) at room temperature, a sharp (2x2) LEED pattern was observed, although the superstructure spots became weaker and diffuse with continued exposure to the electron beam, apparently as a result of the adsorbed layer disordering. Nevertheless, it was found that for an incident beam density of $0.8 \mu\text{A}/\text{cm}^2$ the fractional beams remained visible on the screen for about 2 minutes before disordering dominated. This indicated the maximum period over which individual measurements of beam intensity curves could be made, although a sharp (2x2) LEED pattern could be restored by either rotating the sample away from out of the incident beam or switching off the incident beam for a few seconds. In addition, according to Thiel et al. [104] any thermal dissolution/desorption for chemisorbed oxygen on Rh(111) takes place at around 400 K, and therefore some 100 K higher than the surface temperature used in this work (i.e. room temperature). Thus the LEED measurements here were made for conditions that precluded the adsorbed oxygen atoms from undergoing any appreciable dissolution/desorption processes during the experiment. With the sample cooled to about 215 K, we found it possible to measure with the VLA system, as described in Section 3.5.2, a set of normal-incidence I(E) curves from 60 to 250 eV in increments of 2 eV. Each individual measurement was performed by rotating the face of the sample away out of the electron beam prior to setting the essential parameters for

the VLA system, and then accomplishing the measurement within 2 minutes, starting as soon as the sample was relocated for the normal incidence orientation.

A total of ten inequivalent $I(E)$ curves were measured for normal incidence on the $\text{Rh}(111)-(2 \times 2)-0$ surface; these covered five integral beams and five fractional beams, namely (10), (01), (11), (20), (02), $(1/2 \ 1/2)$, $(1 \ 1/2)$, $(1/2 \ 1)$, $(0 \ 3/2)$ and $(3/2 \ 0)$, using the beam notation indicated in Figure 5.1(b). The unit mesh of the superstructure corresponding to the (2×2) LEED pattern is shown in Figure 5.1(a). The detailed procedures for normalization, averaging and smoothing of $I(E)$ curves were done exactly as described in Section 4.2.

5.3 Calculations

The most-probable models for the $\text{Rh}(111)-(2 \times 2)-0$ surface structure have 0 atoms adsorbed on sites of three-fold coordination. There are two adsorption sites of this type indicated in Figure 1.8(a), namely the 3f and 3h sites as defined in Section 4.1. For simple adsorption on these sites, with the (2×2) translational symmetry, a surface of $\text{Rh}(111)$ has a coverage of 0.25 monolayer (ML), and it belongs to the $p3ml$ diperiodic space group. In addition, we also considered a graphitic overlayer model with 0 atoms adsorbed on both 3f and 3h sites to give a total coverage of 0.5 ML (see Figure 2.4). This model was first proposed for the $\text{Pt}(111)-(2 \times 2)-0$ surface structure [106], although LEED crystallography indicates it is applicable for the $\text{Ni}(111)-(2 \times 2)-\text{H}$ surface structure [107].

$I(E)$ curves for the simple 3f, simple 3h and 3f + 3h graphitic models were calculated using the renormalized forward scattering method

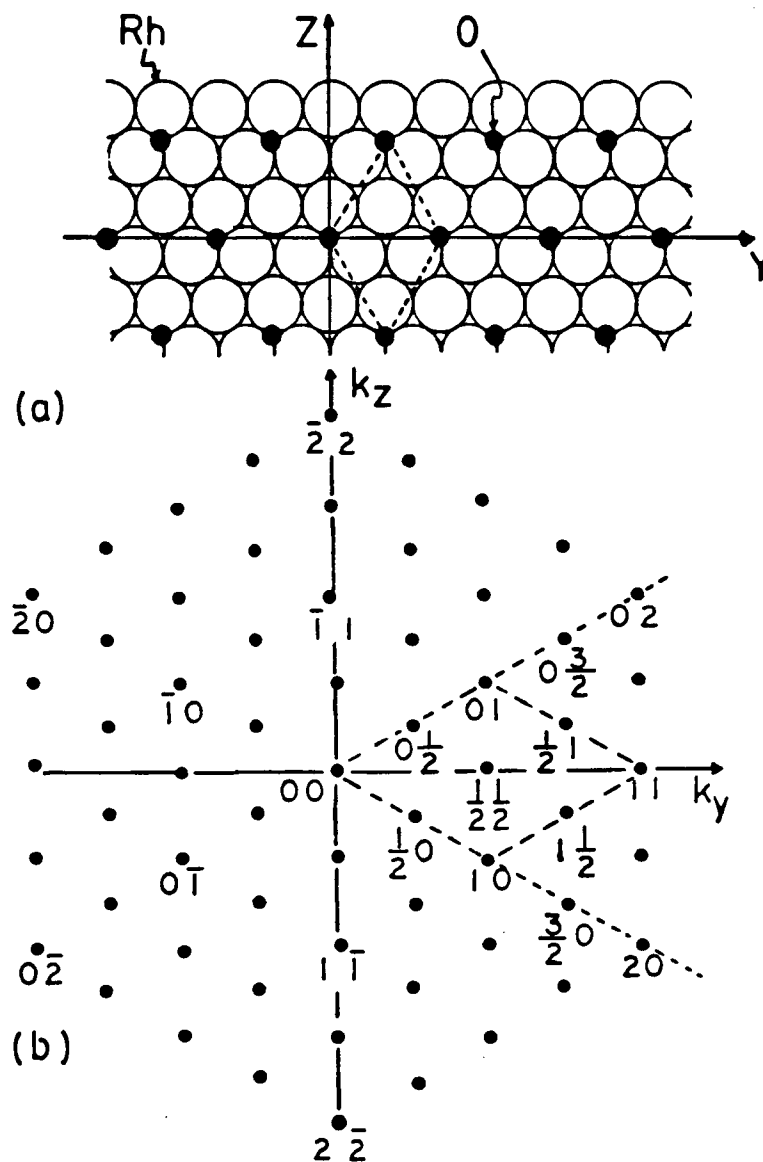


Figure 5.1: (a) Unit mesh of the (2x2) overlayer structure for oxygen adsorbed on Rh(111). (b) Schematic LEED pattern and beam notations corresponding to the overlayer structure of (a).

[44,45], although the composite-layer method as described in Section 2.5 was used to calculate the 0 overlayer diffraction matrices for the 3f + 3h graphitic model. A maximum of 43 inequivalent beams were included in the calculation; the non-structural parameters being assumed to have values which correspond to those used in the previous analysis for Rh(111)- $(\sqrt{3}\times\sqrt{3})30^\circ$ -S. Therefore the atomic potentials were characterized by phase shifts to $l = 7$; for rhodium they were derived from a band structure potential [53], while those for oxygen originated with the superposition potential obtained by Demuth et al. [86]. The real part of the muffin-tin potential (V_{or}) was set initially to 10 eV below the vacuum level, while the imaginary part (V_{oi}) was equated to $0.819 E^{1/3}$; where E is the electron energy (in eV) inside the crystal. The effective Debye temperatures of rhodium and oxygen were taken respectively as 480 and 843 K [44]. The structural models were simplified by fixing all interlayer spacings for rhodium to the bulk value (2.195Å); the 0-Rh interlayer spacings included in the calculations range from 1.064 to 1.564Å for the simple 3f and simple 3h models, but from 1.100 to 1.550Å for the graphitic overlayer.

5.4 Results

Figure 5.2 compares the experimental $I(E)$ curves of the $(1/2\ 1/2)$, $(1\ 1/2)$ and $(0\ 3/2)$ beams with the corresponding $I(E)$ curves calculated for the above three models. Visual comparisons show poor correspondence for the 3h model compared with either the simple 3f model or graphitic model. However, as a result of the disordering effect of the incident beam, the

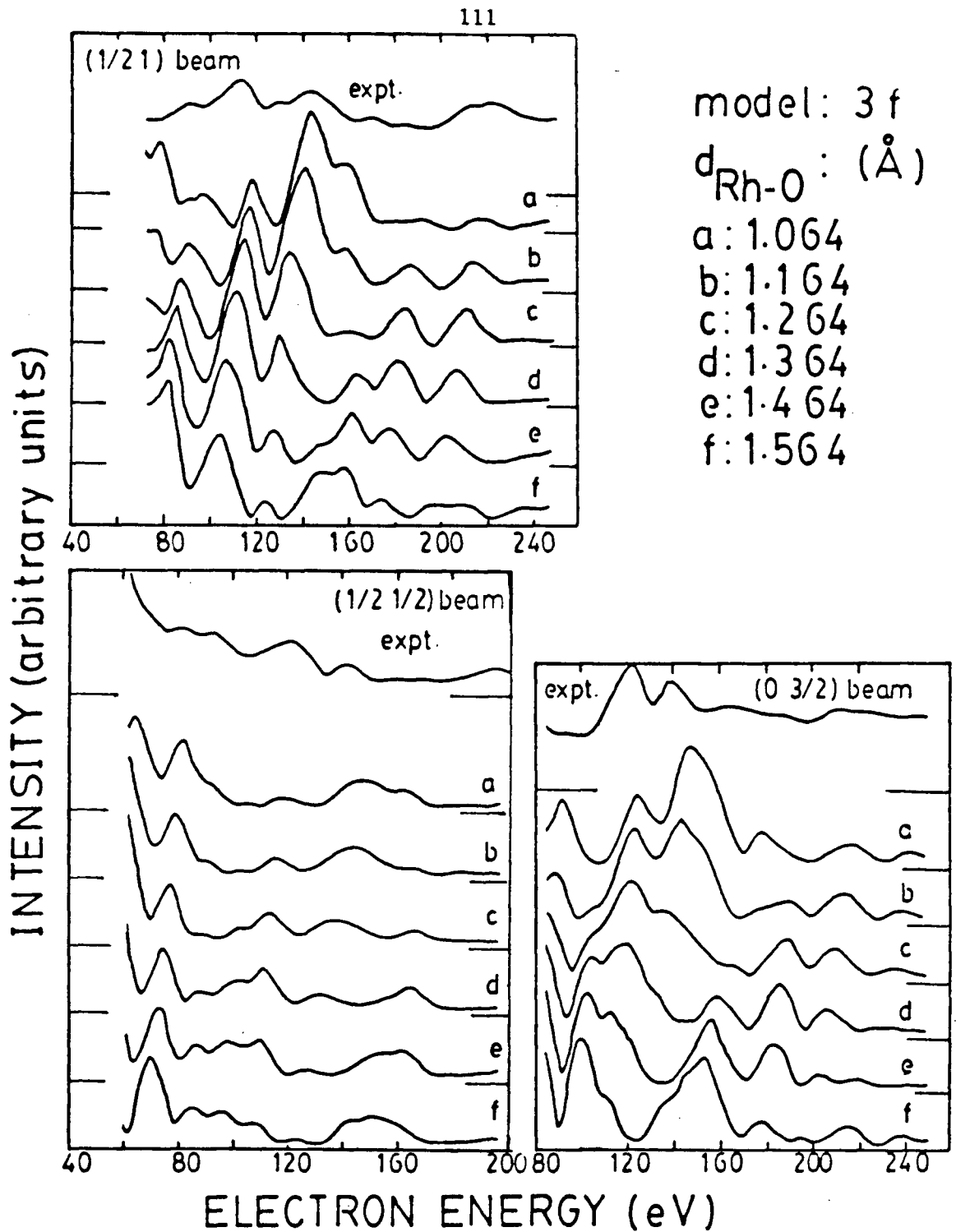


Figure 5.2: Comparison of experimental $I(E)$ curves for $(1/2\ 1)$, $(1/2\ 1/2)$ and $(0\ 3/2)$ diffracted beams from $\text{Rh}(111)-(2 \times 2)-0$ at normal incidence with those calculated for the 3f, 3h and 3f+3h models over a range of the topmost O-Rh interlayer spacings.

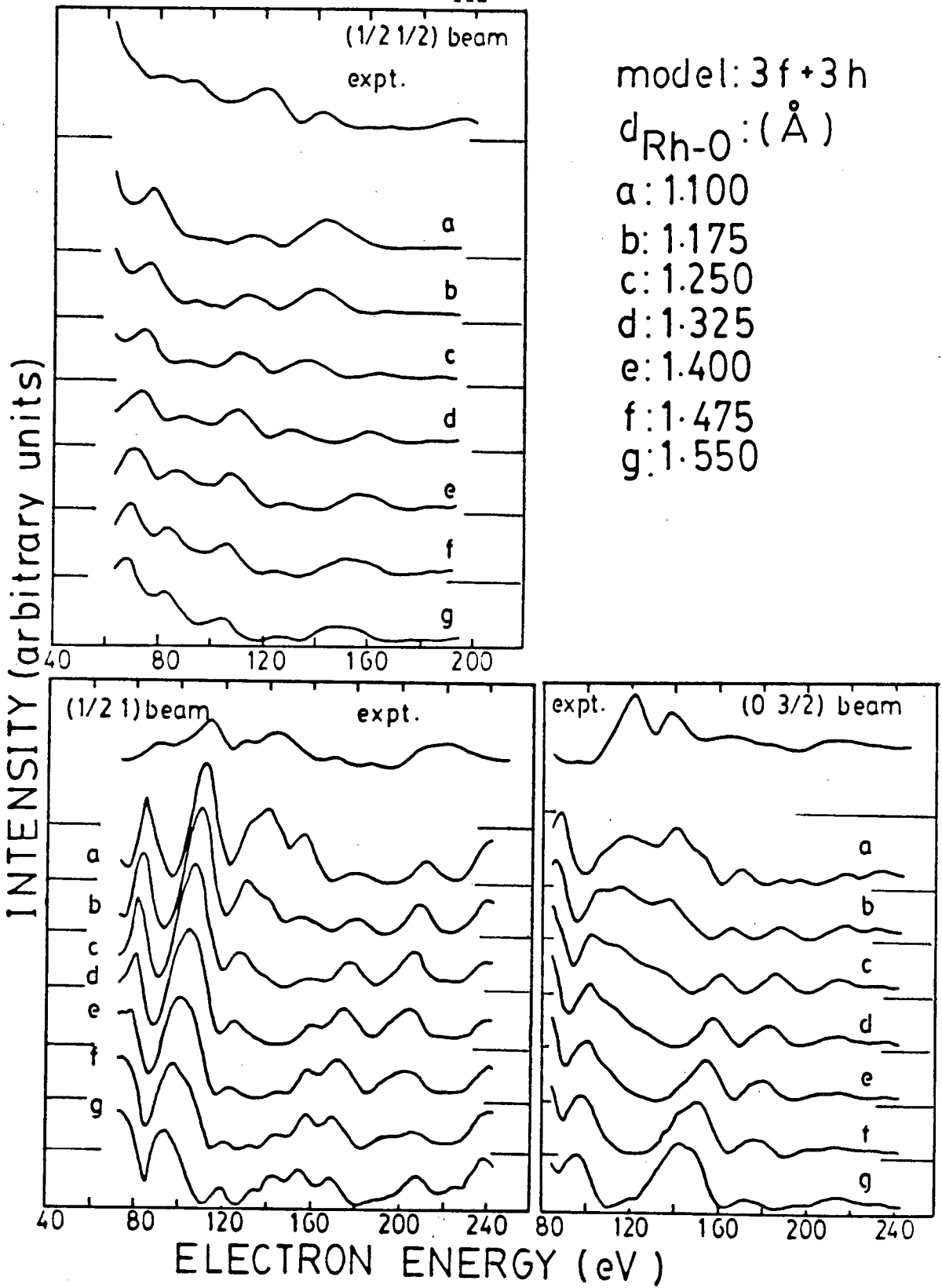


Figure 5.2: (continued)

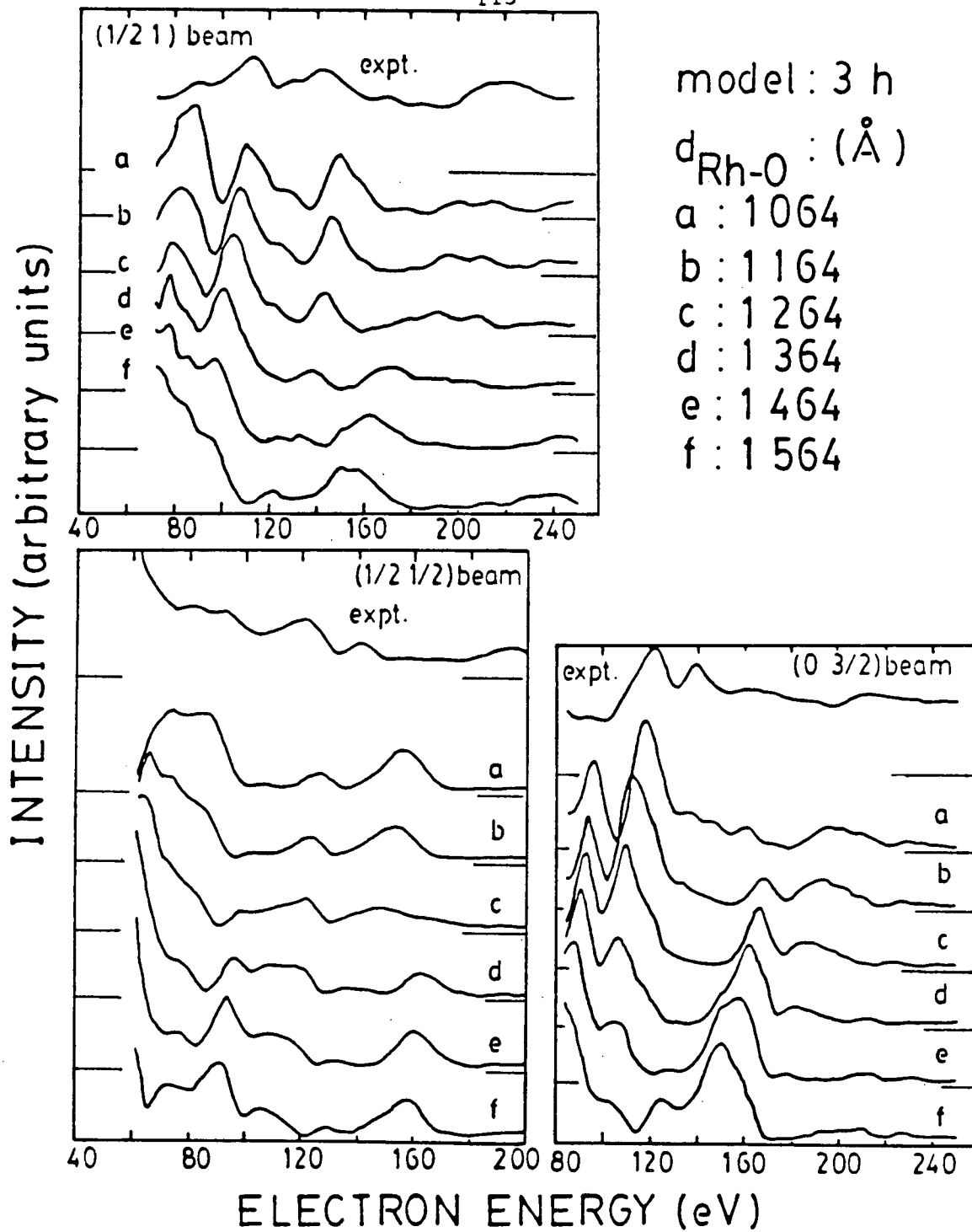


Figure 5.2: (continued)

experimental $I(E)$ curves were inevitably measured with higher than usual background, and in principle this could affect assessments of the favored model from visual comparison alone. Nevertheless, a visual comparison over the complete range of data did suggest that the best correspondence between the experimental and calculated $I(E)$ curves is obtained either for the simple 3f model or for the 3f + 3h graphitic model, with the O-Rh interlayer spacing in the ranges 1.164 to 1.264 Å and 1.100 to 1.175 Å, respectively. The reliability index (R_p) proposed for LEED by Pendry was used in an attempt to make the above observations more precise. Figure 5.3 shows contour plots of R_p as a function of the O-Rh interlayer spacing and V_{or} for each of the three models. This evidence suggests that the 3f model is favored; the minimum value of R_p (0.394), which indicates a moderate level of correspondence between the experimental and calculated $I(E)$ curves, corresponds to an O-Rh interlayer spacing equal to 1.23 Å while V_{or} is -12.6 eV. Figure 5.4 displays comparisons between the experimental $I(E)$ curves and the corresponding $I(E)$ curves calculated for the 3f model with the O-Rh interlayer spacing equal to 1.164 and 1.264 Å.

5.5 Discussion

The evidence presented above indicates that the Rh(111)-(2x2)-O structure has oxygen atoms adsorbed on simple 3f sites of the Rh(111) surface while held at about 1.23 Å above the topmost rhodium layer. This value may be reasonable since the associated value for the O-Rh bond length is 1.98 Å, which agrees closely with the value of 1.99 Å predicted for this system with bond order equal 2/3 [94]. Although this correspondence is

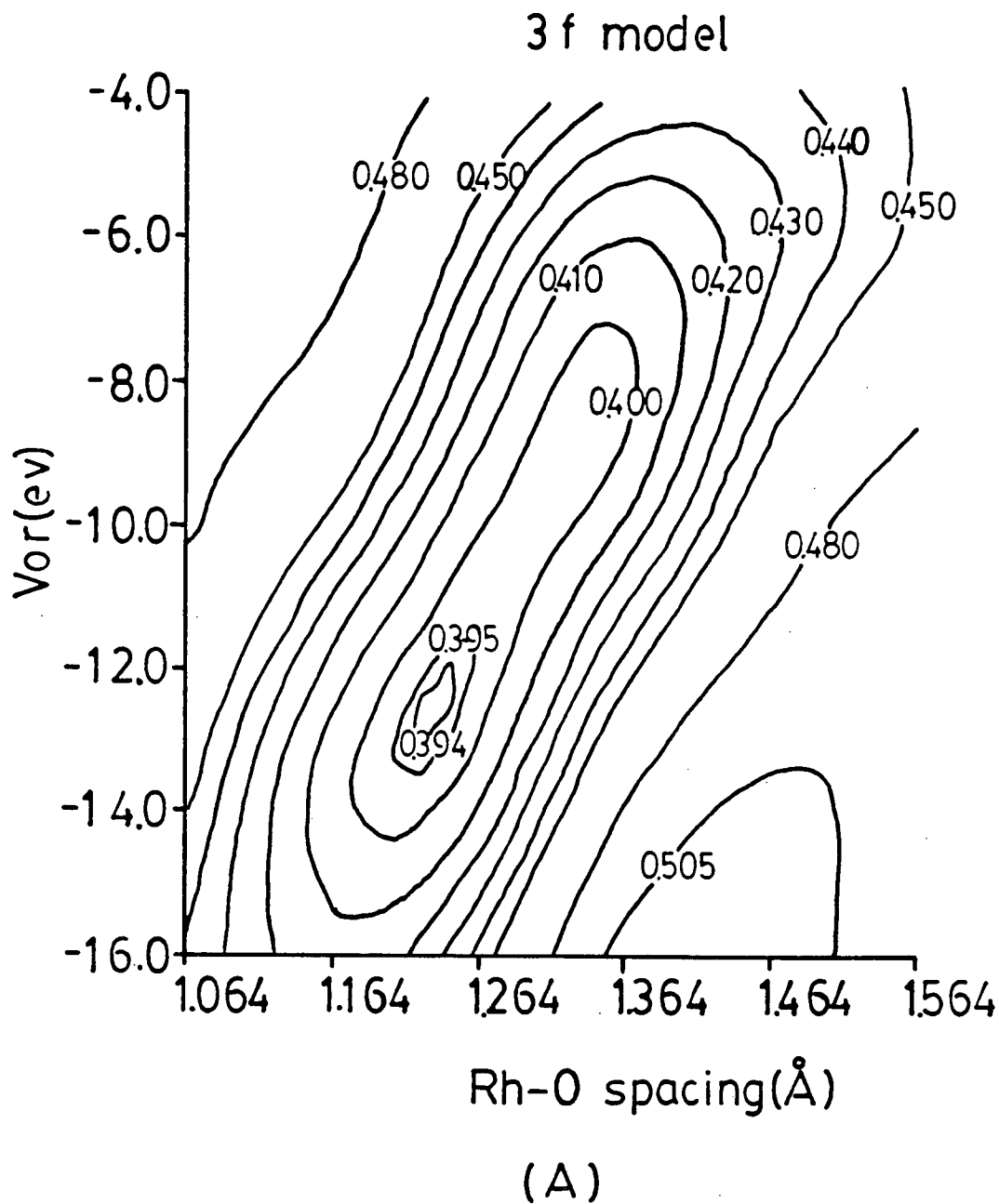


Figure 5.3: Contour plots for Rh(111)-(2x2)-0 of R_p versus V_{or} and the Rh-O interlayer spacing for (a) 3f, (b) 3h and (c) 3f+3h structural models.

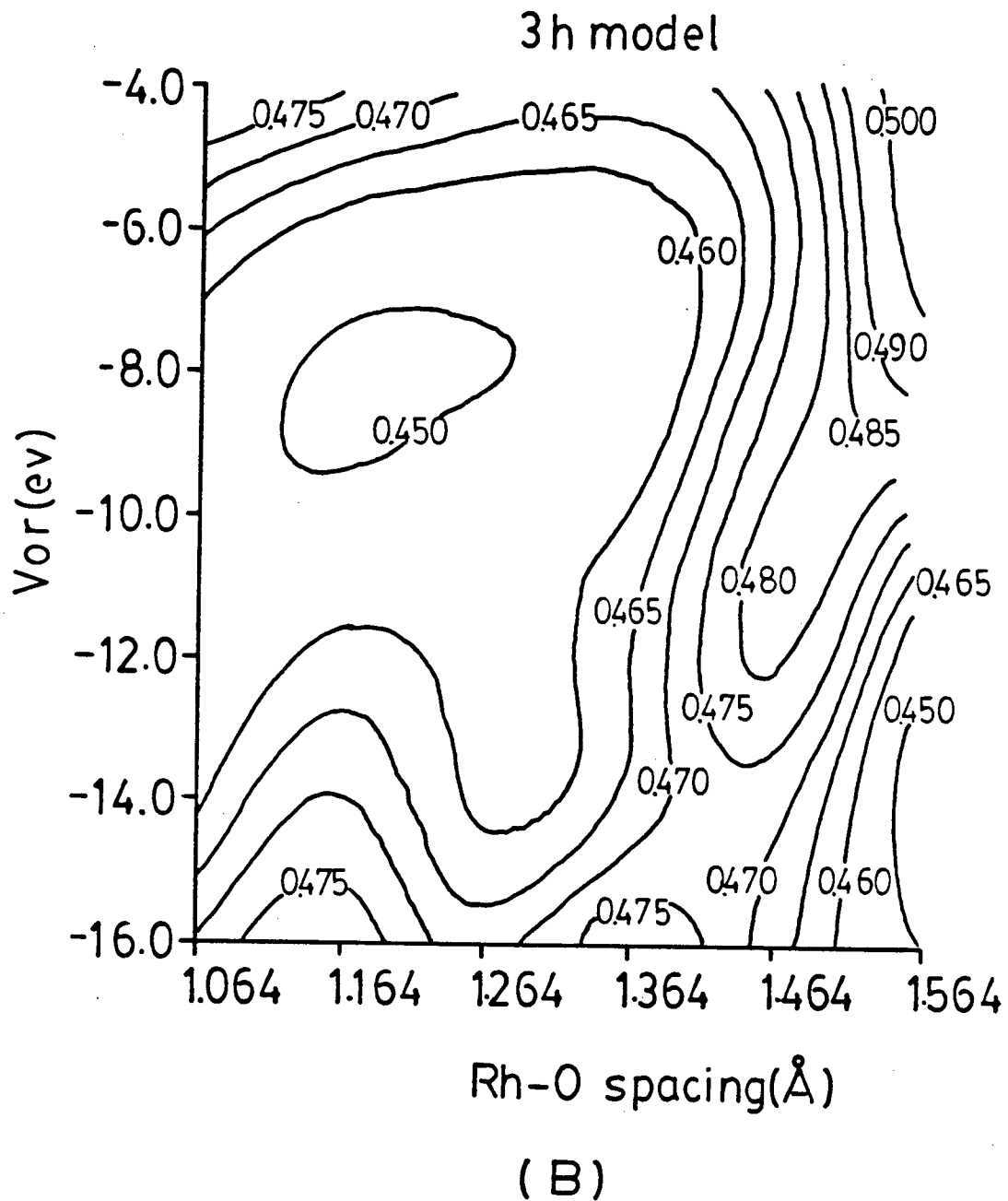


Figure 5.3: (continued)

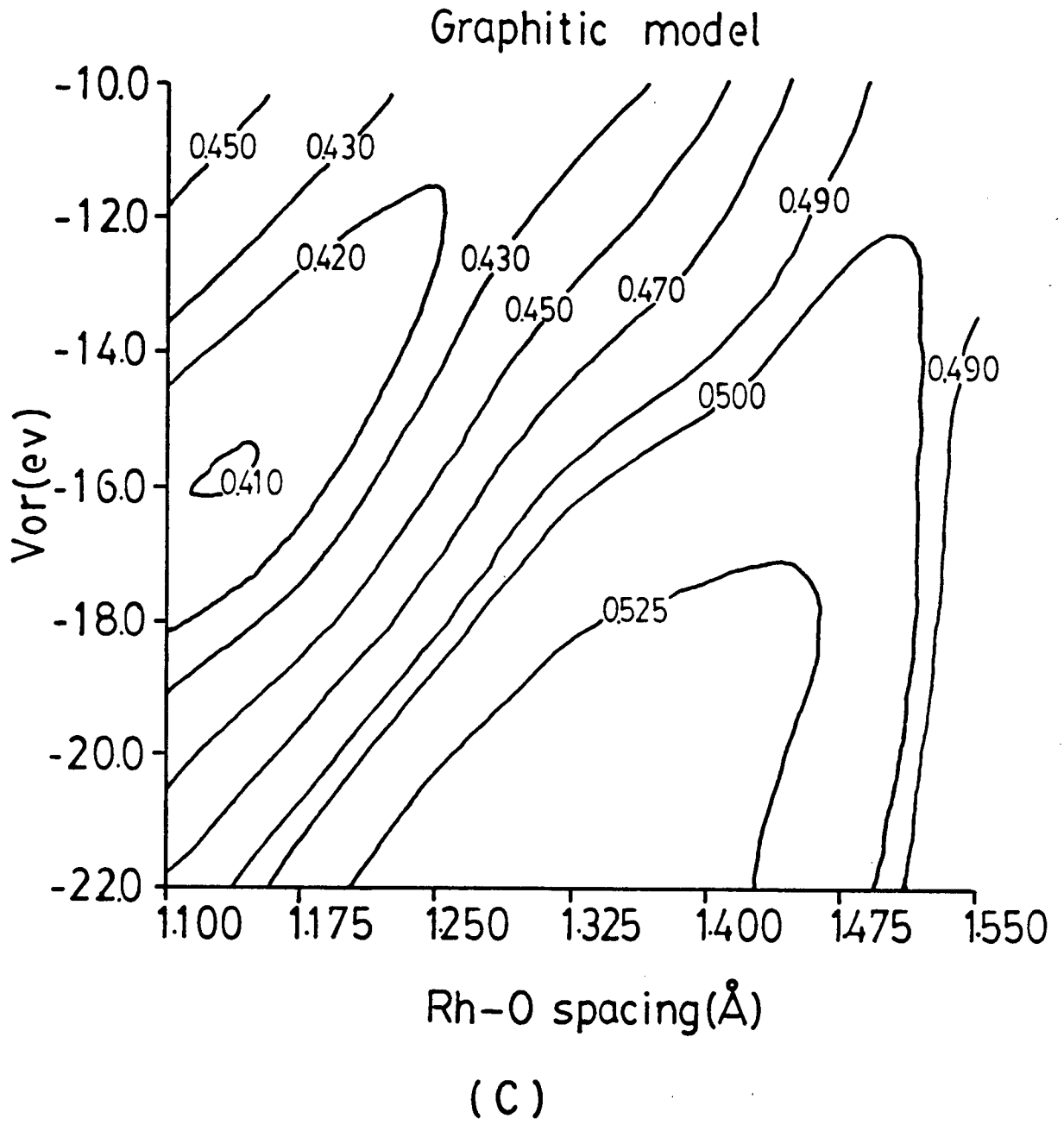


Figure 5.3: (continued)

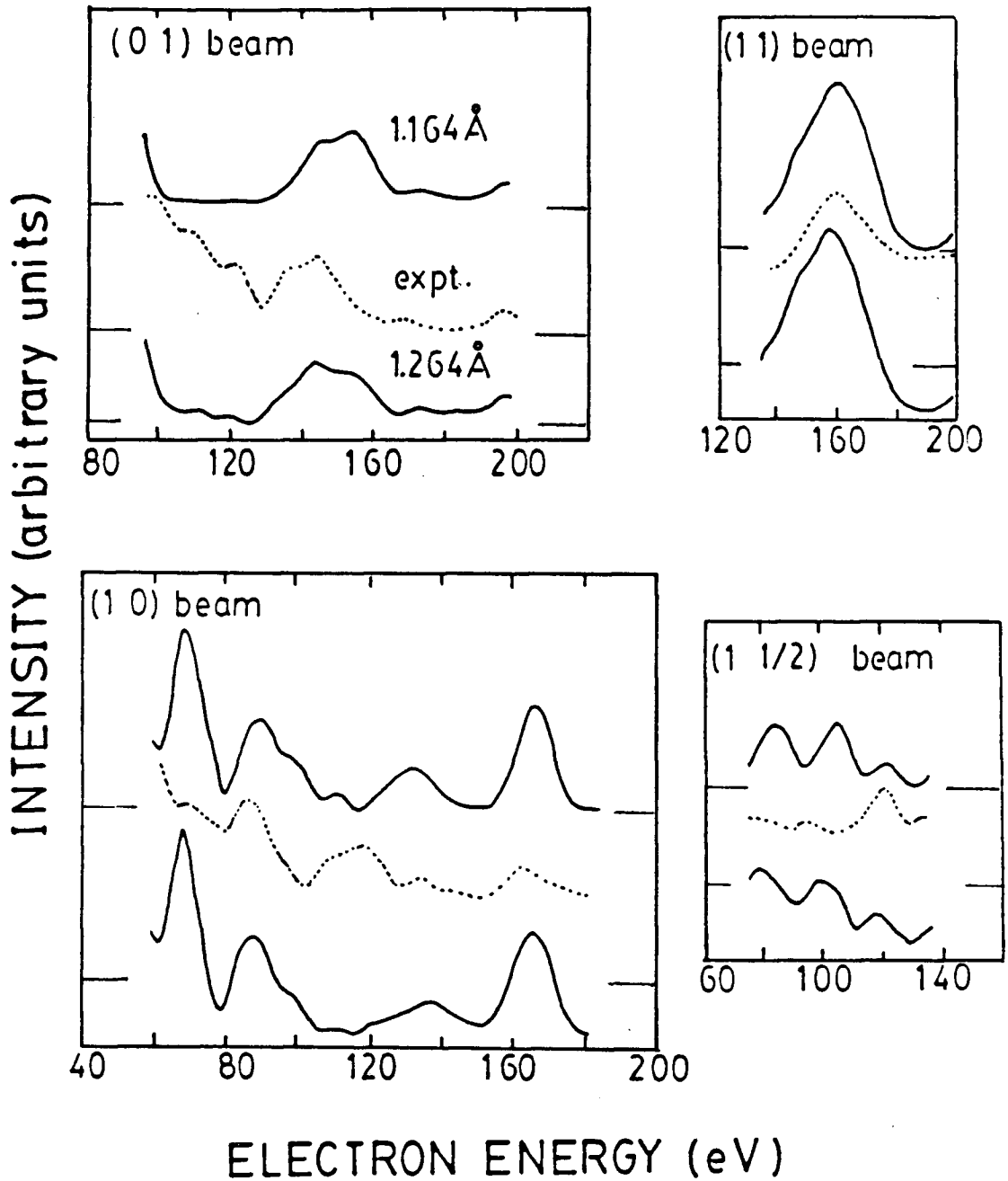


Figure 5.4: Comparison of experimental $I(E)$ curves for some integral-order and fractional-order beams from $\text{Rh}(111)-(2 \times 2)-\text{O}$ at normal incidence with those calculated for the 3f model with oxygen either 1.164 or 1.264 Å above the topmost rhodium layer.

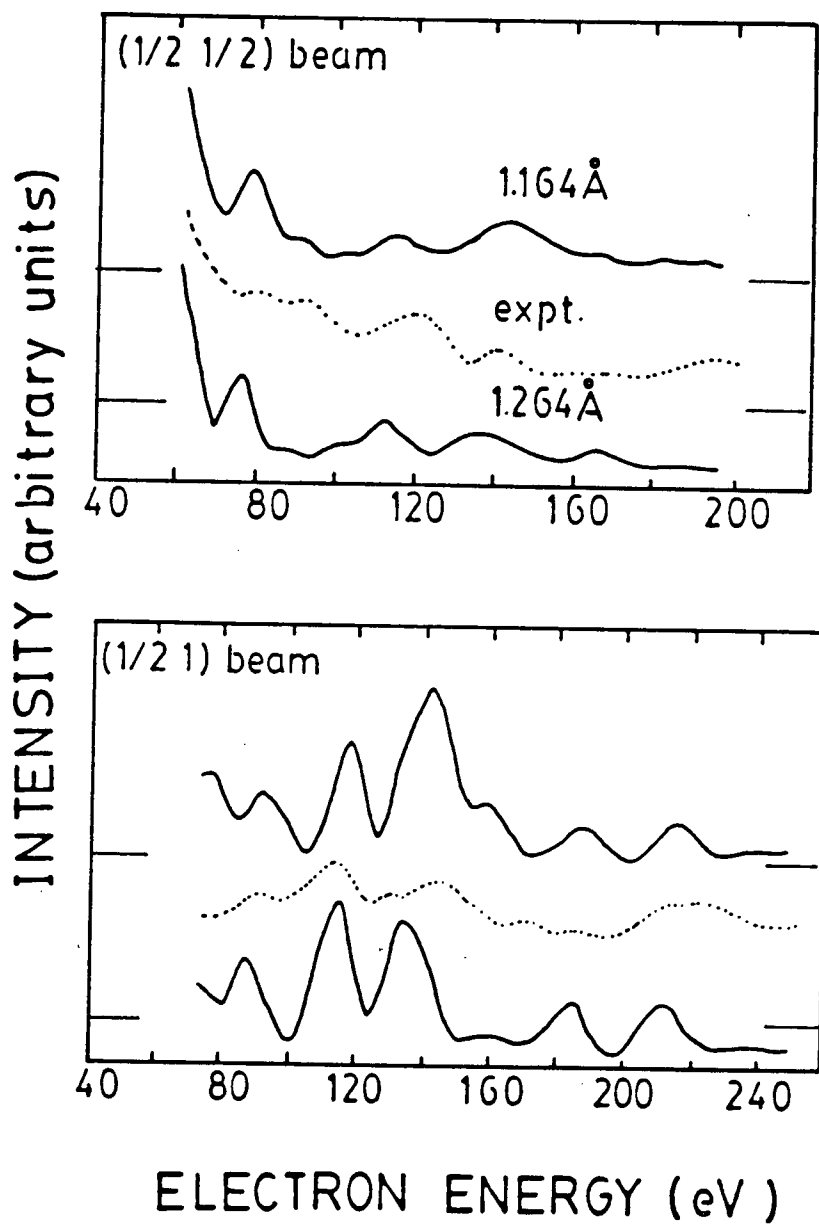


Figure 5.4: (continued)

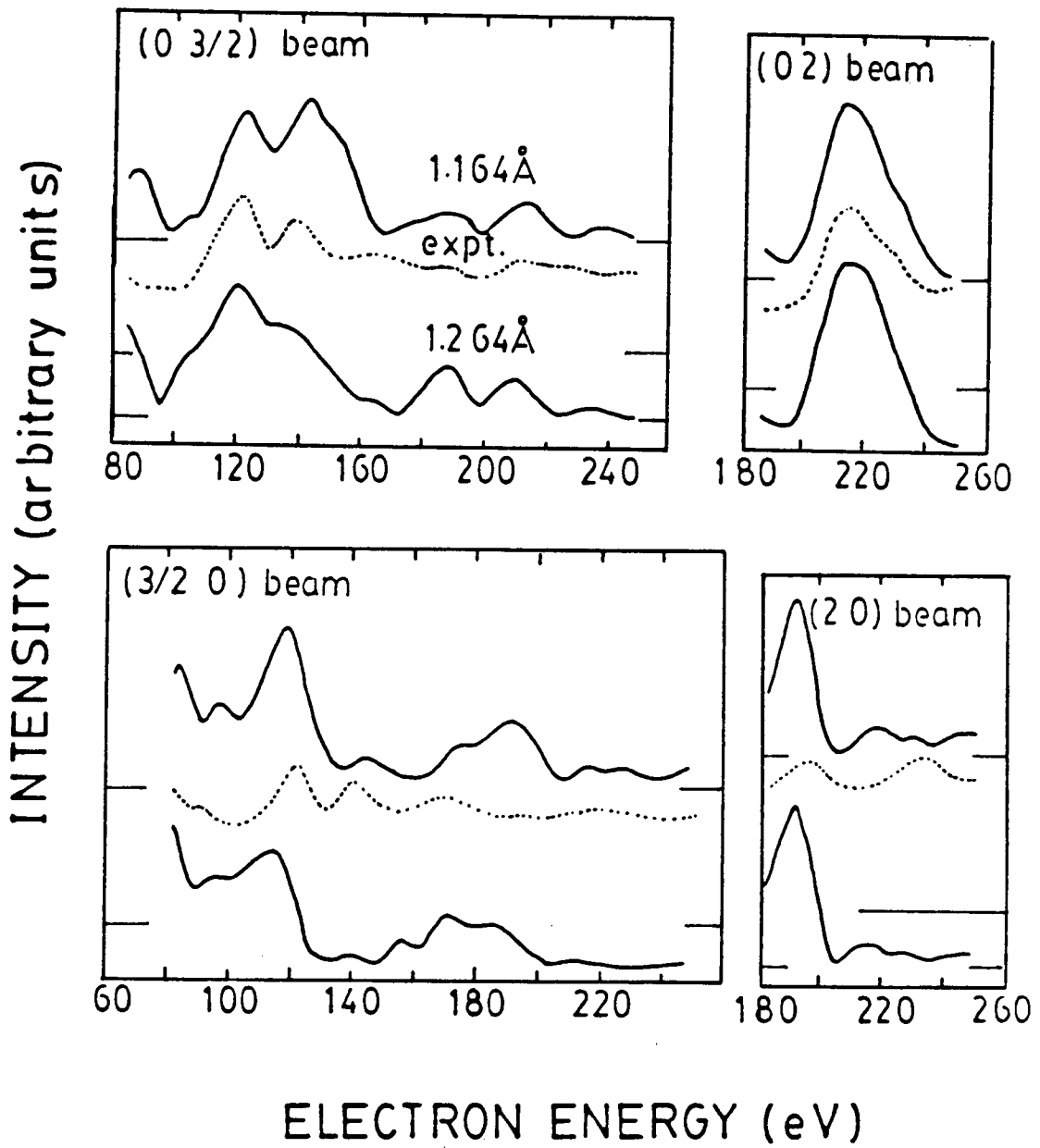


Figure 5.4: (continued)

close, nevertheless contours in the vicinity of R_p equal to 0.400 are rather shallow in the diagonal direction in Figure 5.3(a). The uncertainty in the O-Rh interlayer spacing, derived from the standard error in the R_p values associated with the individual beams [108], is $\pm 0.09 \text{ \AA}$. This relatively large uncertainty is perhaps not unexpected given the tendency for the O layer to disorder while the measurements were being made. Indeed the disordering effect of the incident beam found in this study was such that the LEED crystallographic analysis could not have been possible without a fast measurement system [73]. Moreover this study suggested that the standard procedures used in LEED crystallography [109] can still allow a plausible structural analysis even though some electron beam-induced disordering inevitably occurred while the measurements were being made. Such observations could be helpful for developing interest in using LEED to characterize surface defects [110,111] as well as geometrical structure.

Overall the study here is satisfying in that the measurements made with the LEED video analyzer for a system which is unstable in the electron beam were able to lead to a structural conclusion which appears reasonable; furthermore this evidence supports the use of a Pauling-type bond-order expression for predicting bond lengths for the adsorption of O atoms on other surfaces of rhodium [93,94].

CHAPTER 6

Adsorption of Oxygen on the
(0001) Surface of Zirconium

6.1 Introduction

Zirconium has significant interest in materials science, particularly in the nuclear industry. This is essentially due to its low absorption cross section for neutrons, as well as its high resistance to corrosive environments inside nuclear reactors. The unique corrosion resistance of zirconium and its alloys is believed to depend on the formation of thin protective oxide films on the surface; therefore the oxidation of zirconium has considerable technological interest [42,112]. Many studies of the oxidation of zirconium have been reported, but most of these are concerned either with polycrystalline zirconium or with thick films of oxide formed under high oxygen exposures at high temperatures. Five representative studies using different surface techniques and surface treatments are listed in Table 6.1, although there are considerable variations in the conditions of these experiments. High-temperature heating of the zirconium is effective to obtain a clean surface by diffusing some contaminants (e.g. C, N, O) into the zirconium bulk structure, but it has to be noted that pure α -zirconium (hcp structure) undergoes a phase transition to the β -zirconium form (bcc structure) at 1135 K [116]. Clearly the heating temperature is limited to below this value for cleaning single crystal surfaces. So far only a very limited number of studies have been made for the initial steps of the oxygen chemisorption process on well-characterized zirconium surfaces (i.e. at 0 coverages of the order of one monolayer) [112]. In part this may be attributed to the difficulties of obtaining clean well-characterized zirconium surfaces, the limitations being set both by the high reactivity of this metal and by the bulk phase change. Even

Table 6.1: Five representative studies of the oxidation of zirconium using different surface techniques and surface treatments.

<u>Sample</u>	<u>Cleaning Method</u>	<u>Exposure of O₂ (L)</u>	<u>Surface Technique</u>	<u>Ref.</u>
Zr(0001)	Ar bomb. heat to 873 K	0-1	LEED, AES	[43]
Poly. Zr, Zr(0001), ZrO ₂	Ar bomb. heat to 1000 K	0-10 ⁸	XPS, AES	[112]
Poly. Zr	Ar bomb. heat to ~1100 K	0-50	AES, UPS	[113]
Poly. Zr, ZrO ₂	Ar bomb. heat to ~1650 K [*]	0-10 ⁹	LREELS ^{**} , AES	[114]
Poly. Zr	Ar bomb. heat to ~1800 K [*]	0-6x10 ³	SIMS	[115]

*: Zirconium metal undergoes hcp↔bcc transition at 1135 K.

** : Low resolution electron energy loss spectroscopy.

though surface structure studies are still very limited for zirconium, the same statement also holds for chemisorption at all hcp metals.

Currently there is evidence that oxygen dissociatively chemisorbs on polycrystalline zirconium, and that with heating diffusion into the bulk occurs rather than desorption [113, 117, 118]; consistently, a recent preliminary surface crystallographic analysis with low energy electron diffraction indicated that the surface structure designated $Zr(0001)-(2 \times 2)-0$ involves subsurface adsorption. Nevertheless, this latter analysis remains less than complete from several points of view, including the inabilities to assess: (i) whether the surface really has the (2×2) -type translational symmetry or whether it actually involves rotationally related domains of the (2×1) types [119]; (ii) the role of disorder in surface structure; (iii) the degree of warping of Zr layers in the presence of (2×2) oxygen layers; and (iv) whether 0 should be represented as a negatively charged species. For the crystallographic study, the designation $Zr(0001)-(2 \times 2)-0$ was used as a convenience since, from point (i) above, it is clear that until more information is available for coverage and structure, the designation " (2×2) " cannot be seen as representing more than a shorthand for a surface that gives appropriate half-order diffracted beams. Additional characterizations are therefore needed for surfaces which show (2×2) -type LEED patterns. This leads to the first objective of this chapter, namely to use the LEED spot profile technique and AES to probe further some aspects of oxygen coverage for the initial stages of chemisorption on the $Zr(0001)$ surface [120]. The second objective is to attempt to establish conditions for the initial (i.e. lowest coverage)

ordered Zr(0001)-(1x1)-0 structure and then to make a LEED crystallographic analysis on this structure [121].

6.2 Experimental

6.2.1 Sample Preparation and Cleaning

The zirconium single-crystal sample used in this work was kindly provided by P.R. Norton (AECL, Chalk River Nuclear Laboratories). The surface had been initially oriented to within 2° of the (0001) plane, but on receipt we reoriented it to within 0.5° of this plane and cut it to a suitable size for the sample holder in this laboratory. Then the sample was mechanically polished with increasingly finer diamond paste (9-1 μ); this was followed by a 30 s chemical etch in acid solution (45% HNO₃, 50% H₂O, 5% HF by volume) [122]. Finally the sample was degreased with trichloroethylene and installed in the UHV chamber.

After pumping down, AES showed that the Zr(0001) surface region contained large quantities of carbon and oxygen; this was indicated by the Auger peaks at 272 eV and 510 eV respectively, as in the spectrum for the contaminated Zr(0001) surface shown in Figure 6.1(a). Argon ion bombardment (2 kV, 3 μ A) was then carried out at room temperature until carbon was the only detectable contaminant. It is worthwhile to note that the oxygen contamination could only be removed from the surface if the titanium sublimation pump was operated during the sputtering process. The residual carbon contamination was reduced by annealing the sample at about 700°C for 20 minutes, although heating at 600°C resulted in the segregation of sulfur from the bulk. Several cycles of gentle argon ion bombardment (800 V,

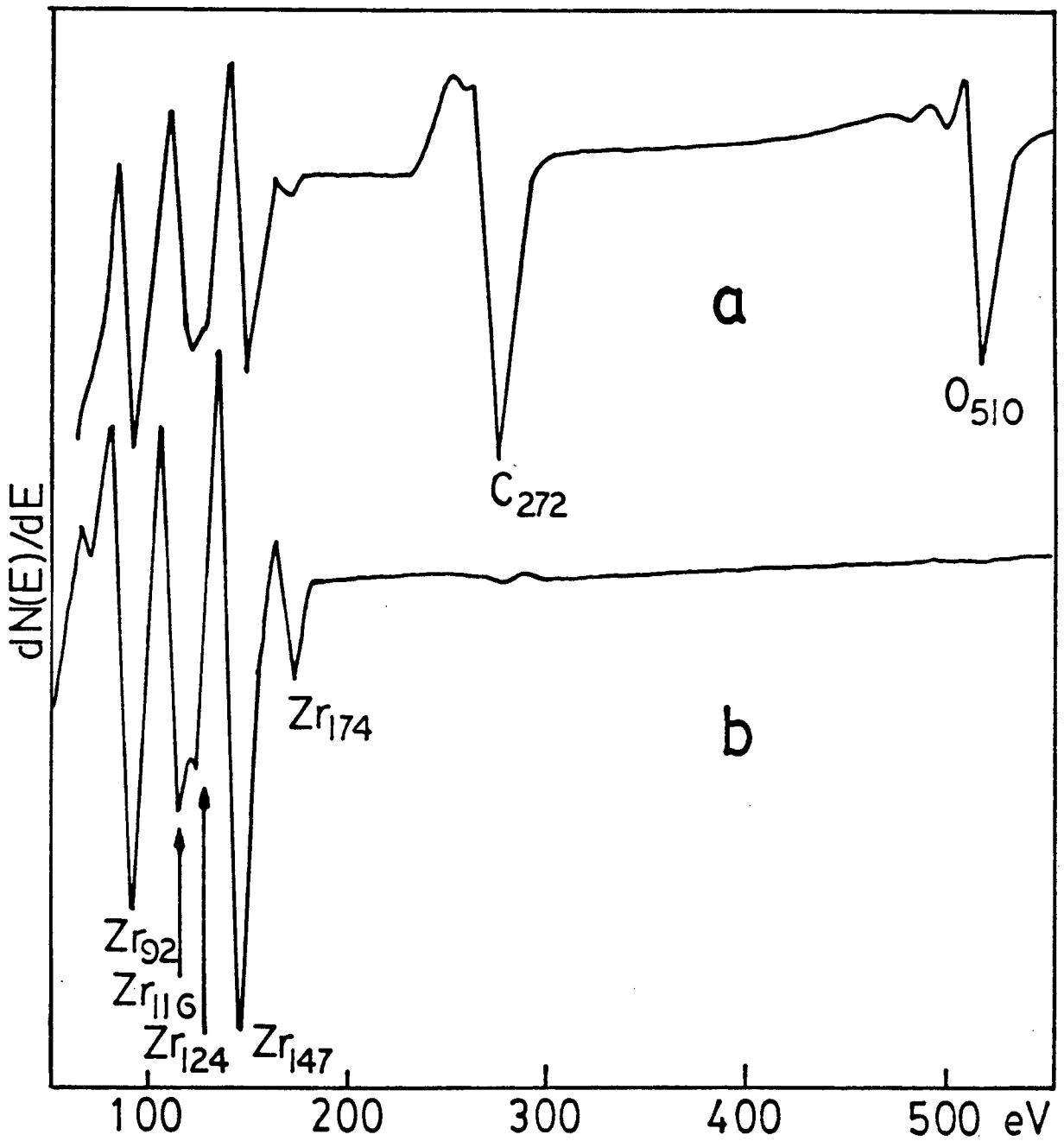


Figure 6.1: Auger spectra of two Zr(0001) surfaces:
(a) as mounted (b) cleaned.

3 μA), followed by annealing at 600°C for 20 minutes, were found effective to minimize the S and C contaminations. The sulfur coverage was difficult to quantify by AES as a result of the overlap of the S (150 eV) and Zr (147 eV) Auger peaks. To monitor the presence of sulfur it was necessary to measure the relative Auger peak heights at 92 eV and 147 eV. The LEED pattern also served as a sulfur detector; even low coverages produced an increased background and a faint (3x3) pattern. However after a total of about 60 hours of gentle argon ion bombardment, covering 15 bombardment-annealing cycles, the Auger peak ratio A_{147}/A_{92} reached a limiting value of approximately 1.40, as is shown in Figure 6.1(b). This spectrum compared well with published data for a clean zirconium surface [123]; in addition a sharp (1x1) LEED pattern with 6-fold symmetry at normal incidence indicated that the Zr(0001) surface was well-ordered.

6.2.2 LEED Pattern for Oxygen Adsorption on Zr(0001)

Exposure of a clean and ordered Zr(0001) surface at room temperature to about 1.2 Langmuir (1 L = 10^{-6} Torr s) of oxygen resulted in the observation of a diffuse (1x1) LEED pattern, although a sharp and apparently stable (2x2)-type pattern could be established by heating briefly to 220°C. It is noted that all heat treatments referred to here involve heating the sample to the stated temperature, followed immediately by cooling back to room temperature (the heating and cooling rates both being approximately 1°C s^{-1}). The (2x2)-type surface corresponds to an oxygen coverage for which the index $R_o = A_{510}/A_{92}$ (i.e. the ratio of the Auger peak height for

O at 510 eV to that of Zr at 92 eV) equals 0.16. For Zr it appears advantageous to use the 92 eV Auger peak which involves emission from the N shell; this limits the influence of attenuation and shift/broadening effects which have been noted in valence shell spectra [113,124]. With greater exposure to oxygen the half-order beams weaken, and sharp higher-coverage (1x1) patterns can be established. For example that with R_o equal to 0.23 is obtained after a 3.6 L exposure and heating to 220°C. LEED also shows that this ordered (1x1)-0 structure readily reconverts to give (2x2)-type patterns on heating at temperatures which are sufficiently high to cause a loss of surface oxygen as a result of bulk diffusion. After each adsorption experiment, the sample was cleaned by Ar^+ bombardment and reordered by heating to 600°C.

6.2.3. AES and LEED Spot Profile Measurements for Zr(0001)-(2x2)-0

An assessment of the conditions under which oxygen at a Zr(0001) surface diffuses into the bulk is needed in order to define appropriate surface preparation procedures. The data in Figure 6.2 apply to an oxygen-treated surface for which R_o is initially 0.16 (referred to as R_o^{int}). This sample was heated to a temperature T and cooled back to room temperature for measuring the new Auger peak height ratio (R_o^T). Figure 6.2 shows a plot of the normalized oxygen peak height ratio (R_o^T/R_o^{int}) obtained for successively increasing T. This curve provides evidence that O diffusion into zirconium effectively starts at around 236°C, and it gives part of the

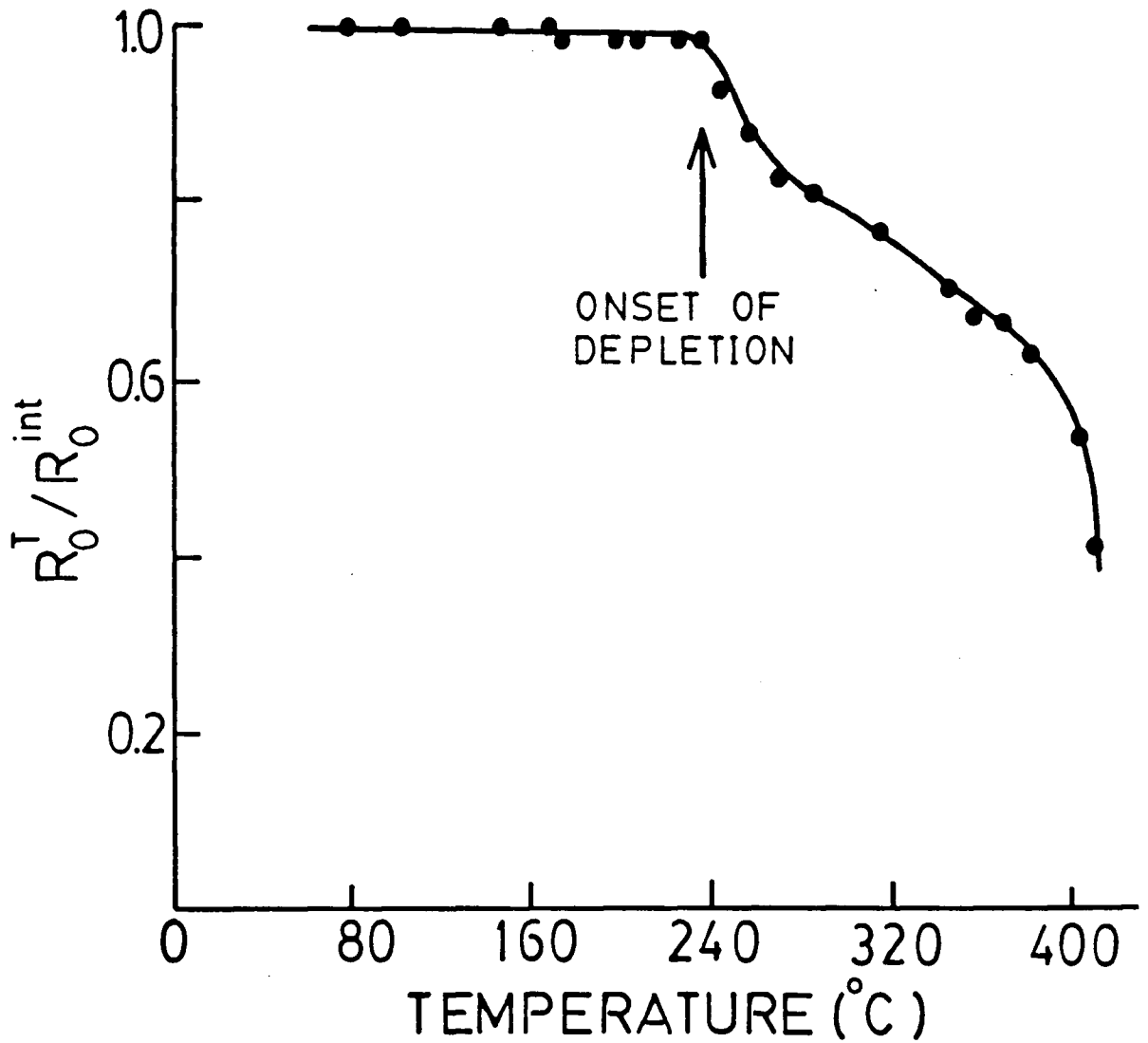


Figure 6.2: Normalized Auger peak height ratio R_0^T/R_0^{int} as a function of heating temperature for oxygen on $\text{Zr}(0001)$; the initial coverage corresponds to $R_0 = 0.16$.

basis for the choice used above of heating to 220°C to encourage surface ordering.

Figure 6.3 reports measurements made with the video LEED analyzer (VLA), described in Section 3.5.3, for the development of the (2x2)-type diffraction pattern with increasing exposure to oxygen; specifically information is given for the (1, 1/2) beam at 66 eV as a function of R_o (the beam notation in this Chapter is the same as that used in Figure 5.1). After each exposure to oxygen, the sample was heated to 220°C and cooled to room temperature before making the measurements. Figures 6.3(a) and (b) plot, respectively, the reciprocal of beam width (FWHM, i.e. full width at half maximum) and the integrated beam intensity (I); in each case values are plotted as a fraction of the maximum value. Variations in beam width reflect variations in size of the ordered regions which contribute to the LEED pattern; specifically larger values of 1/FWHM correspond to larger ordered regions [110]. The information in Figure 6.3 suggests the existence of at least two separate "ordered" regions over the exposure range, an observation that is broadly similar to conclusions reached by Madey et al. [125] in studies of oxygen adsorption on the Ru(0001) surface, although Yates et al. [126] observed only a very small low-coverage peak for oxygen on Rh(111). Nevertheless in neither of these latter cases does an ordered (1x1) adsorption structure exist, and so the detailed observations for O on Zr(0001) are inevitably different from the other cases.

Another approach to the type of information in Figure 6.3 is made by measuring 1/FWHM for the (1, 1/2) beam at 66 eV and room temperature after heating to different higher temperatures. Three initial surfaces were used with oxygen coverages corresponding to $R_o = 0.12, 0.16$ and 0.20 ; they all

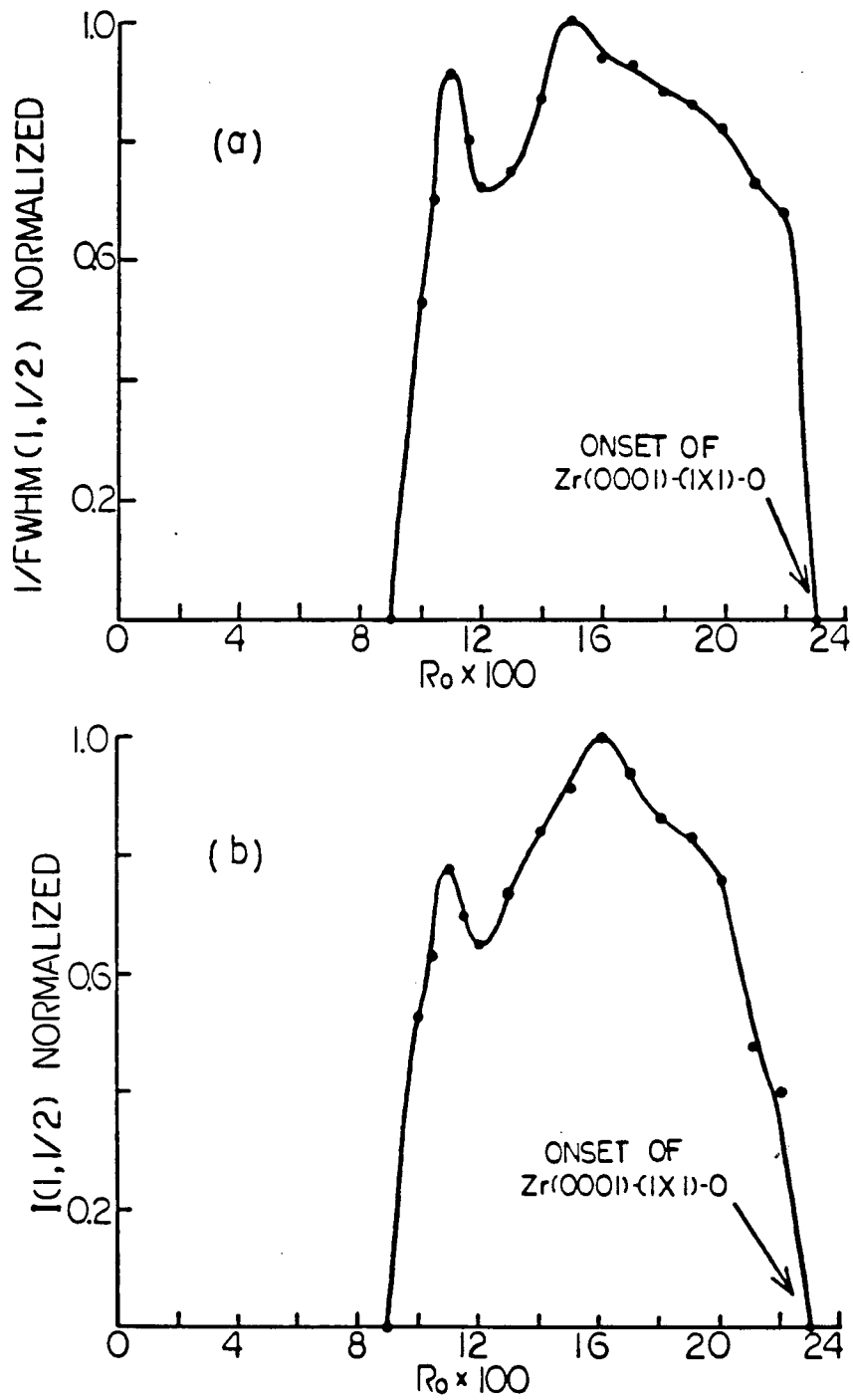


Figure 6.3: Measured variations for the (1, 1/2) beam at 66 eV with oxygen coverage on Zr(0001): (a) normalized $1/\text{FWHM}$, (b) normalized integrated intensity.

gave (2x2)-type LEED patterns and the three parts of Figure 6.3 show the individual plots obtained for $1/\text{FWHM}$ versus temperature. Two effects appear to be associated with the heating: one is the increase in surface ordering as larger surface domains are formed, and the other (for temperatures greater than 236°C) relates to the onset of bulk diffusion which decreases the R_0 value. With the latter, controlled increases in temperature can give systematic variations in the amount of surface oxygen. Starting with the lowest initial coverage (i.e. $R_0 = 0.12$) only one ordered region occurs as the surface oxygen successively orders and depletes (Figure 6.4(a)); indeed this curve for increasing temperature is closely related to that in Figure 6.3(a) as R_0 decreases from 0.12. By contrast, when the initial surface corresponds to $R_0 = 0.20$, three ordered regions are indicated by Figure 6.4(c), although the first one is apparently identified by just the high-coverage shoulder (which is similarly recognized in Figure 6.3(a)). The existence of the high-temperature (low-coverage) peak in Figure 6.4(c) shows that surface ordering can occur simultaneously with the surface depletion process which is initiated at 236°C . For the initial intermediate coverage ($R_0 = 0.16$) considered in 6.4(b), two ordered regions are indicated as R_0 decreases from 0.16, and this is broadly consistent with the peaks at R_0 equal to 0.15 and 0.11 as shown in Figure 6.3(a).

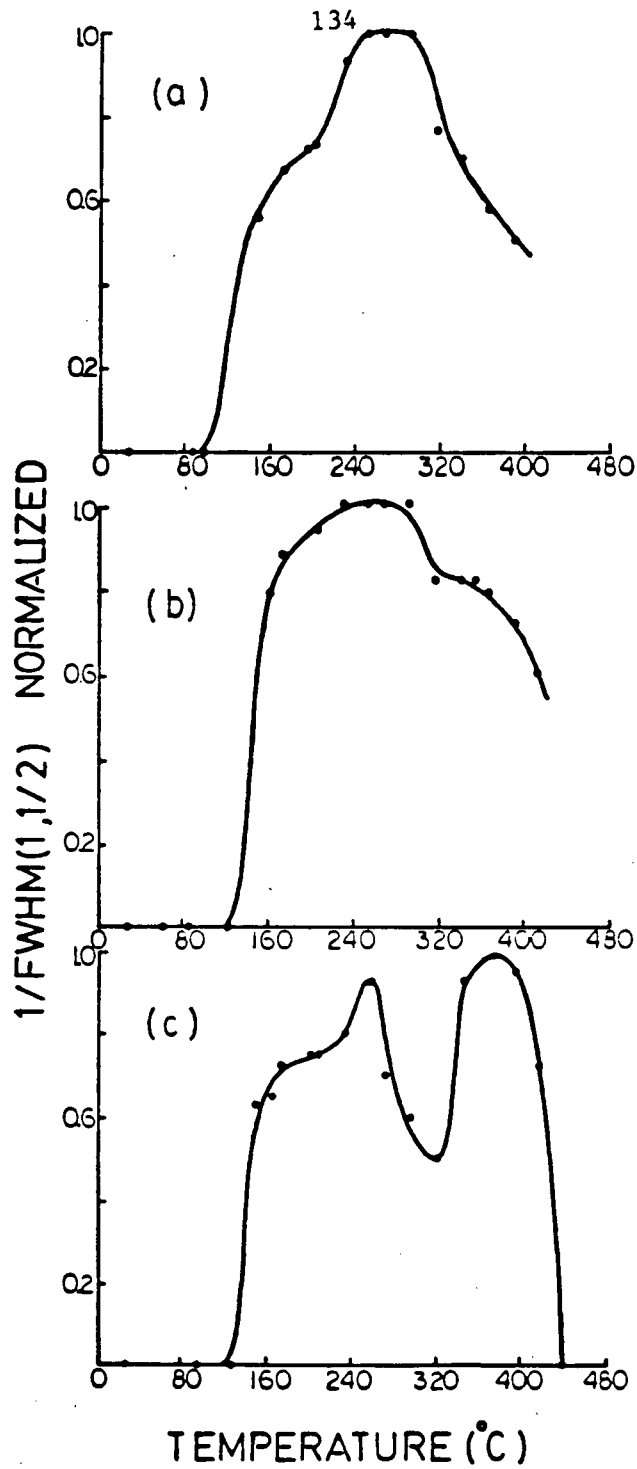


Figure 6.4: Measured variation with heating temperature of normalized $1/\text{FWHM}$ for the (1, 1/2) beam at 66eV for initial oxygen coverages on Zr(0001) with R_0 equal to: (a) 0.12, (b) 0.16 and (c) 0.20.

6.2.4 Measurements of I(E) Curves from the Lowest-Coverage Zr(0001)-(1x1)-0 Surface Structure

In Figure 6.3, it was shown that the exposure of a (0001) surface of zirconium to around 3.6 L of O₂ results in an initial (i.e. lowest coverage) Zr(0001)-(1x1)-0 structure with $R_0 = 0.23$. LEED intensity-versus-energy (I(E)) curves for diffracted beams from this surface were measured with the video LEED analyzer system over the approximate range 50-230 eV. These measurements were made with a constant increment of 2 eV, and a normalization was made to the incident beam current. The incidence settings were fine-tuned on-line to check for the appropriate symmetrical equivalences. In the final processing, I(E) curves measured for symmetrically related beams were averaged and smoothed as described in the previous study for Rh(111)-($\sqrt{3} \times \sqrt{3}$)30°-S. A total of seven independent I(E) curves was so measured from the Zr(0001)-(1x1)-0 surface. These were for the beams (10), (11), (20) at normal incidence; (00), (10), (2-1), (20) at a polar angle of 16° with the azimuthal direction parallel to a mirror plane in the surface, using the beam notation shown in Figure 6.5. The polar angle θ for which the measurements were made was determined from the position of the specular beam in the screen with respect to the normal direction. A previous calibration was made to relate measurements of the specular beam position on the screen to angular rotations of the manipulator from the normal position. For the azimuthal angle ϕ , the sample was oriented so that the incidence direction coincides with a (xz) reflection symmetry plane as is shown in Figure 6.5. Hence appropriate pairs of

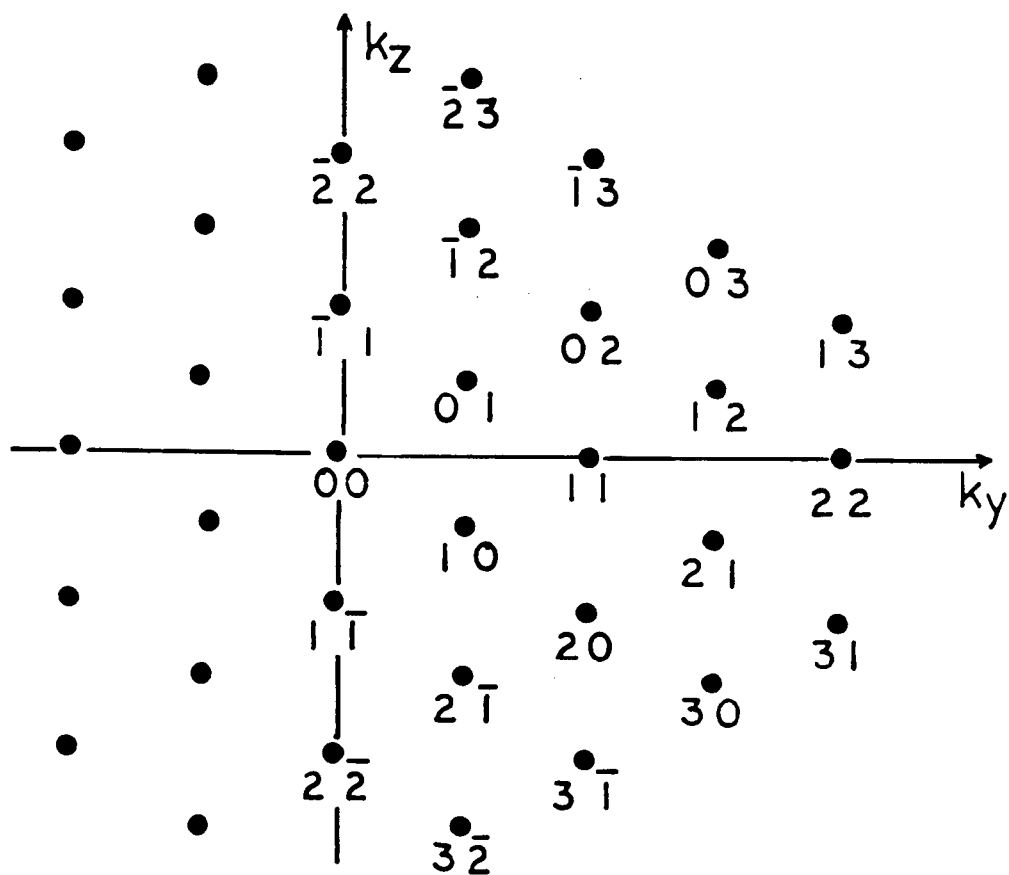


Figure 6.5: Reciprocal net and beam notation for the Zr(0001)-(1x1)-0 structure.

diffracted beams were available to ensure the presence of the reflection symmetry plane at the particular polar angle used (i.e. $\theta = 16^\circ$).

6.3 Multiple Scattering Calculations for Zr(0001)-(1x1)-O

In this work I(E) curves were calculated for various types of models appropriate to the Zr(0001)-(1x1)-O surface, and some of these models are indicated in Table 6.2. The symbols A, B, C identify close-packed zirconium layers which are laterally displaced so that the hcp and fcc structures follow respectively the familiar stacking sequences ABAB... and ABCABC...; the symbols in parentheses have the analogous meaning for oxygen. For example, the model type (B)A(C)BAB..., as is shown in Figure 6.6, indicates zirconium with the unreconstructed stacking sequence while the adsorbed O atoms occupy both overlayer and underlayer sites (these are respectively the "expected" 3-coordinate sites and octahedral hole sites between the first and second metal layers). For each model type, the calculations treated the neighbouring Zr-O interlayer spacing ($d_{\text{Zr-O}}$) as a variable. For the multiple scattering calculations, the overlayer spacings were varied over the range 0.60 to 1.20Å, while the underlayer spacings were varied between 1.20Å and 1.46Å with the O atoms midway between the adjacent Zr layers. However for models with both overlayer and underlayer, the underlayer Zr-O spacing was fixed at 1.35Å; also all directly neighbouring Zr-Zr interlayer spacings were held at the value for zirconium metal (2.57Å) [127].

The multiple-scattering calculations used procedures discussed in Chapter 2. The scattering by the zirconium structure, including incorpo-

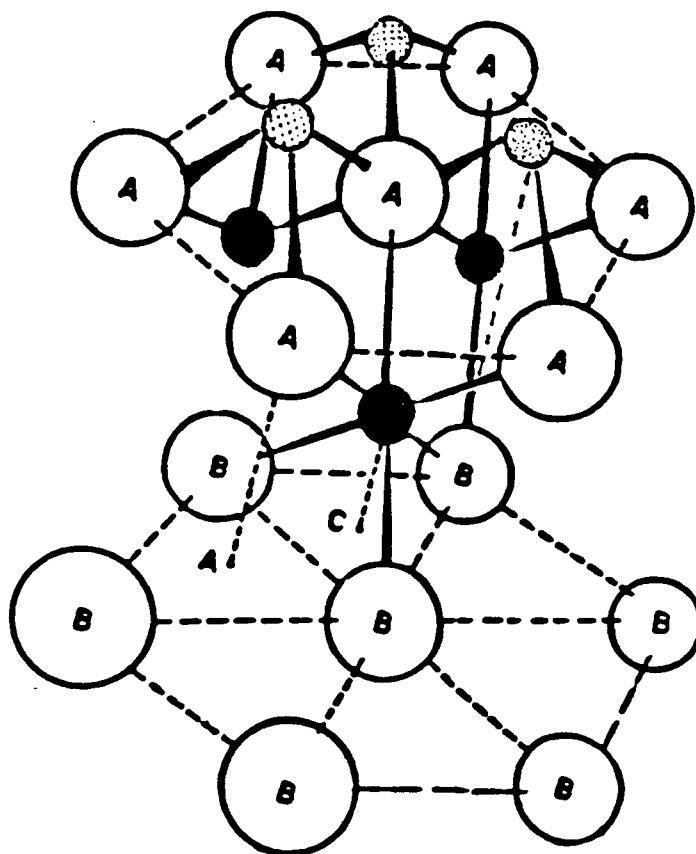


Figure 6.6: Partial view of the $\text{Zr}(0001)-(1 \times 1)-\text{O}$ structure corresponding to the model designated $(\text{B})\text{A}(\text{C})\text{BAB} \dots$. Atoms in the topmost Zr layer are in A-type positions (open solid circles), while the second Zr layer has atoms in B-type positions. The oxygen overlayer (smaller shaded circles) has atoms in B-type positions, while the underlayer O atoms (darker circles) occupy the octahedral holes in C type positions.

rated O layers, was determined with the renormalized forward scattering method, while O overlayers were added with the layer doubling method. For the calculations at normal incidence the 3-fold rotation and mirror reflection symmetries were utilized, while at off-normal incidence only the single mirror reflection plane was present; the maximum number of inequivalent beams available for the calculations at normal and off-normal incidence was 28 and 56 respectively. The calculations treated the solid's potential in the muffin-tin form, and the atomic potentials were characterized by phase shifts up to $l = 7$; for zirconium they were derived from a band structure potential [53], while those for neutral oxygen have the same values as those used in the previous analysis for Rh(111)-(2x2)-O. In addition, a set of oxygen phase shifts obtained by Zhong *et al.* [121,128], specifically for negatively charged O and the structure of bulk ZrO, was also used in some further multiple-scattering calculations for models of the Zr(0001)-(1x1)-O surface. The real part of the constant potential (V_{or}) between the atomic spheres was set initially at -10.0 eV, and the imaginary potential (V_{oi}) was fixed at -5.0 eV; the value of the former was refined during the comparison with the experimental $I(E)$ curves.

6.4 LEED Crystallographic Results for the Initial Zr(0001)-(1x1)-O Structure

Assessments of the quality of correspondence between experimental and calculated curves were made both visually and with Pendry's reliability index (R_p). For each model type contour plots of R_p were made as a

function of $d_{\text{Zr-O}}$ and V_{or} ; the minimum in R_p indicates a condition for best correspondence between the calculated and experimental $I(E)$ curves. The corresponding values of $d_{\text{Zr-O}}$, V_{or} and R_p are reported in Table 6.2. Some immediate conclusions from the results in Table 6.2 are:

- (i) overlayer models are less favored compared with underlayer models;
- (ii) there is no support, for the conditions of our surface preparation, for the proposal that O atoms adsorb simultaneously as an overlayer and as an underlayer between the first and second metal layer [129];
- (iii) the most favored surface structure according to R_p is for the model A(C)B(A)C(B)..., which corresponds to several layers of NaCl-like bulk ZrO(111).

With regard to (iii) above, Figure 6.7 shows that R_p is minimized at a value of 1.34\AA for $d_{\text{Zr-O}}$. This corresponds to a LEED-determined Zr-O bond distance equal to 2.30\AA , in very close agreement with the value (2.31\AA) given by X-ray diffraction for bulk ZrO [130]. Nevertheless the level of correspondence according to R_p reached between experiment and calculation for the model A(C)B(A)C(B)... is rather similar to that for the single underlayer structure designated A(C)BAB... Individual experimental $I(E)$ curves are reported in Figures 6.8 and 6.9 for Zr(0001)-(1x1)-O and they are compared with those calculated for both the single-underlayer (i.e. A(C)BAB...) and the bulk-underlayer (i.e. A(C)B(A)C(B)...) structures; the overall level of correspondence between experiment and calculation is at the moderate level in each case. The relative flatness of some experimental $I(E)$ curves (e.g. for the (10) and (20) beams at

Table 6.2: Values of Zr-O interlayer spacings and V_{or} corresponding to minima in contour plots of R_p for structural models of Zr(0001)-(1x1)-O.

Model	$d_{Zr-O}(\text{\AA})$	$V_{or}(\text{eV})$	R_p
(B)ABAB...(hcp)	1.00	-10.4	0.403
(C)ABAB...(hcp)	0.94	-12.4	0.416
A(C)BAB...(hcp)	1.37	-8.1	0.366
A(B)CAB...(hcp)	1.34	-7.7	0.375
A(B)CBA...(hcp)	1.34	-7.8	0.370
(C)A(C)BA...(hcp)	0.99*	-7.5	0.406
(B)A(C)BA...(hcp)	0.99*	-7.2	0.429
C(B)A(C)BA...(hcp)	1.34	-7.3	0.370
A(C)B(C)A(C)...(hcp)	1.32	-6.0	0.388
A(C)B(A)C(B)...(fcc)	1.34	-6.4	0.350

* d_{Zr-O} for underlayer fixed at 1.35Å.

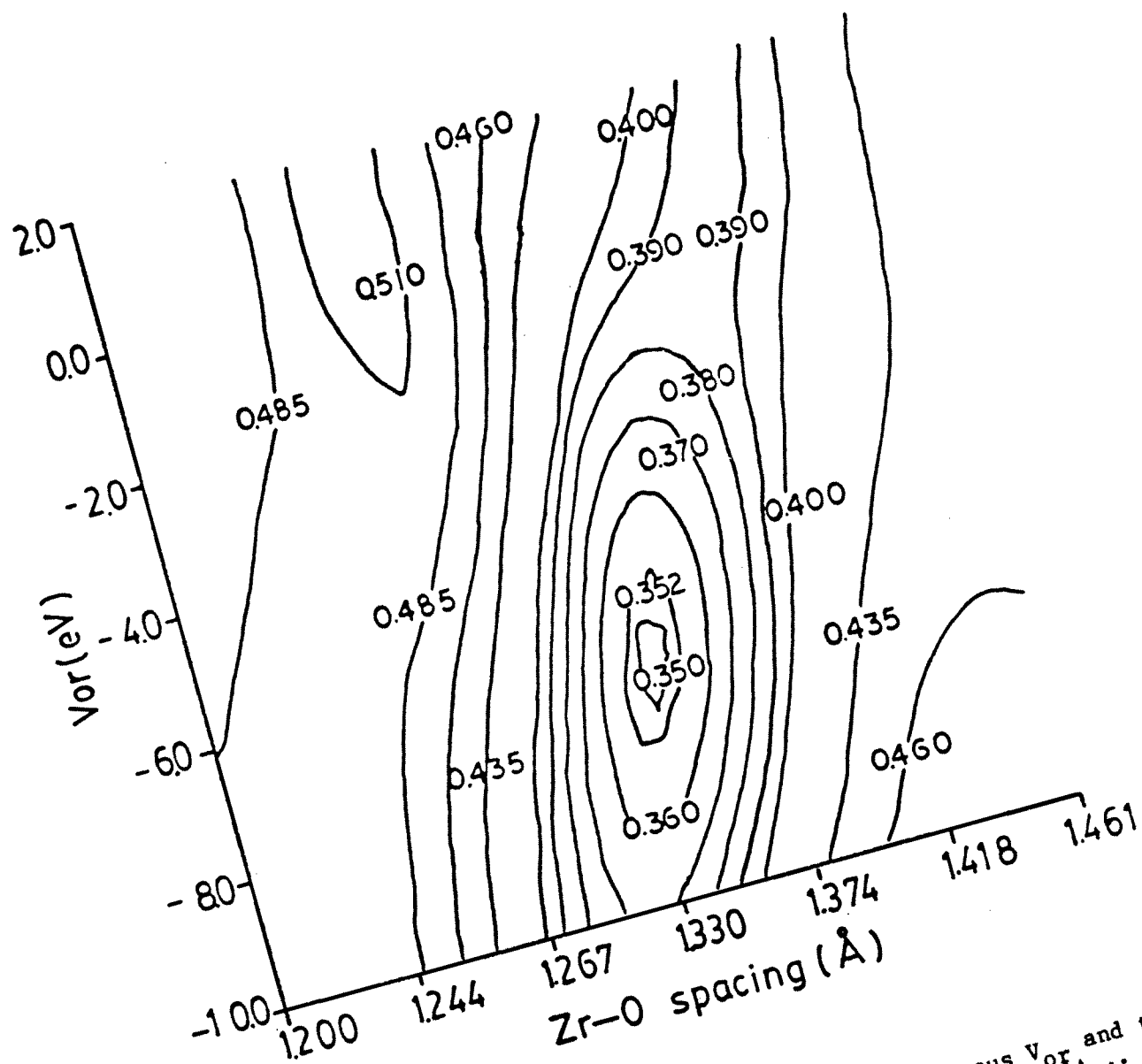


Figure 6.7: Contour plot for $Zr(0001)-(1 \times 1)-O$ of R_p versus V_{or} and the Zr-O interlayer spacing for the model $A(C)B(A)C(B)A \dots$

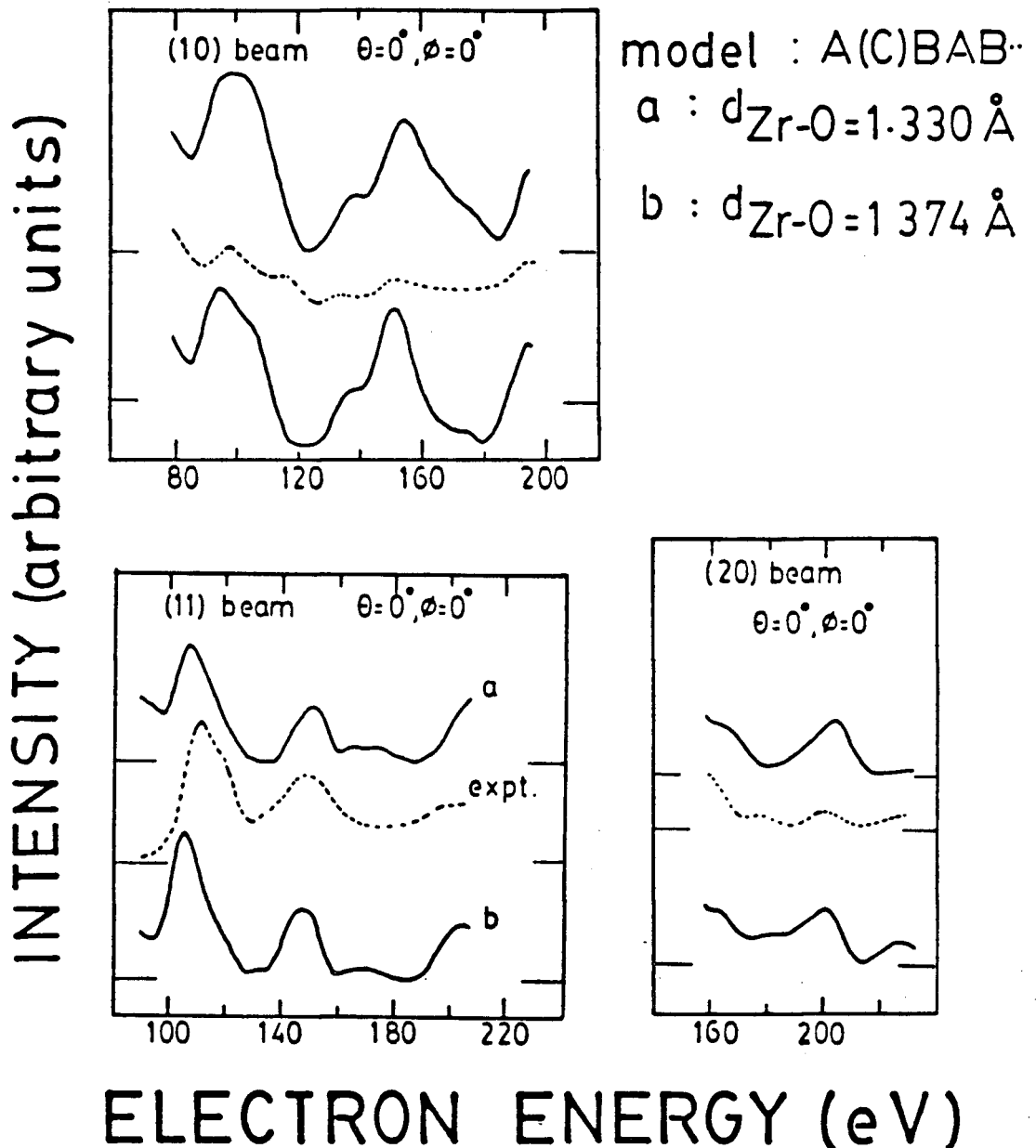


Figure 6.8: Comparison of experimental $I(E)$ curves (dashed) from $\text{Zr}(0001)-(1 \times 1)-0$ with those calculated for the single-underlayer model A(C)BAB... with $d_{\text{Zr-O}}$ equal to 1.33 Å (upper continuous line designated a) and 1.37 Å (lower continuous line designated b).

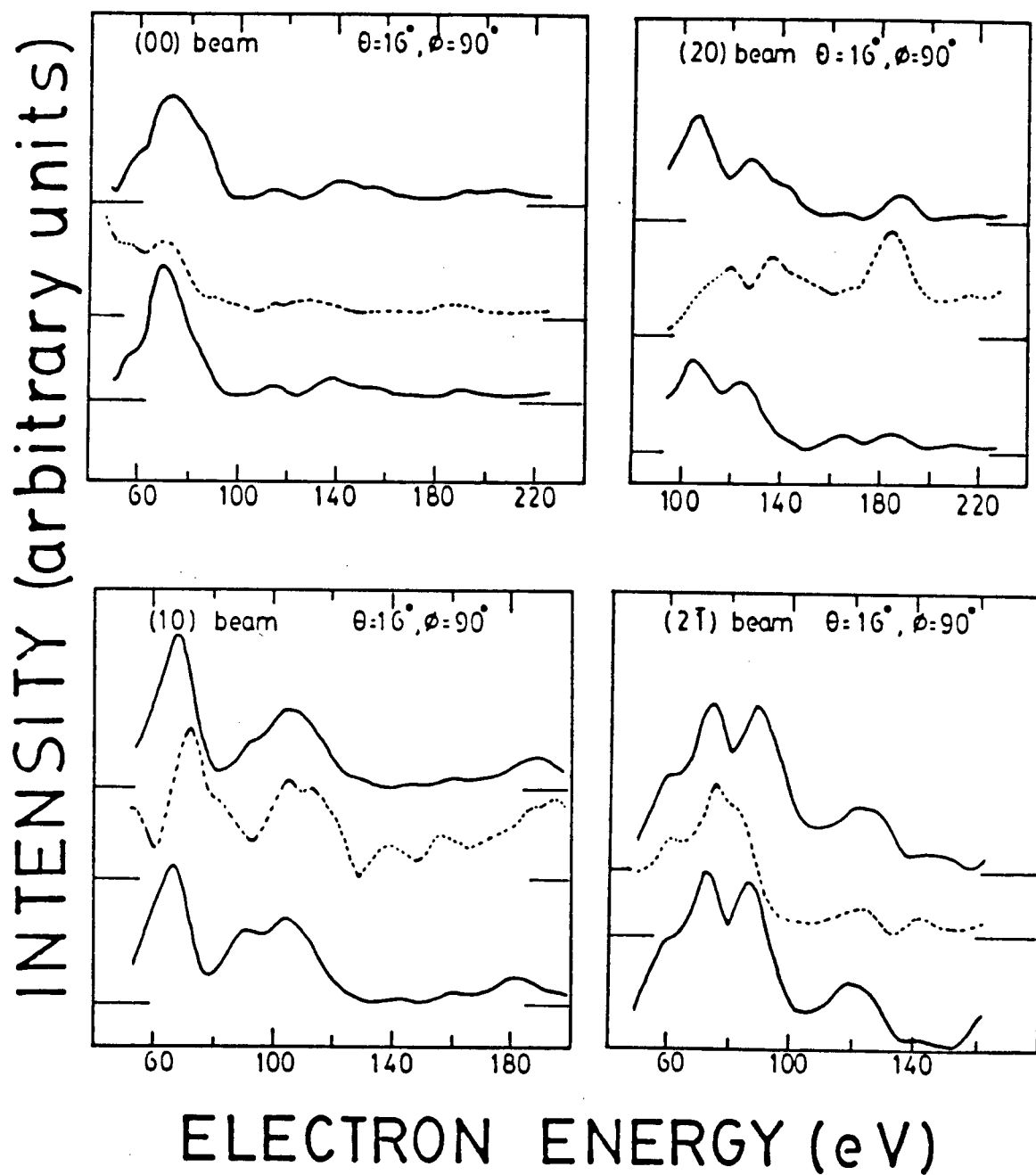


Figure 6.8: (continued)

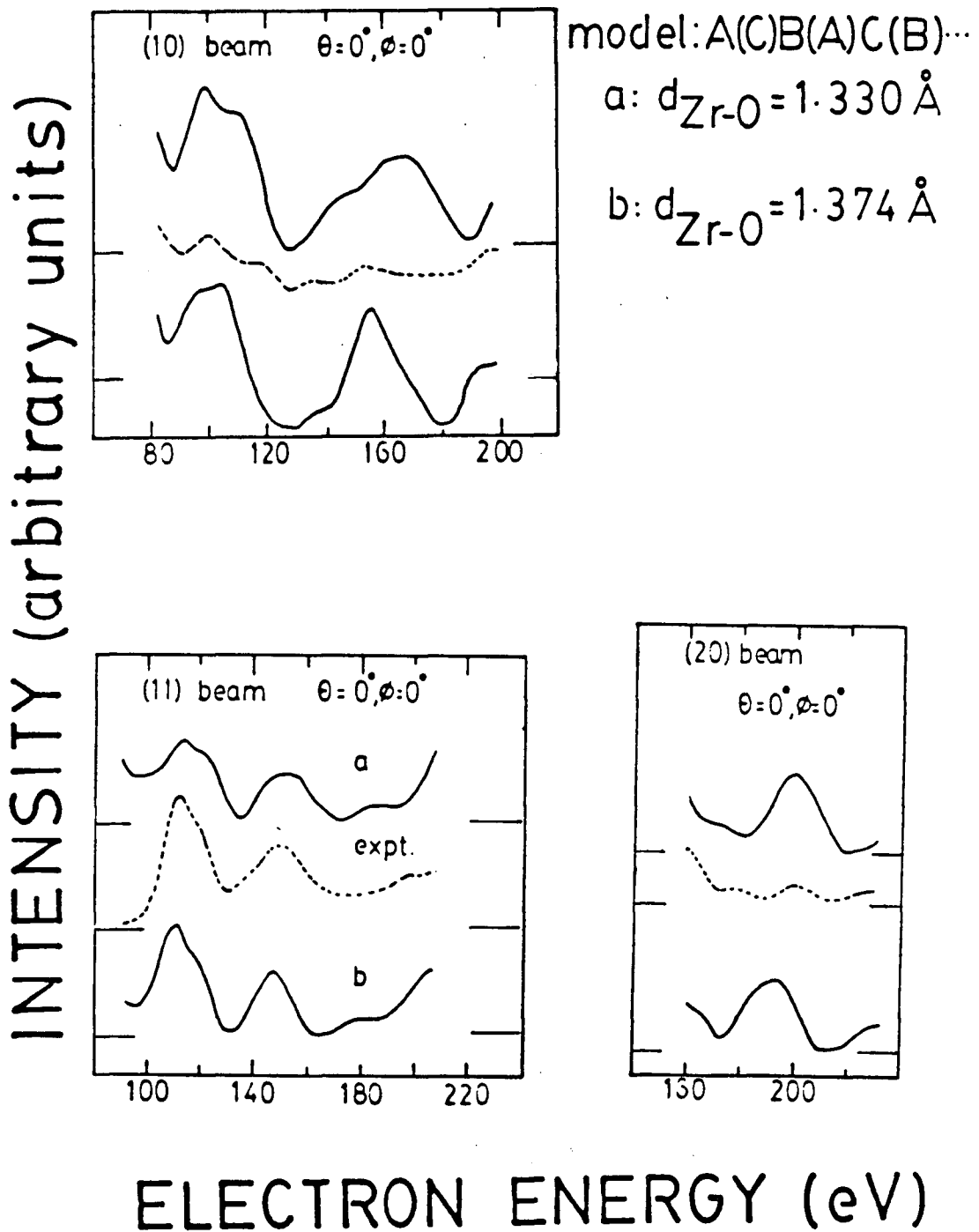


Figure 6.9: Comparison of experimental $I(E)$ curves (dashed) from $\text{Zr}(0001)-(1 \times 1)-0$ with those calculated for the multi-underlayer model $A(C)B(A)C(B)\dots$ with $d_{\text{Zr-O}}$ equal to 1.33 \AA (upper continuous line designated a) and 1.37 \AA (lower continuous line designated b).

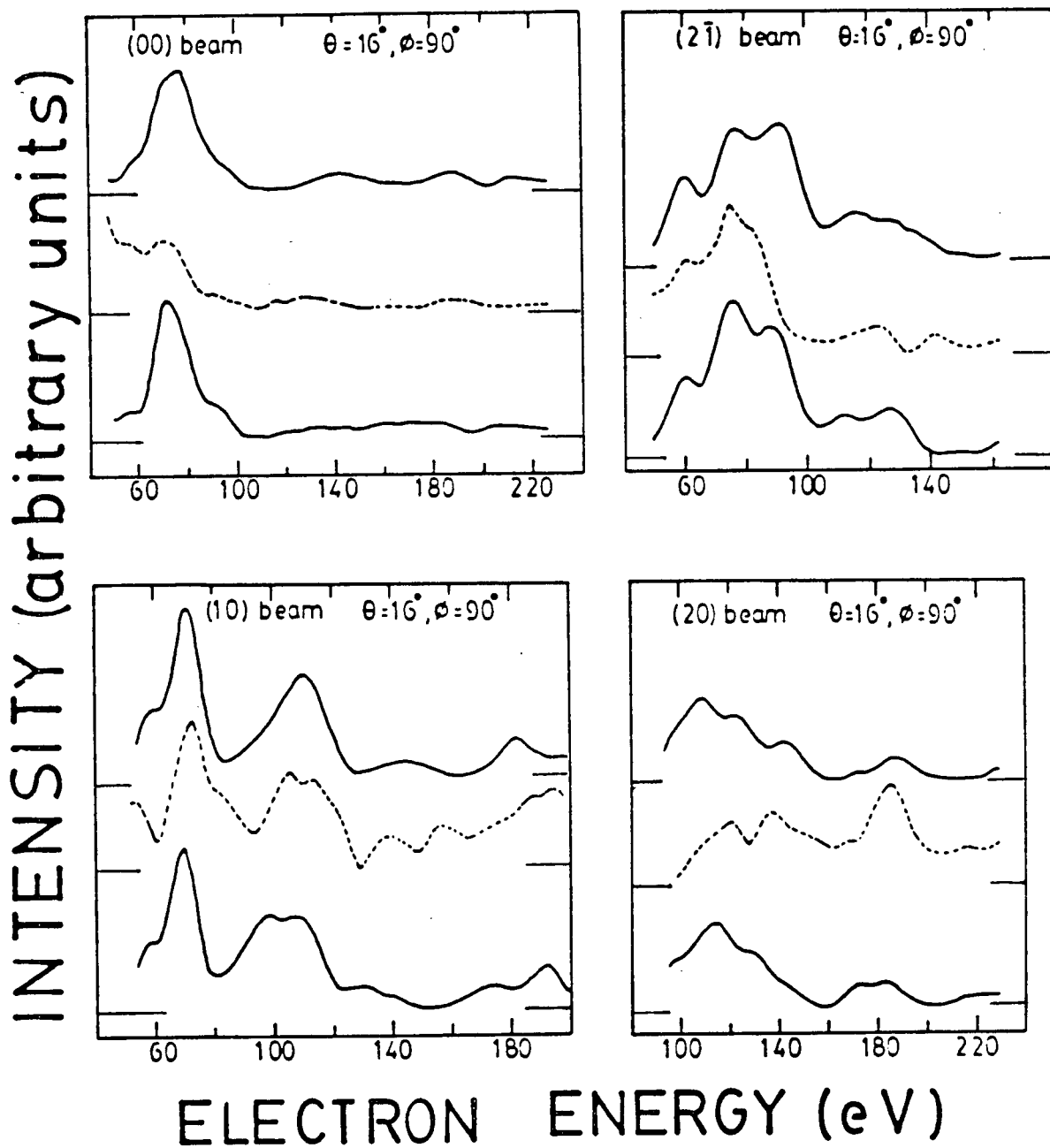


Figure 6.9: (continued)

normal incidence) reflects the fact that the intensities are low and therefore contain significant background contributions.

In an attempt to distinguish between the applicability of the single- and multi-underlayer models, Table 6.3 summarizes results of the new comparisons with R_p for the two model types compared in Figures 6.8 and 6.9, in which the calculations were made using phase shifts for negatively charged O. The results in Table 6.3, along with those obtained for other structural models, suggest that no appreciable change in structural conclusions follow from the use of 0 phase shifts appropriate to a negatively charged atom. The LEED analysis with R_p still favors the multi-underlayer model over the single-underlayer model, and overall we believe this conclusion is also slightly favored by the visual comparisons between the curves shown in Figure 6.8 and 6.9. Some other models, such as C(B)AB... and A(C)B(C)AB..., which were not included in Table 6.2, have been tested in relation to the I(E) curves measured for normal incidence; those data were used to guide the selection of the model types to be tested in greater detail (i.e. against measurements at both normal and off-normal incidence as reported in Table 6.2).

6.5 Discussion

Our current conclusion for the lowest-coverage Zr(0001)-(1x1)-O surface structure is that the O atoms occupy octahedral hole sites, possibly for several layers below the surface, with the Zr-O interlayer spacing equal to $1.35 \pm 0.03 \text{ \AA}$. The structural resemblance to ZrO appears strong, but it is also recognized that the final oxidation product for the

Table 6.3: Values of Zr-O interlayer spacings and V_{or} corresponding to minima in contour plots of R_p for two structural models of Zr(0001)-(1x1)-O using phase shift for negatively charged O.

Model	$d_{Zr-O}(\text{\AA})$	$V_{or}(\text{eV})$	R_p
A(C)BAB...(hcp)	1.37	-6.4	0.401
A(C)B(A)C(B)...(fcc)	1.37	-3.0	0.380

oxygen-zirconium system is ZrO_2 [112]. In addition, an earlier analysis with X-ray photoelectron spectroscopy indicated that a significant change in oxidation behavior of $Zr(0001)$ occurs at around 3.5 L exposure to oxygen [112]. The new information given in the LEED spot profile analysis suggests that the situation is close to that characterized here with $R_o = 0.23$, at which point the lowest-coverage $(1 \times 1)-O$ LEED pattern is first established. This indicates that the initial $(1 \times 1)-O$ structure (i.e. ZrO) is an intermediate in the oxidation process of $Zr(0001)$ surfaces. The initial formation of ZrO_2 may involve the fluorite structure with O occupying all tetrahedra holes in (fcc) zirconium. In this structure the O to Zr ratio is 2:1, although the surface geometrical structure has not yet been explored in the higher O-coverage regime. However, even for the system studied here, some incipient occupation of tetrahedral holes could occur; that along with other surface inhomogeneities may account for some differences found between the experimental and calculated $I(E)$ curves.

The structural information obtained for the initially-formed $Zr(0001)-(1 \times 1)-O$ surface, which apparently reinforces that found previously [43] for the lower-coverage structure $Zr(0001)-(2 \times 2)-O$, provides a basis for interpreting measurements made here in the spot profile analysis for the $Zr(0001)-(2 \times 2)-O$ LEED patterns. The simplest models for the (2×2) structure have an ordered occupation of $1/4$ of the octahedral holes, either between several Zr layers or just between the first and second Zr layers. An increasing O content beyond this occupation level must inevitably increase disorder, which in turn is expected to decrease the half-order beam intensity as well as increase the beam width. In principle these

trends could reverse in the approach to $1/2$ occupation of the available octahedral holes (as required for the (2×1) layer), and the whole cycle repeat between $1/2$ and $3/4$ occupation (where (2×2) ordered layers are again also possible). Beyond the $3/4$ occupational level the half-order beam intensities must decrease as (1×1) regions become increasingly important over those of the (2×2) type.

We were unable to detect half-order beams for values of R_0 less than about 0.09, and hence 0 repulsions apparently prevent the formation of ordered adsorption domains at very low coverage. The maxima shown in Figure 6.3 for R_0 around 0.11 are reasonably assigned to a structure which approximates one of the ideal (2×2) forms with $1/4$ octahedral site occupation, and similarly the maxima at around R_0 equal to 0.15 apparently correspond to a structure with $1/2$ site occupation. A corresponding peak is not resolved for $3/4$ site occupation, but consistently the high-coverage maxima are broad. Indeed, in this range of coverage, the 0 atoms are probably distributed statistically over the possible sites according to the overall coverage. Computer simulation studies on similar systems [131] suggest there may still be sufficient short-range order for a (2×2) -type LEED pattern to be displayed. Certainly studies with the high-resolution spot profile technique [132] would help to probe the surface order in more detail, although the low-temperature shoulder in Figure 6.3 for R_0 close to 0.18 plausibly identifies the 0 structure for $3/4$ site occupation.

CHAPTER 7

A LEED Crystallographic Investigation of a Surface
Structure Designated Zr(0001)-(1x1)-N

7.1 Introduction

The chemisorption of nitrogen on (0001) surfaces of hexagonal close-packed metals has not been widely studied at the quantitative level, although a number of qualitative observations have been reported including those on the surfaces of beryllium [133], ruthenium [134] and rhenium [135]. An exception is the LEED crystallographic analysis for the Ti(0001)-(1x1)-N surface for which Shih et al. [68] reported that N atoms form an underlayer structure by occupying all octahedral holes between the top two layers of titanium. By contrast, the study in the previous chapter for the Zr(0001)-(1x1)-O structure suggested that O atoms occupy octahedral holes, possibly through several layers below the surface. In this chapter we describe a LEED crystallographic study for the chemisorption of nitrogen at the Zr(0001) surface [136]; comparisons will be made with the previous studies for both N adsorbed on Ti(0001) [68] and O adsorbed on Zr(0001) [43,121]. Another point of comparison is with some investigations by Foord et al. [113] for nitrogen adsorption on polycrystalline zirconium; these latter authors concluded that this room-temperature adsorption is dissociative and that the final product is an underlayer structure.

7.2 Experimental

The apparatus and initial cleaning procedures used were as described previously in Section 6.2.1. Adsorption studies were made on a surface which showed sharp (1x1) LEED patterns, and for which no contaminants were detected with AES. Such a surface at room temperature was exposed to

nitrogen gas (Matheson, 99.999% pure) at around 2×10^{-8} Torr. Figure 7.1 reports a typical nitrogen uptake curve as measured by

$$R_N = A_{383}/A_{92}$$

(i.e. the ratio of the Auger peak height for N at 383 eV to that of Zr at 92 eV).

Unlike oxygen on Zr(0001), which shows an initial (2x2) LEED pattern, no superstructure beams were observed with nitrogen adsorption. It was however necessary to order the nitrogen structure by annealing. This was done by heating the surface to 220°C followed by immediate cooling (heating and cooling rates both being around 1°C s^{-1}). The onset of effective bulk diffusion was assessed by measuring R_N values after cooling from progressively higher temperatures following the procedure described in 6.2.2. For a sample, with an initial R_N value of 0.25, the diffusion of N into the bulk becomes significant at around 438°C (Figure 7.2); this is some 200°C more than the corresponding value found earlier for O diffusion.

For the LEED analysis from the initial (1x1)-0 structure on Zr(0001), the appropriate adsorption conditions could be chosen by the criterion that the intensities of the half-order spots vanish from the previous (2x2) diffraction pattern. For N adsorption, the hope was to analyze an analogous surface structure, although it could be recognized only on indirect evidence. Nevertheless three types of measurements show changes for exposures of around 5 to 6 L; specifically: (1) the slope of

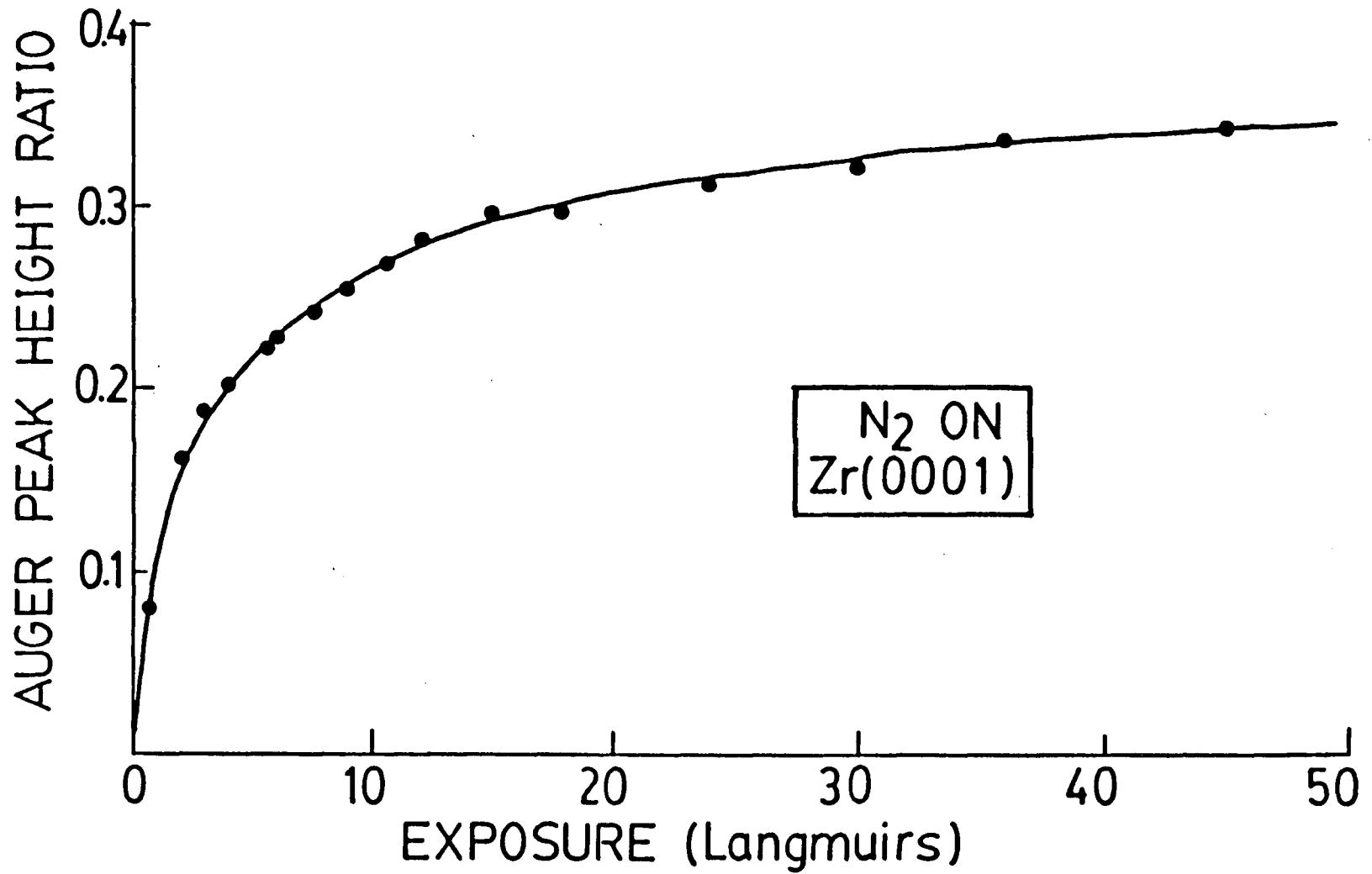


Figure 7.1: Auger peak height ratio N(383eV)/Zr(92eV) plotted as a function of nitrogen exposure.

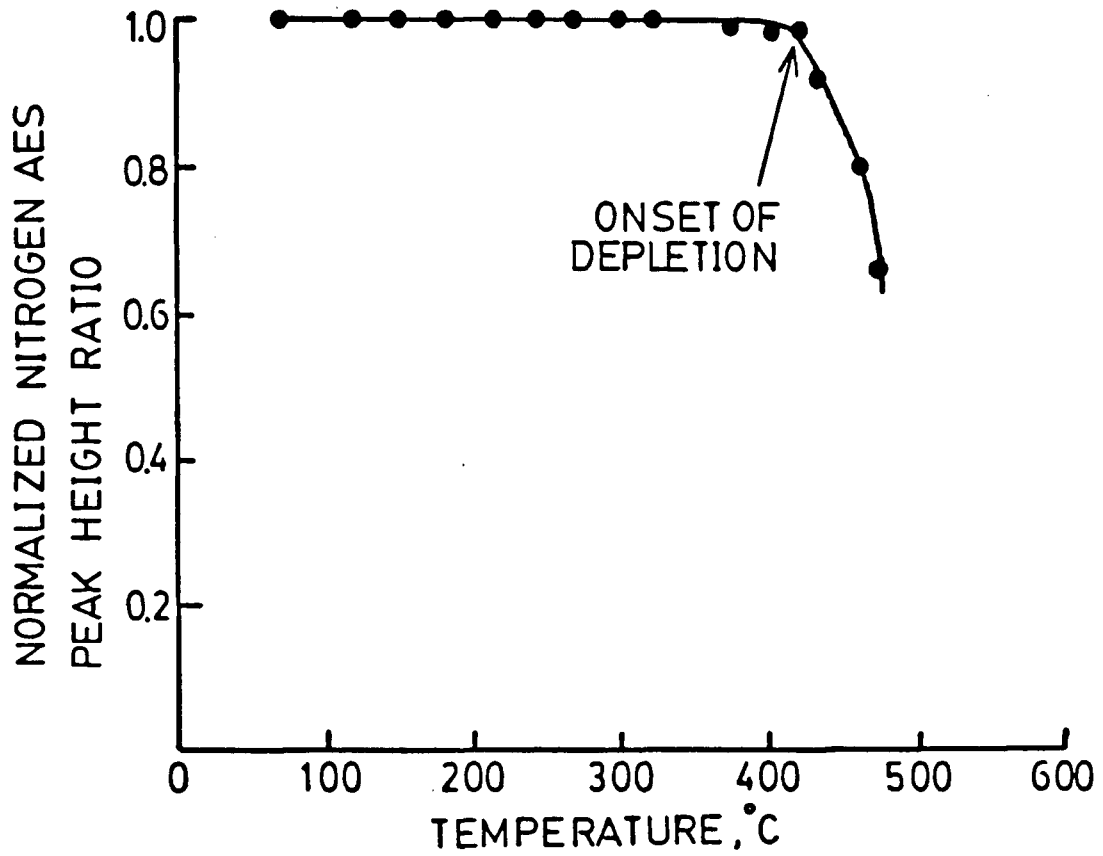


Figure 7.2: Normalized nitrogen Auger peak height ratio R_N^T/R_N^{int} as a function of heating temperature for nitrogen on Zr(0001); the initial coverage corresponds to $R_N = 0.25$.

the lower-coverage part of the N uptake curve starts to reduce, (ii) the Auger peak of Zr at 147 eV suddenly shifts by -1.3 eV as seen in Figure 7.3 (although this peak shift remains constant for further exposures to at least 42 L), and (iii) changes in I(E) curves from those of the clean surface become well-established (Figure 7.4). An exposure of 5.5 L gave a Zr(0001)-(1x1)-N structure for which $R_N = 0.22$, and this structure was used for the LEED analysis. Incidentally Foord *et al.* [113] also reported a significant change in slope at around 6 L in an uptake curve measured by the work function variation as nitrogen is adsorbed on polycrystalline zirconium.

I(E) curves for LEED beams from the Zr(0001)-(1x1)-N structure with $R_N = 0.22$ were measured with a video LEED analyzer for the energy range 50(2)230 eV exactly as described previously for the Zr(0001)-(1x1)-0 structure. Nine independent I(E) curves were measured for the beams (10), (11), (20) at normal incidence, (00), (10), (20), (2-1), (3-1), (3-2) at a polar angle of 18° with the azimuthal direction parallel to a mirror plane in the surface. The same beam notation is used as described previously for the Zr(0001)-(1x1)-0 structure.

7.3 Calculations

All structural models considered in this analysis for the initial Zr(0001)-(1x1)-N surface structure were built from the stacking of hexagonal close packed layers of either N atoms or Zr atoms. These models were restricted to four categories:

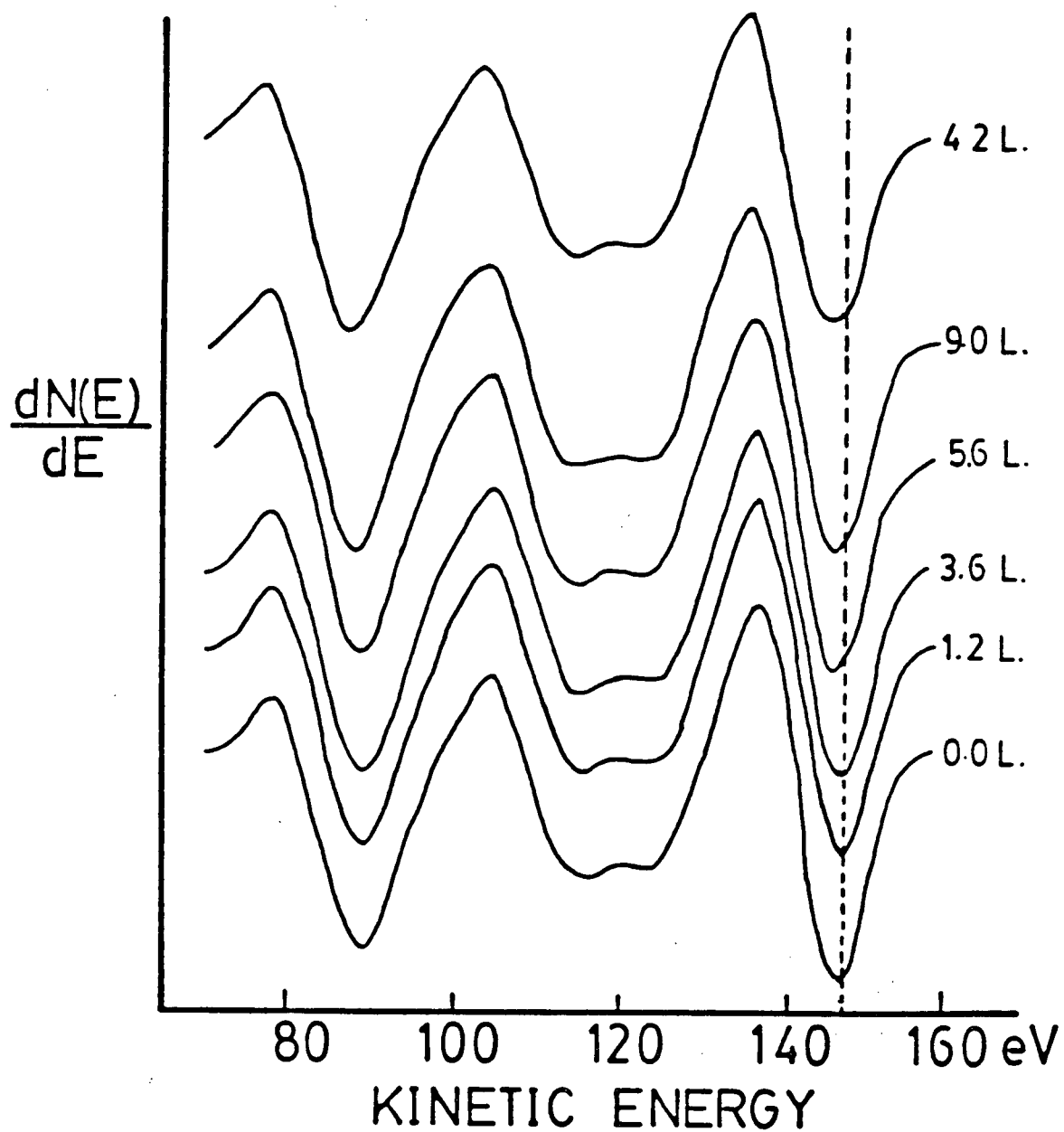


Figure 7.3: Variations of the Zr Auger peak around 147 eV with nitrogen exposure on Zr(0001).

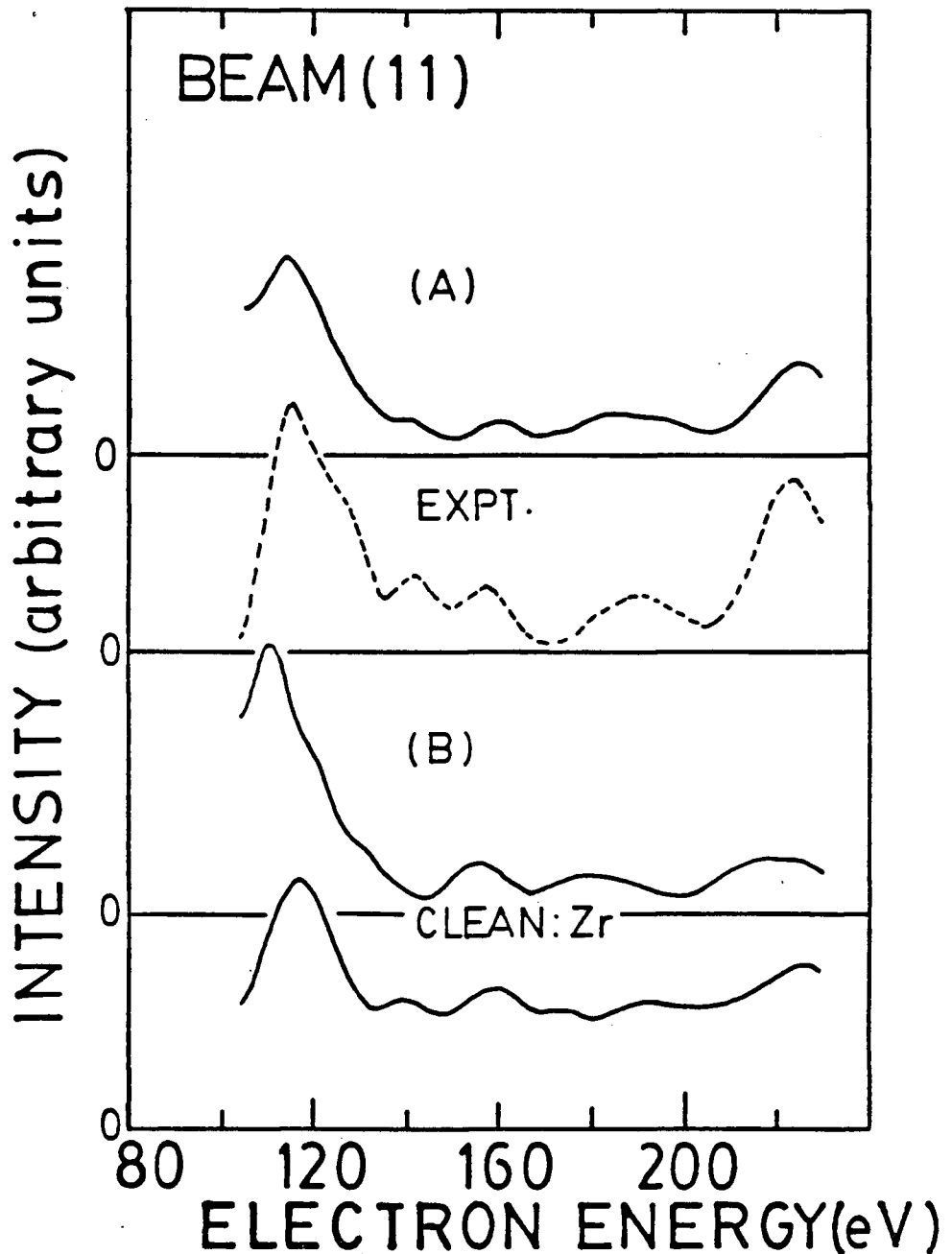


Figure 7.4: Comparisons for (11) and (10) beams at normal incidence of experimental $I(E)$ curves (dashed) from $Zr(0001)-(1 \times 1)-N$ with those measured for clean $Zr(0001)$ and calculated for two models of $Zr(0001)-(1 \times 1)-N$, namely for the model $A(C)BAB\dots$ with d_{Zr-N} equal to 1.287 \AA (curves designated A) and for the model $A(C)B(C)AB\dots$ with d_{Zr-N} equal to 1.330 \AA (curves designated B).

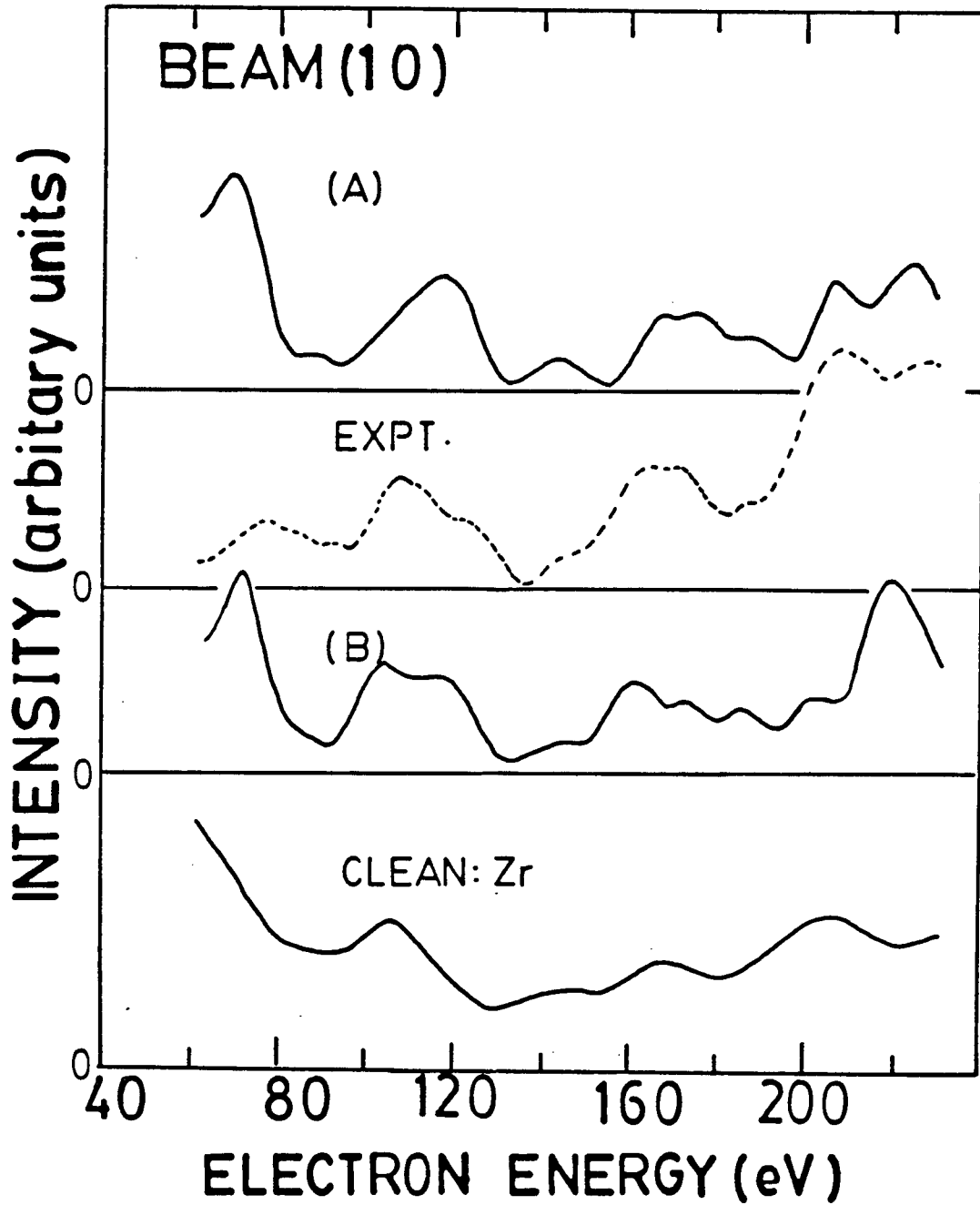


Figure 7.4: (continued)

- (i) Simple overlayer models where N atoms occupy 3-fold coordination sites above the unreconstructed zirconium surface (i.e. models designated (B)ABAB... and (C)ABAB..., where the symbols in parentheses identify lateral positions of N with respect to the hcp structure of zirconium).
- (ii) Underlayer structures where N atoms occupy octahedral holes within an unreconstructed zirconium structure. These models are designated A(C)BAB..., A(C)B(C)ABAB..., A(C)B(C)A(C)B(C)... according to whether the N atoms occupy all octahedral holes respectively between the first and second metal layers, between the first three metal layers, between all metal layers probed by the LEED electrons.
- (iii) Underlayer structures where N atoms occupy all octahedral holes between zirconium layers that have reconstructed to the local fcc type packing arrangement (e.g. A(B)CABAB...).
- (iv) Overlayer plus single underlayer models (e.g. (B)A(C)BABA...).

For each model type, the neighboring Zr-N interlayer spacing ($d_{\text{Zr-N}}$) was varied, specifically from 0.60 to 1.20 Å for overlayer N, and from 1.20 to 1.46 Å for underlayer N. However for the category (iv), with both overlayer and underlayer, the underlayer Zr-N interlayer spacing was fixed at 1.30 Å (the value suggested by results below). All directly neighboring Zr-Zr interlayer spacings were kept at the value (2.57 Å) for zirconium metal [127].

Multiple scattering calculations of I(E) curves were made with standard procedures [44,45]. Specifically the scattering by the zirconium structure, including incorporated N layers, was determined with the

renormalized forward scattering method, while N overlayers were added with the layer doubling method. All computational details followed those used in the previous analysis for Zr(0001)-(1x1)-0, except that the N potential, characterized by phase shifts to $\lambda = 7$, was constructed from a superposition of free atom charge distributions for a hypothetical bcc solid [137].

7.4 Results

Assessments of the quality of correspondence between calculated and experimental $I(E)$ curves for Zr(0001)-(1x1)-N were made both visually and with Pendry's reliability index (R_p). An initial pruning out of some less favored models was made by comparing with just the normal incidence data, although most models were assessed for normal and off-normal incidence data combined. For those latter cases, contour plots of R_p were made as a function of the Zr-N interlayer spacing and the real part of the constant muffin-tin potential (V_{or}); values of d_{Zr-N} which minimize R_p are reported in Table 7.1 for various different structural models. One representative contour plot of R_p for the A(C)BAB... model type is shown in Figure 7.5. In addition, particular comparisons of experimental and calculated $I(E)$ curves for the surfaces A(C)BAB... and A(B)CAB... are shown in Figures 7.6 and 7.7 respectively.

7.5 Discussion

The best correspondence between experimental and calculated $I(E)$ curves for the Zr(0001)-(1x1)-N surface structure has been reached for

Table 7.1: Values of Zr-N interlayer spacings corresponding to minima in contour plots of R_p for structural models of Zr(0001)-(1x1)-N.

Model	$d_{\text{Zr-N}}$ (Å)	R_p
(B)ABAB..(hcp)	0.68	0.374
(C)ABAB..(hcp)	0.99	0.360
(C)B(C)AB..(hcp)	1.08*	0.358
(A)B(C)AB..(hcp)	0.65*	0.400
A(C)BAB..(hcp)	1.30	0.268
A(C)B(C)AB..(hcp)	1.32	0.276
A(C)B(C)A(C)..(hcp)	1.30	0.303
A(B)CABAB..(hcp)	1.30	0.269
C(B)A(C)BA..(hcp)	1.25	0.333
A(C)B(A)C(B)..(fcc)	1.27	0.350

* $d_{\text{Zr-N}}$ for underlayer fixed at 1.30 Å

models in which nitrogen atoms occupy all octahedral holes between the first and second layers of zirconium metal. However the present analysis is unable to distinguish between the surface structure designated A(C)BAB..., which has no zirconium reconstruction, and that designated A(B)CAB... with a local zirconium reconstruction. The latter is equivalent to A(C)BAC..., and for its first six atomic layers it differs from the first structure only by a lateral displacement of zirconium in the fourth metal layer. This relatively small difference in structure, for the probe depth of LEED, results in sets of calculated I(E) curves which are too similar for this technique to distinguish between the surface models (as seen in Figures 7.6 and 7.7). The single underlayer model is clearly favored compared both with overlayer models (including the combined overlayer and single underlayer model [129]) and with multiple underlayer models, although the model designated A(C)B(C)AB..., with a double underlayer of N, also gives a reasonable account of the experimental intensities. Following the experience for oxygen on zirconium, where disorder phenomena appear prominent, the actual nitrogen on zirconium surface studied here could quite plausibly contain single- and double-underlayer domains, perhaps with regions of only partial order. Such effects could limit the correspondence between experimental and calculated I(E) curves to just the moderate level (two representative comparisons are shown in Figure 7.4).

The LEED analysis for the model of Zr(0001)-(1x1)-N designated A(C)BABA... indicates that the interlayer spacing $d_{\text{Zr-N}}$ is equal to 1.30Å and, using the lateral Zr-Zr distance in zirconium metal [127], this gives a Zr-N bond length equal to 2.27Å, which agrees reasonably closely with the

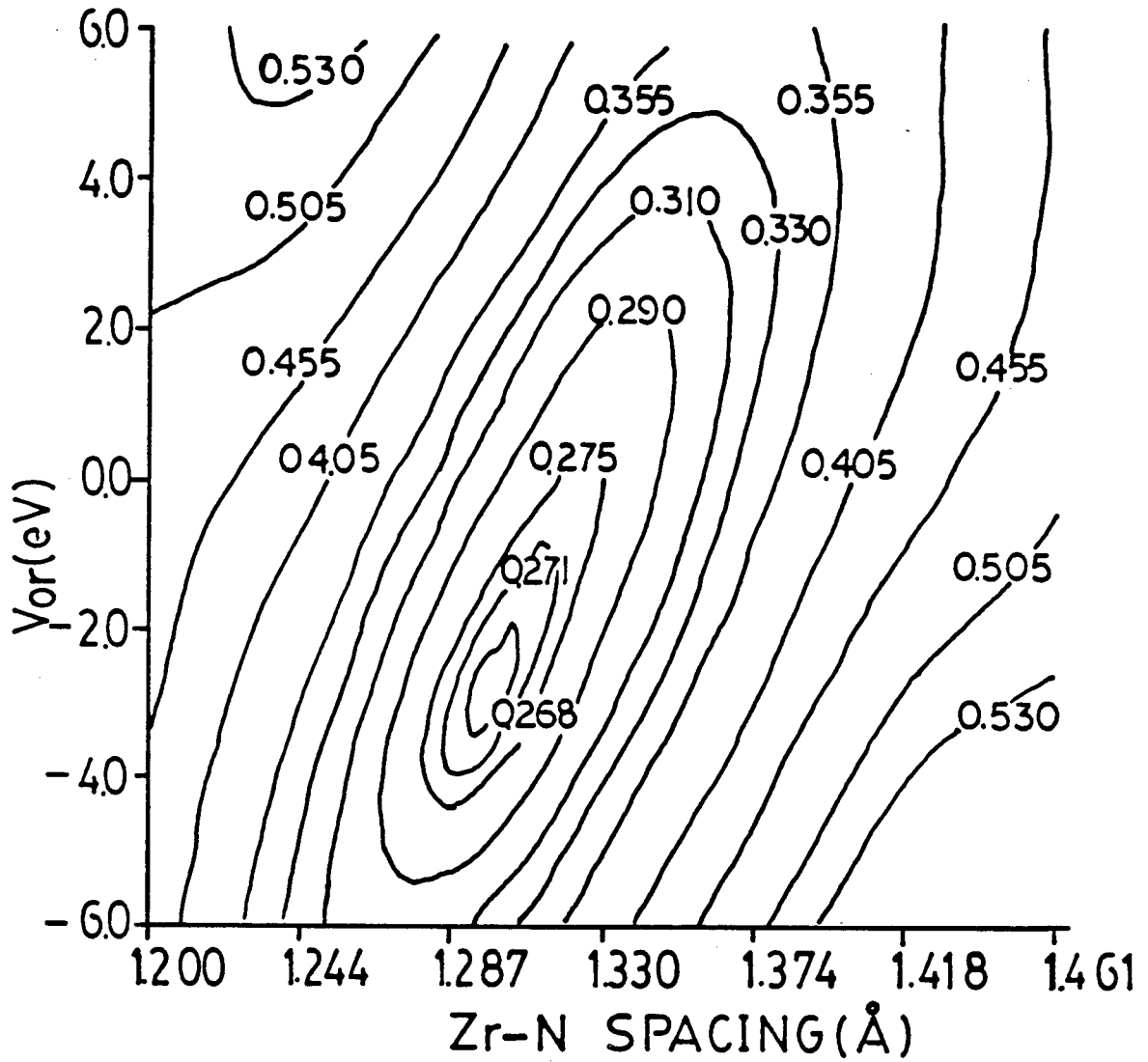


Figure 7.5: Contour plot for Zr(0001)-(1x1)-N of R_p versus V_{or} and the Zr-N interlayer spacing for the model $\bar{A}(C)BAB\dots$.

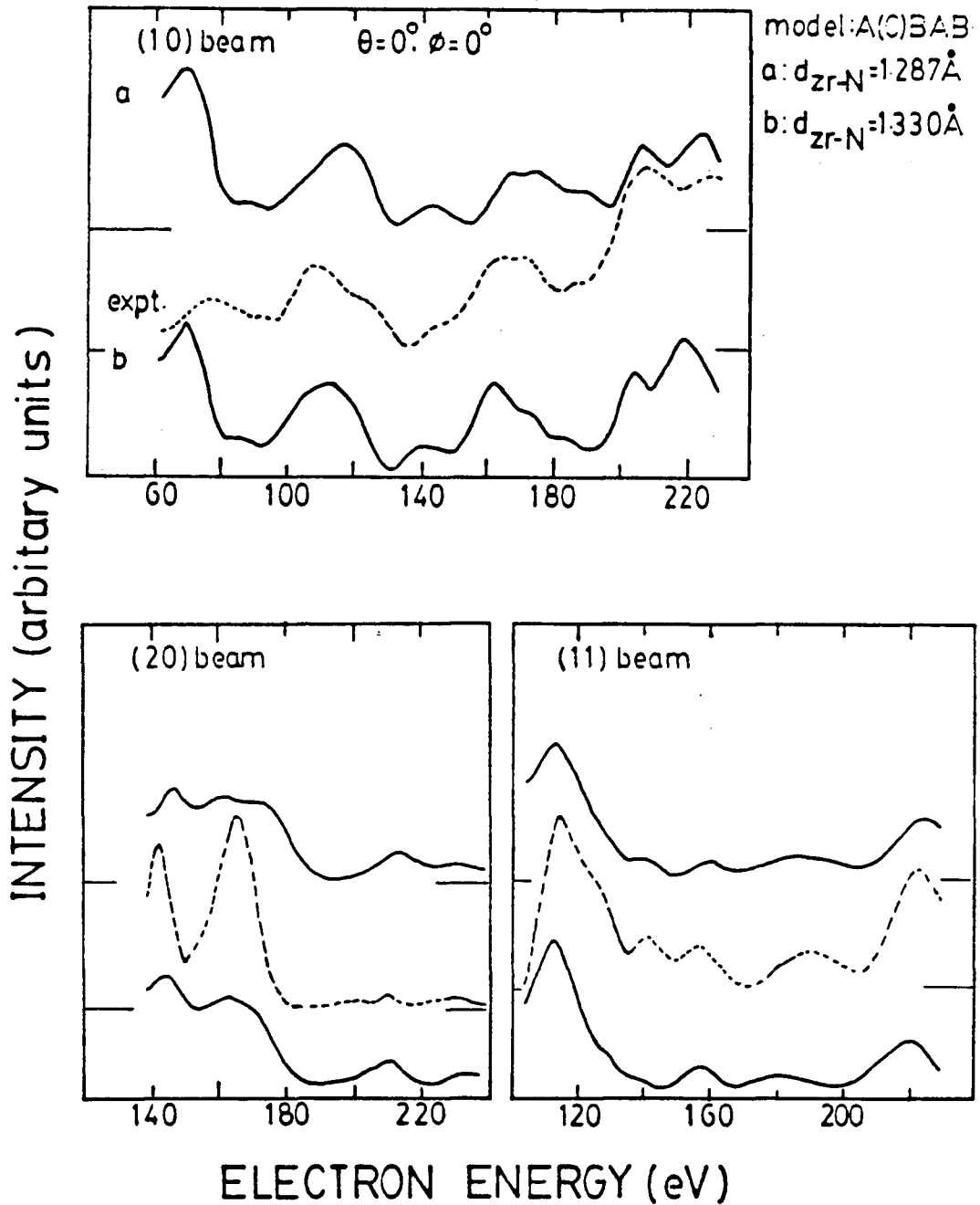


Figure 7.6: Comparison of experimental $I(E)$ curves (dashed) from $\text{Zr}(0001)-(1 \times 1)\text{-N}$ with those calculated for the model A(C)BAB... with $d_{\text{Zr-N}}$ equal to 1.287 Å (upper continuous line designated a) and 1.330 Å (lower continuous line designated b).

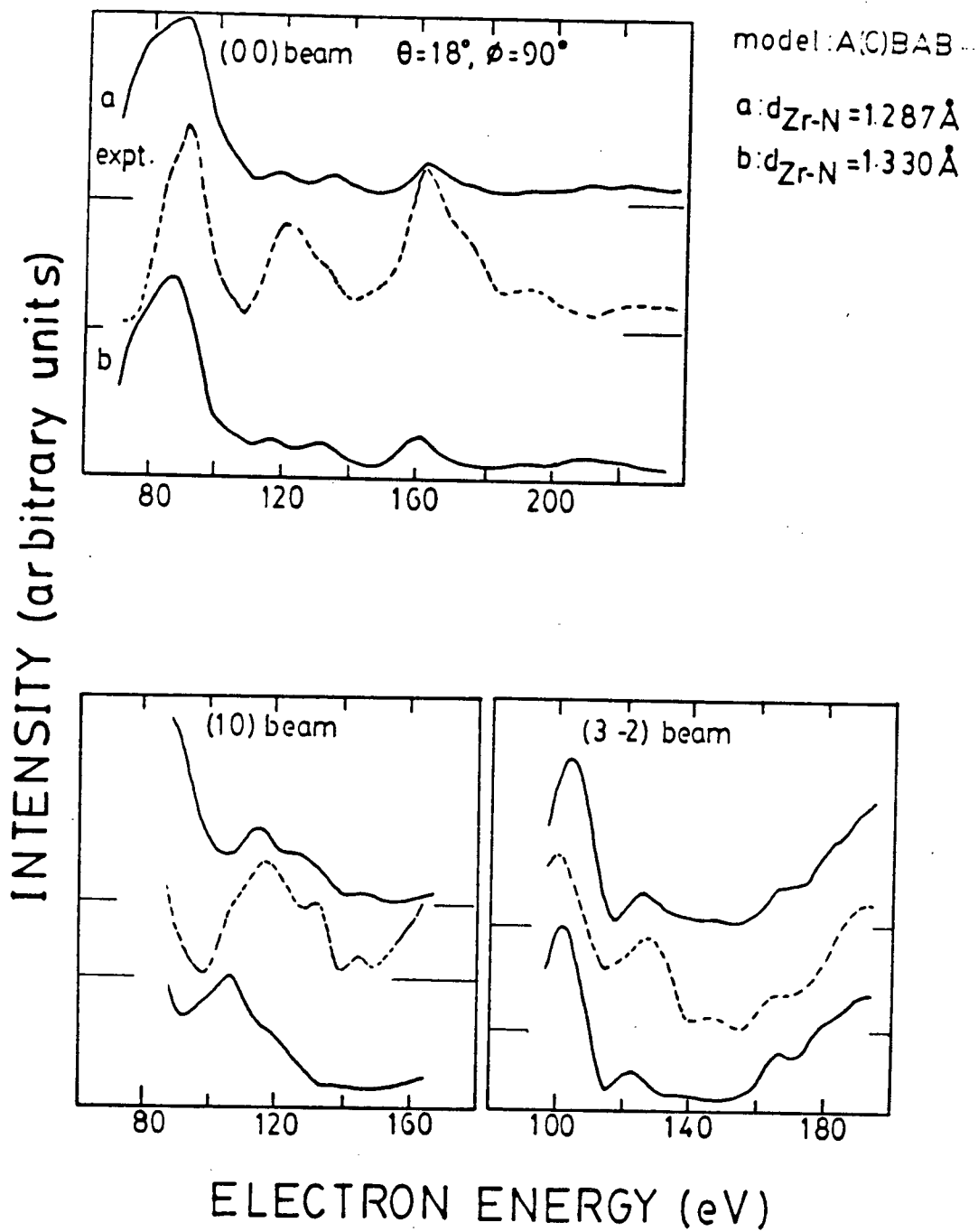


Figure 7.6: (continued)

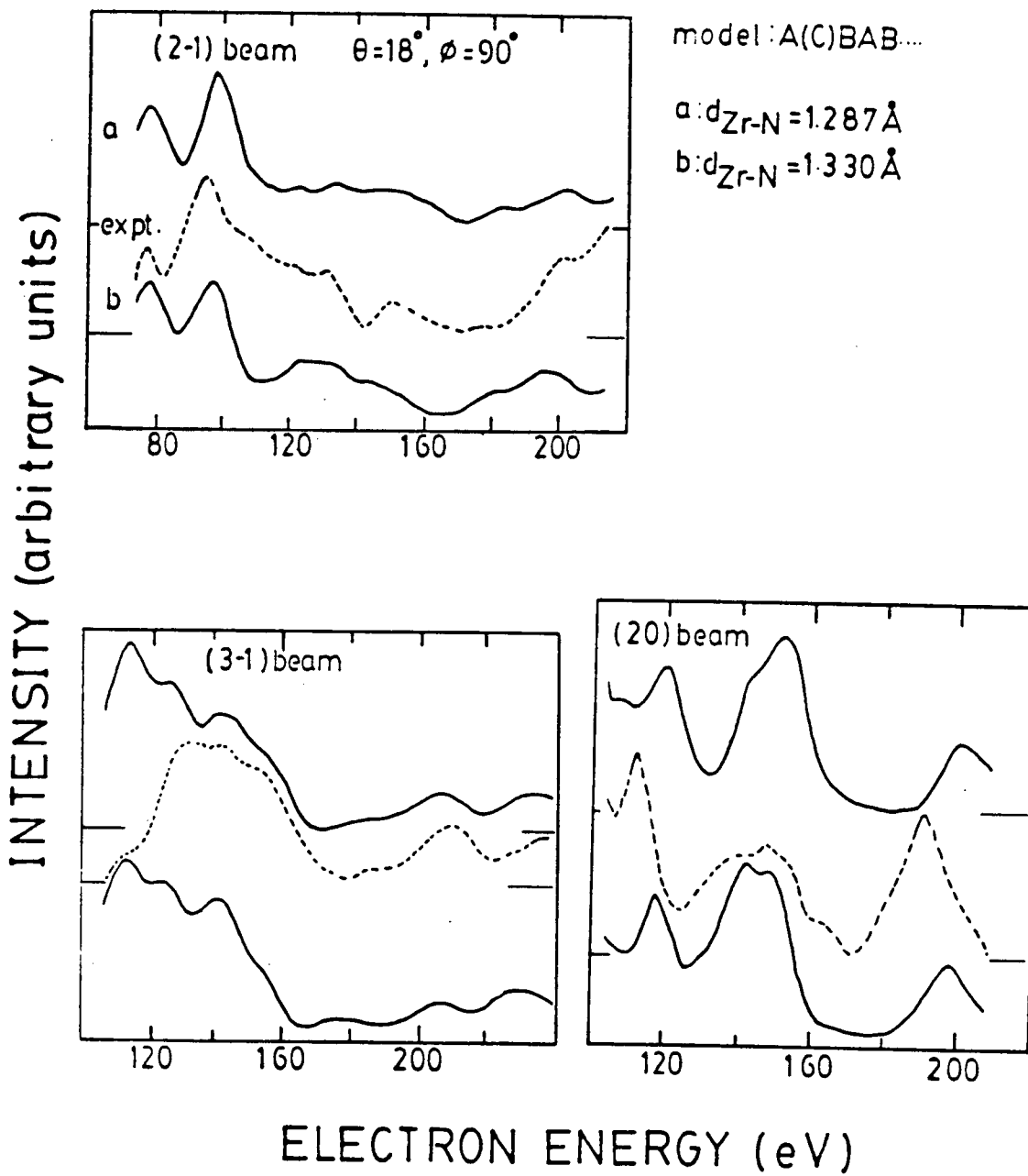


Figure 7.6: (continued)

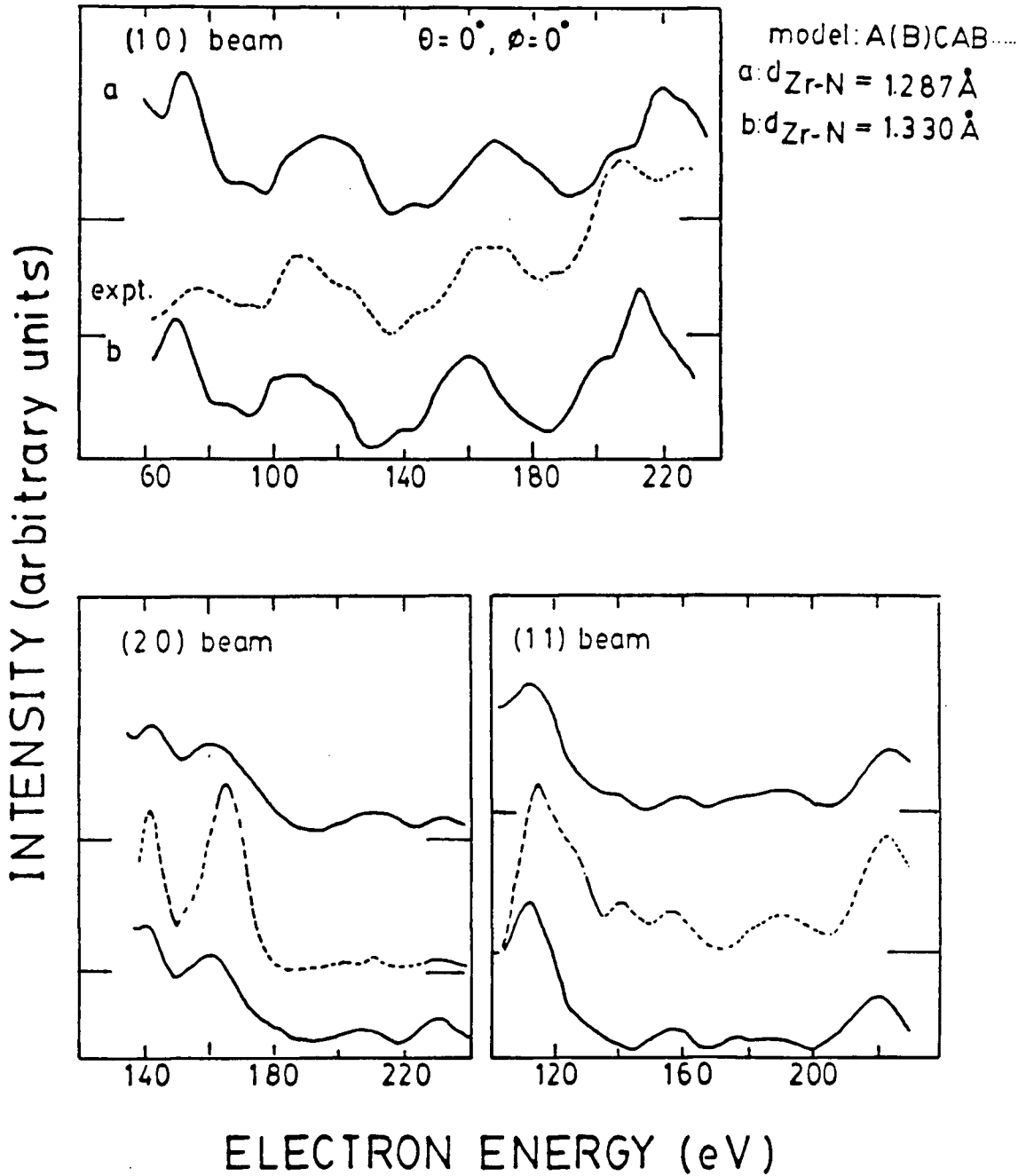


Figure 7.7: Comparison of experimental $I(E)$ curves (dashed) from $\text{Zr}(0001)-(1 \times 1)-\text{N}$ with those calculated for the model $\text{A(B)CAB} \dots$ with $d_{\text{Zr-N}}$ equal to 1.287 \AA (upper continuous line designated a) and 1.330 \AA (lower continuous line designated b).

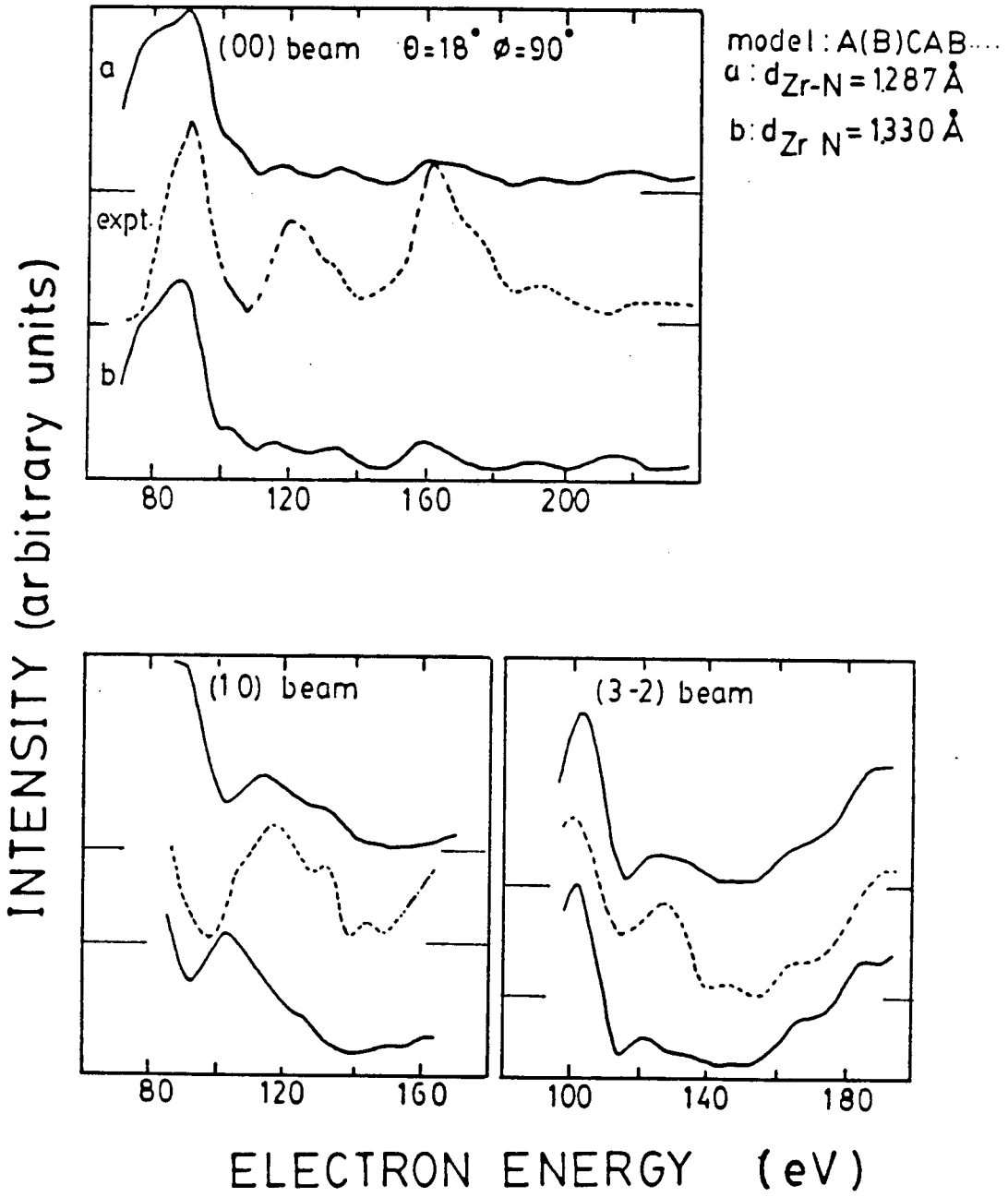


Figure 7.7: (continued)

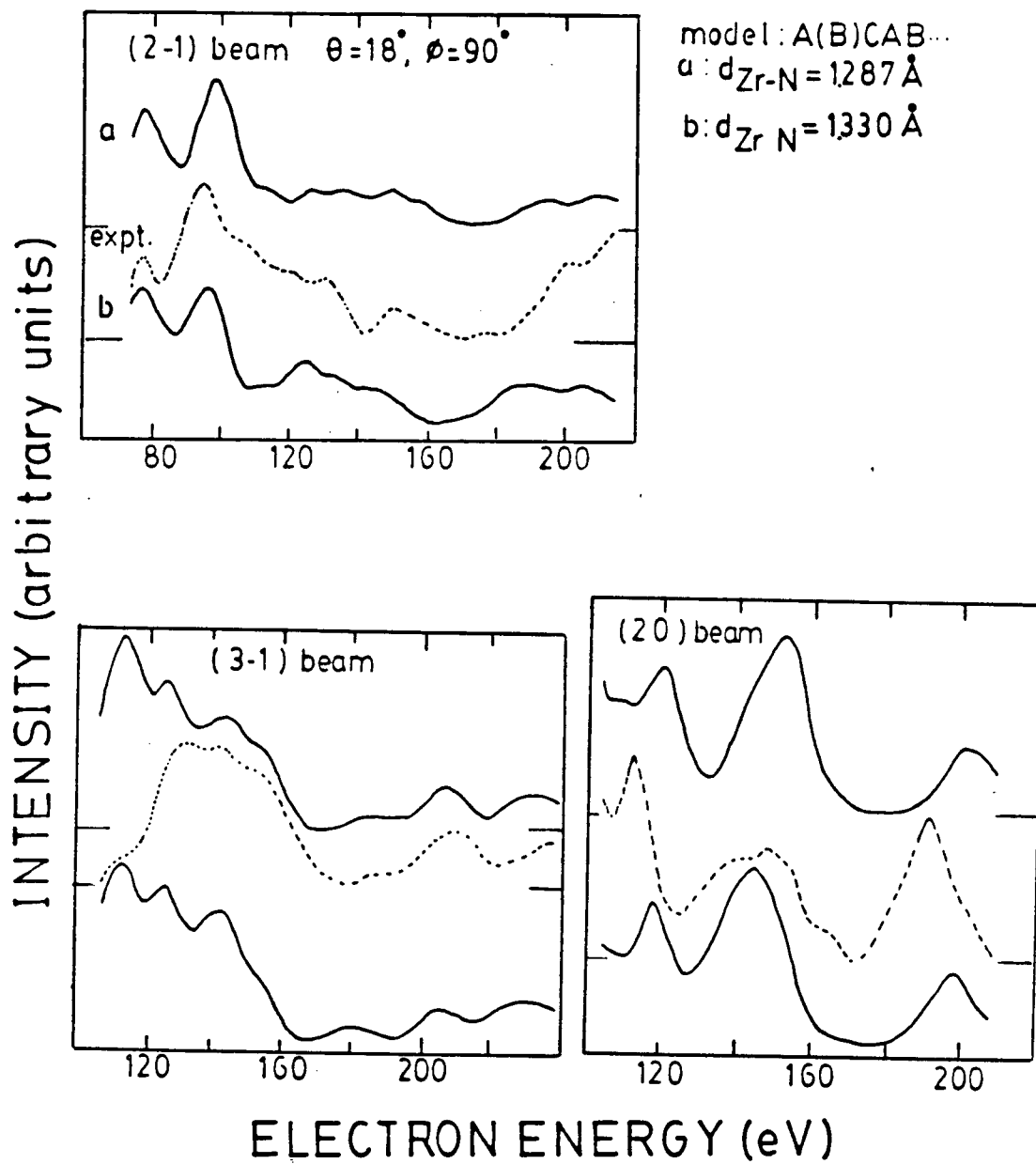


Figure 7.7: (continued)

value of 2.29\AA for bulk ZrN [138]. In this surface structure N incorporates between the first and second zirconium layers to give effectively three layers of ZrN(111), while the metal-metal interlayer spacing is changed hardly significantly from that in the clean metal (2.60\AA in lieu of 2.57\AA). This model for the Zr(0001)-(1x1)-N surface repeats in basic features that reported earlier by Shih et al. for the related structure Ti(0001)-(1x1)-N [58], although these authors apparently did not investigate double and multiple underlayer models.

The use of AES in this work indicates that nitrogen diffusion occurs less readily than oxygen diffusion into the zirconium metal, and similar observations were made by Foord et al. [113]. Consistently with these observations it seems that the LEED analysis for the Zr(0001)-(1x1)-N surface structure can rule out the multiple underlayer model, for the conditions of our surface preparation, although the corresponding statement cannot be made in the previous LEED analysis for Zr(0001)-(1x1)-O. Incidentally, the I(E) curves calculated for multiple underlayer models of Zr(0001)-(1x1)-N have significant differences from those of the corresponding single underlayer models (which result in differences reported in Table 7.1). That indicates the N atoms can contribute significantly to the analysis, even though no new LEED beams are introduced and the Zr-Zr interlayer spacing is hardly changed from that in the clean metal. It is important that LEED can still contribute to the determination of surface structure in cases such as this where, in addition, the adsorbed species is a relatively weak scatterer. For example, I(E) curves calculated from models which ignore the presence of N atoms agree

significantly less well with the experimental $I(E)$ curves from $Zr(0001)$ - (1×1) -N than do $I(E)$ curves calculated with the inclusion of N atoms (as seen in Figure 7.8).

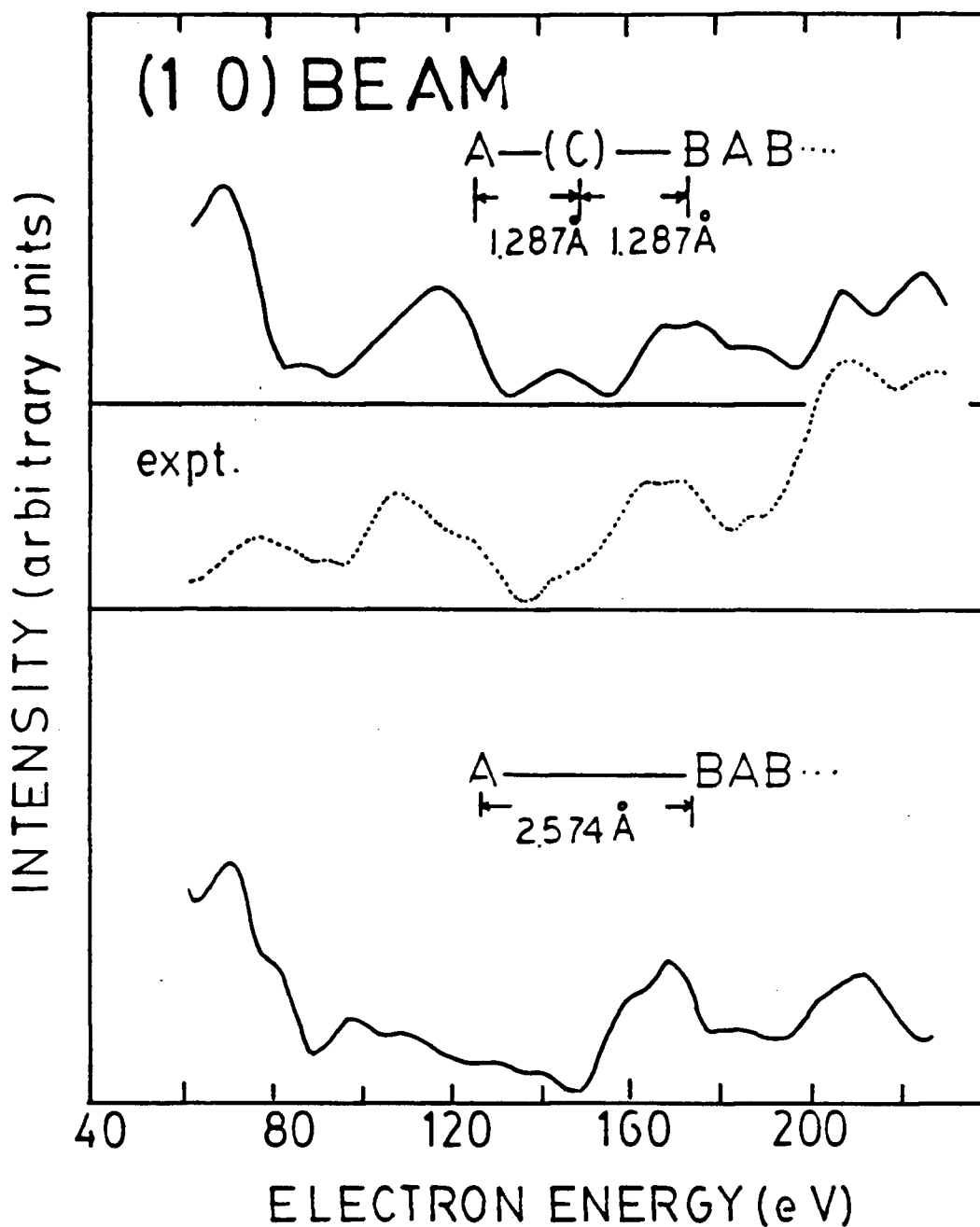


Figure 7.8: Comparison of experimental $I(E)$ curve for the (10) beam from $Zr(0001-(1 \times 1)-N$ for normal incidence with that calculated for the model $A(C)BAB\dots$ with the Zr-N interlayer spacing equal to 1.287\AA , as well as that calculated for the similar model which just differs from the first by neglect of N. The interlayer spacing between first two Zr layers in both models is identical.

CHAPTER 8

Comparison of Oxygen and Sulfur Adsorption
on the (0001) Surface of Zirconium

8.1 Introduction

In the process of cleaning the Zr(0001) surface we have observed that bulk sulfur impurity atoms segregate to the surface on heating above 600°C. This contrasts with the behaviour of the lighter atoms like N and O which preferentially diffuse into the bulk on heating at above 500 K. Since we have studied the chemisorption of oxygen and nitrogen at coverages of the order of one monolayer on the Zr(0001) surface, and provided evidence in Chapters 6 and 7 that both these molecules react with zirconium to form the incipient structures ZrO and ZrN respectively, in this chapter we attempt to use LEED and AES to compare the adsorption and coadsorption of oxygen and H₂S on the Zr(0001) surface [139]. By way of comparison, we propose some possible sulfur "overlayer" models corresponding to an observed Zr(0001)-(3x3)-S structure. LEED I(E) curves have been measured from this surface at normal incidence, although a complete crystallographic analysis has not yet been attempted. Furthermore, it is also of interest to explore whether any surface reaction takes place between adsorbed oxygen and sulfur, as well as to investigate the adsorption properties of oxygen on a sulfur pretreated Zr(0001) surface and vice versa.

8.2 Experimental

These experiments use high-purity oxygen and H₂S gases which were directed to the cleaned and well-ordered Zr(0001) surface via a nozzle in the UHV chamber. For various exposures of the adsorbing gases, the relative amounts of adsorbed species were assessed with appropriate Auger peak height ratios, specifically for oxygen

$$R_o = A_{510}/A_{92}$$

(i.e. the ratio of the Auger peak height for O at 510 eV to that Zr at 92 eV) and for sulfur

$$R_s = A_{150}/A_{92}$$

(where A_{150} is the peak height for overlapping Zr and S Auger signals at 150 eV). After each adsorption experiment, the sample surface was cleaned by argon ion bombardment and re-ordered by heating to 600°C followed by immediate cooling (the heating and cooling rate are approximately 1°C s⁻¹). The clean zirconium surface is characterized with $R_o = 0.0$ and $R_s = 1.40$.

8.3. Results

8.3.1 Oxygen Adsorption

For the convenience of comparison, the adsorption of O₂ on Zr(0001) is briefly described again here. The exposure of a clean, ordered Zr(0001) surface to oxygen at room temperature yields a (1x1) LEED pattern with high background, although (2x2) patterns are observed after heating below 220°C (i.e. at less than the temperature at which diffusion into the bulk occurs); we interpret this heating as providing just an ordering effect. The sharpest (2x2) pattern was obtained for an initial oxygen exposure (1.2 L) which gives R_o equal to 0.16; the associated surface structure appears sufficiently stable at room temperature and 10⁻¹⁰ Torr for the sharp LEED pattern to be maintained for at least 3 days. With larger initial

exposures to oxygen the (2x2) pattern gives way to a (1x1) pattern, which is best established with an exposure of about 3.6 L and a surface coverage corresponding to $R_o = 0.23$. The LEED intensity-versus-energy curves for this structure have clear differences from those of the clean Zr(0001) surface; examples for (11) beams are indicated in Figure 8.1.

8.3.2. Hydrogen Sulfide Adsorption

When a cleaned and ordered Zr(0001) surface was exposed to about 4.2 L of H₂S at room temperature, sulfur adsorption occurred ($R_s = 2.8$), but no extra LEED beams were detectable even after heating to 500°C. However, on heating to 530°C, R_s was found to increase to 3.1, an observation, which in conjunction with a report by Lin and Gilbert [140], appears to be associated with hydrogen desorption. Further, with a short heating to 600°C, a very sharp (3x3) LEED pattern was observed on cooling to room temperature, for which R_s remained at 3.1. Higher S coverages, as monitored by R_s , can be obtained by giving larger initial exposures to H₂S however, following annealing at 600°C, the (3x3) LEED pattern shows increasing disorder as R_s increases beyond 3.1. Intensity-versus-energy (I(E)) curves for the diffracted beams (e.g. Figure 8.2) suggest that the moderate-coverage (3x3) structures, with R_s less than 3.1, correspond to mixed regions of clean surface and of (3x3) domains. The latter regions appear to remain stable for long periods.

I(E) curves for LEED beams from the Zr(0001)-(3x3)-S structure with $R_s = 3.1$ were measured with the video LEED analyzer for the energy range

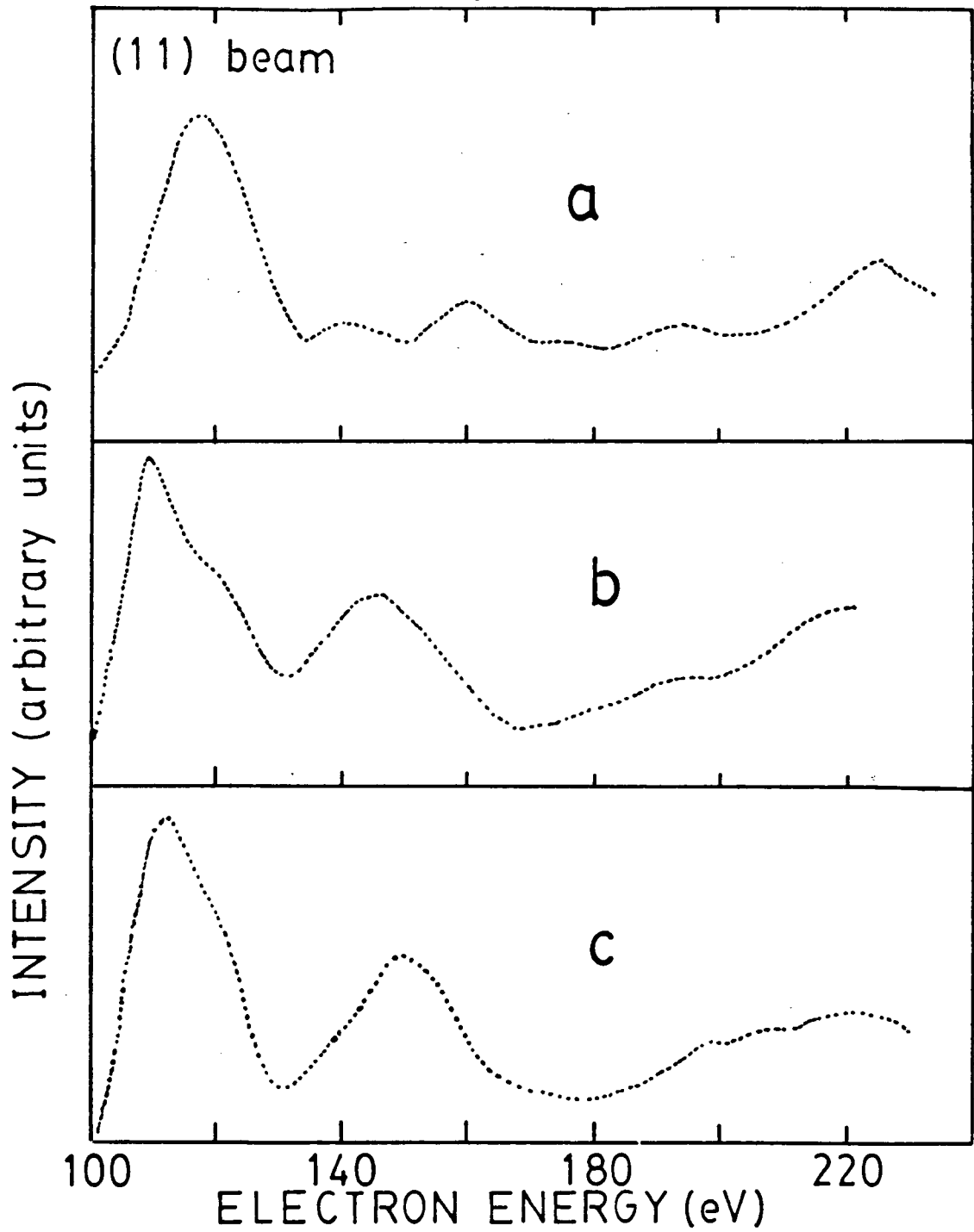


Figure 8.1: Experimental $I(E)$ curves for the (11) beam from (a) clean Zr(0001), (b) Zr(0001)-(2x2)-0 with $R_0 = 0.16$, (c) Zr(0001)-(1x1)-0 with $R_0 = 0.23$.

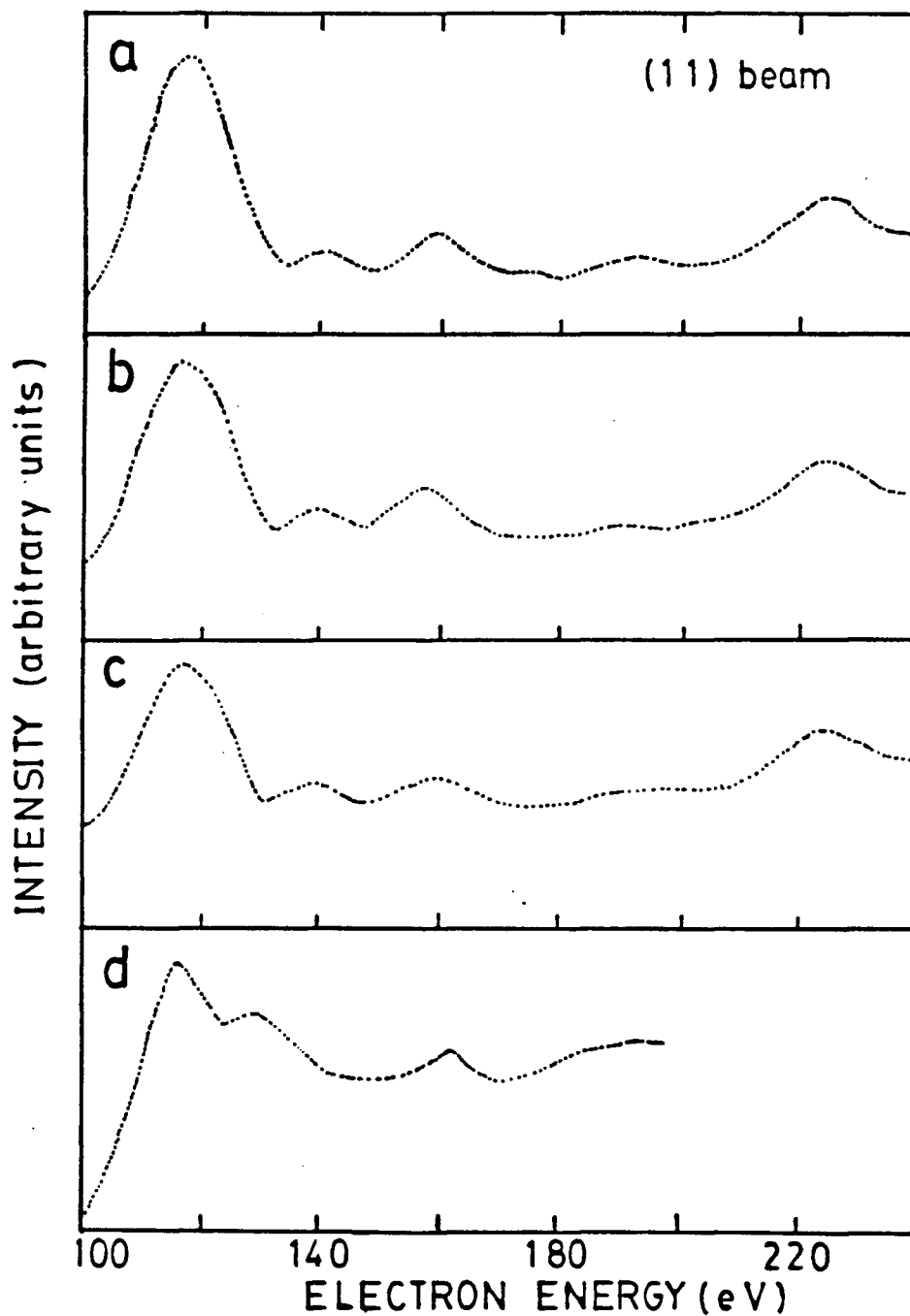


Figure 8.2: Experimental $I(E)$ curves for the (11) beam from (a) clean $Zr(0001)$, (b) $Zr(0001)-(3 \times 3)-S$ with $R_s = 1.9$, (c) $Zr(0001)-(3 \times 3)-S$ with $R_s = 2.4$, (d) $Zr(0001)-(3 \times 3)-S$ with $R_s = 3.1$.

50(2)200 eV exactly as described in Section 3.5.2. Ten independent $I(E)$ curves were measured for normal incidence for the beams designated (10), (11), $(2/3\ 0)$, $(4/3\ 0)$, $(0\ 5/3)$, $(2/3\ 1)$, $(4/3\ 1/3)$, $(1/3\ 1)$, $(2/3\ 2/3)$ and $(2/3\ 1/3)$ using the beam notations in Figure 8.3. The final averaged and smoothed experimental $I(E)$ curves are shown in Figure 8.4.

8.3.3. Oxygen and Hydrogen Sulfide Coadsorption

A series of experiments for assessing structural aspects of the coadsorption of O_2 and H_2S on an initially clean $Zr(0001)$ surface have been made, and the results are summarized in the following subsections.

8.3.3.1 O_2 on $Zr(0001)-(3 \times 3)-S$ with $R_s > 3.1$

No evidence could be found from AES or LEED for oxygen chemisorption occurring on the $(3 \times 3)-S$ surface, with R_s greater than 3.1, when it was exposed to oxygen at room temperature. The same statement holds for these surfaces when annealed following the procedures described above for forming the $Zr(0001)-(2 \times 2)-O$ and $Zr(0001)-(1 \times 1)-O$ surface structures. These observations suggest that the surface combination of S and O (with subsequent desorption of, for example, SO_2) does not occur to any significant extent for the conditions used.

8.3.3.2 O_2 on $Zr(0001)-(3 \times 3)-S$ with $R_s < 3.1$

When a partially-covered $(3 \times 3)-S$ structure was exposed to oxygen, and treated according to the conditions that give the $(2 \times 2)-O$ structure (as

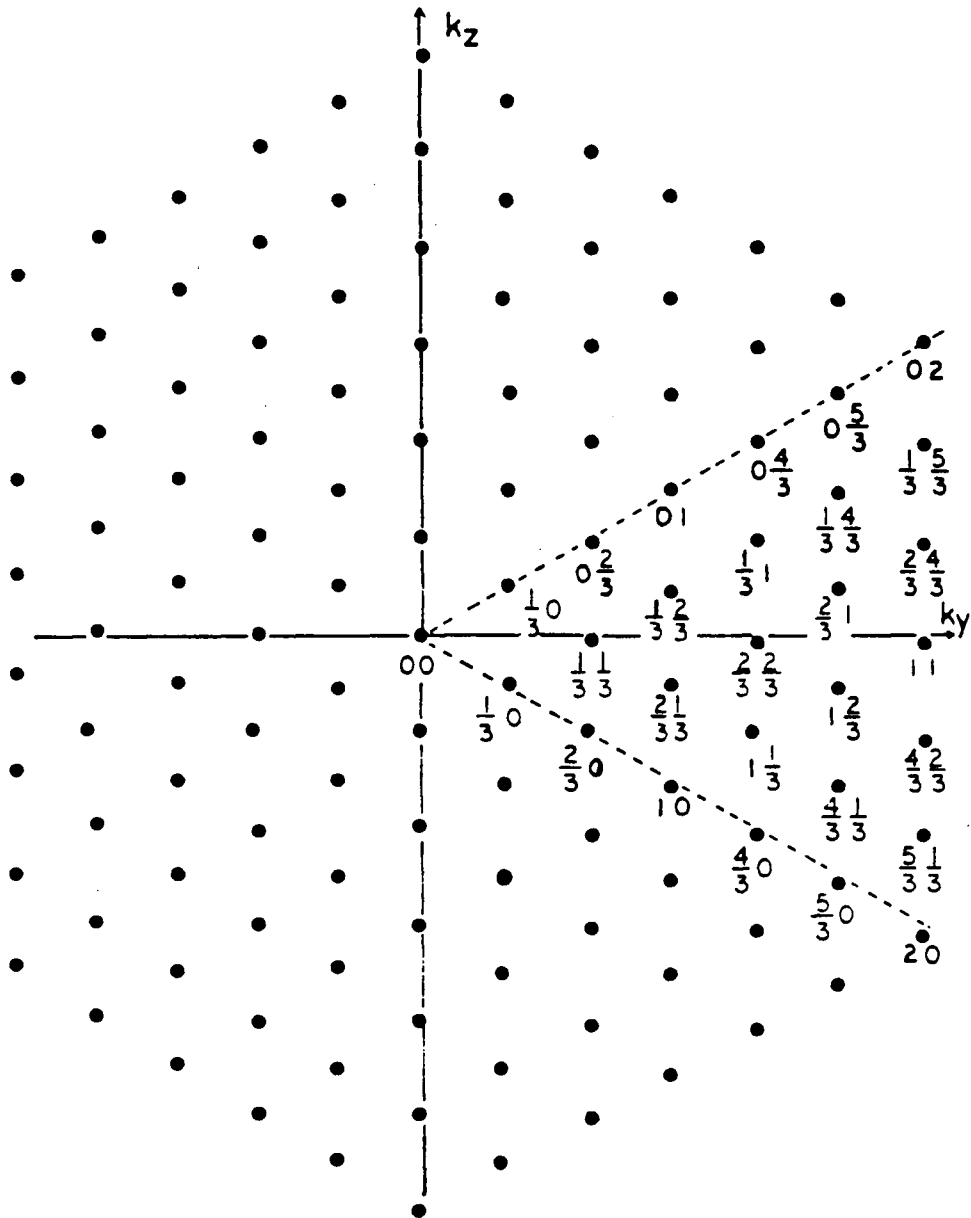


Figure 8.3: Schematic diagram for LEED pattern and beam notation for the $Zr(0001)-(3 \times 3)-S$ structure.

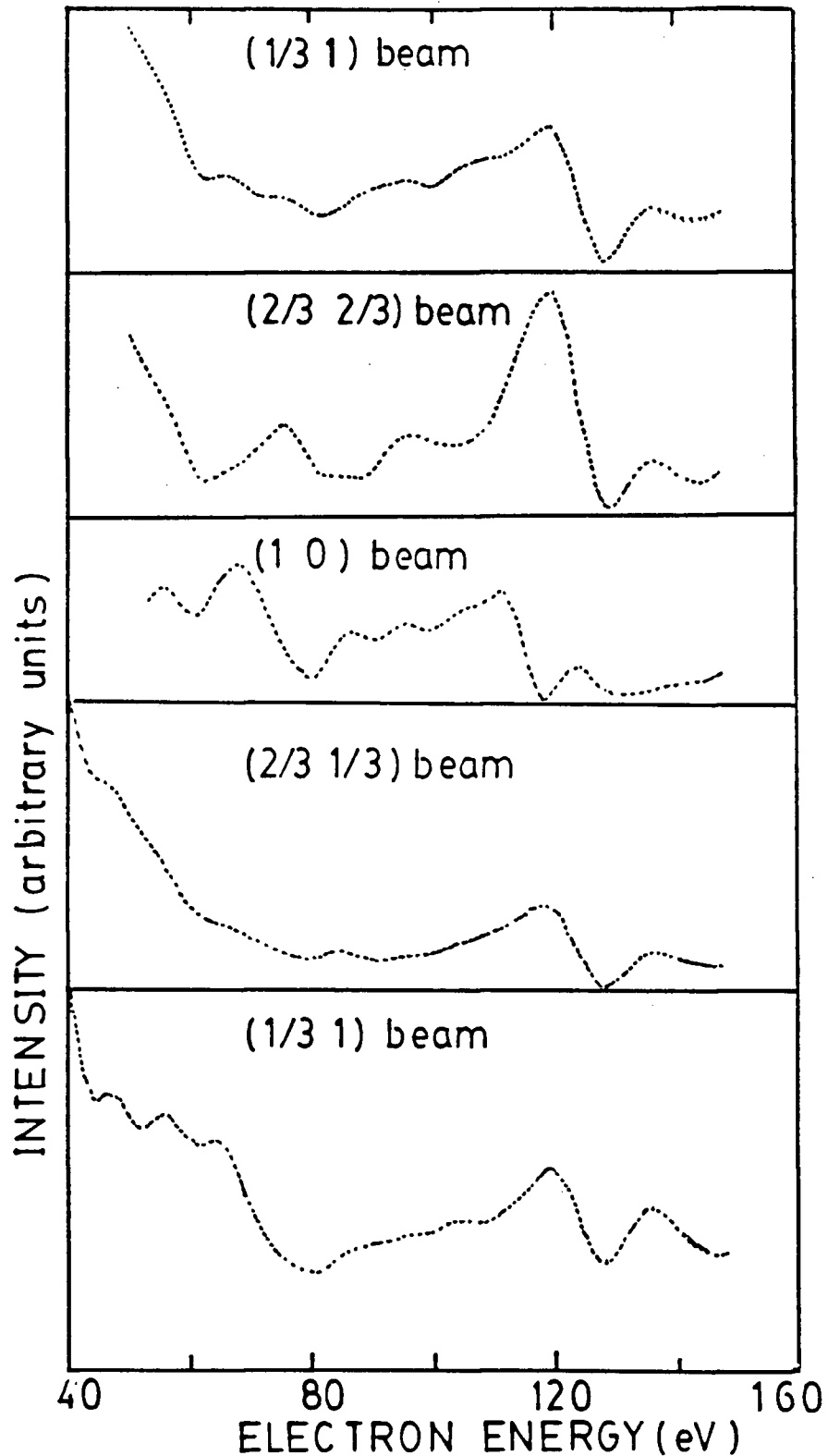


Figure 8.4: $I(E)$ curves measured for normal incidence from the $Zr(0001)-(3 \times 3)-S$ surface with $R_s = 3.1$ for the diffracted beams: $(1/3\ 1)$, $(2/3\ 2/3)$, $(1\ 0)$, $(2/3\ 1/3)$, $(1/3\ 1)$, $(2/3\ 1)$, $(4/3\ 1/3)$, $(4/3\ 0)$ and $(0\ 5/3)$.

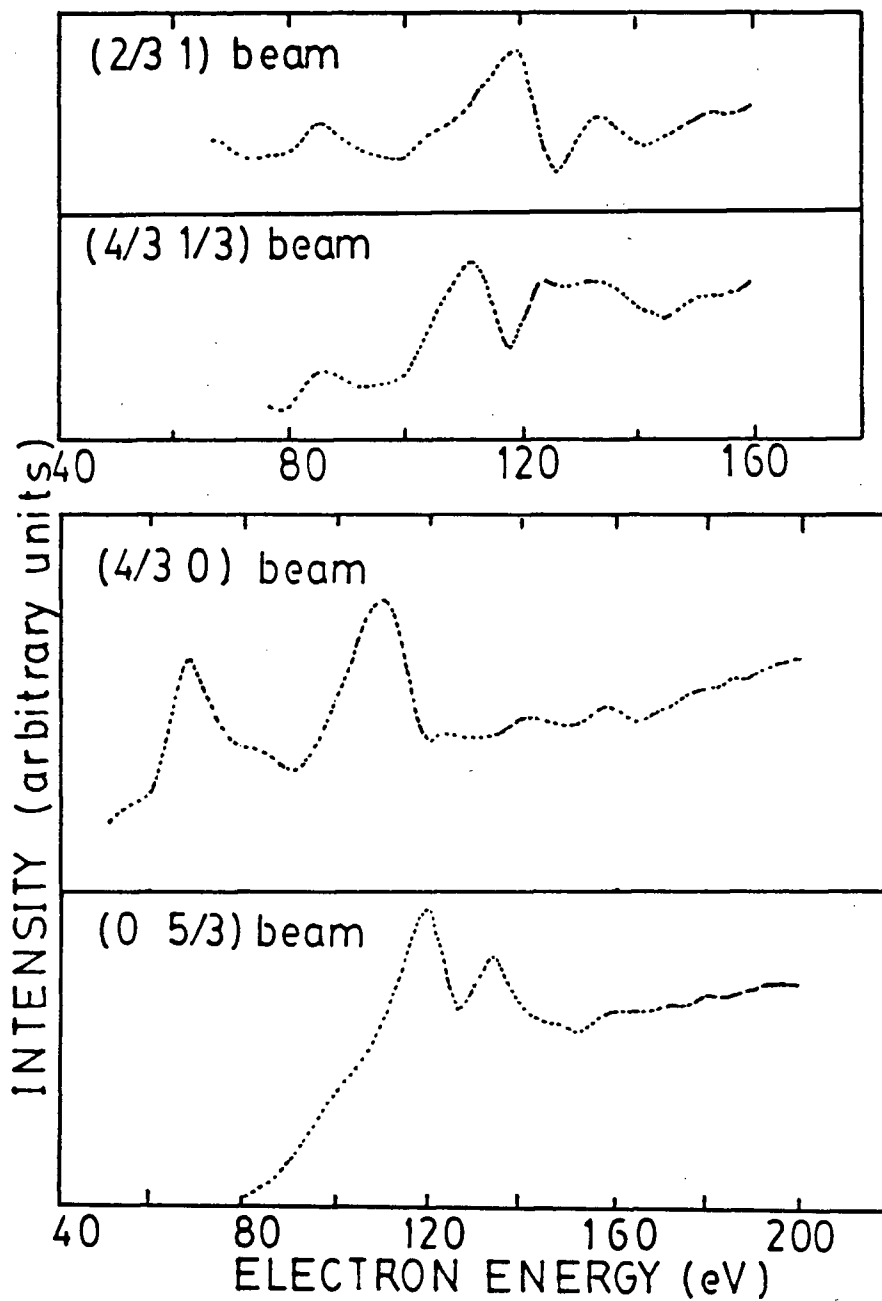


Figure 8.4: (continued)

moderately sharp (3x3) LEED pattern was restored on cooling to room temperature ($R_o = 0.0$, $R_s = 2.3$).

8.3.3.4 H₂S on Zr(0001)-(1x1)-0

The observation in Section 8.3.3.3 was found to extend even to a surface with the highest oxygen coverage considered here (viz. Zr(0001)-(1x1)-0 with $R_o = 0.23$). After exposure to H₂S at room temperature, the LEED pattern becomes diffuse with high background ($R_s = 2.3$, $R_o = 0.26$), but after annealing at 600°C and cooling to room temperature a sharp Zr(0001)-(3x3)-S pattern results with $R_s = 2.9$ and $R_o = 0.0$.

8.3.3.5 Coadsorption without Annealing

AES shows that the basic tendencies observed in 8.3.3.1 and 8.3.3.4 extend also to a Zr(0001) surface which is treated entirely at room temperature. Specifically it was found that oxygen does not significantly adsorb on a high-S-coverage Zr(0001) surface, whereas H₂S will adsorb on a high-O-coverage surface.

8.4 Discussion

This work highlights the contrasting behaviors of oxygen and sulfur chemisorption on the Zr(0001) surface. Thus while the highest coverage oxygen surface is still able to adsorb H₂S, the highest coverage sulfur surface does not adsorb oxygen in detectable amounts. These observations are consistent with oxygen forming subsurface structures (see Chapter 6), whereas sulfur atoms probably form a coincidence-site (3x3) structure in

which the overlayer involves either a sufficiently high density of S atoms to block O adsorption, or a protective combined layer of Zr and S, perhaps with a zirconium sulfide structure. A detailed determination of the geometry of the $\text{Zr}(0001)-(3 \times 3)\text{-S}$ surface structure is needed, but so far the analysis has been inhibited by the large computing cost that is expected to be involved. Nevertheless the general chemical observations reported here do appear to set some limits on possible structural arrangements for the S-chemisorption structure. Some models for S-overlayer structures are shown in Figure 8.5. These cover a range of coverage from $1/9$ to $4/9$ monolayers. The model designated A for the lowest coverage seems unlikely, since it may not be able to block subsequent oxygen adsorption; the structure C was previously proposed for the $\text{Pt}(111)-(3 \times 3)\text{-Cl}$ structure [141], although no confirming evidence has yet been provided. The formation of the immiscible structures corresponding to $\text{Zr}(0001)-(2 \times 2)\text{-O} + \text{Zr}(0001)-(3 \times 3)\text{-S}$ suggests that this coadsorption should be classified as a competitive coadsorption, rather than as a cooperative coadsorption which is most favorable for surface catalysis. Apparently within the adsorbed layers like-like interaction energies are favored over like-unlike interactions. Overall this work provides no evidence for significant sulfur and oxygen combination processes, either when surfaces with coadsorbed S and O are heated, or when S-saturated surfaces are heated in oxygen.

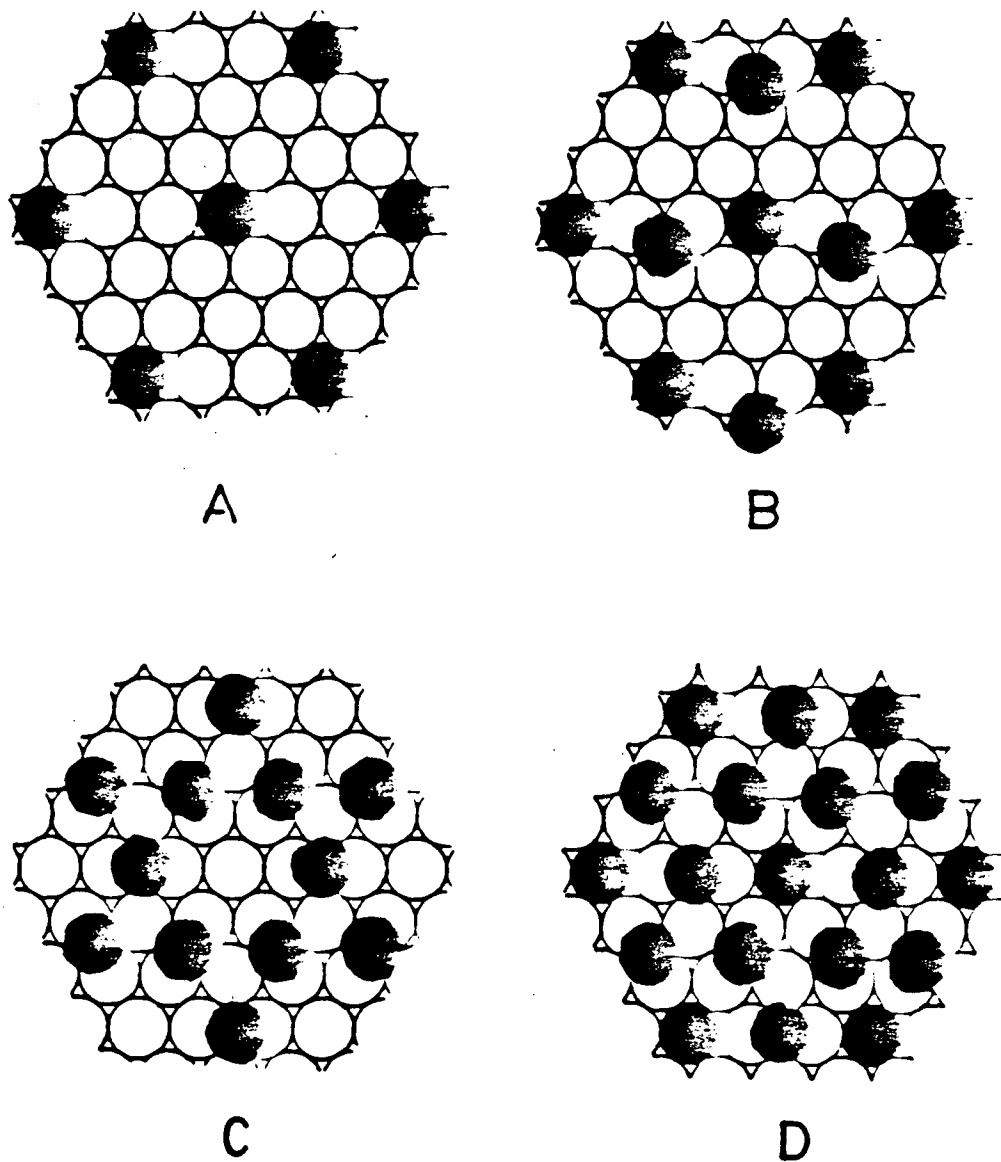


Figure 8.5: Some possible S overlayer structures (shaded circles) for the Zr(0001)-(3x3)-S surface. The sulfur coverages with respect to Zr (open circles) are: (A) 1/9 ML, (B) 2/9 ML, (C) 1/3 ML, (D) 4/9 ML. Lateral shifts of the S overlayers are possible.

8.5 Further work

Two significant temperatures have been identified for the sulfur on Zr(0001) system. One corresponds to the increase in R_g at 530°C, while the other relates to the formation of an ordered (3x3)-S structure on heating at around 600°C. These temperatures appear to be associated with the desorption of hydrogen, and with the S overlayer ordering process respectively; alternatively they may relate to the formation of a zirconium sulfide overlayer structure. More detailed investigations are required, both with the techniques used here and with XPS and thermal desorption spectroscopy (TDS). For example, TDS can be used to examine the desorption of hydrogen around 530°C, whereas XPS can assess the uptake curve of H₂S on Zr(0001) by measuring a sulfur peak without the overlapping peak problem which occurs in AES. Furthermore, it should be useful to examine the extent of surface sulfuration by probing shifts in zirconium 3d structure on exposing to H₂S and heating to give the (3x3)-S structure. Certainly the undertaking of a LEED crystallographic analysis for the Zr(0001)-(3x3)-S surface structure must remain a high priority.

Concluding Remarks

At present LEED crystallography inevitably involves a trial-and-error search for that structure in the multiple-scattering calculations which best agrees with the experimental data. Discrepancies always occur, although in some situations the agreement is better than in others. After determining a surface structure some uncertainties are necessarily left on whether other structures not considered could actually give better accounts of the experimental $I(E)$ curves. Obviously some systems are intrinsically more complicated than others, but in all cases the studies must be done to minimize deficiencies from both the experimental and computational sides. Also all conclusions should be scrutinized to see if they seem reasonable in relation to basic structural chemical principles.

Some discrepancies reported in this thesis between experimental and calculated intensities suggest refinements may be needed, perhaps on both the theoretical and experimental sides. In the analysis of the $\text{Rh}(111)-(\sqrt{3}\times\sqrt{3})30^\circ\text{-S}$ surface structure, the deficiency reported in the $I(E)$ curve calculated for the (01) beam at 170 eV could perhaps be due to neglect of metal relaxations induced by the chemisorbed species; nevertheless from the experimental side surface disorder and defects may have influenced the measurements. That emphasizes a general need to characterize surface defects more closely than we are currently able to do. Our use of the spot profile analysis seems helpful, although the "display-type" LEED system used in this work was not primarily designed for spot profile analysis. A

more helpful approach is provided by the fine-beam system with larger transfer width (e.g. 1000Å) introduced by Henzler [143] and marketed by Leybold-Heraeus. Ideally information from that approach would be complemented by the use of scanning tunneling microscopy, which can provide direct images of atomic defects on surfaces [144].

Our LEED crystallographic study for the Rh(111)-(2x2)-0 surface structure emphasized both the advantages of having a fast video measurement system (the data could not have been measured with the earlier spot photometer or Faraday cup methods) as well as the need to have an awareness of possible electron beam effects. In principle the beam disordering observed could be minimized by using a position-sensitive detector system as described for LEED by McRae et al. [145]. Such an approach can enable the primary beam current to be reduced by three orders of magnitude compared with the system used in the present work.

Deficiencies in the LEED crystallographic analyses of Zr(0001)-(1x1)-0 and Zr(0001)-(1x1)-N possibly arise from the model calculations not considering that the underlayer oxygen or nitrogen atoms may be distributed somewhat statistically over different depths and areas. Such possibilities have not, to my knowledge, been considered yet in LEED structural work. The subject of LEED crystallography is developing fast, and more effort is certainly needed on both the experimental and computational sides. Incomplete levels of correspondence between calculation and experiment are apparent in some of my work, and this indicates that future refinements may be needed. Nevertheless I aimed to show throughout that the results obtained do seem plausible in comparison with information available from the broader context of structural chemistry.

REFERENCES

1. F.R. Shepherd, P.R. Watson, D.C. Frost and K.A.R. Mitchell, *J. Phys.* C11, 4591 (1978).
2. W.T. Moore, P.R. Watson, D.C. Frost and K.A.R. Mitchell, *J. Phys.* C12, L887 (1979).
3. R.E. Schlier and H.E. Farnsworth, *J. Chem. Phys.* 30, 917 (1959).
4. G. Ertl and J. Küpper, "Low Energy Electrons and Surface Chemistry", Verlag Chemie (1985).
5. T.A. Carlson, "Photoelectron and Auger Spectroscopy", Plenum, N.Y. (1975).
6. W. Heiland and E. Taglauer, *Methods Expt. Phys.* 22, 299 (1985).
7. L.J. Clarke, "Surface Crystallography", John Wiley and Sons, London (1985).
8. F. Jona, J.A. Strozier Jr. and W.S. Yang, *Rep. Prog. Phys.* 45, 527 (1982).
9. J.M. Van Hove, C.S. Lent, P.R. Pukite and P.I. Cohen, *J. Vac. Sci. Technol.* B1, 741 (1983).
10. I.K. Robinson, W.K. Waskiewicz, P.H. Fuoss, J.B. Stark and P.A. Bennett, *Phys. Rev.* B33, 7013 (1986).
11. Y. Margoninski, *Contemp. Phys.* 27, 203 (1986).
12. C.S. Fadley, *Prog. Surf. Sci.* 16, 275 (1984).
13. J. Stohr, in "X-ray Absorption: Principles, Applications, Techniques of EXAFS, SEXAFS, XANES", eds. R. Prins and D.C. Koningsberger, Wiley, N.Y. (1985).
14. P. Eisenberger, P. Citrin, R. Hewitt and B. Kincaid, *Crit. Rev. Solid State and Material Sci.* 10, 191 (1981).
15. G. de Ross, J.M. Fluit, J.H.M. deWit and J.W. Geus, *Surf. Interface Anal.* 3, 229 (1981).
16. H. Ibach and D.L. Mills, "Electron Energy Loss Spectroscopy and Surface Vibrations", Academic Press, N.Y. (1982).

17. F.J. Himpsel, *Adv. Phys.* 32, 1 (1983).
18. E.A. Wood, *J. Appl. Phys.* 35, 1306 (1964).
19. N.F.M. Henry and K. Lonsdale, eds. "International Tables for X-ray Crystallography", Vol. 1, The Kynoch Press, Birmingham (1952).
20. L.C. Feldman and J.W. Mayer, "Fundamental of Surface and Thin Film Analysis", North-Holland, London (1986).
21. H. Ibach in "Electron Spectroscopy for Surface Analysis" Topics in Current Physics Vol. 4, ed. H. Ibach, Springer-Verlag (1974).
22. A. Messiah, "Quantum Mechanics Vol. 2", North-Holland Publ. Co., Amsterdam (1961).
23. E. Merzbacher, "Quantum Mechanics", John Wiley and Sons, N.Y. (1961).
24. B.W. Holland and D.P. Woodruff, *Surf. Sci.* 36, 488 (1973).
25. R.L. Park and H.H. Madden, *Surf. Sci.* 11, 188 (1968).
26. P.J. Estrup and E.G. McRae, *Surf. Sci.* 25, 1 (1971).
27. L.D. Roelofs and P.J. Estrup, *Surf. Sci.* 125, 51 (1983).
28. R.L. Park, J.E. Houston and D.G. Schreiner, *Rev. Sci. Instr.* 42, 60 (1971).
29. G. Comsa, *Surf. Sci.* 81, 57 (1979).
30. W.S. Yang, F. Jona and P.M. Marcus, *Phys. Rev.* B28, 2049 (1983).
31. P. Auger, *J. Phys. Radium* 6, 205 (1925).
32. P.W. Palmberg, G.E. Riach, R.E. Weber and N.C. MacDonald, "Handbook of Auger Spectra" Physical Electronics Industries Inc., Minnesota, 1972.
33. M.E. Packer and J.M. Wilson, "Auger Transitions" Institute of Physics, London, 1973.
34. C.D. Wagner, *Disc. Faraday Soc.* 60, 291 (1975).
35. D. Briggs and M.P. Seah "Practical Surface Analysis by Auger and X-ray Photoelectron Spectroscopy", John Wiley and Sons, London (1983).
36. G.C. Bond, "Catalysis by Metals", Academic Press, London, 320 (1962).
37. G.A. Mills and F.W. Steffgen, *Catalysis Rev.* 8, 159 (1974).

38. M. Shelef, *Catalysis Rev.* 11 (1975).
39. G.C. Bond, "Catalysis by Metals", Academic Press, London, 447 (1962).
40. S. Hengrasmee, P.R. Watson, D.C. Frost and K.A.R. Mitchell, *Surf. Sci.* 87, L249 (1979).
41. S. Hengrasmee, P.R. Watson, D.C. Frost and K.A.R. Mitchell, *Surf. Sci.* 92, 71 (1980).
42. J.H. Schemel and H.S. Rosenbaum, "Zirconium in Nuclear Applications", Am. Soc. for Testing and Materials, Special Tech. Publ. 551, Philadelphia (1973).
43. K.C. Hui, R.H. Milne, K.A.R. Mitchell, W.T. Moore and M.Y. Zhou, *Solid State Commun.* 56, 83 (1985).
44. M.A. Van Hove and S.Y. Tong, "Surface Crystallography by LEED", Springer Verlag, Berlin (1979).
45. J.B. Pendry, "Low Energy Electron Diffraction", Academic Press, N.Y. (1975).
46. A magnetic tape provided by M.A. Van Hove (University of California, Berkeley), 1983.
47. D.S. Boudreaux and V. Heine, *Surf. Sci.* 8, 426 (1967).
48. J.C. Slater, *Phys. Rev.* 51, 840 (1937).
49. D. Aberdam, R. Baudoing and C. Gaubert, *Surf. Sci.* 62, 567 (1977).
50. D.W. Jepsen, P.M. Marcus and F. Jona, *Phys. Rev.* B5, 3933 (1972).
51. P.M. Marcus, F. Jona, S. Finch and H. Bay, *Surf. Sci.* 103, 141 (1981).
52. J.E. Demuth, P.M. Marcus and D.W. Jepsen, *Phys. Rev.* B11, 1460 (1975).
53. V.L. Moruzzi, J.F. Janak and A.R. Williams, "Calculated Electronic Properties of Metals", Pergamon Press, N.Y. (1978).
54. C.B. Duke, *Adv. Chem. Phys.* 27, 1 (1974).
55. P.M. Marcus, J.E. Demuth and D.W. Jepsen, *Surf. Sci.* 53, 501 (1975).

56. C.J. Davisson and L.H. Germer, Phys. Rev. 30, 705 (1927).
57. A.A. Maradudin, E.W. Montroll, G.H. Weiss and I.P. Ipatova, "Theory of Lattice Dynamics in the Harmonic Approximation", Academic Press, N.Y. (1971).
58. P.M. Marcus, in "Determination of Surface Structure by LEED", eds. P.M. Marcus and F. Jona, Plenum Press, N.Y. (1984).
59. J.L. Beeby, J. Phys. C1, 82 (1968).
60. S.Y. Tong and M.A. Van Hove, Phys. Rev. B16, 1459 (1977).
61. J.B. Pendry, Phys. Rev. Lett. 27, 856 (1971).
62. S.Y. Tong, Prog. Surf. Sci. 7, 1 (1975).
63. M.A. Van Hove and R.J. Koestner, in "Determination of Surface Structure by LEED", eds. P.M. Marcus and F. Jona, Plenum Press, N.Y. (1984).
64. E. Zanazzi and F. Jona, Surf. Sci. 62, 61 (1977).
65. J.B. Pendry, J. Phys. C13, 937 (1980).
66. W.T. Moore, D.C. Frost and K.A.R. Mitchell, J. Phys. C15, L5 (1982).
67. N.F.M. Henry, H. Lipson and W.A. Wooster, "The Interpretation of X-ray Diffraction Photographs", MacMillan, London (1960).
68. H.D. Shih, F. Jona, D.W. Jepsen and P.M. Marcus, Surf. Sci. 60, 115 (1976).
69. T.E. Madey, H.A. Engelhart and D. Menzel, Surf. Sci. 48, 304 (1975).
70. N.J. Taylor, Rev. Sci. Instrum. 40, 792 (1969).
71. F. Jona, Surf. Sci. 68, 204 (1977).
72. M.B. Webb and M.G. Lagally, Solid State Phys. 28, 301 (1973).
73. M.G. Lagally and J.A. Martin, Rev. Sci. Instr. 54, 1273 (1983).
74. H.L. Davis and J.R. Noonan, Surf. Sci. 115, L75 (1982).
75. P.C. Wong, M.Y. Zhou, K.C. Hui and K.A.R. Mitchell, Surf. Sci. 163, 172 (1985).
76. J.E. Demuth, D.W. Jepsen and P.M. Marcus, Phys. Rev. Letters 32, 1182 (1974).

77. C.M. Chan and W.H. Weinberg, *J. Chem. Phys.* 71, 3988 (1979).
78. F. Maca, M. Scheffler and W. Berndt, *Surf. Sci.* 160, 467 (1985).
79. K. Hayek, H. Glassl, A. Gutmann, H. Leonhard, M. Prutton, S.P. Tear and M.R. Welton-Cook, *Surf. Sci.* 152/3, 419 (1985).
80. K.A.R. Mitchell, *Surf. Sci.* 149, 93 (1985).
81. R.J. Koestner, M.A. Van Hove and G.A. Somorjai, *Surf. Sci.* 107, 439 (1981).
82. M.A. Van Hove, R.J. Koestner, J.C. Frost and G.A. Somorjai, *Surf. Sci.* 129, 482 (1983).
83. R.J. Koestner, M.A. Van Hove and G.A. Somorjai, *Surf. Sci.* 121, 321 (1982).
84. D.G. Castner, B.A. Sexton and G.A. Somorjai, *Surf. Sci.* 71, 519 (1978).
85. S.R. Keleman and T.E. Fischer, *Surf. Sci.* 87, 53 (1979).
86. J.E. Demuth, D.W. Jepsen and P.M. Marcus, *Surf. Sci.* 45, 733 (1974).
87. E. Parthe, D. Hohnke and F. Hullinger, *Acta Cryst.* 23, 832 (1976).
88. S. Geller, *Acta Cryst.* 15, 1198 (1962).
89. P. Colamarino and P. Orioli, *J. Chem. Soc. Dalton Trans* 845 (1976).
90. R.J. Butcher and E. Sinn, *J. Am. Chem. Soc.* 98, 2440 (1976).
91. R.H. Morris, Ph.D. Thesis, University of British Columbia (1978).
92. K.A.R. Mitchell, *J. Chem. Phys.* 73, 5904 (1980).
93. K.A.R. Mitchell, S.A. Schlatter and R.N.S. Sodhi, *Can. J. Chem.* 64, 1435 (1986).
94. K.A.R. Mitchell, S.A. Schlatter, *Can. J. Chem.* 63, 3631 (1985).
95. I.D. Brown and D. Altermatt, *Acta Cryst. B.* 41, 244 (1985).
96. H.D. Shih, F. Jona, D.W. Jepsen and P.M. Marcus, *Phys. Rev. Letters* 46, 731 (1981).
97. J.F. van der Veen, R.M. Tromp, R.G. Smeenk and F.W. Saris, *Surf. Sci.* 82, 468 (1979).

98. G.A. Somorjai, "Chemistry in Two Dimensions: Surfaces", Cornell University Press, Ithaca, N.Y., 1981.
99. J. Stohr, L.I. Johansson, S. Brennan, M. Hecht and J.N. Miller, Phys. Rev. B22, 4052 (1980).
100. F. Soria, V. Martinez, M.C. Munoz and J.L. Sacedon, Phys. Rev. B24, 2926 (1981).
101. D. Norman, S. Brennan, R. Jaeger and J. Stohr, Surf. Sci. 105, L297 (1981).
102. C.M. Chan and W.H. Weinberg, J. Chem. Phys. 71, 2788 (1979).
103. P.M. Marcus, J.E. Demuth and D.W. Jepsen, Surf. Sci. 53, 501 (1975).
104. P.A. Thiel, J.T. Yates, Jr. and W.H. Weinberg, Surf. Sci. 82, 22 (1979).
105. P.C. Wong, K.C. Hui, M.Y. Zhou and K.A.R. Mitchell, Surf. Sci. 165, L21 (1986).
106. J.A. Joebstl, J. Vacuum Sci. Technol. 12, 347 (1975).
107. K. Christmann, R.J. Behn, G. Ertl, M.A. Van Hove and W.H. Weinberg, J. Chem. Phys. 70, 4168 (1979).
108. W.T. Moore, S.J. White, D.C. Frost and K.A.R. Mitchell, Surf. Sci. 116, 261 (1982).
109. F. Jona, J.A. Strozier and W.S. Yang, Rept. Prog. Phys. 45, 527 (1982).
110. D.G. Welkie and M.G. Lagally, Thin Solid Films 93, 219 (1982).
111. M. Henzler, Surf. Sci. 132, 82 (1983).
112. R.L. Tapping, J. Nucl. Mat. 107, 151 (1982).
113. J.S. Foord, P.J. Goddard and R.M. Lambert, Surf. Sci. 94, 339 (1980).
114. K.O. Axelsson, K.E. Keck and B. Kasemo, Appl. Surf. Sci. 25, 217 (1986).
115. D.P. Valyukhov, M.A. Golubin, D.M. Grebenshchiko and V.I. Shestopalova, Soviet Phys. Solid State 24, 1594 (1982).
116. W.B. Pearson, A Handbook of Lattice Spacings and Structures of Metals and Alloys, Pergamon Press, 1958.

117. G.B. Hoflund, D.F. Cox and R.E. Gilbert, *J. Vac. Sci. Technol.* A1, 1837 (1983).
118. G.B. Hoflund, D.A. Asbury, D.F. Cox and R.E. Gilbert, *Appl. Surf. Sci.* 22/23, 252 (1985).
119. K.C. Hui and K.A.R. Mitchell, *Can. J. Phys.* 63, 1377 (1985).
120. P.C. Wong and K.A.R. Mitchell, *Can. J. Phys.* (1987), 65, 464 (1987).
121. P.C. Wong, K.C. Hui, B.K. Zhong and K.A.R. Mitchell, *Solid State Commun.* 62, 293 (1987).
122. F.M. Cain Jr., "Zirconium and Zirconium Alloys", American Soc. Metals (1953).
123. T.W. Hass, R.H. Grant and G.J. Dooley, *Phys. Rev.* B1, 1449 (1970).
124. M.Y. Zhou, R.H. Milne, M.A. Karolewski, D.C. Frost and K.A.R. Mitchell, *Surf. Sci.* 139, L181 (1984).
125. T.E. Madey, H.A. Engelhart and D. Menzel, *Surf. Sci.* 48, 304 (1975).
126. J.T. Yates, Jr., P.A. Thiel and W.H. Weinberg, *Surf. Sci.* 82, 45 (1979).
127. R.B. Russell, *J. Appl. Phys.* 24, 232 (1953).
128. K.C. Hui, Ph.D. Thesis, University of British Columbia (1986).
129. R.L. Strong and J.L. Erskine, *J. Vac. Sci. Technol.* A3, 1428 (1985).
130. R.W.G. Wyckoff, *Crystal Structures*, Vol. 1, Interscience, N.Y. (1963).
131. G. Ertl and J. Küppers, *Surf. Sci.* 21, 61 (1970).
132. M. Henzler, *Appl. Surf. Sci.* 11/12, 450 (1980).
133. R.O. Adams, in "The Structure and Chemistry of Solid Surfaces", Ed. G.A. Somorjai, John Wiley and Sons, N.Y. (1969), paper 70.
134. L.R. Danielson, M.J. Dresser, E.E. Donaldson and J.T. Dickinson, *Surf. Sci.* 71, 599 (1978).
135. M.J. Grunze, J. Fuhler, M. Neumann, C.R. Brundle, D.J. Auerbach and J. Behm, *Surf. Sci.* 139, 109 (1984).

136. P.C. Wong and K.A.R. Mitchell, Surf. Sci., 187, L599 (1987).
137. R. Imbihl, R.J. Behm, G. Ertl and W. Mortitz, Surf. Sci. 123, 129 (1982).
138. E. Rudy and F. Benesovsky, Monatsh. Chem. 92, 415 (1961).
139. P.C. Wong and K.A.R. Mitchell, Can. J. Chem. 64, 2409 (1986).
140. J.M. Lin and R.E. Gilbert, Appl. Surf. Sci. 18, 315 (1984).
141. W. Erley, Surf. Sci. 94, 281 (1980).
142. T.M. Lu and M.G. Lagally, Surf. Sci. 99, 695 (1980).
143. U. Scheithauer, G. Meyer and M. Henzier, Surf. Sci. 178, 441 (1986).
144. G. Binnig and H. Rohrer, IBM J. Res. Develop 30, 355 (1986).
145. E.G. McRae and R.A. Malic, Surf. Scic. 177, 74 (1986).